

DISSERTATION

STATIC AND DYNAMIC STUDY OF METAL SALT HYDRATES OF WEAKLY-
COORDINATING FLUOROANIONS BY VIBRATIONAL SPECTROSCOPY,
GRAVIMETRY, AND AN ANALYSIS OF PREVIOUSLY PUBLISHED X-RAY
STRUCTURES

Submitted by

Matthew R. Lacroix

Department of Chemistry

In partial fulfillment of the requirements

For the Degree of Doctor of Philosophy

Colorado State University

Fort Collins, Colorado

Spring 2021

Doctoral Committee:

Advisor: Steven H. Strauss

Eugene Chen

Jeff Bandar

John Ridley

Copyright by Matthew Lacroix 2021
All Rights Reserved

ABSTRACT

STATIC AND DYNAMIC STUDY OF METAL SALT HYDRATES OF WEAKLY-COORDINATING FLUOROANIONS BY VIBRATIONAL SPECTROSCOPY, GRAVIMETRY, AND AN ANALYSIS OF PREVIOUSLY PUBLISHED X-RAY STRUCTURES

Eighteen metal salt hydrates ($\text{Li}(\text{H}_2\text{O})_4(\text{Al}(\text{OC}(\text{CF}_3)_3)_4)$, $\text{Li}(\text{H}_2\text{O})(\text{B}(3,5\text{-C}_6\text{H}_3(\text{CF}_3)_2)_4)$, $\text{Li}(\text{H}_2\text{O})_n(\text{Ga}(\text{C}_2\text{F}_5)_4)$, $\text{Li}(\text{H}_2\text{O})(\text{PF}_6)$, $\text{Na}(\text{H}_2\text{O})(\text{PF}_6)$, $\text{Li}_2(\text{H}_2\text{O})_4(\text{B}_{12}\text{F}_{12})$, $\text{Na}_2(\text{H}_2\text{O})_2(\text{B}_{12}\text{F}_{12})$, $\text{K}_2(\text{H}_2\text{O})_2(\text{B}_{12}\text{F}_{12})$, $\text{Rb}_2(\text{H}_2\text{O})_2(\text{B}_{12}\text{F}_{12})$, $\text{Cs}_2(\text{H}_2\text{O})(\text{B}_{12}\text{F}_{12})$, $\text{Mg}(\text{H}_2\text{O})_6(\text{B}_{12}\text{F}_{12})$, $\text{Ca}(\text{H}_2\text{O})_n(\text{B}_{12}\text{F}_{12})$, $\text{Sr}(\text{H}_2\text{O})_n(\text{B}_{12}\text{F}_{12})$, $\text{Ba}(\text{H}_2\text{O})_n(\text{B}_{12}\text{F}_{12})$, $\text{Co}(\text{H}_2\text{O})_6(\text{B}_{12}\text{F}_{12})$, $\text{Ni}(\text{H}_2\text{O})_6(\text{B}_{12}\text{F}_{12})$, $\text{Zn}(\text{H}_2\text{O})_6(\text{B}_{12}\text{F}_{12})$, and $\text{Li}_2(\text{H}_2\text{O})_2(\text{TiF}_6)$) containing weakly coordinating anions were analyzed using room temperature ATR-FTIR spectroscopy. The goal was to investigate the relative strengths of water–anion hydrogen bonds in the solid-state. In all but one case, these hydrogen bonds take the form of O–H···F hydrogen bonds. The one exception is in the salt $\text{Li}_2(\text{H}_2\text{O})_4(\text{B}_{12}\text{F}_{12})$ where there are both O–H···F and O–H···O hydrogen bonds present. Based on the magnitude of the redshift of the $\nu(\text{OH})$ band(s) a qualitative scale for the comparison of the relative hydrogen bond strength is constructed. Included in this scale are additional metal salt hydrates taken from the literature. This spectroscopic study has produced some of the only room temperature spectra for water participating in hydrogen bonding in the solid-state where the $\nu_{\text{asym}}(\text{OH})$ and $\nu_{\text{sym}}(\text{OH})$ bands are individually resolvable. The weak nature of the O–H···F hydrogen bonds allows for resolution of $\nu(\text{OH})$ bands only 5 cm^{-1} apart in some cases. The two metal salt hydrates ($\text{Li}(\text{H}_2\text{O})_4(\text{Al}(\text{OC}(\text{CF}_3)_3)_4)$ and $\text{Li}(\text{H}_2\text{O})(\text{B}(3,5\text{-C}_6\text{H}_3(\text{CF}_3)_2)_4)$) are shown to possess the weakest O–H···F hydrogen bonds observed in the solid state at room temperature.

The salt $\text{Li}_2(\text{H}_2\text{O})_4(\text{B}_{12}\text{F}_{12})$ contains a cyclic $(\text{H}_2\text{O})_4$ water cluster, also known as the *R4* cluster, is presented, and discussed in the context of the FTIR spectrum of water clusters. Due to the nature of the weak O–H···F hydrogen bonding between the cluster and the surrounding anions the E and B fundamental

vibrations for the cluster were able to be determined. The peak-to-peak separation, and relative intensities of these two bands are consistent with computational results from the literature. This is the first time that the $R4$ water cluster has been successfully studied via FTIR spectroscopy without the presence of other clusters leading to ambiguity in the results.

Finally, direct observation of the effect of cation acidity on the relative strength of water–anion hydrogen bonding has been directly observed for the first time in the metal hexahydrate salts $M(H_2O)_6(B_{12}F_{12})$ ($M = Mg, Co, Ni, Zn$). These results, along with the correlation curves constructed in this work, show that it is not possible to assign relative hydrogen bond strength based on $O-H\cdots X$ bond length, nor is it possible to accurately approximate $O-H\cdots X$ bond length based on degree of $\nu(OH)$ redshift. Instead, it is shown that the relative basicity of the anion is the primary factor governing the relative hydrogen bond strength, and thus the degree of redshifting experienced by the $\nu(OH)$ band(s). The cation acidity also is shown to have a lesser, but observable, effect on the relative strength of $O-H\cdots X$ hydrogen bond. In addition to broadening our fundamental understanding of hydrogen bonding in the solid state, this work also shows that FTIR spectroscopy can be a useful tool for rapidly assigning relative basicity of new weakly coordinating anions without need the for complex protonation experiments.

ACKNOWLEDGEMENTS

The first three people I would like to acknowledge and thank are my wife Brianna Faulkner, and my parents Richard and Patty Lacroix. Each has given me their full support throughout my life, and I am truly grateful to have each of them in my life. Brianna, especially during my time at CSU, has been my rock. Without her constant support and reassurance I am not sure I would have been able to make it this far. I am truly blessed to have my best friend as a partner. My parents have likewise been a source of constant support throughout my time at CSU. My father often excitedly telling all his friends that his “son is going to be a doctor.” The excitement with which he would say this has often been a source of inspiration to push through the hard times and continue to work towards this momentous milestone in my life. My mother was always willing and excited to speak with me over the phone, or fly me home for the holidays, when I needed to get my mind off work and just relax for a short period of time. I would also like to thank my extended family, my in-laws, and my wife’s extended family for all of support and good memories over the years.

I would also like to thank Professor Steve Strauss and Olga Boltalina. I remember meeting both of you for the first-time during visitation and the excitement you had for discussing your research was partially what drew me to the group. During visitation, rotations, and when I eventually joined the group you both have always made me feel welcome and that my contributions were valued. You both have taught me so much, both scientifically and generally. Always being available when I had questions or needed guidance was truly invaluable. Some of my favorite memories from group meetings were those held after you returned from your many trips, and all of the beautiful pictures of birds you would share at the beginnings of those meetings.

I would like to thank Professor Yong Liu at the University of Colorado Denver for his assistance, without which most of this work would not have been possible. I would like to thank Professor Nancy Levinger for all of her support when it came to successfully completing my independent research proposal, which turned into a more daunting process than I had originally thought. I would like to thank Ben Reynolds and Lonnie Thomas for their assistance during each of the many semesters of general chemistry that I taught. I would like to thank Professors Amy Prieto, Jamie Neilson, and Rick Finke, as well as Chris Rithner and

Brian Newell in the CIF for numerous conversations and assistance with various aspects of my research at CSU. I would also like to give special thanks to both Jamie and Amy, as well as their groups, for supplying me with some of the essential chemicals I needed to prepare the materials I studied in this work. Without those chemicals, as many as half of these compounds would have been much more difficult to prepare. I would like to thank Professor Ingo Krossing at the University of Freiburg, Professor Berthold Hoge at Bielefeld University, Professor Shiv Halasyamani at the University of Houston, and Professor Andrew Weller at the University of Oxford for providing me with samples of metal salt hydrates synthesized in their labs for my analysis. I would like to thank Professor Matt Shores and Romeo Portillo for their assistance when a critical ATR-FTIR experiment came up, and an instrument was not available. I would also like to thank the members of my group Eric Bukovsky, Kerry Rippey, Nick Deweerd, Brian Reeves, Colin Brook, and W. Matt Jones. Each of you were invaluable resources during my time at CSU. Be it your participation in my practice talks, to showing me how to do a particular lab technique, I would not have been successful without each of you.

Finally, I would like to thank all of the friends I have made along the way. From my friends back in San Diego (Justin, Nick, Alex, Zack, Austin, Mason, Nick, Eddie, Alex, Rebi, Mike, Hadrian, John, Dan, Matt, Marsh, Ariana, and Ben) to the friends I made here in Colorado (Jake, Rei, Heidi, Ryan, Russel, Mortaza, Kelly, Max, Rex, Alison, Jakki, Harmony, John, James, Logan, Ben, Foster, Brad, and all of the people from the many events at Total Escape Games) without all of you, life would have been much less exciting. I am happy to think of you all as friends for life, even if we drift apart over the coming decades.

TABLE OF CONTENTS

ABSTRACT.....	ii
ACKNOWLEDGEMENT	iv
LIST OF TABLES	xi
LIST OF FIGURES	xiii
CHAPTER 1 INTRODUCTION	1
1.1 Background and Introduction to the Research.....	1
References	10
CHAPTER 2 UNUSUALLY SHARP FTIR $\nu(\text{OH})$ BANDS AND WEAK HYDROGEN BONDING IN ALKALI METAL SALT HYDRATES OF WEAKLY-COORDINATING FLUOROANIONS	20
2.1 Introduction and Relevant Literature	20
2.2 Experimental	23
2.2.1 Reagents and Solvents	23
2.2.2 General Procedures	23
2.2.3 Synthesis of $\text{K}_2(\text{H}_2\text{O})_2(\text{B}_{12}\text{F}_{12})$	24
2.2.4 Preparation of $(\text{H}_3\text{O})_2(\text{B}_{12}\text{F}_{12})$.....	24
2.2.5 Synthesis of $\text{Rb}_2(\text{H}_2\text{O})_2(\text{B}_{12}\text{F}_{12})$	24
2.2.6 Synthesis of $\text{Cs}_2(\text{H}_2\text{O})(\text{B}_{12}\text{F}_{12})$	25
2.2.7 Synthesis of $\text{Na}_2(\text{H}_2\text{O})_2(\text{B}_{12}\text{F}_{12})$	25

2.2.8 Synthesis of $\text{Li}_2(\text{H}_2\text{O})_4(\text{B}_{12}\text{F}_{12})$	25
2.2.9 Synthesis of $\text{Li}_2(\text{H}_2\text{O})_2(\text{TiF}_6)$	25
2.2.10 ATR-FTIR Spectroscopy.....	26
2.3 Results and Discussion.....	27
2.3.1 A Note on Methodology	27
2.3.2 Isomorphous $\text{M}_2(\text{H}_2\text{O})_2(\text{B}_{12}\text{F}_{12})$ (M = K, Rb)	29
2.3.3 $\text{Cs}_2(\text{H}_2\text{O})(\text{B}_{12}\text{F}_{12})$	30
2.3.4 $\text{Na}_2(\text{H}_2\text{O})_2(\text{B}_{12}\text{F}_{12})$	31
2.3.5 $\text{Li}(\text{H}_2\text{O})_4(\text{Al}(\text{OC}(\text{CF}_3)_3)_4)$	32
2.3.6 $\text{Li}(\text{H}_2\text{O})(\text{B}(3,5\text{-C}_6\text{H}_3(\text{CF}_3)_2)_4)$	33
2.3.7 $\text{Li}(\text{H}_2\text{O})_n(\text{Ga}(\text{C}_2\text{F}_5)_4)$	34
2.3.8 $\text{Li}_2(\text{H}_2\text{O})_2(\text{TiF}_6)$	34
2.3.9 $\text{Li}(\text{H}_2\text{O})(\text{PF}_6)$	35
2.3.10 $\text{Na}(\text{H}_2\text{O})(\text{PF}_6)$	35
2.3.11 The Weakest $\text{O}(\text{H})\cdots\text{F}$ Hydrogen Bonds	36
2.3.12 Asymmetric Hydrogen Bonding Environments in Hydrates.....	39
2.3.13 Correlations of $\nu(\text{OD})$ or $\nu(\text{OH})$ with $\text{O}\cdots\text{X}$ for $\text{HOH}\cdots\text{X}$ and $\text{HOD}\cdots\text{X}$ Hydrogen Bonds (X = F, O)	41
2.4 Conclusions and Future Work.....	44
2.4.1 Conclusion	44

2.4.2 Future Work	45
References	46
CHAPTER 3 OBSERVATION OF B AND E $\nu(\text{OH})$ FTIR BANDS AND COUPLING OF STRONG O–H···O AND WEAK O–H···F VIBRATIONS IN THE CYCLIC S_4 $(\text{H}_2\text{O})_4$ CLUSTERS IN CRYSTALLINE $\text{Li}_2(\text{H}_2\text{O})_4(\text{B}_{12}\text{F}_{12})$	120
3.1 Introduction and Relevant Literature	120
3.2 Experimental	122
3.2.1 Reagents and General Procedures	122
3.2.2 FTIR Spectroscopy	123
3.3 Results and Discussion	123
3.3.1 Spectroscopic data	123
3.3.2 Structure of $\text{Li}_2(\text{H}_2\text{O})_4(\text{B}_{12}\text{F}_{12})$	125
3.3.3 Structure and FTIR Spectrum of the $\text{K}_2(\text{H}_2\text{O})_2(\text{B}_{12}\text{F}_{12})$	126
3.3.4 ATR-FTIR Spectra of $\text{Li}_2(\text{H}_2\text{O})_4(\text{B}_{12}\text{F}_{12})$ and Its Deuterated Isotopologs	127
3.3.5 Assignment of O–H Stretching and H–O–H Bending Normal Modes to Bands in Vibrational Spectra of Cyclic S_4 $(\text{H}_2\text{O})_4$ Clusters	130
3.4 Conclusions and Future Work	132
3.4.1 Conclusions	132
3.4.2 Future Work	132
References	134

CHAPTER 4 WEAK O–H···F HYDROGEN BONDING IN $M(H_2O)_n(B_{12}F_{12})$ SALT HYDRATES (M = Mg, Ca, Sr, Ba, Co, Ni, Zn).....	167
4.1 Introduction and Relevant Literature	167
4.2 Experimental	169
4.2.1 Reagents and Solvents	169
4.2.2 General Procedures	169
4.2.3 Synthesis of $M(H_2O)_6(B_{12}F_{12})$ (M = Mg, Co, Ni, Zn)	169
4.2.4 Synthesis of $Ca(H_2O)_7(B_{12}F_{12})$, $Sr(H_2O)_7(B_{12}F_{12})$, $Ba(H_2O)_5(B_{12}F_{12})$.....	170
4.2.5 FTIR Spectroscopy	170
4.2.6 Thermogravimetric Analysis	171
4.3 Results and Discussion.....	171
4.3.1 Isomorphous $M(H_2O)_6(B_{12}F_{12})$ (M = Mg, Co, Ni, Zn)	171
4.3.2 Direct Spectroscopic Observation of the Effect of Cation Acidity on Water– Anion Hydrogen Bond Strength	175
4.3.3 SC-XRD Structures and TGA of $M(H_2O)_n(B_{12}F_{12})$ salts (M = Ca^{2+}, Sr^{2+}, Ba^{2+}; n = 1, 4, 5, 7)	176
4.3.4 FTIR Spectra of $M(H_2O)_n(B_{12}F_{12})$ salts (M = Ca^{2+}, Sr^{2+}, Ba^{2+}; n = 1, 4, 5, 7).....	179
4.4 Conclusions and Future Work.....	181
4.4.1 Conclusions.....	181
4.4.2 Future Work.....	182
References	183

LIST OF ABBREVIATIONS.....	218
----------------------------	-----

LIST OF TABLES

Table 2.1. FTIR $\nu(\text{OH})$ and $\nu(\text{OD})$ frequencies with full-widths at half-maximum absorbance (FWHM) and X-ray diffraction $\text{O}(\text{H/D})\cdots\text{F}$ distances	113
Table 2.2. $\nu(\text{OD})$ frequencies and $R(\text{O}\cdots\text{F})$ distances for structurally-characterized compounds with an uncoupled HOD molecule coordinated to the metal ion that makes one or more $\text{O}-\text{D}\cdots\text{F}$ hydrogen bonds.....	116
TTable 2.3. Selected distances and angles for the three structures of $\text{K}(\text{H}_2\text{O})_2\text{F}$ in ref. 107.....	118
Table 2.4. Selected distances and angles for the neutron diffraction structure of $\text{Zn}(\text{H}_2\text{O})_4\text{F}_2$.	119
Table 3.1. Structural parameters for calculated and experimental cyclic $(\text{H}_2\text{O})_4$ clusters	164
Table 3.2. Infrared $\nu(\text{OH})$ stretching frequencies for $(\text{H}_2\text{O})_4$, $(\text{D}_2\text{O})_4$, $[\text{HOD}(\text{D}_2\text{O})_3]$, and $[\text{HOD}(\text{H}_2\text{O})_3]$ clusters	165
Table 3.3. Experimental and calculated $\delta(\text{HOH})$ or $\delta(\text{DOD})$ values for $(\text{H}_2\text{O})_4$ or $(\text{D}_2\text{O})_4$ clusters	166
Table 4.1. Calculated vapor pressure above saturated salt solutions	208
Table 4.2. Crystal Data and Final Refinement Parameters for the X-ray Diffraction Structures	209
Table 4.3. Bond distances and bond valences for the SC-XRD structure of $\text{Mg}(\text{H}_2\text{O})_6(\text{B}_{12}\text{F}_{12})$	210
Table 4.4. Bond distances and bond valences for the SC-XRD structure of $\text{Co}(\text{H}_2\text{O})_6(\text{B}_{12}\text{F}_{12})$	210
Table 4.5. Bond distances and bond valences for the SC-XRD structure of $\text{Ni}(\text{H}_2\text{O})_6(\text{B}_{12}\text{F}_{12})$	211
Table 4.6. Bond distances and bond valences for the SC-XRD structure of $\text{Zn}(\text{H}_2\text{O})_6(\text{B}_{12}\text{F}_{12})$	211
Table 4.7. Comparisons of $\text{M}-\text{O}$ and $\text{O}(\text{H})\cdots\text{X}$ distances in some metal salt hexahydrates ^a	212
Table 4.8. FTIR Stretching and Bending Vibration Frequencies for $\text{M}(\text{H}_2\text{O})_6^{2+}$ Salt Hydrates	214
Table 4.9. Bond distances and bond valences for the SC-XRD structure of $\text{Ca}(\text{H}_2\text{O})_7(\text{B}_{12}\text{F}_{12})$	216

Table 4.10. Bond distances and bond valences for the SC-XRD structure of $\text{Sr}(\text{H}_2\text{O})_7(\text{B}_{12}\text{F}_{12})$	216
Table 4.11. Bond distances and bond valences for the SC-XRD structure of $\text{Ba}(\text{H}_2\text{O})_4(\text{B}_{12}\text{F}_{12})$	217
Table 4.12. Bond distances and bond valences for the SC-XRD structure of $\text{Ba}(\text{H}_2\text{O})_5(\text{B}_{12}\text{F}_{12})$	217

LIST OF FIGURES

Figure 1.1. ATR-FTIR spectrum of H ₂ O in a frozen N ₂ matrix at 11 K.....	16
Figure 1.2 An example of a linear O–H···F and a bifurcated pair of O–H···O hydrogen bonds.	17
Figure 1.3. ATR-FTIR spectrum of H ₂ O(<i>l</i>) deposited on a ZnSe ATR crystal collected at room temperature..	18
Figure 1.4. FTIR spectra of Mg(H ₂ O) ₆ (BrO ₃) ₂ , the Tutton salt K ₂ Zn(H ₂ O) ₆ (SO ₄) ₂ , and (NH ₄) ₂ M(H ₂ O) ₆ (SO ₄) ₂	19
Figure 2.1. ATR-FTIR spectrum of H ₂ O(<i>l</i>) deposited on a ZnSe ATR crystal collected at room temperature..	56
Figure 2.2. FTIR spectra of Mg(H ₂ O) ₆ (BrO ₃) ₂ , the Tutton salt K ₂ Zn(H ₂ O) ₆ (SO ₄) ₂ , and (NH ₄) ₂ M(H ₂ O) ₆ (SO ₄) ₂	57
Figure 2.3. FTIR spectra of Rb ₆ (H ₂ O) ₄ (Mo ₇ O ₂₄) and Rb ₂ (H ₂ O) ₂ (B ₁₂ F ₁₂).	58
Figure 2.4. The ν(OH) regions in the FTIR spectra of K(H ₂ O)(SnCl ₃) and K ₂ (H ₂ O) ₂ (B ₁₂ F ₁₂)... ..	59
Figure 2.5. The ν(OH) regions of FTIR spectra of Mg(H ₂ O) ₆ (BF ₄) ₂ at 295 K and 8.5 K.....	60
Figure 2.6. Schematic diagram of the instrumental set up.....	61
Figure 2.7. ATR-FTIR spectrum of H ₂ O in a frozen N ₂ matrix at 11 K.....	62
Figure 2.8. ATR-FTIR spectrum of a microcrystalline sample containing a small amount of Cs ₂ (HOD)(B ₁₂ F ₁₂) and Cs ₂ (D ₂ O)(B ₁₂ F ₁₂).	63
Figure 2.9. Comparison of the isomorphous crystals structures of K ₂ (H ₂ O) ₂ (B ₁₂ F ₁₂) Rb ₂ (H ₂ O) ₂ (B ₁₂ F ₁₂).	64
Figure 2.10. Lorentzian least-squares fit to the ν(OH) bands in the ATR-FTIR spectrum of K ₂ (H ₂ O) ₂ (B ₁₂ F ₁₂)(<i>s</i>).	65
Figure 2.11. Lorentzian least-squares fit to the ν(OH) bands in the FTIR spectrum of Rb ₂ (H ₂ O) ₂ (B ₁₂ F ₁₂)(<i>s</i>)	66
Figure 2.12. ATR-FTIR spectra of thin films of microcrystalline K ₂ (H ₂ O) ₂ (B ₁₂ F ₁₂) and Rb ₂ (H ₂ O) ₂ (B ₁₂ F ₁₂).	67
Figure 2.13. The ν(OH) ATR-FTIR region of a spectrum for a microcrystalline sample containing Rb ₂ (H ₂ O) ₂ (B ₁₂ F ₁₂) and Rb ₂ (HOD)(H ₂ O)(B ₁₂ F ₁₂).	68

Figure 2.14. ATR-FTIR spectra of microcrystalline samples containing $K_2(HOD)(H_2O)(B_{12}F_{12})$	69
Figure 2.15. The $\nu(OD)$ ATR-FTIR region of a spectrum for a microcrystalline sample containing $Rb_2(HOD)(H_2O)(B_{12}F_{12})$ and $Rb_2(D_2O)(H_2O)(B_{12}F_{12})$	70
Figure 2.16. A portion of the X-ray crystal structure of $Cs_2(H_2O)(B_{12}F_{12})$	71
Figure 2.17. Lorentzian least-squares fit to the $\nu(OH)$ bands in the ATR-FTIR spectrum of $Cs_2(H_2O)(B_{12}F_{12})$	72
Figure 2.18. Lorentzian least-squares fit to the $\delta(HOH)$ band in the FTIR spectrum of $Cs_2(H_2O)(Z)$	73
Figure 2.19. ATR-FTIR spectra of a microcrystalline sample containing $Cs_2(HOD)(B_{12}F_{12})$ and $Cs_2(H_2O)(B_{12}F_{12})$	74
Figure 2.20. Lorentzian least-squares fit to the four $\nu(OD)$ peaks in the FTIR spectrum of $Cs_2(D_2O)(Z)(s)$	75
Figure 2.21. Lorentzian least-squares fit to the $\nu(OH)$ bands in the ATR-FTIR spectrum of $Na_2(H_2O)_2(Z)$	76
Figure 2.22. ATR-FTIR spectrum of a sample containing $Na_2(HOD)(H_2O)(B_{12}F_{12})$ and $Na_2(D_2O)(H_2O)(B_{12}F_{12})$	77
Figure 2.23. Two portions of the X-ray crystal structure of $Li(H_2O)_4(Al(OC(CF_3)_3)_4)$	78
Figure 2.24. ATR-FTIR spectra of microcrystalline samples of $Li(H_2O)_4(Al(OC(CF_3)_3)_4)$, $Li(H_2O)(B(3,5-C_6H_3(CF_3)_2)_4)$, and $Li(H_2O)_n(Ga(C_2F_5)_4)$	79
Figure 2.25. The $\nu(OH)$ region of the ATR-FTIR spectrum of a microcrystalline sample containing $Li(HOD)(D_2O)_3(Al(PFTB)_4)$ and $Li(H_2O)(D_2O)_3(Al(PFTB)_4)$	80
Figure 2.26. The $\delta(HOH)/\delta(HOD)$ regions of ATR-FTIR spectra of microcrystalline samples of a mixture of $Li(HOD)(D_2O)_3(Al(PFTB)_4)$, $Li(H_2O)(D_2O)_3(Al(PFTB)_4)$, and $Li(H_2O)_4(Al(PFTB)_4)$	81
Figure 2.27. ATR-FTIR spectra of a sample containing $Li(HOD)(H_2O)_3(Al(OC(CF_3)_3)_4)$ and $Li(D_2O)(H_2O)_3(Al(OC(CF_3)_3)_4)$	82
Figure 2.28. The $\nu(OH)$ regions of ATR-FTIR spectra for microcrystalline samples of $Li(H_2O)_4(Al(PFTB)_4)$	83
Figure 2.29. A portion of the single-crystal X-ray structure of $Li(H_2O)(B(3,5-C_6H_3(CF_3)_2)_4)$	84
Figure 2.30. ATR-FTIR spectra of the $\nu(OH)$ region of a microcrystalline sample containing $Li(HOD)(B(3,5-C_6H_3(CF_3)_2)_4)$ and $Li(H_2O)(B(3,5-C_6H_3(CF_3)_2)_4)$	85

Figure 2.31. The $\nu(\text{OH})$ regions of ATR-FTIR spectra for microcrystalline sample of $\text{Li}(\text{H}_2\text{O})_n(\text{Ga}(\text{C}_2\text{F}_5)_4)$.	86
Figure 2.32. ATR-FTIR spectrum of the $\nu(\text{OD})$ region of a microcrystalline sample containing $\text{Li}(\text{HOD})(\text{H}_2\text{O})_{n-1}(\text{Ga}(\text{C}_2\text{F}_5)_4)$ and $\text{Li}(\text{D}_2\text{O})(\text{H}_2\text{O})_{n-1}(\text{Ga}(\text{C}_2\text{F}_5)_4)$.	87
Figure 2.33. A portion of the X-ray crystal structure of $\text{Li}_2(\text{H}_2\text{O})_2(\text{TiF}_6)$.	88
Figure 2.34. FTIR $\nu(\text{OH})$ region for a sample of $\text{Li}_2(\text{H}_2\text{O})_2(\text{TiF}_6)$ and FTIR $\nu(\text{OD})$ region for a sample containing $\text{Li}_2(\text{HOD})(\text{H}_2\text{O})(\text{TiF}_6)$ and $\text{Li}_2(\text{D}_2\text{O})(\text{H}_2\text{O})(\text{TiF}_6)$.	89
Figure 2.35. The $\nu(\text{OH})$ regions for two samples containing different amounts of $\text{Li}(\text{HOD})(\text{PF}_6)$ and $\text{Li}(\text{H}_2\text{O})(\text{PF}_6)$.	90
Figure 2.36. FTIR $\nu(\text{OD})$ regions for two samples containing different amounts of $\text{Li}(\text{HOD})(\text{PF}_6)$ and $\text{Li}(\text{H}_2\text{O})(\text{PF}_6)$.	91
Figure 2.37. Portions of the single-crystal X-ray structure of $\text{Na}(\text{H}_2\text{O})(\text{PF}_6)$.	92
Figure 2.38. ATR-FTIR spectra of microcrystalline sample of $\text{Na}(\text{H}_2\text{O})(\text{PF}_6)$.	93
Figure 2.39. The $\nu(\text{OH})$ and $\nu(\text{OD})$ regions of the ATR-FTIR spectrum of a microcrystalline sample containing $\text{Na}(\text{HOD})(\text{PF}_6)$, $\text{Na}(\text{D}_2\text{O})(\text{PF}_6)$, and $\text{Na}(\text{H}_2\text{O})(\text{PF}_6)$.	94
Figure 2.40. The $\delta(\text{HOH})$ and $\delta(\text{HOD})$ region of the ATR-FTIR spectrum of a microcrystalline sample containing $\text{Na}(\text{HOD})(\text{PF}_6)$ and $\text{Na}(\text{H}_2\text{O})(\text{PF}_6)$.	95
Figure 2.41. FTIR spectra, of monomeric H_2O , HOD , and D_2O absorbed in polyvinylidene difluoride.	96
Figure 2.42. The FTIR spectrum of $[\text{NEt}_4]_4[\text{Hg}(\text{CB}_{11}\text{F}_{11})_2]_2 \cdot \text{H}_2\text{O}$ and a Lorentzian least-squares fit to the two $\nu(\text{OH})$ bands.	97
Figure 2.43. Portion of the X-ray crystal structure of $[\text{NEt}_4]_2[\text{Hg}(\text{H}_2\text{O})(\text{CB}_{11}\text{F}_{11})_2]$.	98
Figure 2.44. The calculated structures of $\text{HOH} \cdots \text{FCH}_3$ and the $\text{H}_2\text{O}-\text{CF}_4$ van der Waals complex.	99
Figure 2.45. Plot of $\nu(\text{OD})$ values in ascending order for compounds with one HOD molecule per formula unit.	100
Figure 2.46. The FTIR $\nu(\text{OH})$ region for $\text{Li}_2(\text{HOD})(\text{D}_2\text{O})_3(\text{B}_{12}\text{F}_{12})$ and a portion of the X-ray crystal structure of $\text{Li}_2(\text{H}_2\text{O})_4(\text{B}_{12}\text{F}_{12})$.	101
Figure 2.47. ATR-FTIR spectra of microcrystalline samples of $\text{Na}_2(\text{H}_2\text{O})_2(\text{B}_{12}\text{F}_{12})$ and $\text{Na}(\text{H}_2\text{O})(\text{PF}_6)$.	102
Figure 2.48. The $\nu(\text{OH})$ and $\nu(\text{OD})$ regions of the ATR-FTIR spectrum of a microcrystalline sample containing $\text{Na}(\text{HOD})(\text{PF}_6)$, $\text{Na}(\text{D}_2\text{O})(\text{PF}_6)$, and $\text{Na}(\text{H}_2\text{O})(\text{PF}_6)$.	103

Figure 2.49. Comparison of portions of the single-crystal X-ray structures of $K_2(H_2O)_2(B_{12}F_{12})$ and $K(H_2O)_2F$	104
Figure 2.50. A portion of the neutron diffraction structure of $K(H_2O)_2F$	105
Figure 2.51. A portion of the X-ray crystal structure of $K(H_2O)(MnF_4)$	106
Figure 2.52. A portion of the neutron diffraction crystal structure of $Zn(H_2O)_4F_2$	107
Figure 2.53. Two $\nu(OH)$ vs. $R(O(H)\cdots O)$ hydrogen-bond correlation curves.. ..	108
Figure 2.54. Plots of (i) $\nu(OD)$ vs. $O(H)\cdots F$ distance for fluoroanion salt hydrates containing a single HOD ligand coordinated to a metal cation and (ii) $\nu(OD)$ vs. $O(D)\cdots O$ distance for oxoanion salt hydrates containing a single HOD ligand coordinated to a metal cation.	109
Figure 2.55. A portion of the neutron diffraction crystal structure of $Li(H_2O)_3(ClO_4)$ and variable temperature FTIR spectra of $Li(HOD)(H_2O)_2(ClO_4)$	110
Figure 2.56. A portion of the neutron diffraction crystal structure of $Na(H_2O)(ClO_4)$ and variable temperature FTIR spectra of $Na(HOD)(ClO_4)$	111
Figure 2.57. FTIR spectrum of $Na_2(H_2O)_6(B_{12}Cl_{12})$ at 22 °C.....	112
Figure 3.1. The $\nu(OH_b)$ region of a neon matrix with $(H_2O)_n$ clusters ($n = 3-6$).	141
Figure 3.2. FTIR spectra of the $\nu(OH)$ regions of argon matrices containing $(H_2O)_n$ clusters ($n = 2-5$).	142
Figure 3.3. FTIR spectrum of $(D_2O)_n$ clusters in a frozen Ar matrix at 5.3 K.....	143
Figure 3.4. IR cavity ringdown spectrum in the $\nu(OD)$ region of fully deuterated water clusters taken under expansion conditions favoring small clusters ($n \leq 6$).....	144
Figure 3.5. FTIR spectrum of $\nu(OH)$ region of $Cu(3\text{-aminomethylpyridine})(H_2O)(\text{oxalate})\cdot 2H_2O$.,	145
Figure 3.6. Raman spectrum of $\nu(OH)$ region of $Cu(3\text{-aminomethylpyridine})(OH_2\text{oxalate})\cdot 2H_2O$.,	146
Figure 3.7. FTIR spectrum of $[Fe_3(\mu^3-O)(\mu^2-CH_3COO)_6(C_5H_5NO)_2(H_2O)]ClO_4\cdot 4H_2O$	147
Figure 3.8. The X-ray crystal structure of $Li_2(H_2O)_4(B_{12}F_{12})$	148
Figure 3.9. The ATR-FTIR $\nu(OH)$ stretching region of microcrystalline samples of $Li_2(H_2O)_4(B_{12}F_{12})$ and $Li_2(HOD)(D_2O)_3(B_{12}F_{12})$	149
Figure 3.10. The entire ATR-FTIR spectrum of a microcrystalline sample of $Li_2(H_2O)_4(B_{12}F_{12})$	150

Figure 3.11. The ATR-FTIR $\nu(\text{OD})$ stretching region of microcrystalline samples of $\text{Li}_2(\text{D}_2\text{O})_4(\text{B}_{12}\text{F}_{12})$ and $\text{Li}_2(\text{HOD})(\text{D}_2\text{O})_3(\text{B}_{12}\text{F}_{12})$	151
Figure 3.12. Lorentzian fits to the $\nu(\text{OH})$ bands for the O–H···O hydrogen bonds in ATR-FTIR spectra of $\text{Li}_2(\text{H}_2\text{O})_4(\text{B}_{12}\text{F}_{12})$ and $\text{Li}_2(\text{HOD})(\text{D}_2\text{O})_3(\text{B}_{12}\text{F}_{12})$ and Lorentzian fits to the $\nu(\text{OD})$ bands for the O–D···O hydrogen bonds in ATR-FTIR spectra of $\text{Li}_2(\text{D}_2\text{O})_4(\text{B}_{12}\text{F}_{12})$ and $\text{Li}_2(\text{HOD})(\text{H}_2\text{O})_3(\text{B}_{12}\text{F}_{12})$	152
Figure 3.13. Four-peak Lorentzian fit to the entire $\nu(\text{OH})$ region of the ATR-FTIR spectrum of microcrystalline $\text{Li}_2(\text{H}_2\text{O})_4(\text{B}_{12}\text{F}_{12})$	153
Figure 3.14. ATR-FTIR spectra in the $\delta(\text{HOH})$ bending region of microcrystalline samples of $\text{Li}_2(\text{H}_2\text{O})_4(\text{B}_{12}\text{F}_{12})$ and $\text{K}_2(\text{H}_2\text{O})_4(\text{B}_{12}\text{F}_{12})$	154
Figure 3.15. Lorentzian fits to $\delta(\text{HOH})$ peaks in the ATR-FTIR spectra of $\text{Li}_2(\text{H}_2\text{O})_4(\text{B}_{12}\text{F}_{12})$ and $\text{K}_2(\text{H}_2\text{O})_2(\text{B}_{12}\text{F}_{12})$	155
Figure 3.16. The $\delta(\text{HOH})/\nu(\text{BF})/\delta(\text{DOD})$ region of FTIR spectra of $\text{Li}_2(\text{D}_2\text{O})_4(\text{B}_{12}\text{F}_{12})$ (top) and $\text{Li}_2(\text{H}_2\text{O})_4(\text{B}_{12}\text{F}_{12})$ (bottom).....	156
Figure 3.17. The proposed interconversion of disordered hydrogen-bonded H atoms in the X-ray crystal structure of $\text{Li}_2(\text{H}_2\text{O})_4(\text{B}_{12}\text{F}_{12})$	157
Figure 3.18. The predicted $\text{C}_2(\text{H}_2\text{O})_4$ cluster adsorbed to the $\text{NaCl}(001)$ surface	158
Figure 3.19. Calculated and experimental $(\text{H}_2\text{O})_4$ clusters	159
Figure 3.20. The ATR-FTIR spectrum of an evaporated microcrystalline film of $\text{K}_2(\text{H}_2\text{O})_2(\text{B}_{12}\text{F}_{12})$	160
Figure 3.21. Mass-selective depletion IR spectra for $(\text{H}_2\text{O})_n$ clusters in liquid He droplets.	161
Figure 3.22. Simplified representations of the A, B, and E O–H stretching and H–O–H bending vibrations of a cyclic $(\text{H}_2\text{O})_4$ cluster with S_4 symmetry.....	162
Figure 3.23. IR-CRLAS spectrum of $(\text{H}_2\text{O})_n$ clusters.....	163
Figure 4.1. Expansions of the $\nu(\text{OH})$ regions of ATR-FTIR spectra of $\text{M}(\text{H}_2\text{O})_6(\text{Z})$ ($\text{M} = \text{Mg}, \text{Co}, \text{Ni}, \text{Zn}$).....	187
Figure 4.2. Photographs of crystals of $\text{Co}(\text{H}_2\text{O})_6(\text{B}_{12}\text{F}_{12})$ and $\text{Ni}(\text{H}_2\text{O})_6(\text{B}_{12}\text{F}_{12})$	188
Figure 4.3. TGA-MS plot for two cycles of hydration/dehydration of $\text{K}_2(\text{B}_{12}\text{F}_{12})$ at 25 °C.....	189
Figure 4.4. The low-temperature structure of $\text{Mg}(\text{H}_2\text{O})_6(\text{SiF}_6)$	190
Figure 4.5. The structure of $\text{Ni}(\text{H}_2\text{O})_6(\text{TiF}_6)$	191
Figure 4.6. Part of the structures of $(\text{Zn}(\text{H}_2\text{O})_6)_2(\text{ZrF}_8)$	192

Figure 4.7. The $\nu(\text{OH})$ regions of ATR-FTIR spectra of microcrystalline $\text{M}(\text{H}_2\text{O})_6(\text{B}_{12}\text{F}_{12})$ ($\text{M} = \text{Mg}, \text{Co}, \text{Ni}, \text{Zn}$).....	193
Figure 4.8. The $\nu(\text{OD})$ regions of ATR-FTIR spectra of $\text{Mg}(\text{HOD})(\text{H}_2\text{O})_5(\text{B}_{12}\text{F}_{12})$ and $\text{Co}(\text{HOD})(\text{H}_2\text{O})_5(\text{B}_{12}\text{F}_{12})$	194
Figure 4.9. Experimental ATR-FTIR spectra of $\text{Mg}(\text{H}_2\text{O})_6(\text{B}_{12}\text{F}_{12})$ and $\text{Mg}(\text{D}_2\text{O})_6(\text{B}_{12}\text{F}_{12})$ and their deconvolution into four Lorentzian peaks	195
Figure 4.10. Experimental ATR-FTIR spectrum of $\text{Co}(\text{H}_2\text{O})_6(\text{B}_{12}\text{F}_{12})$ and deconvolution of a portion of the experimental spectrum into four Lorentzian peaks.....	196
Figure 4.11. Plot of $\nu(\text{OD})$ values in ascending order for compounds with one HOD molecule per formula unit.....	197
Figure 4.12. Plot of $\nu(\text{OD})$ vs. $\text{O}(\text{D})\cdots\text{F}$ distance for metal salt hydrates containing one HOD molecule.....	198
Figure 4.13. The offset stacks of corrugated pseudo-close-packed layers of Z^{2-} anion centroids in the structure of $\text{Ca}(\text{H}_2\text{O})_7(\text{B}_{12}\text{F}_{12})$	199
Figure 4.14. The $\text{O}(\text{H})\cdots\text{F}$ (2.880(6)–2.902(6) Å) and $\text{O}(\text{H})\cdots\text{O}$ (3.016(6) Å) hydrogen bonding distances in the structure of $\text{Sr}(\text{H}_2\text{O})_7(\text{B}_{12}\text{F}_{12})$	200
Figure 4.15. The structure of $\text{Ba}(\text{H}_2\text{O})_5(\text{Z})$	201
Figure 4.16. The structure of $\text{Ba}(\text{H}_2\text{O})_4(\text{Z})$	202
Figure 4.17. Thermogravimetric behavior of $\text{Ca}(\text{H}_2\text{O})_n(\text{Z})(s)$	203
Figure 4.18. Thermogravimetric behavior of $\text{Ba}(\text{H}_2\text{O})_n(\text{Z})(s)$	204
Figure 4.19. ATR-FTIR spectra of a microcrystalline $\text{Ca}(\text{H}_2\text{O})_n(\text{B}_{12}\text{F}_{12})$	205
Figure 4.20. Room-temperature ATR-FTIR spectra showing the reaction $\text{Sr}(\text{H}_2\text{O})_n(\text{B}_{12}\text{F}_{12}) \leftrightarrow \text{Sr}(\text{H}_2\text{O})_m(\text{B}_{12}\text{F}_{12})$	206
Figure 4.21. Comparison of the FTIR spectra of microcrystalline $\text{Ba}(\text{H}_2\text{O})_8(\text{B}_{12}\text{F}_{12})$ at 25 °C in $\text{N}_2/15(1)$ torr $\text{H}_2\text{O}(g)$, $\text{Ba}(\text{H}_2\text{O})_n(\text{B}_{12}\text{F}_{12})$ at 25 °C in dry N_2 ($n = 4-5$), and $\text{Ba}(\text{H}_2\text{O})(\text{B}_{12}\text{F}_{12})$ at 80 °C in dry N_2	207

CHAPTER 1 INTRODUCTION

1.1 Background and Introduction to the Research

The earliest work on the hydrogen bond traces back to the beginning of the 1900's.¹ Since then it has played an increasingly important role in our understanding of intermolecular interactions. The impact hydrogen bonding has on numerous fields cannot be overstated. In biochemistry hydrogen bonding plays a significant role in determining protein conformation,²⁻³ molecular recognition,^{4,5} and self-assembly of certain systems and aggregates.⁶⁻⁸ Formation of water–water hydrogen bonds results in small water clusters, which plays a large part in aspects of atmospheric science, such as cloud formation.⁹ These are only two of the numerous topics tied to hydrogen bonding. This is why, especially over the last 30 years,¹ scientists have so heavily focused on understanding the hydrogen bond, and systems it influences.

The sheer breadth of topics and systems related to hydrogen bonding is too broad to be summarized at once and focusing on a narrow range of systems or conditions is necessary. For this dissertation, the focus will be on solid metal salt hydrates. From a material science perspective one of the outstanding questions in the field relates to the hydration and dehydration of ionic solids, an interest to many fields.¹⁰⁻²⁴ For construction materials, the degree of hydration in cement can affect the microstructure of concrete, which can then effect numerous material properties such as strength and porosity.¹⁷ In pharmacology, if a drug gains or loses a number of H₂O molecules from either a dry or humid atmosphere, respectively, then the bioactivity or stability of the pharmaceutical can radically change.¹² There are even researchers looking to exploit the exothermic/endergonic nature of hydration and dehydration reactions in metal salt hydrates for the purpose of thermal energy storage.¹⁴⁻¹⁶ In surveying all of these fields, and their interest in hydrated ionic solids, one thing becomes obvious: a general mechanism for the hydration/dehydration of an ionic solid does not exist. The closest thing to mechanistic studies of hydration and dehydration of ionic solids in the literature are the numerous reports of mathematical fits to data from non-isothermal dehydration experiments.²⁵ These fits are called mechanisms and endeavor to explain the process of nucleation and growth during dehydration, but this is a far cry from a general mechanism, or series of mechanisms, for this processes from a chemist's standpoint.²⁶ The benefits of such a mechanism, or series of mechanisms, would be that they would inform

on the structural and physical properties that control the stability of different hydration states and the factors governing the rates of hydration or dehydration. This level of understanding of the structure–property relationship for the hydration/dehydration of ionic solids would be invaluable to all the above-listed fields for the rational design of new materials or to provide insight into why current materials behave the way they do.

Arriving at a general mechanism, or series of mechanisms, for the hydration or dehydration of ionic solids would likely require a significant portion of a researcher’s career to accomplish. As such, it is prudent to break it down into smaller portions that can be thoroughly investigated. Then, as these separate components are explored, they can be brought together into a single unifying model. One feature shared by many salt hydrates is hydrogen bonding between the crystalline H₂O molecules and the anions. Due to how influential intermolecular interactions, hydrogen bonding included, are to the organization of molecules in the solid state, the strength of the water–anion hydrogen bond(s) could be an extremely important aspect controlling the temperature range where hydration or dehydration occurs, as well as what hydration state(s) are stable under ambient conditions. This is why studying hydrogen bonding in ionic solids is the focus of this work. To do so, measuring the relative strengths of the water–anion hydrogen bonds is the best starting point.

One of the oldest, and well known, methods for studying hydrogen bonding, and the relative strength of the hydrogen bonds, is IR spectroscopy. The region of the IR spectrum where the $\nu(\text{OH})$ stretching vibrations occur (3800–3200 cm^{-1}) is generally devoid of other IR active vibrations. This makes unambiguous assignment of bands in this region to $\nu(\text{OH})$ stretching vibrations very straightforward. In addition to the ease of assigning bands in this region, these bands are also highly susceptible to the presence of O–H···X hydrogen bonding. In the most traditional sense of the term hydrogen bond,¹ which will be used in this dissertation, formation of a hydrogen bond lengthens the equilibrium O–H distance,¹ which in turn changes the vibrational characteristics of the O–H oscillator. Lengthening of O–H bond causes a redshift in the energy required to stimulate a vibration. The magnitude of the redshift is thus related to the strength of the hydrogen bond; with a stronger hydrogen bond resulting in a more significant redshift.¹ In addition to a redshift in the $\nu(\text{OH})$ band position, broadening of the band(s), and an increase in the integrated intensity of the band(s) also occurs upon hydrogen bond formation.¹ Of these three metrics, the magnitude of the redshift is the best suited to studying relative hydrogen bond strengths, because measuring center to center distances between band positions is less

likely to be affected by band asymmetry or other distortions to bands shape. Further, band widths and integrated intensities are susceptible to changes in temperature, and thus more difficult to compare across different experiments/materials unless all of the IR spectra are collected at the same temperature, which is difficult to control when comparing results from the literature. This does not mean that bandwidths, measured using full width at half max (FWHM), or peak fits to determine integrated intensity, are utterly meaningless. Both measures of FWHM and Lorentzian peak fitting are utilized to compare and investigate the $\nu(\text{OH})$ bands in this dissertation, but the claims and assignments of relative hydrogen bond strengths come directly from the magnitude of the $\Delta\nu(\text{OH})$ band position, compared to an isolated water molecule.

To utilize $\Delta\nu(\text{OH})$ band position to determine the relative hydrogen bond strength, a reference is required. The reference used within this work is the $\nu(\text{OH})$ band positions coming from isolated H_2O molecule. This reference makes the most sense as all of the hydrogen bonds studied in this work are between H_2O molecules, acting as the hydrogen bond donor, and weakly coordinating anion (WCAs), acting as hydrogen bond acceptor. Use of an isolated H_2O molecule is necessary to accurately capture the $\nu(\text{OH})$ band positions for the O–H oscillator of an H_2O molecule, when no other forces or interactions are perturbing the oscillator. This can be accomplished in one of two ways; first one could measure the IR spectrum of a dilute sample H_2O in the gas phase. Unfortunately, an isolated $\text{H}_2\text{O}(\text{g})$ molecule may not accurately represent an H_2O molecule inside of a crystalline solid. The second method for measuring a reference value is to encase a dilute sample of H_2O in a frozen matrix of an *inert* gas such as He,²⁷ N_2 ,²⁸ or CH_4 .²⁹ In these experiments the nonpolar molecules forming the matrix are treated as minimally interacting with the H_2O molecules. This approximation assumes induced dipoles are not occurring between the H_2O molecules and the matrix. By comparing the positions of the $\nu_{\text{asym}}(\text{OH})$ and $\nu_{\text{sym}}(\text{OH})$ bands for an isolated water molecule in the gas phase (3756 and 3657, respectively)³⁰ with an isolated water molecule in a frozen He matrix at 0.37 K (3755 and 3656, respectively),²⁷ a frozen N_2 matrix at 11 K (3734 and 3638, respectively),²⁸ or in a frozen CH_4 matrix at 7 K (3720 and 3630, respectively)²⁹ it can be seen there *is* a difference. Across these three different scenarios the difference between gas phase and solid phase experiments is only ca. $1\text{--}36\text{ cm}^{-1}$ for $\nu_{\text{asym}}(\text{OH})$ and ca. $1\text{--}37\text{ cm}^{-1}$ for $\nu_{\text{sym}}(\text{OH})$, a small, but noticeable red-shift. This still illustrates that the inert nature of the matrix is only an approximation. For the remainder of the dissertation the values 3734 cm^{-1} and 3638 cm^{-1} , the values

for an H₂O molecule isolated in an Ar matrix at 11 K,²⁸ will be used for the $\nu_{\text{asym}}(\text{OH})$ and $\nu_{\text{sym}}(\text{OH})$ band positions, respectively, for an isolated H₂O molecule in the solid state.

Studying the relative hydrogen bond strengths between crystalline water molecules and the anions they hydrogen bond with is further complicated by the symmetry of the H₂O molecule. The two O–H oscillators are symmetry equivalent, and thus their vibrations are degenerate in energy. When oscillators with degenerate, or similar, energies are located on the same molecule, or within close proximity in the solid state (factor group splitting),³¹ it is possible for them to couple.¹ In the case of the H₂O molecule, the $\nu(\text{OH})$ stretching vibration for the O–H oscillator becomes the $\nu_{\text{asym}}(\text{OH})$ and $\nu_{\text{sym}}(\text{OH})$ coupled stretching vibrations (Figure 1.1). These two stretching vibrations are located at different positions in the IR spectrum than the stretching vibration for the uncoupled O–H oscillator. The $\nu_{\text{asym}}(\text{OH})$ blue-shifts to higher wavenumbers and $\nu_{\text{sym}}(\text{OH})$ red-shifts to lower wavenumbers. The complication this causes is that any observed $\Delta\nu(\text{OH})$ due to hydrogen bonding will not be representative of the effect that hydrogen bond has on the O–H oscillator, but instead the effect it has on the coupled O–H oscillators. This is not ideal, as any work studying O–H...X hydrogen bonding should apply to the uncoupled O–H oscillator, a more widely applicable systems, than the specific HO–H...X system. To uncouple the O–H oscillators, while preserving the structure of the system being studied, isotopic substitution of an HOD molecule for an H₂O molecule can be utilized.³² The energy of an O–D oscillator is ca. 1200 cm⁻¹ less than the energy of the corresponding O–H oscillator in the undeuterated analog. The disparity between the two is so large that coupling of the oscillators is minimal. Replacing one H₂O molecule, per formula unit with an HOD molecule will allow for direct observation of the band positions for the uncoupled $\nu(\text{OD})$ stretching vibration. At most, one molecule of H₂O per formula unit should be replaced by an HOD molecules. Any more, and through space coupling of two O–D oscillators in the solid state can potentially cause problems.³¹ Due to the dilute nature of HOD, compared to H₂O (or in some cases D₂O), it is often more convenient to measure $\Delta\nu(\text{OD})$, and not $\Delta\nu(\text{OH})$. This is due to the uncoupled $\nu(\text{OH})$ stretching vibration coexisting with the $\nu_{\text{asym}}(\text{OH})$ and $\nu_{\text{sym}}(\text{OH})$ bands from the bulk of the sample. As with the isolated H₂O molecule, the $\nu(\text{OD})$ band positions for an isolated HOD molecule can be measured in the gas phase (2720 cm⁻¹)³³⁻³⁵ or in a frozen Ar matrix at 17 K (2709 cm⁻¹),³⁶⁻³⁷ and used as a reference.

In addition to the qualitative comparisons that arise from measuring the magnitude of the redshift and ordering the relative hydrogen bond strengths of different compounds by this metric, quantitative correlations are also possible. Two such correlations are (i) the length of the covalent O–H bond vs. the magnitude of the redshift³⁸ and (ii) the length of the O(D)···X bond vs. the $\nu(\text{OD})$ band value for a compound with only one O–D bond.^{32,39-43} The first type of correlation plots is much more difficult to construct due to the imprecise positions of the H atoms in relation to the O atoms to which they are covalently bonded. Unless a researcher is specifically concerned with locating H atoms precisely and uses neutron diffraction to collect data with which the structure is determined, H atoms positions in most structures from the literature are not known precisely enough to provide meaningful O–H bond lengths. The second type of correlation plot can utilize structures with imprecise H atom positions by using O(H)···X distances. All this requires is measuring the distance between the O and X atoms along the hydrogen bond vector. In the cases where the O–H···X hydrogen bond is presumably linear this is a reasonable approximation, but as will become obvious in later chapters this is often not the case. Hydrogen bonds in the solid state are known to not be strictly linear in many cases, nor are they only composed of a single acceptor.¹ Hydrogen bonds with O–H···X angles (henceforth $\angle(\text{OHX})$) less than 180° are common, and it is not unreasonable to have O–H···X hydrogen bonds with $\angle(\text{OHX})$ angles that range between $110\text{--}180^\circ$.¹ Further, bifurcated and trifurcated hydrogen bonds, where the H atom forms interactions with multiple electronegative atoms at one time, further complicate the geometry of the O–H···X hydrogen bond and cause deviations from linearity¹ (examples of both linear and bifurcated hydrogen bonds are shown in Figure 1.2.). In these cases an O(H)···X bond distance can be recorded in place of an H···X bond distance. While less accurate, and not accounting for the effect $\angle(\text{OHX})$ bond angle plays, this approximation is regularly used.^{32,39-43} This approximation is convenient when utilizing XRD structures from the literature when the H atoms positions are not precisely located or located at all. The correlation between $\nu(\text{OH})$ band position and O(H)···X (X = O, F) bond length is discussed in depth in Chapters 2 and 4 of this dissertation.

In theory, studying the relative strength of hydrogen bonding via IR spectroscopy should be straightforward based on everything discussed up to this point; in practice that is not the case. Hydrogen bonds between water molecules and other molecules in the liquid or solid state are often so strong that the $\nu_{\text{asym}}(\text{OH})$

and $\nu_{\text{sym}}(\text{OH})$ bands broaden and shift so much that they become a single broad band centered around 3400 cm^{-1} (with a FWHM $> 400 \text{ cm}^{-1}$). The FTIR spectrum of liquid water on a ZnSe ATR crystal is shown in Figure 1.3 (a nearly identical spectrum is observed for $\text{H}_2\text{O} (s)$ as well) and is a far cry from the spectrum for an isolated water molecule in a frozen matrix shown in Figure 1.1. This is not isolated to just solid and liquid water, but also to metal salt hydrates, the focus of this dissertation. Most ionic solids that possess crystalline water molecules have IR spectra where the $\nu(\text{OH})$ bands are not individually resolvable (Figure 1.4). The result is that when new salt hydrates are presented in the literature, if an IR spectrum is even collected, little, if anything, is mentioned about the $\nu(\text{OH})$ region. When there is mention of the region, minimal comments are made, and often are limited to identifying the presence of hydrogen bonding.⁴⁴ The result is that investigation of hydrogen bonding in the solid state is extremely limited, even more so for solid-salt hydrates.

What little work that exists for the field of studying hydrogen bonding in the solid state via IR spectroscopy is almost entirely performed under cryogenic conditions.⁴⁵⁻⁴⁷ Lowering of the temperature often results in narrowing of the $\nu(\text{OH})$ bands, and in some cases, these bands become individually resolvable. As stated, the number of low temperature IR studies of the $\nu(\text{OH})$ region of metal salt hydrates are few,⁴⁸ but they demonstrate that this information is accessible with careful experimental design. Further, utilizing cryogenic temperatures for experimentation, coupled with more advanced forms of IR spectroscopy, different systems, such as cation–water complex ions⁴⁹ and isolated water clusters^{9,50-55} can also be experimentally studied via the positions, multiplicity, and band shape of the $\nu(\text{OH})$ bands in the IR spectrum. While these studies have allowed scientists the ability to overcome the issues caused by significant broadening of the $\nu(\text{OH})$ bands resulting from strong hydrogen bonding, these cryogenic conditions and specialized equipment cannot be the only way to study these systems and represent a huge limitation in the advancement of this field.

If room temperature IR spectroscopy of solid salt hydrates is going to be used to study the relative hydrogen bond strength of water–anion hydrogen bonds, then a new approach is required. Strong, or relatively strong, hydrogen bonds are responsible for the excessive broadening of the $\nu(\text{OH})$ band(s) that prevent $\Delta\nu(\text{OH})$ comparisons. To avoid this issue, in theory, systems with only relatively weak hydrogen bonding between the H_2O molecules and the anion(s) should result in narrower $\nu(\text{OH})$ bands. If sufficiently narrow, then it should be possible to observe the individual bands, or accurately deconvolute and model the individual

bands if some overlap is encountered. This hypothesis is the basis for the work in this dissertation. A group of anions, colloquially known as WCAs,⁵⁶⁻⁵⁹ will be utilized to test this hypothesis. A WCA is a large polyatomic anion with many peripheral electronegative atoms, often F atoms. The basicity of a WCA is minimal as they are the conjugate bases of known, or theorized, superacids. The extremely low basicity results in a weak cation–anion interaction, causing an increase in the reactivity of the cation.⁵⁹ These WCAs have been utilized by researchers to stabilize and isolate extremely reactive cations,^{56,60} or improve the catalytic activity of a cation.⁶¹ The minimal basicity of the WCAs can similarly be used to only generate very weak O–H···F hydrogen bonds in metal salt hydrates where the charge of the anion is distributed over many weak O–H···F hydrogen bonds, instead of a single strong electrostatic interaction. Like many other ionic solids, the metal salts of WCAs are hygroscopic, and when exposed to a humid atmosphere, metal salt hydrates of WCAs can be generated for study. In these systems the cation should interact strongly with crystalline H₂O molecules, based on the acidity of the cation, but the H₂O molecules, or more specifically the H atoms of the O–H moieties, should only participate in weak hydrogen bonding with the anion.

The work presented in this dissertation is focused on utilizing room temperature ATR-FTIR spectroscopy in tandem with SC-XRD to compare the magnitude of observed redshifts for the $\nu(\text{OH})$ bands with O(H)···F bond lengths for a series of metal salt hydrates containing WCAs. In doing so, some of the weakest known O–H···F hydrogen bonds were observed and reported. In addition, when the redshifts as a function of O(H)···X (X = O, F) bond lengths are plotted for the salts presented in this chapters, as well as other values from the literature,^{32,39-43} significant scatter from curves fit to the data show that O(H)···F bond length is not a good enough metric to predict the magnitude of the $\nu(\text{OH})$ band redshift, or vice versa. Moreover, it is the coordination strength, or basicity, of the anion that plays a dominant role in strength of the hydrogen bond, and thus the magnitude of the redshift.

In Chapter 2 of this dissertation eleven alkali metal salt hydrates are presented and discussed with each of the anions used ($\text{Al}(\text{OC}(\text{CF}_3)_3)_4^-$, $\text{B}(3,5\text{-C}_6\text{H}_3(\text{CF}_3)_2)_4^-$, $\text{Ga}(\text{C}_2\text{F}_5)_4^-$, PF_6^- , $\text{B}_{12}\text{F}_{12}^{2-}$, TiF_6^{2-}) being a WCA. In the ATR-FTIR spectrum of each of these eleven salt hydrates two sharp $\nu(\text{OH})$ bands are observed. This represent some of the only IR spectra where the $\nu_{\text{asym}}(\text{OH})$ and $\nu_{\text{sym}}(\text{OH})$ bands are resolvable, with baseline separation, in the solid state at room temperature. This is due to the extremely weak O–H···F

hydrogen bonds formed between the ligand water molecules and the anions. The weakest O–H···F hydrogen bonds were recorded for $\text{Li}(\text{H}_2\text{O})_4(\text{Al}(\text{OC}(\text{CF}_3)_3)_4)$, $\text{Li}(\text{H}_2\text{O})(\text{B}(3,5\text{-C}_6\text{H}_3(\text{CF}_3)_2)_4)$, and $\text{Li}(\text{H}_2\text{O})_n\text{Ga}(\text{C}_2\text{F}_5)_4$. Based on the magnitude of the $\nu(\text{OH})$ redshift, $\text{Li}(\text{H}_2\text{O})_4(\text{Al}(\text{OC}(\text{CF}_3)_3)_4)$ and $\text{Li}(\text{H}_2\text{O})(\text{B}(3,5\text{-C}_6\text{H}_3(\text{CF}_3)_2)_4)$ both possess O–H···F hydrogen bonds that are weaker than those in $\text{PVDF}(\text{H}_2\text{O})$, a neutral molecule, and the previous record holder for the weakest observed O–H···F hydrogen bond in the solid state.

Chapter 3 focuses on the compound $\text{Li}_2(\text{H}_2\text{O})_4(\text{B}_{12}\text{F}_{12})$ presented in the previous chapter. Special attention is paid to this salt for two reasons, (i) of all of the alkali metal salt hydrates discussed in Chapter 2 it is the only salt hydrate with both O–H···O and O–H···F hydrogen bonds, and (ii) the structure contains the $R4^{62}$ cyclic $(\text{H}_2\text{O})_4$ water cluster. The presence of both O–H···O and O–H···F hydrogen bonding in the same salt hydrate allows for direct comparison of the effect of each type of hydrogen bond on the magnitude of the $\nu(\text{OH})$ redshift within the same compound. Interestingly, in most solids where O–H···O hydrogen bonding is observed, the individual $\nu(\text{OH})$ bands are too broad to be individually resolved, as discussed above, but that is not the case in $\text{Li}_2(\text{H}_2\text{O})_4(\text{B}_{12}\text{F}_{12}^{2-})$. Two bands, one for each O–H moiety participating in O–H···O and O–H···F hydrogen bonding, are observed. From these two bands stark differences in the effect of the relative strengths of the different types of hydrogen bonding is apparent. Each band can further be deconvoluted into two overlapping bands representative of the B and E fundamental vibrations for the cyclic $(\text{H}_2\text{O})_4$ cluster which has S_4 symmetry. Direct observation of the B and E fundamentals, the ratio of the integrated intensities, and the peak separation are consistent with published values calculated by theorists and represent the first time these values have been experimentally observed unambiguously. Finally, evidence for the intramolecular coupling between the O–H···O and O–H···F hydrogen bonded O–H moieties in $\text{Li}_2(\text{H}_2\text{O})_4(\text{B}_{12}\text{F}_{12}^{2-})$ is presented and discussed.

Chapter 4 is an extension of the work presented in Chapter 2. In this chapter seven additional salt hydrates ($\text{Mg}(\text{H}_2\text{O})_6(\text{B}_{12}\text{F}_{12})$, $\text{Ca}(\text{H}_2\text{O})_n(\text{B}_{12}\text{F}_{12})$, $\text{Sr}(\text{H}_2\text{O})_n(\text{B}_{12}\text{F}_{12})$, $\text{Ba}(\text{H}_2\text{O})_n(\text{B}_{12}\text{F}_{12})$, $\text{Co}(\text{H}_2\text{O})_6(\text{B}_{12}\text{F}_{12})$, $\text{Ni}(\text{H}_2\text{O})_6(\text{B}_{12}\text{F}_{12})$, and $\text{Zn}(\text{H}_2\text{O})_6(\text{B}_{12}\text{F}_{12})$) are discussed. The four isomorphous hexahydrate salts all possess two sets of unique *fac*- $(\text{H}_2\text{O})_3$ ligands. The difference between these two types of H_2O positions results in two sets of $\nu_{\text{asym}}(\text{OH})$ and $\nu_{\text{sym}}(\text{OH})$ bands, for a total of 4 $\nu(\text{OH})$ bands in the IR spectrum. Use of isotopically dilute solutions containing a small amount of $\text{M}(\text{HOD})(\text{H}_2\text{O})_5(\text{B}_{12}\text{F}_{12})$ ($\text{M} = \text{Mg}, \text{Co}, \text{Ni}, \text{Zn}$) allowed for

these two positions to be differentiated spectroscopically. Relative to each other, the redshift for the bands in each spectrum followed the trend $\text{Mg} < \text{Co} \sim \text{Ni} < \text{Zn}$. This trend is consistent with the pK_a of the solvated cations. This is one of the first times where the acidity of a series of metal cation is shown to directly impact the hydrogen bond strength of the water–anion hydrogen bond experimentally. Three additional n -hydrates, $\text{Ca}(\text{H}_2\text{O})_n(\text{B}_{12}\text{F}_{12})$, $\text{Sr}(\text{H}_2\text{O})_n(\text{B}_{12}\text{F}_{12})$, $\text{Ba}(\text{H}_2\text{O})_n(\text{B}_{12}\text{F}_{12})$, are presented and discussed. The IR spectra for these three salt hydrates are the most complex of all the spectra examined in this dissertation. Coupled with the hexahydrates, all of the salt hydrates with divalent cations possess red-shift magnitudes greater than the monovalent cation salt hydrates discussed in Chapter 2, except for the $\nu(\text{OH})$ band assigned to the $\text{O}-\text{H}\cdots\text{O}$ hydrogen bond in $\text{Li}_2(\text{H}_2\text{O})_4(\text{B}_{12}\text{F}_{12}^{2-})$. This further illustrates the effect of the cation’s charge and acidity on the strength of the water–anion hydrogen bond.

This work shows that room temperature IR spectroscopy can be used to study weak $\text{O}-\text{H}\cdots\text{F}$ hydrogen bonding in metal salt hydrates if the hydrogen bond is sufficiently weak. Not only is it possible, but the weakest known $\text{O}-\text{H}\cdots\text{F}$ hydrogen bonds in the solid state have been observed. Additionally, direct observation of the effect of cation pK_a on the strength of water–anion hydrogen bond strength has been presented for the first time experimentally. In addition to water–anion hydrogen bonding, identification and characterization of discrete water clusters occurring within metal salt hydrates can be scrutinized by IR spectroscopy for the first time with no ambiguity. Finally, these results are not restricted only to the study of the different types of interactions occurring within a metal salt hydrate. They reveal a new technique for rapidly screening new WCAs to establish a relative basicity scale for all known WCA that does not require complex protonation experiments.

References

1. Steiner, T. The Hydrogen Bond in the Solid State. *Angew. Chem., Int. Ed.* **2002**, *41*, 48–76.
2. Pace, C. N.; Fu, H.; Lee Fryar, K.; Landua, J.; Trevino, S. R.; Schell, D.; Thurkill, R. L.; Imura, S.; Scholtz, J. M.; Gajiwala, K.; Sevcik, J.; Urbanikova, L.; Myers, J. K.; Takano, K.; Hebert, E. J.; Shirley, B. A.; Grimsley, G. R. Contribution of hydrogen bonds to protein stability. *Protein Sci.* **2014**, *23*, 652–661.
3. Pauling, L.; Corey, R. B.; Branson, H. R. The structure of proteins: Two hydrogen-bonded helical configurations of the polypeptide chain. *Proceedings of the National Academy of Sciences* **1951**, *37*, 205–211.
4. Martinez-Felipe, A.; Brebner, F.; Zaton, D.; Concellon, A.; Ahmadi, S.; Piñol, M.; Oriol, L. Molecular Recognition via Hydrogen Bonding in Supramolecular Complexes: A Fourier Transform Infrared Spectroscopy Study. *Molecules* **2018**, *23*, 2278.
5. Fersht, A. R. The hydrogen bond in molecular recognition. *Trends in Biochemical Sciences* **1987**, *12*, 301–304.
6. Sleczkowski, P.; Dappe, Y. J.; Croset, B.; Shimizu, Y.; Tanaka, D.; Minobe, R.; Uchida, K.; Lacaze, E. Two-Dimensional Self-Assembly Monitored by Hydrogen Bonds for Triphenylene-Based Molecules: New Role for Azobenzenes. *Journal of Physical Chemistry C* **2016**, *120*, 22388–22397.
7. Lackinger, M.; Griessl, S.; Heckl, W. M.; Hietschold, M.; Flynn, G. W. Self-Assembly of Trimesic Acid at the Liquid–Solid Interface: A Study of Solvent-Induced Polymorphism. *Langmuir* **2005**, *21*, 4984–4988.
8. Rhys, N. H.; Dougan, L. The emerging role of hydrogen bond interactions in polyglutamine structure, stability and association. *Soft Matter* **2013**, *9*, 2359–2364.
9. Ceponkus, J.; Uvdal, P.; Nelander, B. Water Tetramer, Pentamer, and Hexamer in Inert Matrices. *J. Phys. Chem. A* **2012**, *116*, 4842–4850.
10. Feng, X.; Garboczi, E. J.; Bentz, D. P.; Stutzman, P. E.; Mason, T. O. Estimation of the degree of hydration of blended cement pastes by a scanning electron microscope point-counting procedure. *Cem Concr Res* **2004**, *34*, 1787–1793.
11. Liao, W.; Sun, X.; Kumar, A.; Sun, H.; Ma, H. Hydration of Binary Portland Cement Blends Containing Silica Fume: A Decoupling Method to Estimate Degrees of Hydration and Pozzolanic Reaction. *Frontiers in Materials* **2019**, *6*.
12. Jurczak, E.; Mazurek, A. H.; Szeleszczuk, Ł.; Pisklak, D. M.; Zielińska-Pisklak, M. Pharmaceutical Hydrates Analysis-Overview of Methods and Recent Advances. *Pharmaceutics* **2020**, *12*, 959.

13. Donkers, P. A. J.; Sögütöglu, L. C.; Huinink, H. P.; Fischer, H. R.; Adan, O. C. G. A review of salt hydrates for seasonal heat storage in domestic applications. *Applied Energy* **2017**, *199*, 45–68.
14. Donkers, P. A. J.; Beckert, S.; Pel, L.; Stallmach, F.; Steiger, M.; Adan, O. C. G. Water Transport in $\text{MgSO}_4 \cdot 7\text{H}_2\text{O}$ During Dehydration in View of Thermal Storage. *Journal of Physical Chemistry C* **2015**, *119*, 28711-28720.
15. Donkers, P. A. J.; Linnow, K.; Pel, L.; Steiger, M.; Adan, O. C. G. $\text{Na}_2\text{SO}_4 \cdot 10\text{H}_2\text{O}$ dehydration in view of thermal storage. *Chemical Engineering Science* **2015**, *134*, 360-366.
16. Donkers, P. A. J.; Pel, L.; Adan, O. C. G. Dehydration/hydration of granular beds for thermal storage applications: A combined NMR and temperature study. *Int. J. Heat Mass Transfer* **2017**, *105*, 826.
17. Chidiac, S. E.; Shafikhani, M. Cement degree of hydration in mortar and concrete. *Journal of Thermal Analysis and Calorimetry* **2019**, *138*, 2305–2313.
18. N., R. C.; K., D. M.; S., M.; K., P. G. Non-isothermal Studies of the Dehydration of Double Salt Hydrates and Their Deuterium Oxide Analogues, I. *Bulletin of the Chemical Society of Japan* **1978**, *51*, 506-511.
19. Koga, N.; Tanaka, H. Kinetics and mechanism of the isothermal dehydration of zinc acetate dihydrate. *Thermochimica Acta* **1997**, *303*, 69-76.
20. Fini, A.; Fazio, G.; Alvarez-Fuentes, J.; Fernandez-Hervas, M. J.; Holgado, M. A. Dehydration and rehydration of a hydrate diclofenac salt at room temperature. *Int. J. Pharm.* **1999**, *181*, 11-21.
21. Zhang, Z.; Lu, X.; Yan, Y.; Wang, T. The dehydration of $\text{MgCl}_2 \cdot 6\text{H}_2\text{O}$ by inhibition of hydrolysis and conversion of hydrolysate. *Journal of Analytical and Applied Pyrolysis* **2019**, *138*, 114-119.
22. Pathak, A. D.; Nedeá, S.; Zondag, H.; Rindt, C.; Smeulders, D. A DFT-based comparative equilibrium study of thermal dehydration and hydrolysis of CaCl_2 hydrates and MgCl_2 hydrates for seasonal heat storage. *Phys Chem Chem Phys* **2016**, *18*, 10059-10069.
23. Pang, X.; Meyer, C. Modeling cement hydration by connecting a nucleation and growth mechanism with a diffusion mechanism. Part II: Portland cement paste hydration. *Sci Eng Compos Mater* **2016**, *23*.
24. Little, B. K.; Emery, S. B.; Nittinger, J. C.; Fantasia, R. C.; Lindsay, C. M. Physiochemical Characterization of Iodine(V) Oxide, Part 1: Hydration Rates. *Propellants Explos. Pyrotech.* **2015**, *40*, 595-603.
25. Lumpkin, J. A.; Perlmutter, D. D. Diffusional limitations on the kinetics of dehydration reactions of hydrated barium chloride. *Thermochimica Acta* **1992**, *202*, 151-171.

26. Finney, E. E.; Finke, R. G. Is There a Minimal Chemical Mechanism Underlying Classical Avrami-Erofe'ev Treatments of Phase-Transformation Kinetic Data. *Chem. Mater.* **2009**, *21*, 4692.
27. Kuyanov, K. E.; Slipchenko, M. N.; Vilesov, A. F. Spectra of the ν_1 and ν_3 bands of water molecules in helium droplets. *Chem. Phys. Lett.* **2006**, *427*, 5–9.
28. Nelander, B. Infrared Spectrum of the Water Formaldehyde Complex in Solid Argon and Solid Nitrogen. *J. Chem. Phys.* **1980**, *72*, 77–84.
29. Yamakawa, K.; Ehara, N.; Ozawa, N.; Arakawa, I. Infrared spectroscopy of water clusters isolated in methane matrices: Effects of isotope substitution and annealing. *AIP Adv.* **2016**, *6*, 075302.
30. Fraley, P. E.; Rao, K. N. High Resolution Infrared Spectra of Water Vapor ν_1 and ν_3 Bands of H_2^{16}O . *Journal of Molecular Spectroscopy* **1969**, *29*, 348–364.
31. Cotton, F. A. *Chemical Applications of Group Theory*; Wiley 1963.
32. Mikenda, W.; Steinböck, S. Stretching frequency versus bond distance correlation of O–D(H)···F hydrogen bonds in solid hydrates *Journal of Molecular Structure* **1994**, *326*, 123–130.
33. Barker, E. F.; Slesator, W. W. The Infrared Spectrum of Heavy Water. *J. Chem. Phys.* **1935**, *3*, 660–663.
34. Benedict, W. W.; Gailar, N.; Plyler, E. K. Rotation-Vibration Spectra of Deuterated Water Vapor. *J. Chem. Phys.* **1956**, *24*, 1139–1165.
35. Rank, D. H.; Larsen, K. D.; Bordner, E. B. The Raman Spectrum of Heavy Water Vapor. *J. Chem. Phys.* **1934**, *2*, 464–467.
36. Ayers, G. P.; Pullin, A. D. E. The I.R. Spectra of Matrix Isolated Water Species – I. Assignment of Bands to $(\text{H}_2\text{O})_2$, $(\text{D}_2\text{O})_2$, and HDO Dimer Species in Argon Matrices. *Spectrochim. Acta, Part A* **1976**, *32A*, 1629–1639.
37. Engdahl, A.; Nelander, B. Water in Krypton Matrices. *J. Mol. Struct.* **1989**, *193*, 101–109.
38. Boyer, M. A.; Marsalek, O.; Heindel, J. P.; Markland, T. E.; McCoy, A. B.; Xantheas, S. S. Beyond Badger's Rule: The Origins and Generality of the Structure-Spectra Relationship of Aqueous Hydrogen Bonds. *J. Phys. Chem. Lett.* **2019**, *10*, 918–924.
39. Novak, A. *Hydrogen Bonding in Solids. Correlation of Spectroscopic and Crystallographic Data Structure and Bonding* Springer: Berlin, 1974. *18*, 177–216.
40. Libowitzky, E. Correlation of O–H Stretching Frequencies and O–H···O Hydrogen Bond Lengths in Minerals. *Monatsh. Chem.* **1999**, *130*, 1047–1059.

41. Nakamoto, K.; Margoshes, M.; Rundle, R. E. Stretching Frequencies as a Function of Distances in Hydrogen Bonds. *J. Am. Chem. Soc.* **1955**, *77*, 6480–6486.
42. Pimentel, G. C.; Sederholm, C. H. Correlation of Infrared Stretching Frequencies and Hydrogen Bond Distances in Crystals. *J. Chem. Phys.* **1956**, *24*, 639–641.
43. Mikenda, W. Stretching Frequency versus Bond Distance Correlation of OD(H)···Y (Y = N, O, S, Se, Cl, Br, I) Hydrogen Bonds in Solid Hydrates. *J. Mol. Struct.* **1986**, *147*, 1.
44. Semerci, F.; Yeşilel, O. Z.; Ölmez, H.; Büyükgüngör, O. Supramolecular Assemblies of Copper(II)–pyridine-2,3-dicarboxylate Complexes with N-Donor Ligands and Clustered Water Molecules. *Inorg. Chim. Acta* **2014**, *409*, 407–417.
45. Hetmańczyk, J.; Hetmańczyk, Ł. Vibrational and reorientational dynamics and thermal properties in [Mg(H₂O)₄](ReO₄)₂ supported by periodic DFT study. *Vib. Spectrosc.* **2018**, *94*, 49–60.
46. Mikuli, E.; Hetmańczyk, J.; Grad, B.; Kozak, A.; Wasicki, J. W.; Bilski, P.; Holderna-Natkaniec, K.; Medycki, W. The relationship between reorientational molecular motions and phase transitions in [Mg(H₂O)₆](BF₄)₂, studied with the use of ¹H and ¹⁹F NMR and FT-MIR. *J. Chem Phys* **2015**, *142*, 069507.
47. Hetmańczyk, J.; Hetmańczyk, Ł.; Migdał-Mikuli, A.; Mikuli, E.; Druźbicki, K.; Weselucha-Birczyńska, A.; Proniewicz, L. M. Vibrations and reorientations of H₂O molecules and NO₃⁻ anions in [Ca(H₂O)₄](NO₃)₂ studied by incoherent inelastic neutron scattering, Raman light scattering, and infrared absorption spectroscopy. *J. Chem. Phys.* **2009**, *131*, 094506.
48. Hetmańczyk, J.; Hetmańczyk, Ł.; Migdał-Mikuli, A.; Mikuli, E.; Weselucha-Birczyńska, A. Raman light scattering, infrared absorption and DSC studies of the phase transition and vibrational and reorientational dynamics of H₂O ligands and ClO₄⁻ anions in [Ba(H₂O)₃](ClO₄)₂. *J. Raman Spectrosc.* **2012**, *43*, 1118.
49. Vaden, T. D.; Weinheimer, C. J.; Lisy, J. M. Evaporatively Cooled M⁺(H₂O)Ar Cluster Ions: Infrared Spectroscopy and Internal Energy Conversion. *J. Chem. Phys.* **2004**, *121*, 3102–3107.
50. Honegger, E.; Leutwyler, S. Intramolecular Vibrations of Small Water Clusters. *J. Chem. Phys.* **1988**, *88*, 2582–2595.
51. Xantheas, S. S.; Dunning, T. H. Ab Initio Studies of Cyclic Water Clusters (H₂O)_n, n = 1–6. I. Optimal Structures and Vibrational Spectra. *J. Chem. Phys.* **1993**, *99*, 8774–8792.
52. Huisken, F.; Kaloudis, M.; Kulcke, A. Infrared Spectroscopy of Small Size-Selected Water Clusters. *J. Chem. Phys.* **1996**, *104*, 17–25.
53. Maheshwary, S.; Patel, N.; Sathyamurthy, N.; Kulkarni, A. D.; Gadre, S. R. Structure and Stability of Water Clusters (H₂O)_n, n = 8–20: An Ab Initio Investigation. *J. Phys. Chem. A* **2001**, *105*, 10525–10537.

54. Qian, P.; Lu, L. N.; Song, W.; Yang, Z. Z. Study of Water Clusters in the $n = 2-34$ Size Regime, Based on the ABEEM/MM Model. *Theor. Chem. Acc.* **2009**, *123*, 487–500.
55. Ceponkus, J.; Engdahl, A.; Uvdal, P.; Nelander, B. Structure and Dynamics of Small Water Clusters, Trapped in Inert Matrices. *Chem. Phys. Lett.* **2013**, *581*, 1–9.
56. Bihlmeier, A.; Gonsior, M.; Raabe, I.; Trapp, N.; Krossing, I. From weakly coordinating to non-coordinating anions? A simple preparation of the silver salt of the least coordinating anion and its application to determine the ground state structure of the $\text{Ag}(\eta^2\text{-P}_4)_2^+$ cation. *Chem. Eur. J.* **2004**, *10*, 5041–51.
57. Krossing, I. Weakly Coordinating Anions: Fluorinated Alkoxyaluminates; *Comprehensive Inorganic Chemistry II 2nd ed* Elsevier Amsterdam 2013. 681–705 and references therein.
58. Strauss, S. H. The Search for larger more weak Anions. *Chem. Rev.* **1993**, *93*, 927–942.
59. Krossing, I.; Raabe, I. Non Coordinating Anions K Fact or Fiction? A Survey of Likely Candidates. *Angew. Chem., Int. Ed.* **2004**, *43*, 2066–2090 and references therein.
60. Engesser, T. A.; Lichtenthaler, M. R.; Schleep, M.; Krossing, I. Reactive p-block cations stabilized by weakly coordinating anions. *Chem Soc Rev* **2016**, *45*, 789–899.
61. Barbarich, T. J.; Handy, S. T.; Miller, S. M.; Anderson, O. P.; Grieco, P. A.; Strauss, S. H. $\text{LiAl}(\text{OC}(\text{Ph})(\text{CF}_3)_2)_4$: A Hydrocarbon-Soluble Catalyst for Carbon–Carbon Bond-Forming Reactions *Organometallics* **1996**, *15*, 3776–3778.
62. Infantes, L.; Motherwell, S. Water Clusters in Organic Molecular Crystals. *CrystEngComm* **2002**, *4*, 454–461.
63. Preisinger, A.; Zottl, M.; Mereiter, K.; Mikenda, W. S., S.; Dufek, P.; Schwarz, K.; Blaha, P. Hydrogen Bonding in Potassium Fluoride Dihydrate: A Crystallographic, Spectroscopic, and Theoretical Study. *Inorg. Chem.* **1994**, *33*, 4774–4780.
64. Berglund, B.; Tellgren, R.; Thomas, J. O. Hydrogen bond studies. CXVI A neutron diffraction study of the structure of sodium perchlorate monohydrate, $\text{NaClO}_4 \cdot \text{H}_2\text{O}$, at 298 K. *Acta Crystallogr., Sect. B: Struct. Crystallogr. Cryst. Chem.* **1976**, *32*, 2444–2449.
65. Peter, S.; Suchanek, E.; Eßer, D.; Lutz, H. D. The Crystal Structure of Twinned $\text{Mg}(\text{BrO}_3)_2 \cdot 6\text{H}_2\text{O}$. *Z. Naturforsch* **1996**, *51*, 1072–1078.
66. Vijila Manonmoni, J.; Bhagavannarayana, G.; Ramasamy, G. M., S.; Amutha, M. Growth, structure and spectral studies of a novel mixed crystal potassium zinc manganese sulphate. *Spectrochim. Acta Part A* **2014**, *117*, 9–12.
67. Ghosh, S.; Oliveira, M.; Pacheco, T. S.; Perpétuo, G. J.; Franco, C. J. Growth and characterization of ammonium nickel-cobalt sulfate Tutton's salt for UV light applications. *J. Cryst. Growth* **2018**, *487*, 104–115.

68. Herzberg, G. Infrared and Raman Spectra of Polyatomic Molecules; *Molecular Spectra and Molecular Structure. II*. New York, NY, 1945.

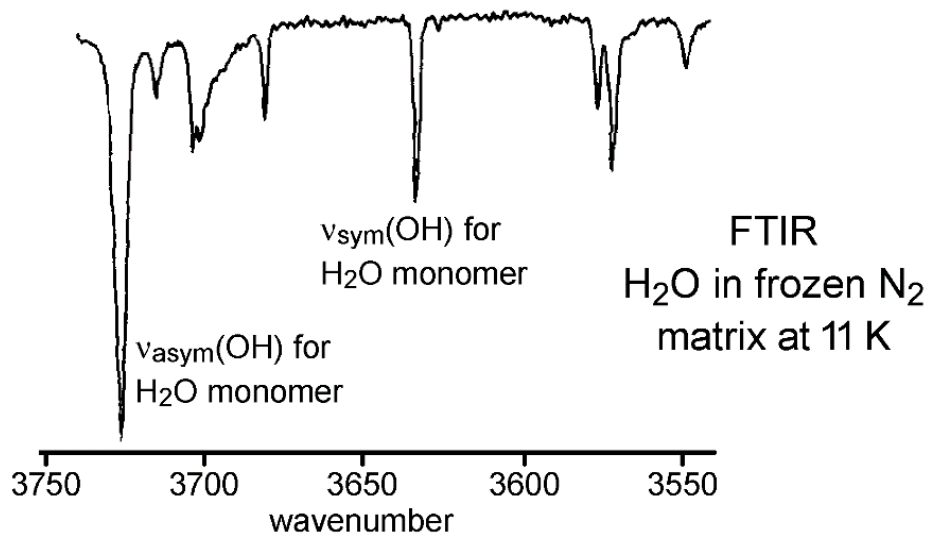


Figure 1.1. ATR-FTIR spectrum of H₂O in a frozen N₂ matrix at 11 K (ref. 28). The bands labelled as $\nu_{\text{asym}}(\text{OH})$ and $\nu_{\text{sym}}(\text{OH})$ are due to monomeric H₂O molecules. The other bands are due to dimers and higher oligomers. This figure was adapted from a figure in ref. 28.

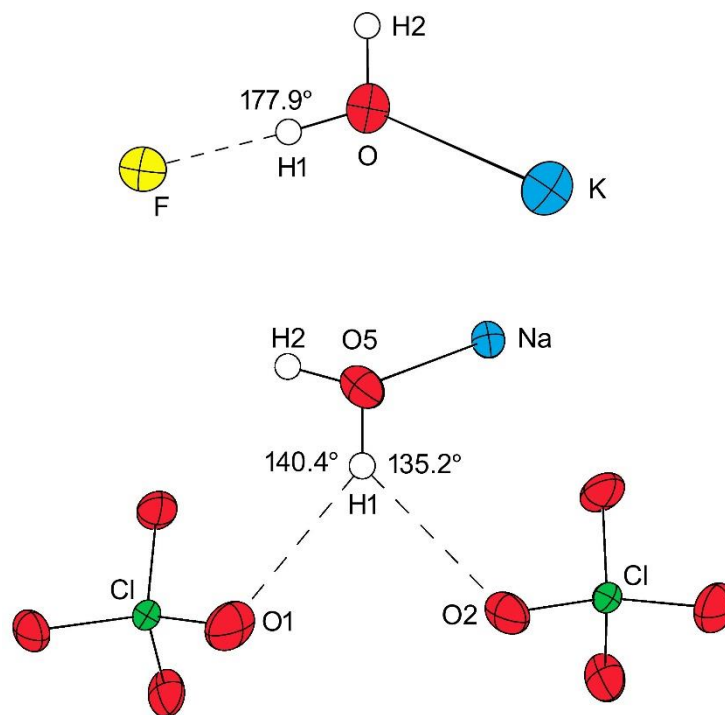


Figure 1.2 An example of a linear O–H···F hydrogen bond in $\text{K}(\text{H}_2\text{O})_2\text{F}$ (top, ref 63) and a bifurcated pair of O–H···O hydrogen bonds in $\text{Na}(\text{H}_2\text{O})\text{ClO}_4$ (bottom, ref 64). Only the relevant portions of the structures, which were determined by neutron diffraction, are shown. Interatomic distances (Å) and angles (deg) in the structure of $\text{K}(\text{H}_2\text{O})_2\text{F}$ are: O–H1, 0.971(4); O···F, 2.734(3); H1···F, 1.764(3); O–H1···F, 177.9(2). Interatomic distances (Å) and angles (deg) in the structure of $\text{Na}(\text{H}_2\text{O})\text{ClO}_4$ are: O5–H1, 0.905(6); O5···O1, 3.141(3); O5···O2, 3.087(3); H1···O1, 2.389(7); H1···O2, 2.378(10); O5–H1···O1, 140.4(9); O5–H1···O2, 135.2(9). The two figures were adapted from figures in the respective references.

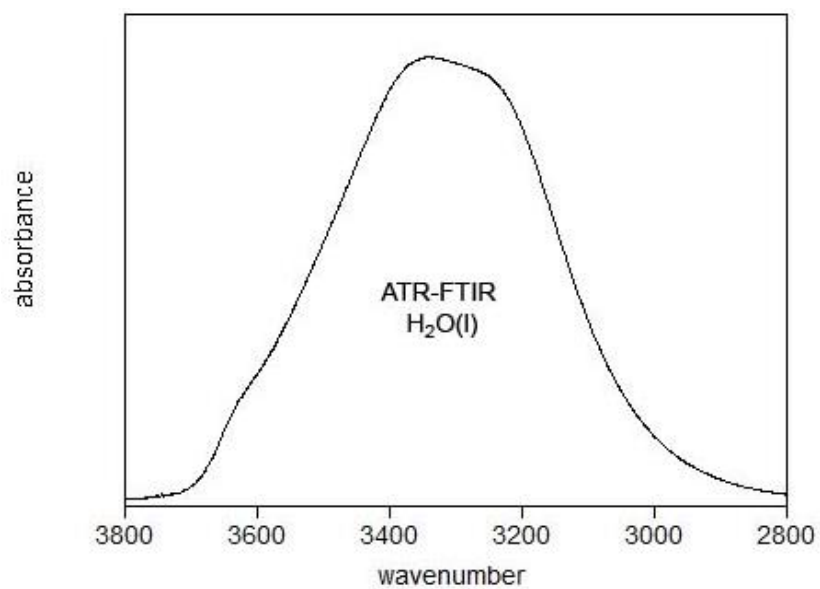


Figure 1.3. ATR-FTIR spectrum of H₂O(*l*) deposited on a ZnSe ATR crystal collected at room temperature. The band is centered ca. 3300 cm⁻¹ with a fwhm > 400 cm⁻¹.

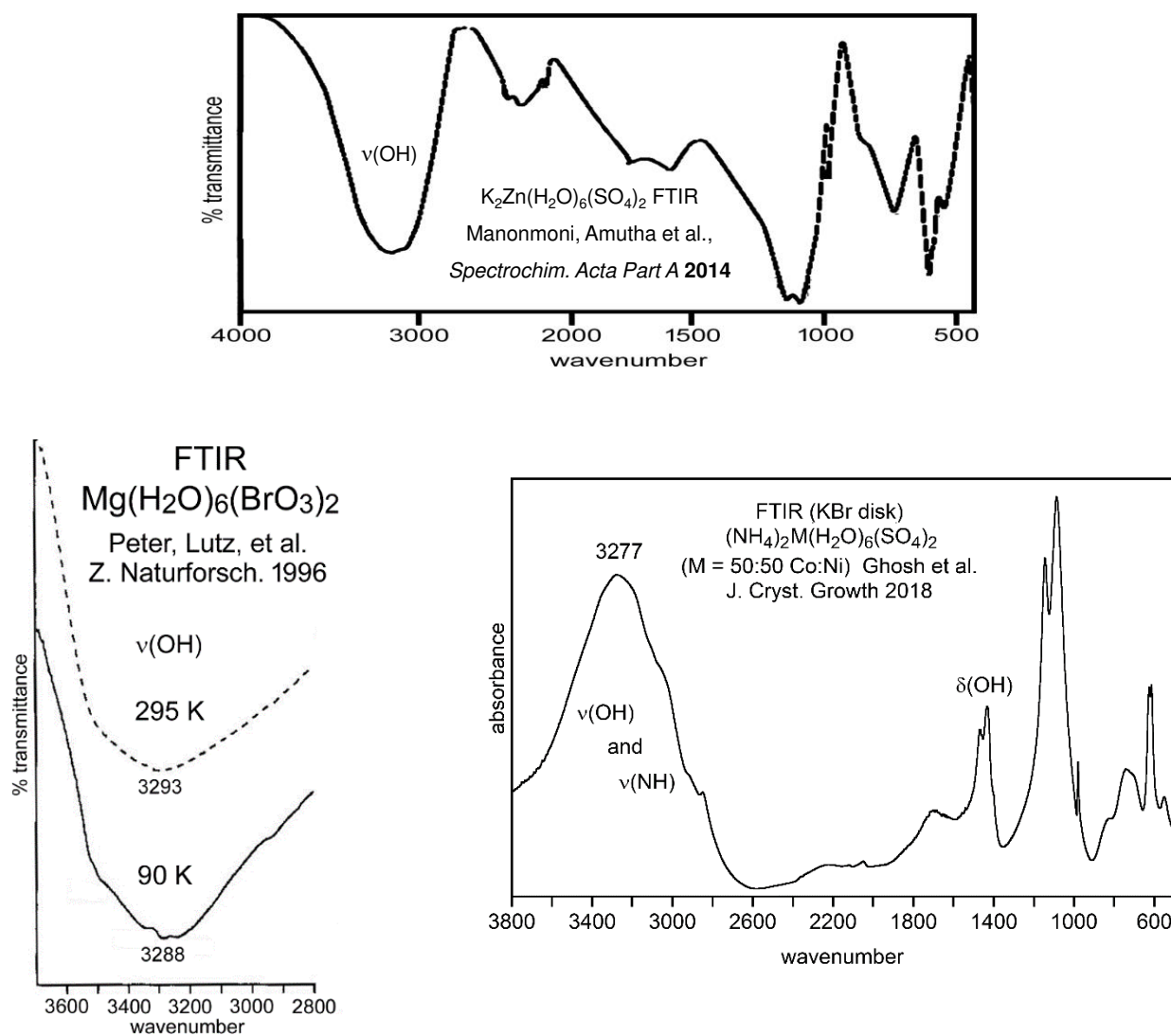


Figure 1.4. FTIR spectra of $Mg(H_2O)_6(BrO_3)_2$ (ref. 65), the Tutton salt $K_2Zn(H_2O)_6(SO_4)_2$ (ref. 66), and $(NH_4)_2M(H_2O)_6(SO_4)_2$ (ref. 67; M = 50:50 Co:Ni). The $\nu(OH)$ bands at 3000–3300 cm^{-1} are significantly redshifted relative to $\nu_{asym}(OH)$ and $\nu_{sym}(OH)$ for $H_2O(g)$ (3756 and 3655 cm^{-1} , respectively⁶⁸). The first two figures were adapted from figures in the respective references. The author thanks Prof. Santunu Ghosh for kindly supplying a digital data file with which the spectrum of $(NH_4)_2M(H_2O)_6(SO_4)_2$ was prepared.

CHAPTER 2 UNUSUALLY SHARP FTIR $\nu(\text{OH})$ BANDS AND WEAK HYDROGEN BONDING IN ALKALI METAL SALT HYDRATES OF WEAKLY-COORDINATING FLUOROANIONS

2.1 Introduction and Relevant Literature

It is well known that $\text{O-H}\cdots\text{X}$ hydrogen bonding weakens and lengthens O-H bonds, red-shifts and broadens vibrational $\nu(\text{OH})$ bands, and significantly increases the integrated intensities of those bands¹⁻¹⁴ Two $\nu(\text{OH})$ bands are present in the IR spectrum of an isolated, gas-phase H_2O molecule. These bands result from the coupling of the two symmetry equivalent O-H oscillators resulting in a $\nu_{\text{asym}}(\text{OH})$ band and a $\nu_{\text{sym}}(\text{OH})$ band, and appear at 3756 and 3657 cm^{-1} , respectively.¹⁵ When measured at room-temperature, the IR spectrum of $\text{H}_2\text{O}(l)$ only has one extremely broad band at ca. 3300 cm^{-1} as can be seen in Figure 2.1. A similar result is seen in the case of $\text{H}_2\text{O}(s)$, though depending on the temperature of the sample there may be some narrowing of the broad $\nu(\text{OH})$ band.¹⁶ In both of these scenarios the formation of $\text{H}_2\text{O}\cdots\text{HOH}$ hydrogen bonds causes the $\nu_{\text{asym}}(\text{OH})$ and a $\nu_{\text{sym}}(\text{OH})$ bands to broaden and redshift until they coalesce into the single broad peak shown in Figure 2.1. Individual $\nu_{\text{asym}}(\text{OH})$ and a $\nu_{\text{sym}}(\text{OH})$ bands in the liquid or solid state can be resolved by measuring the spectrum of an isolated H_2O molecule contained in an inert matrix, such as in liquid helium at 0.37 K (3755 and 3656 cm^{-1}),¹⁷ in an N_2 matrix at 11 K (3734 and 3638 cm^{-1}),¹⁸ or in a frozen CH_4 matrix at 7 K (3720 and 2630 cm^{-1}).¹⁹ The inert matrices effectively screens the H_2O molecules from each other, preventing the formation of hydrogen bonds. Compared to the values measured for an isolated H_2O molecule in the gas phase, the values measured for isolated H_2O molecules in an inert matrix are only redshifted between 1–36 cm^{-1} . These small redshifts indicate virtually no interaction between the O-H oscillator and the matrix in the case of H_2O in a liquid He drop at 0.37 K ($\Delta\nu(\text{OH}) = 1 \text{ cm}^{-1}$) and only extremely weak interactions with the CH_4 matrix at 7 K ($\Delta\nu_{\text{asym}}(\text{OH}) = 36 \text{ cm}^{-1}$ and $\Delta\nu_{\text{sym}}(\text{OH}) = 27 \text{ cm}^{-1}$). This methodology, of using $\Delta\nu(\text{OH})$ to assign relative hydrogen bond strength based on the magnitude of $\Delta\nu(\text{OH})$, is the primary way relative hydrogen bond strengths will be assessed in this chapter. To a lesser extent, the difference in peak widths (FWHM) can also be used to discuss relative hydrogen bond strength, but additional factors, such as temperature, can affect peak widths so it is not an ideal metric to use. A larger

red shift ($\Delta\nu(\text{OH})$) indicates a stronger hydrogen bond, while a smaller red shift indicates a weaker hydrogen bond. This allows for the creation of a qualitative scale of relative hydrogen bond strengths. This methodology has been applied to the study of $\nu(\text{NH})$ bands by Reed and coworkers²⁰ and Jenne and coworkers²¹ to show the hydrogen bond acceptor strength order for a series of different salts with the NHOC_3^+ cation. The order being: $\text{NO}_3^- \gg \text{ClO}_4^- \gg \text{BF}_4^- > \text{SbF}_6^- > \text{AsF}_6^- \sim \text{PF}_6^- \sim \text{B}_{12}\text{F}_{12}^{2-} > 1\text{-Me-CB}_{11}\text{F}_{11}^-$.²² While this is only a qualitative scale, it is the best way of experimentally studying the relative strength of hydrogen bonding, short of determination of hydrogen bond enthalpies, which except for some trivial cases is not possible.

Coalescence of the $\nu_{\text{asym}}(\text{OH})$ and a $\nu_{\text{sym}}(\text{OH})$ bands into a single broad peak makes such analysis impossible, due to the loss of the individual $\nu_{\text{asym}}(\text{OH})$ and a $\nu_{\text{sym}}(\text{OH})$ bands. The loss of the individual $\nu_{\text{asym}}(\text{OH})$ and a $\nu_{\text{sym}}(\text{OH})$ bands also happens with solid metal salt hydrates.^{16,23-27} Formation of water–anion hydrogen bonds results in similar broad $\nu(\text{OH})$ bands at ca. 3300 cm^{-1} for many salt hydrates. Figure 2.2 shows a number of solid metal salt hydrates, and in all cases there is a single broad $\nu(\text{OH})$ band at ca. 3300 cm^{-1} . This feature is so well known, that when observed, it is all the evidence required for the assignment of hydrogen bonds.¹⁻² Unfortunately, other than identifying the presence of hydrogen bonding there is not much worthwhile information to be gained by this peak, and researchers largely gloss over this region of the FTIR spectrum, if it is mentioned at all.²⁸⁻²⁹ This results in a large gap in the understanding of the effects of the presence of water in ionic solids. Occasionally, as in the top spectrum of Figure 2.3, the individual $\nu(\text{OH})$ bands that are obscured by the broadening due to hydrogen bonding can be approximated. These positions are reported, but like with other spectra, not much else is said. Some studies attempt to overcome this limitation by studying metal salt hydrates at cryogenic conditions where narrowing of the broad band occurs^{16,30} (i.e., see Figures 2.4 and 2.5), but even these studies are few and only begin to approach studying the system in any depth. Some attention, and success, studying the effect of $\text{M}^{n+} \cdots \text{OH}_2$ interactions via studying the $\nu(\text{OH})$ band positions have been published.³¹⁻³² Again, these studies employ cryogenic conditions and an inert matrix, typically a noble gas, to generate and measure these species *in situ*.³¹⁻³² As a result these experiments are highly specialized and ultimately only appear to look at the effects of cation–water interactions by way of perturbations to the O–H oscillator, but not at hydrogen bonding or water–anion interactions.

In theory, it should be possible to study the water–anion interactions in metal salt hydrates with FTIR at room-temperature, provided that the water–anion interactions are sufficiently weak enough that the $\nu_{\text{asym}}(\text{OH})$ and a $\nu_{\text{sym}}(\text{OH})$ bands have not coalesced and can be individually resolved. To do this, selection of an anion, or series of anions, that only weakly interact with their cation, or ligands coordinated to the cation, becomes the critical component. The family of anions known as WCAs³³⁻³⁴ make the ideal candidates for study. In salts with WCAs the interactions between the cation and the anion are minimized by delocalizing the charge of the anion over a large polyatomic structure with electronegative atoms, such as F atoms, on the periphery. With the charge localized on the F atoms the formation of multiple M–F coordination bonds results in the anion being able to ion pair with the cation, but each individual interaction is as weak as possible.³⁵ This results in a highly reactive cation that is only weakly associated with the anion.³⁴ In theory this can be translated to the $\text{M}(\text{H}_2\text{O})_n^{m+}$ cation complexes in salt hydrates. The O–H···F hydrogen bonds between ligand water molecules and F atoms on the anion should be weak as well, potentially to the point where the $\nu_{\text{asym}}(\text{OH})$ and a $\nu_{\text{sym}}(\text{OH})$ bands are resolvable.

In this chapter the FTIR spectra and the chemical structure, determined by X-ray diffraction, of 11 different alkali metal salt hydrates of WCAs will be discussed. The 11 salts are made using 5 different alkali metal cations (Li^+ , Na^+ , K^+ , Rb^+ , Cs^+) and 6 different WCAs (PF_6^- , $\text{Ga}(\text{C}_2\text{F}_5)_4^-$, $\text{B}(3,5\text{-C}_6\text{H}_3(\text{CF}_3)_2)_4^-$, $\text{Al}(\text{OC}(\text{CF}_3)_3)_4^-$, $\text{B}_{12}\text{F}_{12}^{2-}$, TiF_6^{2-}). In the ATR-FTIR spectra of all 11 salt hydrates the $\nu_{\text{asym}}(\text{OH})$ and a $\nu_{\text{sym}}(\text{OH})$ bands are resolvable at room temperature. Furthermore, determination of the $\nu(\text{OD})$ stretching frequency for a single HOD molecule per formula unit allowed for comparison of $\nu(\text{OD})$ band positions vs O(H)···F bond distance. The resulting correlation curves displayed a large amount of scatter, making determination of $\nu(\text{OD})$ based on the vs O(H)···F bond distance, or vice versa, highly unreliable without more accurate H atom positions in the X-ray structure. In the case of the salt hydrates $\text{Li}(\text{HOD})(\text{H}_2\text{O})_3(\text{Al}(\text{OC}(\text{CF}_3)_3)_4)$, $\text{Li}(\text{HOD})(\text{B}(3,5\text{-C}_6\text{H}_3(\text{CF}_3)_2)_4)$, and $\text{Li}(\text{HOD})(\text{H}_2\text{O})_{n-1}(\text{Ga}(\text{C}_2\text{F}_5)_4)$ the FTIR spectrum of a single HOD molecule per formula unit revealed $\nu(\text{OD})$ values less red-shifted from the ideal position for an HOD in an inert matrix. Prior to this, PVDF(HOD) and $\text{CH}_3\text{F}(\text{HOD})$ were the weakest hydrogen bonds experimentally observed by FTIR between an HOD molecule and a F atom and reported in the literature.

All of the work presented in this chapter has been published in the form of two academic papers.³⁶⁻³⁷ One in *Inorganic Chemistry* titled *Hydrated Metal Ion Salts of the Weakly Coordinating Fluoroanions PF₆⁻, TiF₆²⁻, B₁₂F₁₂²⁻, Ga(C₂F₅)₄⁻, B(3,5-C₆H₃(CF₃)₂)₄⁻, and Al(OC(CF₃)₃)₄⁻. In Search of the Weakest HOH...F Hydrogen Bonds*. The author of this dissertation was the first author and the only graduate student or postdoc author. The second publication was a communication in the *Journal of Fluorine Chemistry* titled *Unusually sharp FTIR ν(OH) bands and very weak O–H...F hydrogen bonds in M₂(H₂O)_{1,2}B₁₂F₁₂ hydrates (M=Na–Cs)*. The author of this dissertation was the first author and one of two graduate student or postdoc authors along with Xiaoyan Gao, a visiting graduate student researcher in the lab of Dr. Yong Liu of the University of Colorado, Denver. The structures presented in this chapter were collected and determined by previous Strauss group members.

2.2 Experimental

2.2.1 Reagents and Solvents

Solid K₂(B₁₂H₁₂) (Air Products) was dissolved in H₂O and brought to dryness with a rotary evaporator a minimum of three times before being dried under dynamic vacuum overnight to remove any residual methanol contained within the solid. The following reagents and solvents were obtained from the indicated supplier: deuterium oxide (D₂O, Cambridge Isotopes 99.9% D); LiCl (Mallinckrodt, ACS reagent grade); RbCl (K&K, 99%); Acetonitrile (CH₃CN), NaOH, NaCl, (Sigma-Aldrich); Li₂CO₃, (Fisher Scientific); LiPF₆ (Oakwood Chemicals, 99.99%); NaPF₆ (Strem Chemicals, 99%); TiO₂ (JT Baker); hydrofluoric acid (GFS Chemicals, 48%). The mixed N₂/F₂ gas (Matheson, 80:20 N₂:F₂) was used as received. Purolite UCW 9126 cation exchange resin was used as received. Samples of the compounds Li(H₂O)₄Al(OC(CF₃)₃)₄ (Prof. Ingo Krossing, Univ. of Freiburg), Li(H₂O)_n(Ga(C₂F₅)₄) (Prof. Berthold Hoge, Bielefeld Univ.), and Li(H₂O)(B(3,5-C₆H₃(CF₃)₂)₄) (Prof. Andrew Weller, Univ. of Oxford) were gifts from the indicated colleagues and were used as received.

2.2.2 General Procedures

Anhydrous compounds were prepared using standard airless-ware glassware and a Schlenk-style vacuum line and store in a dinitrogen filled glovebox. Distilled water was deionized with a Barnstead

Nanopure system. The deionized distilled water (dd-H₂O) had a resistivity greater than 18 MΩ (all samples of H₂O used in this work correspond to dd-H₂O prepared in this way).

2.2.3 Synthesis of K₂(H₂O)₂(B₁₂F₁₂)

Potassium dodecafluoro-*closo*-dodecaborate (K₂B₁₂F₁₂) was synthesized by direct fluorination of K₂B₁₂H₁₂ with 80:20 N₂/F₂ in CH₃CN at 0 °C and purified as previously described.³⁸⁻⁴⁰ [**Caution!** *The original purification procedure involving H₂O₂ is not recommended because of the potential isolation of explosive K₂(H₂O)_{2-x}(H₂O)_x(B₁₂F₁₂). An alternate, safer procedure is recommended.*³⁸] The substitution of F atoms for H atoms was monitored periodically using negative-ion electrospray-ionization mass spectrometry (NI-ESI-MS), as previously described. The final degree of F/H metathesis, determined by NI-ESI-MS and ¹⁹F{¹¹B} and ¹¹B{¹⁹F} NMR spectroscopy as previously described, was found to be 99.5+%. Recrystallization from water removed trace amounts of BF₄⁻ that was present. Removal of any brown-yellow colored impurity was accomplished by passing a solution of the as synthesized K₂(B₁₂F₁₂) over an alumina column as described previously.⁴¹

2.2.4 Preparation of (H₃O)₂(B₁₂F₁₂)

Hydronium dodecafluoro-*closo*-dodecaborate ((H₃O)₂(B₁₂F₁₂)) was prepared by passing a 10 wt% aqueous solution of K₂(B₁₂F₁₂) over the acid form of a cation-exchange column (Purolite UCW 9126 resin) that had been previously treated with a 10 vol% solution of aqueous HCl. After passing the solution of K₂(B₁₂F₁₂) through the column, continuous washes of dd-H₂O were passed through the column until the run-off read a neutral pH. The initial solution, and dd-H₂O washes, were collected and concentrated with rotary evaporation. The concentrated solution was standardized via NaOH titration prior to use.

2.2.5 Synthesis of Rb₂(H₂O)₂(B₁₂F₁₂)

An aqueous mixture of RbCl and Ag₂(CH₃CH)₄(B₁₂F₁₂)⁴² was filtered to remove AgCl. Slow evaporation of the filtrate resulted in single crystals suitable for XRD and TGA. Optimization of crystalline Rb₂(H₂O)₂(B₁₂F₁₂) isolated was not attempted, and therefore a yield was not determined.

2.2.6 Synthesis of $\text{Cs}_2(\text{H}_2\text{O})(\text{B}_{12}\text{F}_{12})$

An aqueous solution of $(\text{H}_3\text{O})_2(\text{B}_{12}\text{F}_{12})$ was titrated with a standardized solution of CsOH . Slow evaporation of the resulting solution yielded colorless crystals of $\text{Cs}_2(\text{H}_2\text{O})(\text{B}_{12}\text{F}_{12})$ suitable for XRD. Optimization of crystalline $\text{Cs}_2(\text{H}_2\text{O})(\text{B}_{12}\text{F}_{12})$ isolated was not attempted, and therefore a yield was not determined.

2.2.7 Synthesis of $\text{Na}_2(\text{H}_2\text{O})_2(\text{B}_{12}\text{F}_{12})$

An aqueous solution of $\text{K}_2(\text{B}_{12}\text{F}_{12})$ was converted to $\text{Na}_2(\text{B}_{12}\text{F}_{12})$ using Purolite UCW 9126 cation-exchange resin. The cation-exchange resin was prepared using a 10 wt % solution of ACS Reagent grade NaCl . Passing the $\text{K}_2(\text{B}_{12}\text{F}_{12})$ solution through the ion-exchange column twice (passing a 10 wt % solution of ACS Reagent grade NaCl through the column between passes of the $\text{K}_2(\text{B}_{12}\text{F}_{12})$ solution to regenerate the column) resulted in a solution of $\text{Na}_2(\text{B}_{12}\text{F}_{12})$ with an amount of K^+ ions measuring less than 0.007 mol% as measured by inductively coupled plasma atomic emission spectroscopy (ICP-AES). Solid $\text{Na}_2(\text{H}_2\text{O})_2(\text{B}_{12}\text{F}_{12})$ was isolated by drying the solution of $\text{Na}_2(\text{B}_{12}\text{F}_{12})$ by rotary evaporation and transferring the resulting solid to a desiccator containing solid NaOH , as a desiccant, overnight.

2.2.8 Synthesis of $\text{Li}_2(\text{H}_2\text{O})_4(\text{B}_{12}\text{F}_{12})$

An aqueous solution of $\text{K}_2(\text{B}_{12}\text{F}_{12})$ was converted to $\text{Li}_2(\text{B}_{12}\text{F}_{12})$ using Purolite UCW 9126 cation-exchange resin. The cation-exchange resin was prepared using a 10 wt % solution of ACS Reagent grade LiCl . Passing the $\text{K}_2(\text{B}_{12}\text{F}_{12})$ solution through the ion-exchange column twice (passing a 10 wt % solution of ACS Reagent grade LiCl through the column between passes of the $\text{K}_2(\text{B}_{12}\text{F}_{12})$ solution to regenerate the column) resulted in a solution of $\text{Li}_2(\text{B}_{12}\text{F}_{12})$ with an amount of K^+ ions measuring less than 0.01 mol% as measured by inductively coupled plasma atomic emission spectroscopy (ICP-AES). Solid $\text{Li}_2(\text{H}_2\text{O})_4(\text{B}_{12}\text{F}_{12})$ was isolated by drying the solution of $\text{Li}_2(\text{B}_{12}\text{F}_{12})$ by rotary evaporation and transferring the resulting solid to a desiccator containing solid NaOH , as a desiccant, overnight.

2.2.9 Synthesis of $\text{Li}_2(\text{H}_2\text{O})_2(\text{TiF}_6)$

Solid LiCO_3 and TiO_2 in a molar ratio of 2:1 was dissolved in a solution of 48% HF (aq) inside of a Teflon container. The mixture was heated to 60 °C and allowed to stir vigorously for 1 hour before being allowed to cool to room temperature. Slow evaporation of the solution produced colorless crystals of

$\text{Li}_2(\text{H}_2\text{O})_2(\text{TiF}_6)$. No attempt was made to optimize the isolation of the crystalline materials, therefore a yield was not determined.

2.2.10 ATR-FTIR Spectroscopy

Variable-humidity ATR-FTIR spectra were recorded with a Nicolet 6700 FTIR spectrometer equipped with a stainless-steel Harrick Horizon™ ATR variable-temperature/variable-humidity flow reactor described in detail in previous publications⁴³⁻⁴⁵ (schematic shown in Figure 2.6) or a Nicolet IS-50 FTIR spectrometer. The Nicolet 6700 FTIR spectrometer had a custom stainless steel reactor with a ZnSe crystal for *in situ* measurement of heterogeneous reactions between liquid/solid and gases on the crystal's surface.⁴³ The choice of ZnSe was based on the large penetration depth, estimated to be $1.1 \mu\text{m}$ at 1700 cm^{-1} .⁴³ Aliquots of dilute solutions of the compounds in H_2O , D_2O , 90:10 (v:v) $\text{H}_2\text{O}:\text{D}_2\text{O}$, or a 90:10 (v:v) $\text{D}_2\text{O}:\text{H}_2\text{O}$ mixture were allowed to evaporate to incipient dryness on a $5 \text{ cm} \times 1 \text{ cm} \times 0.2 \text{ cm}$ ZnSe ATR crystal (New Era Enterprise) after it was placed in the flow reactor of the Nicolet 6700 instrument. No attempt was made to control the size or distribution of the microcrystalline particles that formed. The IR beam was directed into the ATR crystal at an incident angle of 45° by mirrors after leaving the interferometer, and the reflected light was returned to a liquid N_2 cooled MCT detector. The vapor pressure of the H_2O over the sample was controlled in real time as spectra were recorded with a purge of dry N_2 gas, or N_2 passed through either a V-Gen M1-120 dew point generator, or a bubbler containing a saturated aqueous salt solution. The rate of gas flow through the 5 cm^3 stainless steel reactor was controlled using an Alicat Scientific flowmeter. The flow rate was 1 L min^{-1} for dry N_2 passed through the dew point generator, and 0.060 L min^{-1} for dry N_2 passed through the solution in the bubbler. Spectra were recorded at specific intervals of time depending on the experiment (typically 128 scans at 1 cm^{-1} resolution, unless otherwise indicated).

Samples of $\text{M}_n(\text{HOD})_m(\text{H}_2\text{O})_{m-1}\text{X}$ and $\text{M}_n(\text{HOD})_m(\text{D}_2\text{O})_{m-1}\text{X}$ ($\text{M} = \text{Li}^+, \text{Na}^+, \text{K}^+, \text{Rb}^+, \text{Cs}^+$; $\text{X} = \text{PF}_6^-$, $\text{Al}(\text{OC}(\text{CF}_3)_3)_4^-$, $\text{B}(3,5\text{-C}_6\text{H}_3(\text{CF}_3)_2)_4^-$, $\text{Ga}(\text{C}_2\text{F}_5)_4^-$, $\text{B}_{12}\text{F}_{12}^{2-}$, TiF_6^{2-}) were prepared by dissolving the appropriate salt in either a 90:10 (v:v) mixture of $\text{H}_2\text{O}:\text{D}_2\text{O}$ or a 90:10 (v:v) mixture of $\text{D}_2\text{O}:\text{H}_2\text{O}$. Aliquots of the solution were allowed to dry on the ZnSe ATR crystal until insipient dryness under a purge of N_2 .

2.3 Results and Discussion

2.3.1 A Note on Methodology

The primary tool used to study the relative strength of O–H···X hydrogen bonding is with IR spectroscopy.^{2,6,8,46-49} Unfortunately, even though the values of $\nu(\text{OH})$ and $\nu(\text{OD})$ are quantitative, and precise to $\pm 1 \text{ cm}^{-1}$ in most of the presented spectra, interpretation of said spectra is restricted to qualitative comparisons. When comparing the O–H···F (or O–D···F) hydrogen bonds for two different compounds, compound A vs. compound B, if compound A has its $\nu(\text{OH})$ (or $\nu(\text{OD})$) bands at higher wavenumbers compared to compound B it means that the hydrogen bond in compound A is weaker than the one in compound B. Furthermore, although O–H and O–D distances can be slightly different for a given hydrogen bond, for the purpose of this work it is assumed that $\text{O}(\text{H})\cdots\text{F} = \text{O}(\text{D})\cdots\text{F}$. This assumption is believed to be valid because (i) the maximum geometric isotope effect (GIE) on $\text{O}(\text{H/D})\cdots\text{F}$ distances, 0.03 \AA , is only observed for strong hydrogen bonds (i.e., for $\text{O}(\text{H})\cdots\text{F} = 2.4\text{--}2.6 \text{ \AA}$),⁵⁰⁻⁵¹ (ii) the hydrogen bonds in the compounds studied are weak, and (iii) the $\text{O}(\text{H/D})\cdots\text{F}$ GIE should be negligible for a lattice with only a small percentage of D/H substitution.

Due to the C_{2v} symmetry of the H_2O molecule, the two O–H oscillators are symmetry equivalent, and thus degenerate in energy leading to coupling and the appearance of two $\nu(\text{OH})$ signals as seen in Figure 2.7. The band at 3734 cm^{-1} corresponds to the asymmetric coupled stretching vibration, labeled $\nu_{\text{asym}}(\text{OH})$, and the band at 3638 cm^{-1} corresponds to the symmetric coupled stretching vibration, labeled $\nu_{\text{sym}}(\text{OH})$. Additionally, in the solid state when multiple H_2O ligands are present, the possibility for intermolecular coupling of O–H oscillators also exists and can further complicate a spectrum. This can be avoided by preparing samples with a low percentage of deuterium substitution.⁶ For metal hydrates, this results in a small percentage of $\text{M}(\text{HOD})(\text{H}_2\text{O})_{n-1}^{\text{m}+}$ complexes, and sometimes a small amount of $\text{M}(\text{D}_2\text{O})(\text{H}_2\text{O})_{n-1}^{\text{m}+}$ complexes, among the predominant $\text{M}(\text{H}_2\text{O})_n^{\text{m}+}$ complexes in the sample. This will give rise, in principle, to a $\nu(\text{OD})$ band for each $\text{HOD}\cdots\text{F}$ environment in the formula unit. To observe separate $\nu(\text{OD})$ bands in the room temperature FTIR spectrum of a sample with slightly different $\text{HOD}\cdots\text{F}$ environments in a single compound, it is necessary that the bands have narrow bandwidths (i.e., small FWHM). This necessity is exemplified in Figure 2.8, which depicts the $\nu(\text{OD})$ region of the FTIR spectrum of a sample of

$\text{Cs}_2(\text{H}_2\text{O})(\text{B}_{12}\text{F}_{12})$ containing a small amount of $\text{Cs}_2(\text{HOD})(\text{B}_{12}\text{F}_{12})$. Two $\nu(\text{OD})$ bands, at 2669 and 2664 cm^{-1} , were observed. These two bands correspond to two different $\text{HOD}\cdots\text{F}$ environments with $\text{O}(\text{D})\cdots\text{F}$ distances of 3.103(3) and 2.997(3) Å, respectively. This spectrum is discussed further in section 2.3.3, but highlights how essential narrow bandwidths are to resolving small environmental differences spectroscopically. The data listed in Table 2.1 show that the FTIR bands for the metal salt hydrates of all of the WCAs presented in this chapter were sufficiently sharp in room temperature FTIR spectra to allow $\nu(\text{OD})$ bands with frequencies that differ by 5 cm^{-1} or more to be resolved. This example, and others discussed in this chapter, are the first examples of room temperature FTIR spectra where $\text{O}-\text{H}\cdots\text{X}$ hydrogen bonds are sufficiently weak enough to be individually resolved.

In rare cases, complete deuterium substitution can change the solid-state structure of a compound (i.e., isotope polymorphism⁵²⁻⁵³). Examples are $\text{P}_{21/c}(\text{COOH})\cdot 2\text{H}_2\text{O}$ ⁵⁴ vs $\text{P}_{21/a}(\text{COOD})\cdot 2\text{D}_2\text{O}$ ⁵⁵ (different herringbone packing patterns) and trifluoroacetic acid tetrahydrate (ionic $(\text{H}_3\text{O}_2)[(\text{CF}_3\text{COO})_2\text{H}]\cdot 6\text{H}_2\text{O}$ vs molecular $\text{CF}_3\text{COOD}\cdot 4\text{D}_2\text{O}$).⁵⁶ However, this is not expected to be a problem for metal salt hydrates with ca. 5–10% D/H exchange.

It has long been known that hydrogen bonds involving D are stronger than those involving H, all other things being equal, because of the difference in zero point energies. For example, the energy difference between the two isotopomers $\text{DOH}\cdots\text{OH}_2$ and $\text{HOD}\cdots\text{OH}_2$ has been estimated to be 60 cm^{-1} (0.72 kJ mol^{-1}).⁵⁷⁻⁵⁹ Experimentally, the isotopomer $\text{HOD}\cdots\text{FCH}_3$ was observed in a frozen Ar matrix, but $\text{DOH}\cdots\text{FCH}_3$ was not (the difference in zero point energies was calculated to be 0.69 kJ mol^{-1} ;⁶⁰ the $\text{HOH}\cdots\text{FCH}_3$ complex has also been studied by other theorists⁶¹⁻⁶²). Similarly, the isotopomer $\text{HOD}\cdots\text{FCH}_2\text{F}$, with a rotational temperature of ca. 10 K, was observed in the gas phase, but $\text{DOH}\cdots\text{FCH}_2\text{F}$ was not.⁶³ (The $\text{DOH}\cdots\text{FCH}_2\text{F}$ complex was also studied theoretically.⁶³⁻⁶⁴) Nevertheless, at room temperature the small zero point energy differences will have a negligible effect on the relative populations of $\text{DOH}\cdots\text{F}$ vs $\text{HOD}\cdots\text{F}$ species in the samples studied in this chapter.

In many of the structures discussed in this chapter one or more of the $\text{O}-\text{H}$ (or $\text{O}-\text{D}$) moieties of the crystalline water molecule are hypothesized to form bifurcated hydrogen bonds. A bifurcated hydrogen bond is when there are two hydrogen bond donors per one hydrogen bond acceptor. A bifurcated hydrogen bond

is assigned when, in a crystal structure, the O–H moiety of interest lays between two F atoms instead of pointing at a single F atom. In the case of a bifurcated hydrogen bond both O(H)···F distances are reported.

2.3.2 Isomorphous $M_2(H_2O)_2(B_{12}F_{12})$ ($M = K, Rb$)

The salts $K_2(H_2O)_2(B_{12}F_{12})$ ⁶⁵ and $Rb_2(H_2O)_2(B_{12}F_{12})$ ⁶⁶ both crystalize in the $P2_1/c$ space group and are isomorphous with each other. Drawings of a portion of each structure is shown in Figure 2.9. The two symmetry related metal cations and two symmetry related H_2O molecules form a $[M_2(H_2O)_2]^{2+}$ ($M = K, Rb$) quadrilateral with 2.770(6) and 2.772(6) Å O–K distances and a K–O–K' angle of 100.3° for the $K_2(H_2O)_2(B_{12}F_{12})$ compound and 2.857(1) and 2.915(1) Å O–Rb distances and a Rb–O–Rb' angle of 112.4° for the $Rb_2(H_2O)_2(B_{12}F_{12})$ compound. For the $K_2(H_2O)_2(B_{12}F_{12})$ compound there are three O(H)···F bonds that could reasonably form O–H···F hydrogen bonds. One of the O–H moieties forms an O–H···F hydrogen bond with an O(H)···F distance of 2.978(1) Å. The other O–H moiety lays between two O(H)···F vectors, indicating a bifurcated hydrogen bond with O(H)···F distances of 2.972(1) and 2.978(1) Å, and a F···O···F' angle of 57.1°. In the $Rb_2(H_2O)_2(B_{12}F_{12})$ compound the O(H)···F distance is 2.857(2) Å for the O–H moiety laying along a single O(H)···F vector. The other O–H moiety lays between two O(H)···F vectors, indicating a bifurcated hydrogen bond with O(H)···F distances of 2.859(2) and 2.931(2) Å, and a F···O···F' angle of 60.7°.

The $\nu(OH)$ region of FTIR spectra of $K_2(H_2O)_2(B_{12}F_{12})$ and $Rb_2(H_2O)_2(B_{12}F_{12})$ are shown in Figure 2.10 and 2.11, respectively. The two spectra are directly compared in Figure 2.12 where they are plotted with the same x-axis range. In the FTIR spectrum of the $\nu(OH)$ region of $K_2(H_2O)_2(B_{12}F_{12})$ the bands at 3637 and 3576 cm^{-1} are assigned to the $\nu_{asym}(OH)$ and the $\nu_{sym}(OH)$ coupled stretching vibrations, respectively. A two peak Lorentzian least squares fit of the spectrum is shown in Figure 2.10. In the FTIR spectrum of the $\nu(OH)$ region of $Rb_2(H_2O)_2(B_{12}F_{12})$ the bands at 3653 and 3585 cm^{-1} are assigned to the $\nu_{asym}(OH)$ and the $\nu_{sym}(OH)$ coupled stretching vibrations, respectively. A two peak Lorentzian least squares fit of the spectrum is shown in Figure 2.11. The FTIR spectrum of the $\nu(OH)$ region of the FTIR spectrum of a mixture of $Rb_2(HOD)(H_2O)(B_{12}F_{12})$ and $Rb_2(H_2O)_2(B_{12}F_{12})$ is shown in Figure 2.13. The bands at 3625 and 3614 cm^{-1} are assigned to the $\nu(OH)$ stretching vibration for the HOD molecule in $Rb_2(HOD)(H_2O)(B_{12}F_{12})$. The presence of two bands for this single O–H moiety likely arises from the two significantly different O–H···F

hydrogen bonding environments that the H atom can occupy. Figure 2.13 also contains a four peak Lorentzian least squares fit of the four bands in this spectrum. The FTIR spectrum of the $\nu(\text{OD})$ region for a mixture of $\text{K}_2(\text{HOD})(\text{H}_2\text{O})(\text{B}_{12}\text{F}_{12})$ and $\text{K}_2(\text{D}_2\text{O})(\text{H}_2\text{O})(\text{B}_{12}\text{F}_{12})$ is shown in Figure 2.14. The two bands at 2700 and 2615 cm^{-1} are assigned to the $\nu_{\text{asym}}(\text{OD})$ and the $\nu_{\text{sym}}(\text{OD})$ coupled stretching vibrations, respectively, for the D_2O molecule in $\text{K}_2(\text{D}_2\text{O})(\text{H}_2\text{O})(\text{B}_{12}\text{F}_{12})$. The band at 2652 cm^{-1} is assigned to the $\nu(\text{OD})$ stretching vibration of the HOD molecule in $\text{K}_2(\text{HOD})(\text{H}_2\text{O})(\text{B}_{12}\text{F}_{12})$. There is a prominent shoulder on the higher wavenumber side of the band at 2652 cm^{-1} indicating a possible second $\nu(\text{OD})$ stretching vibration of the HOD molecule in $\text{K}_2(\text{HOD})(\text{H}_2\text{O})(\text{B}_{12}\text{F}_{12})$ arising from the different $\text{O}-\text{D}\cdots\text{F}$ hydrogen bonding environments that the D atom can occupy. The $\nu(\text{OD})$ region of the FTIR spectrum of a mixture of $\text{Rb}_2(\text{HOD})(\text{H}_2\text{O})(\text{B}_{12}\text{F}_{12})$ and $\text{Rb}_2(\text{D}_2\text{O})(\text{H}_2\text{O})(\text{B}_{12}\text{F}_{12})$ is shown in Figure 2.15. The bands at 2711 and 2623 cm^{-1} are assigned to the $\nu_{\text{asym}}(\text{OD})$ and $\nu_{\text{sym}}(\text{OD})$ coupled stretching vibrations, respectively, for the D_2O molecule in $\text{Rb}_2(\text{D}_2\text{O})(\text{H}_2\text{O})(\text{B}_{12}\text{F}_{12})$. The bands at 2668 and 2660 cm^{-1} are assigned to the $\nu(\text{OD})$ stretching vibration for the HOD molecule in $\text{Rb}_2(\text{HOD})(\text{H}_2\text{O})(\text{B}_{12}\text{F}_{12})$. The presence of two bands for this single $\text{O}-\text{D}$ moiety likely arises from the two significantly different $\text{O}-\text{D}\cdots\text{F}$ hydrogen bonding environments that the D atom can occupy. Figure 2.15 also contains a four peak Lorentzian least squares fit of the four bands in this spectrum.

2.3.3 $\text{Cs}_2(\text{H}_2\text{O})(\text{B}_{12}\text{F}_{12})$

The orthorhombic structure of $\text{Cs}_2(\text{H}_2\text{O})(\text{B}_{12}\text{F}_{12})$, which crystalizes in the space group $P2_12_12_1$ was originally published in ref. 67. There is only one crystallographically unique water molecule. The bonding environment around this water molecule is depicted in Figure 2.16 and contains two $\text{Cs}-\text{O}$ coordination bonds and the nine nearest neighbor $\text{O}(\text{H})\cdots\text{F}$ bonds. The water molecule is coordinated to two symmetry equivalent Cs atoms, with $\text{Cs}-\text{O}$ and $\text{Cs}'-\text{O}$ distances of 3.137(2) and 3.310(2) Å and a $\text{Cs}-\text{O}-\text{Cs}'$ angle of 116.9°. This results in the formation of infinite $[-\text{Cs}-\mu-\text{H}_2\text{O}-\text{Cs}-\mu-\text{H}_2\text{O}-]_{\infty}$ chains along the crystallographic C-axis. The crystallographically unique Cs atom that is not part of this chain has no $\text{Cs}-\text{OH}_2$ coordination bonds, only $\text{Cs}\cdots\text{F}$ interactions. The nine $\text{O}(\text{H})\cdots\text{F}$ bonds in the drawing shown in Figure 2.16 have $\text{O}(\text{H})\cdots\text{F}$ distances that range from 2.997(3) and 4.050(3) Å. The two most relevant of these are the two $\text{O}(\text{H})\cdots\text{F}$ bonds lying closest along the $\text{O}-\text{H}$ bonds. These $\text{O}(\text{H})\cdots\text{F}$ bonds are the most likely to represent $\text{O}-\text{H}\cdots\text{F}$ hydrogen bonds

with O(H)···F distances of 2.997(3) and 3.103(3) Å. The O–H1···F9 bond angle is 157° and for O–H2···F4 the angle is 148°.

The FTIR spectrum of the $\nu(\text{OH})$ region of $\text{Cs}_2(\text{H}_2\text{O})(\text{B}_{12}\text{F}_{12})$ is shown in Figure 2.17. The band at 3658 cm^{-1} corresponds to the $\nu_{\text{asym}}(\text{OH})$ coupled stretching vibration, and the band at 3588 cm^{-1} corresponds to the $\nu_{\text{sym}}(\text{OH})$ coupled stretching vibration. The broad feature at ca. 3400 cm^{-1} is hypothesized to be a thin layer of adsorbed water on the surface of the ATR crystal arising from holding the sample under a pressure of H_2O (g) to collect the spectrum. The $\delta(\text{HOH})$ region of the FTIR spectrum of $\text{Cs}_2(\text{H}_2\text{O})(\text{B}_{12}\text{F}_{12})$ is shown in Figure 2.18. The $\nu(\text{OD})$ region of a mixture of $\text{Cs}_2(\text{D}_2\text{O})(\text{B}_{12}\text{F}_{12})$ and $\text{Cs}_2(\text{HOD})(\text{B}_{12}\text{F}_{12})$ is shown in Figure 2.8. The band at 2715 cm^{-1} corresponds to the $\nu_{\text{asym}}(\text{OD})$ coupled stretching vibration, and the band at 2624 cm^{-1} corresponds to the $\nu_{\text{sym}}(\text{OD})$ coupled stretching vibration. The $\nu(\text{OH})$ and $\nu(\text{OD})$ regions of the FTIR spectrum of a sample of $\text{Cs}_2(\text{H}_2\text{O})(\text{B}_{12}\text{F}_{12})$ containing a small amount of $\text{Cs}_2(\text{HOD})(\text{B}_{12}\text{F}_{12})$ are shown in Figure 2.19 and 2.8, respectively. The two bands at 3626 and 3621 cm^{-1} in Figure 2.19 represent the DO–H···F hydrogen bonds, with the 3626 cm^{-1} band assigned to the DO–H2···F4 hydrogen bond and the 3621 cm^{-1} band assigned to the DO–H1···F9 hydrogen bond. The two bands at 2669 and 2664 cm^{-1} in Figure 2.8 represent the HO–D···F hydrogen bonds, with the 2669 cm^{-1} band assigned to the HO–D2···F4 hydrogen bond and the 2664 cm^{-1} band assigned to the HO–D1···F9 hydrogen bond. Lorentzian least square fits of the $\nu(\text{OH})$ region of $\text{Cs}_2(\text{H}_2\text{O})(\text{B}_{12}\text{F}_{12})$ is shown in Figure 2.17. A four peak Lorentzian least square fit of the $\nu(\text{OD})$ region of $\text{Cs}_2(\text{D}_2\text{O})(\text{B}_{12}\text{F}_{12})$ and $\text{Cs}_2(\text{HOD})(\text{B}_{12}\text{F}_{12})$ is shown in Figure 2.20. Finally, a Lorentzian least squares fit of the $\delta(\text{HOH})$ region of the FTIR spectrum of $\text{Cs}_2(\text{H}_2\text{O})(\text{B}_{12}\text{F}_{12})$ is shown in Figure 2.18.

2.3.4 $\text{Na}_2(\text{H}_2\text{O})_2(\text{B}_{12}\text{F}_{12})$

The $\nu(\text{OH})$ region of the FTIR spectrum of $\text{Na}_2(\text{H}_2\text{O})_2(\text{B}_{12}\text{F}_{12})$ is shown in Figure 2.21. The band at 3651 cm^{-1} is assigned to the $\nu_{\text{asym}}(\text{OH})$ coupled stretching vibration, and the band at 3556 cm^{-1} is assigned to the $\nu_{\text{sym}}(\text{OH})$ coupled stretching vibration. The $\nu(\text{OD})$ region of the FTIR spectrum of a sample of $\text{Na}_2(\text{H}_2\text{O})_2(\text{B}_{12}\text{F}_{12})$ containing a small amount of $\text{Na}_2(\text{HOD})(\text{D}_2\text{O})(\text{B}_{12}\text{F}_{12})$ is shown in Figure 2.22. The band at 2706 cm^{-1} is assigned to the $\nu_{\text{asym}}(\text{OD})$ coupled stretching vibration, and the band at 2608 cm^{-1} is assigned to the $\nu_{\text{sym}}(\text{OD})$ coupled stretching vibration. The remaining two bands in this region, at 2680 and 2628 cm^{-1} , respectively, are assigned to the $\nu(\text{OD})$ stretching vibration of the HOD molecule. The presence of two distinct

bands with this assignment it would indicate that there are two different HO–D···F environments the D atom can occupy. Due to the lack of a crystal structure for the $\text{Na}_2(\text{H}_2\text{O})_2(\text{B}_{12}\text{F}_{12})$ salt this is only a tentative assignment at this time. Lorentzian least squares peak fits of the $\nu(\text{OH})$ region is shown in Figure 2.21.

2.3.5 $\text{Li}(\text{H}_2\text{O})_4(\text{Al}(\text{OC}(\text{CF}_3)_3)_4)$

The X-ray crystal structure of $\text{Li}(\text{H}_2\text{O})_4(\text{Al}(\text{OC}(\text{CF}_3)_3)_4)$ was originally published in 2009.⁶⁸ Drawings of two portions of the structure are shown in Figure 2.23. The four coordinated H_2O molecules of the $\text{Li}(\text{H}_2\text{O})_4^+$ complex are all symmetry-related. The two $\text{O}(\text{H})\cdots\text{F}$ distances for the symmetry-related coordinated water molecules are 3.102(2) and 3.157(2) Å, with $\text{O}-\text{H}\cdots\text{F}$ bond angles of 130° and 148° , respectively. There are two longer additional $\text{O}-\text{H}\cdots\text{F}$ bonds with $\text{O}(\text{H})\cdots\text{F}$ distances of 3.296(2) and 3.297(2) Å and $\text{O}-\text{H}\cdots\text{F}$ angles of 134° and 146° . The four $\text{O}-\text{H}\cdots\text{F}$ bonds can be thought of as two $\text{O}-\text{H}$ moieties each participating in a bifurcated hydrogen bond with different bonding environments. The two $\text{F}\cdots\text{O}\cdots\text{F}'$ bond angles for the different environments are 62.4° and 53.2° , respectively.

The $\nu(\text{OH})$ region of the FTIR spectrum of $\text{Li}(\text{H}_2\text{O})_4(\text{Al}(\text{OC}(\text{CF}_3)_3)_4)$ is shown in Figure 2.24. The bands at 3719 and 3644 cm^{-1} are assigned to the $\nu_{\text{asym}}(\text{OH})$ and the $\nu_{\text{sym}}(\text{OH})$ coupled stretching vibrations, respectively. The $\nu(\text{OH})$ region of the FTIR spectrum of a mixture of $\text{Li}(\text{H}_2\text{O})(\text{D}_2\text{O})_3(\text{Al}(\text{OC}(\text{CF}_3)_3)_4)$ and $\text{Li}(\text{HOD})(\text{D}_2\text{O})_3(\text{Al}(\text{OC}(\text{CF}_3)_3)_4)$ is shown in Figure 2.25. The bands at 3711 and 3640 cm^{-1} are assigned to the $\nu_{\text{asym}}(\text{OH})$ and the $\nu_{\text{sym}}(\text{OH})$ coupled stretching vibrations, respectively, for the H_2O molecule in $\text{Li}(\text{H}_2\text{O})(\text{D}_2\text{O})_3(\text{Al}(\text{OC}(\text{CF}_3)_3)_4)$, and the band at 3676 cm^{-1} is assigned to the $\nu(\text{OH})$ stretching vibration for an HOD molecule in $\text{Li}(\text{HOD})(\text{D}_2\text{O})_3(\text{Al}(\text{OC}(\text{CF}_3)_3)_4)$. The $\delta(\text{HOH})$ region of the FTIR spectrum of $\text{Li}(\text{H}_2\text{O})_4(\text{Al}(\text{OC}(\text{CF}_3)_3)_4)$ is shown in Figure 2.26. The band at 1626 cm^{-1} is assigned to the $\delta(\text{HOH})$ bending vibration for $\text{Li}(\text{H}_2\text{O})_4(\text{Al}(\text{OC}(\text{CF}_3)_3)_4)$. The $\nu(\text{OD})$ region of the FTIR spectrum of a mixture of $\text{Li}(\text{HOD})(\text{H}_2\text{O})_3(\text{Al}(\text{OC}(\text{CF}_3)_3)_4)$ and $\text{Li}(\text{D}_2\text{O})(\text{H}_2\text{O})_3(\text{Al}(\text{OC}(\text{CF}_3)_3)_4)$ is shown in Figure 2.27. The two bands at 2755 and 2660 cm^{-1} are assigned to the $\nu_{\text{asym}}(\text{OD})$ and the $\nu_{\text{sym}}(\text{OD})$ coupled stretching vibrations, respectively, of $\text{Li}(\text{D}_2\text{O})(\text{H}_2\text{O})_3(\text{Al}(\text{OC}(\text{CF}_3)_3)_4)$. The band at 2706 is assigned to the $\nu(\text{OD})$ stretching vibration for HOD molecule in $\text{Li}(\text{HOD})(\text{H}_2\text{O})_3(\text{Al}(\text{OC}(\text{CF}_3)_3)_4)$. The $\delta(\text{HOH})$ region of the FTIR spectrum of $\text{Li}(\text{HOD})(\text{D}_2\text{O})_3(\text{Al}(\text{OC}(\text{CF}_3)_3)_4)$ and $\text{Li}(\text{H}_2\text{O})(\text{D}_2\text{O})_3(\text{Al}(\text{OC}(\text{CF}_3)_3)_4)$ is shown in Figure 2.26. The bands at 1632 and 1438 cm^{-1} are assigned to $\delta(\text{HOH})$ and $\delta(\text{HOD})$, respectively, for a mixture of

$\text{Li}(\text{H}_2\text{O})(\text{D}_2\text{O})_3(\text{Al}(\text{OC}(\text{CF}_3)_3)_4)$ and $\text{Li}(\text{HOD})(\text{D}_2\text{O})_3(\text{Al}(\text{OC}(\text{CF}_3)_3)_4)$. Lorentzian least squares fits of the $\nu(\text{OH})$ region of the FTIR spectrum of $\text{Li}(\text{H}_2\text{O})_4(\text{Al}(\text{OC}(\text{CF}_3)_3)_4)$ and a mixture of $\text{Li}(\text{HOD})(\text{D}_2\text{O})_3(\text{Al}(\text{OC}(\text{CF}_3)_3)_4)$ and $\text{Li}(\text{H}_2\text{O})(\text{D}_2\text{O})_3(\text{Al}(\text{OC}(\text{CF}_3)_3)_4)$ is shown in Figure 2.28 and 2.25, respectively. Lorentzian least squares fits of the $\nu(\text{OD})$ region of the FTIR spectrum of a mixture of $\text{Li}(\text{HOD})(\text{H}_2\text{O})_3(\text{Al}(\text{OC}(\text{CF}_3)_3)_4)$ and $\text{Li}(\text{D}_2\text{O})(\text{H}_2\text{O})_3(\text{Al}(\text{OC}(\text{CF}_3)_3)_4)$ is shown in Figure 2.27.

2.3.6 $\text{Li}(\text{H}_2\text{O})(\text{B}(3,5\text{-C}_6\text{H}_3(\text{CF}_3)_2)_4)$

A drawing of a portion of the X-ray structure of $\text{Li}(\text{H}_2\text{O})(\text{B}(3,5\text{-C}_6\text{H}_3(\text{CF}_3)_2)_4)$, using data published in 2019,⁶⁹ is shown in Figure 2.29. In the figure only the three $\text{O}(\text{H})\cdots\text{F}$ bonds relevant to $\text{O}-\text{H}\cdots\text{F}$ hydrogen bonding are included. One of the $\text{O}-\text{H}$ moieties, lies along the $\text{O}(\text{H})\cdots\text{F1}$ interaction, likely forming a single $\text{O}-\text{H}\cdots\text{F}$ hydrogen bond. The $\text{O}(\text{H})\cdots\text{F}$ bond distance is 2.995(6) Å with an $\text{O}-\text{H}\cdots\text{F}$ bond angle of 167°. The H atom of the other $\text{O}-\text{H}$ moiety lies between two F atoms, indicating that it is likely that this is a bifurcated hydrogen bond. The two $\text{O}(\text{H})\cdots\text{F}$ distances are 2.995(6) and 3.077(6) Å, with $\text{O}-\text{H}\cdots\text{F}$ angles of 140° and 157°, respectively.

The $\nu(\text{OH})$ region of the FTIR spectrum of $\text{Li}(\text{H}_2\text{O})(\text{B}(3,5\text{-C}_6\text{H}_3(\text{CF}_3)_2)_4)$ is shown in Figure 2.24. The bands at 3718 and 3639 cm^{-1} are assigned to the $\nu_{\text{asym}}(\text{OH})$ and $\nu_{\text{sym}}(\text{OH})$ coupled stretching vibrations, respectively. The FTIR spectrum of $\nu(\text{OH})$ region for a mixture of $\text{Li}(\text{HOD})(\text{B}(3,5\text{-C}_6\text{H}_3(\text{CF}_3)_2)_4)$ and $\text{Li}(\text{H}_2\text{O})(\text{B}(3,5\text{-C}_6\text{H}_3(\text{CF}_3)_2)_4)$ is shown in Figure 2.30. The bands at 3718 and 3639 cm^{-1} are assigned to the $\nu_{\text{asym}}(\text{OH})$ and $\nu_{\text{sym}}(\text{OH})$ coupled stretching vibrations, respectively, for the H_2O molecule in $\text{Li}(\text{H}_2\text{O})(\text{B}(3,5\text{-C}_6\text{H}_3(\text{CF}_3)_2)_4)$, while the band at 3679 is assigned to the $\nu(\text{OH})$ stretching vibration of the HOD molecule in $\text{Li}(\text{HOD})(\text{B}(3,5\text{-C}_6\text{H}_3(\text{CF}_3)_2)_4)$. Figure 2.30 also contains the three peak Lorentzian least squares fit of the bands within this region. The $\nu(\text{OD})$ region of the FTIR spectrum of a mixture of $\text{Li}(\text{HOD})(\text{B}(3,5\text{-C}_6\text{H}_3(\text{CF}_3)_2)_4)$ and $\text{Li}(\text{D}_2\text{O})(\text{B}(3,5\text{-C}_6\text{H}_3(\text{CF}_3)_2)_4)$ is shown in Figure 2.30. The bands at 2760 and 2659 cm^{-1} are assigned to the $\nu_{\text{asym}}(\text{OD})$ and $\nu_{\text{sym}}(\text{OD})$ coupled stretching vibrations for the D_2O molecule in $\text{Li}(\text{D}_2\text{O})(\text{B}(3,5\text{-C}_6\text{H}_3(\text{CF}_3)_2)_4)$, respectively and the band at 2705 cm^{-1} is assigned to the $\nu(\text{OD})$ stretching vibration of the HOD molecule in $\text{Li}(\text{HOD})(\text{B}(3,5\text{-C}_6\text{H}_3(\text{CF}_3)_2)_4)$. The three peak Lorentzian least squares fit of these bands is also shown in Figure 2.30.

2.3.7 $\text{Li}(\text{H}_2\text{O})_n(\text{Ga}(\text{C}_2\text{F}_5)_4)$

The $\nu(\text{OH})$ region of the FTIR spectrum of $\text{Li}(\text{H}_2\text{O})_n(\text{Ga}(\text{C}_2\text{F}_5)_4)$ is shown in Figure 2.24. The bands at 3702 and 3630 cm^{-1} are assigned to the $\nu_{\text{asym}}(\text{OH})$ and the $\nu_{\text{sym}}(\text{OH})$ coupled stretching vibrations, respectively. A two peak Lorentzian least squares fit of this spectrum is shown in Figure 2.31. The FTIR spectrum of the $\nu(\text{OD})$ region of a mixture of $\text{Li}(\text{HOD})(\text{H}_2\text{O})_{n-1}(\text{Ga}(\text{C}_2\text{F}_5)_4)$ and $\text{Li}(\text{D}_2\text{O})(\text{H}_2\text{O})_{n-1}(\text{Ga}(\text{C}_2\text{F}_5)_4)$ is shown in Figure 2.32. A three peak Lorentzian least squares fit of this spectrum is shown in Figure 2.32. The bands at 2749 and 2654 cm^{-1} are assigned to the $\nu_{\text{asym}}(\text{OD})$ and the $\nu_{\text{sym}}(\text{OD})$ coupled stretching vibrations of the D_2O molecule in $\text{Li}(\text{D}_2\text{O})(\text{H}_2\text{O})_{n-1}(\text{Ga}(\text{C}_2\text{F}_5)_4)$, respectively. The band at 2697 cm^{-1} is assigned to the $\nu(\text{OD})$ stretching vibration of the HOD molecule in $\text{Li}(\text{HOD})(\text{H}_2\text{O})_{n-1}(\text{Ga}(\text{C}_2\text{F}_5)_4)$. A three peak Lorentzian least squares fit of this spectrum is shown in Figure 2.32.

2.3.8 $\text{Li}_2(\text{H}_2\text{O})_2(\text{TiF}_6)$

The X-ray structure of $\text{Li}_2(\text{H}_2\text{O})_2(\text{TiF}_6)$ was originally published in 1973.⁷⁰ A drawing of a portion of the structure is shown in Figure 2.33. In the structure there is only one crystallographically unique H_2O molecule. The H atom positions in the structure were not determined or modeled as part of the solution. As a result it is not easy to predict which of the $\text{O}(\text{H})\cdots\text{F}$ bonds are most probable to participate in $\text{O}-\text{H}\cdots\text{F}$ hydrogen bonding. Based on the position of the O atom, with respect to the two Li^+ cations it is coordinated to, there are four potential $\text{O}(\text{H})\cdots\text{F}$ bonds that could participate in $\text{O}-\text{H}\cdots\text{F}$ hydrogen bonding. Of these 4 bonds there are two sets of two symmetry equivalent $\text{O}(\text{H})\cdots\text{F}$ bonds. The two different $\text{O}(\text{H})\cdots\text{F}$ distances are 3.007(6) and 3.048(6) Å, respectively. While it is not unreasonable to hypothesize that the $\text{O}-\text{H}\cdots\text{F}$ hydrogen bond is formed between the $\text{O}-\text{H}$ moiety and a single F atom, with both of the $\text{O}-\text{H}\cdots\text{F}$ hydrogen bonds being identical, either with $\text{O}(\text{H})\cdots\text{F}$ distances of 3.007(6) or 3.048(6) Å, based on the position of the $\text{Li}\cdots\text{O}\cdots\text{Li}'$ coordination bonds it is more likely that the $\text{O}-\text{H}$ moieties lay between two F atoms with different $\text{O}(\text{H})\cdots\text{F}$ interaction distances. This would create a local T_d bonding environment around the O atom. This arrangement will result in a pair of bifurcated hydrogen bonds with an $\text{F}\cdots\text{O}\cdots\text{F}'$ bond angle of 67.0°.

The $\nu(\text{OH})$ region of the FTIR spectrum of $\text{Li}_2(\text{H}_2\text{O})_2(\text{TiF}_6)$ is shown in Figure 2.34. The band at 3583 cm^{-1} is assigned to the $\nu_{\text{asym}}(\text{OH})$ coupled stretching vibration, and the band at 3541 cm^{-1} is assigned to the $\nu_{\text{sym}}(\text{OH})$ coupled stretching vibration. The $\nu(\text{OD})$ region of the FTIR spectrum of a mixture of

$\text{Li}_2(\text{HOD})(\text{H}_2\text{O})(\text{TiF}_6)$ and $\text{Li}_2(\text{D}_2\text{O})(\text{H}_2\text{O})(\text{TiF}_6)$ is shown in Figure 2.34. The band at 2663 cm^{-1} is assigned to the $\nu_{\text{asym}}(\text{OD})$ coupled stretching vibration and the band at 2592 cm^{-1} is assigned to the $\nu_{\text{sym}}(\text{OD})$ coupled stretching vibration for the D_2O molecule in $\text{Li}_2(\text{D}_2\text{O})(\text{H}_2\text{O})(\text{TiF}_6)$. The band at 2623 cm^{-1} is assigned to the $\nu(\text{OD})$ stretching vibration for the HOD molecule in $\text{Li}_2(\text{HOD})(\text{H}_2\text{O})(\text{TiF}_6)$.

2.3.9 $\text{Li}(\text{H}_2\text{O})(\text{PF}_6)$

The $\nu(\text{OH})$ region of the FTIR spectrum of a mixture of $\text{Li}(\text{H}_2\text{O})(\text{PF}_6)$ and $\text{Li}(\text{HOD})(\text{PF}_6)$ is shown in Figure 2.35. The bands at 3602 and 3549 cm^{-1} are assigned to the $\nu_{\text{asym}}(\text{OH})$ and $\nu_{\text{sym}}(\text{OH})$ coupled stretching vibrations for the H_2O molecule in $\text{Li}(\text{H}_2\text{O})(\text{PF}_6)$, respectively, and the band at 3579 cm^{-1} is assigned to the $\nu(\text{OH})$ stretching vibration of HOD in $\text{Li}(\text{HOD})(\text{PF}_6)$. Figure 2.35 also contains a three peak Lorentzian least squares fit of the three bands in this region of the spectrum. The $\nu(\text{OD})$ region of the FTIR spectrum of a mixture of $\text{Li}(\text{D}_2\text{O})(\text{PF}_6)$ and $\text{Li}(\text{HOD})(\text{PF}_6)$ is shown in Figure 2.36. The bands at 2680 and 2597 cm^{-1} are assigned to the $\nu_{\text{asym}}(\text{OD})$ and $\nu_{\text{sym}}(\text{OD})$ coupled stretching vibrations for the D_2O molecule in $\text{Li}(\text{D}_2\text{O})(\text{PF}_6)$, respectively, and the band at 2636 cm^{-1} is assigned to the $\nu(\text{OD})$ stretching vibration of HOD in $\text{Li}(\text{HOD})(\text{PF}_6)$. Figure 2.36 also contains a four peak Lorentzian least squares fit of the three bands in this region of the spectrum. The fourth modeled peak was used to account for an impurity peak, labeled with an asterisk, that appears a few wavenumbers higher than the band assigned to the HOD vibration.

2.3.10 $\text{Na}(\text{H}_2\text{O})(\text{PF}_6)$

A drawing of the X-ray structure of $\text{Na}(\text{H}_2\text{O})(\text{PF}_6)$, which was generated using data published in 2003,⁷¹ is shown in Figure 2.37. The only symmetry unique H_2O molecule is coordinated to a pair of Na^+ cations forming infinite $[-\text{Na}-\mu-\text{H}_2\text{O}-\text{Na}-\mu-\text{H}_2\text{O}-]_{\infty}$ chain. The $\text{Na}-\text{O}-\text{Na}$ bond angle is 111° . The two $\text{O}-\text{H}$ moieties of the water molecule form symmetry identical $\text{O}-\text{H}\cdots\text{F}$ hydrogen bonds with an $\text{O}(\text{H})\cdots\text{F}$ bond distance of $3.064(2)\text{ \AA}$.

The $\nu(\text{OH})$ region of the FTIR spectrum of $\text{Na}(\text{H}_2\text{O})(\text{PF}_6)$ is shown in Figure 2.38. The bands at 3639 and 3570 cm^{-1} are assigned to the $\nu_{\text{asym}}(\text{OH})$ and $\nu_{\text{sym}}(\text{OH})$ coupled stretching vibrations, respectively. The $\nu(\text{OH})$ region of the FTIR spectrum of a mixture of $\text{Na}(\text{H}_2\text{O})(\text{PF}_6)$ and $\text{Na}(\text{HOD})(\text{PF}_6)$ is shown in Figure 2.39. As in Figure 2.38 the bands at 3639 and 3570 cm^{-1} are assigned to the $\nu_{\text{asym}}(\text{OH})$ and $\nu_{\text{sym}}(\text{OH})$ coupled stretching vibrations for the H_2O molecule in $\text{Na}(\text{H}_2\text{O})(\text{PF}_6)$, respectively, and the band at 3606 cm^{-1} is

assigned to the $\nu(\text{OH})$ stretching vibration of HOD in $\text{Na}(\text{HOD})(\text{PF}_6)$. Figure 2.39 also contains a three peak Lorentzian least squares fit of the three bands in this region of the spectrum. The $\nu(\text{OD})$ region of the FTIR spectrum of a mixture of $\text{Na}(\text{D}_2\text{O})(\text{PF}_6)$ and $\text{Na}(\text{HOD})(\text{PF}_6)$ is shown in Figure 2.39. The bands at 2704 and 2612 cm^{-1} are assigned to the $\nu_{\text{asym}}(\text{OD})$ and $\nu_{\text{sym}}(\text{OD})$ coupled stretching vibrations for the D_2O molecule in $\text{Na}(\text{D}_2\text{O})(\text{PF}_6)$, respectively, and the band at 2654 cm^{-1} is assigned to the $\nu(\text{OD})$ stretching vibration of HOD in $\text{Na}(\text{HOD})(\text{PF}_6)$. Figure 2.39 also contains a three peak Lorentzian least squares fit of the three bands in this region of the spectrum. Finally the $\delta(\text{HOH})$ region of a mixture of $\text{Na}(\text{H}_2\text{O})(\text{PF}_6)$ and $\text{Na}(\text{HOD})(\text{PF}_6)$ is shown in Figure 2.40. The band at 1628 cm^{-1} is assigned to the $\delta(\text{HOH})$ bending vibration and the band at 1433 cm^{-1} is assigned to the $\delta(\text{HOD})$ bending vibration.

2.3.11 The Weakest O(H)···F Hydrogen Bonds

With respect to the $\nu(\text{OH})$ criterion (section 2.3.1), focusing on the H_2O molecules in which both O–H bonds form hydrogen bonds to F atoms (i.e., compounds with $\text{F}\cdots\text{HOH}\cdots\text{F}$ moieties), before this work the weakest hydrogen bonds determined by this qualitative criterion were in $\text{PVDF}(\text{H}_2\text{O})$ ($\nu(\text{OH}) = 3707$ and 3623 cm^{-1} ; see Figure 2.41) and $[\text{NEt}_4]_2[\text{Hg}(\text{H}_2\text{O})(\text{CB}_{11}\text{F}_{11})]$ (3681 and 3587 cm^{-1} ; the spectrum is shown in Figure 2.42 and its structure is shown in Figure 2.42).^{37,72} The author now reports that the $\text{F}\cdots\text{HOH}\cdots\text{F}$ hydrogen bonds in $\text{Li}(\text{H}_2\text{O})_4(\text{Al}(\text{OC}(\text{CF}_3)_3)_4)$ ($\nu(\text{OH}) = 3719$ and 3644 cm^{-1}), $\text{Li}(\text{H}_2\text{O})(\text{B}(3,5\text{-C}_6\text{H}_3(\text{CF}_3)_2)_4)$ ($\nu(\text{OH}) = 3718$ and 3639 cm^{-1}), and $\text{Li}(\text{H}_2\text{O})_n\text{Ga}(\text{C}_2\text{F}_5)_4$ (3702 and 3630 cm^{-1} ; see Figure 2.24) are significantly weaker than $[\text{NEt}_4]_2[\text{Hg}(\text{H}_2\text{O})(\text{CB}_{11}\text{F}_{11})]$. In fact, by the $\nu(\text{OH})$ criterion, the $\text{HOH}\cdots\text{F}$ hydrogen bonds in $\text{Li}(\text{H}_2\text{O})_4(\text{Al}(\text{OC}(\text{CF}_3)_3)_4)$ and $\text{Li}(\text{H}_2\text{O})(\text{B}(3,5\text{-C}_6\text{H}_3(\text{CF}_3)_2)_4)$ are even weaker than $\text{PVDF}(\text{H}_2\text{O})$. They are the weakest $\text{HOH}\cdots\text{F}$ hydrogen bonds reported to date.

The complex formed between H_2O and CH_3F in an Ar matrix has only has one O–H···F hydrogen bond.⁶⁰ The $\nu_{\text{asym}}(\text{OH})$ stretching frequency for this matrix isolated complex, 3722 cm^{-1} , is red-shifted by 12 cm^{-1} from the 3734 cm^{-1} $\nu_{\text{asym}}(\text{OH})$ value for an Ar-matrix isolated H_2O monomer.¹⁸ One might anticipate that an O–H···F hydrogen bond between H_2O and CF_4 would be even weaker than the $\text{HOH}\cdots\text{F}$ hydrogen bond, and indeed $\nu_{\text{asym}}(\text{OH})$ is 3730 cm^{-1} for the H_2O – CF_4 complex in an Ar matrix.⁷³ However, unlike the DFT⁶⁰ or MP2-aug-cc-pVQZ⁷⁴ optimized

structure of $\text{H}_2\text{O}\cdots\text{FCH}_3$, both of which are shown in Figure 2.44, the MP2-aug-cc-pVQZ optimized structure of the $\text{H}_2\text{O}-\text{CF}_4$ complex, also shown in Figure 2.44, does not have an $\text{O}-\text{H}\cdots\text{F}$ hydrogen bond.⁷³ Therefore, comparison of $\nu(\text{OH})$ frequencies for the $\text{HOH}\cdots\text{FCH}_3$ hydrogen bond complex and the $\text{H}_2\text{O}-\text{CF}_4$ van der Waals complex is not meaningful.

As discussed above in section 2.3.1, the $\nu(\text{OD})$ criterion provides a more meaningful measure of relative hydrogen bonds strength. According to this criterion, the weakest $\text{HOD}\cdots\text{F}$ hydrogen bonds reported before this work were in PVDF(HOD) ($\nu(\text{OH}) = 2696 \text{ cm}^{-1}$)⁷⁵ and $\text{CH}_3\text{F}\cdots\text{DOH}$ complex in an Ar matrix at 15 K ($\nu(\text{OD}) = 2685 \text{ cm}^{-1}$).⁶⁰ The $\nu(\text{OD})$ band for the $\text{HO}-\text{D}\cdots\text{F}$ hydrogen bond between absorbed HOD and a PVDF C-F bond was the closest approach to the presumed $\nu(\text{OD})$ upper limit for HOD with no hydrogen bonding, which is either an isolated HOD molecule in an Ar matrix at 17 K for a solid-state upper limit (2709 cm^{-1})⁷⁶⁻⁷⁸ or an isolated HOD molecule in the gas phase (2720 cm^{-1}).⁷⁹⁻⁸¹

The 17 compounds with $\nu(\text{OD}) > 2600 \text{ cm}^{-1}$, including 12 for which spectra are presented in this Chapter, and 1 who's spectrum is presented in Chapter 4, are shown in a progression approaching the 2709 and 2720 cm^{-1} upper limits in Figure 2.45. It is clear that the weakest $\text{HOD}\cdots\text{F}$ hydrogen bonds ever reported are in the lithium salts of the three fluoroanions with multiple CF_3 or C_2F_5 substituents. The $\nu(\text{OD})$ values for $\text{Li}(\text{HOD})(\text{H}_2\text{O})_3(\text{Al}(\text{OC}(\text{CF}_3)_3)_4)$ and $\text{Li}(\text{HOD})(\text{B}(3,5-\text{C}_6\text{H}_3(\text{CF}_3)_2)_4)$ are only 3 and 4 cm^{-1} , respectively, below the solid-state 2709 cm^{-1} limit for HOD surrounded by only Ar atoms at 15 K, and the $\nu(\text{OD})$ value for $\text{Li}(\text{HOD})(\text{H}_2\text{O})_{n-1}(\text{Ga}(\text{C}_2\text{F}_5)_4)$ is only 12 cm^{-1} below 2709 cm^{-1} . It is not surprising that the $\text{HOD}\cdots\text{F}$ hydrogen bonds in the other lithium hydrates, $\text{Li}_2(\text{HOD})(\text{H}_2\text{O})_3(\text{B}_{12}\text{F}_{12})$ ($\nu(\text{OD}) = 2642 \text{ cm}^{-1}$), $\text{Li}(\text{HOD})(\text{PF}_6)$ ($\nu(\text{OD}) = 2636 \text{ cm}^{-1}$), and $\text{Li}_2(\text{HOD})(\text{H}_2\text{O})(\text{TiF}_6)$ ($\nu(\text{OD}) = 2632 \text{ cm}^{-1}$) are significantly stronger than the $\text{HOD}\cdots\text{F}$ hydrogen bonds in $\text{Li}(\text{HOD})(\text{H}_2\text{O})_3(\text{Al}(\text{OC}(\text{CF}_3)_3)_4)$, $\text{Li}(\text{HOD})(\text{B}(3,5-\text{C}_6\text{H}_3(\text{CF}_3)_2)_4)$, and $\text{Li}(\text{HOD})(\text{H}_2\text{O})_{n-1}(\text{Ga}(\text{C}_2\text{F}_5)_4)$ because B-F, P-F, and Ti-F bonds are undoubtedly more polar than C-F bonds. However, it come as a surprise that the $\text{HOD}\cdots\text{F}$ hydrogen bonds in $\text{Li}(\text{HOD})(\text{H}_2\text{O})_3(\text{Al}(\text{OC}(\text{CF}_3)_3)_4)$, $\text{Li}(\text{HOD})(\text{B}(3,5-\text{C}_6\text{H}_3(\text{CF}_3)_2)_4)$, and $\text{Li}(\text{HOD})(\text{H}_2\text{O})_{n-1}(\text{Ga}(\text{C}_2\text{F}_5)_4)$ appear to be as weak as, or weaker than, the $\text{HOD}\cdots\text{F}$ hydrogen

bonds involving *neutral* fluorocarbon compounds, namely, PVDF(HOD) and HOD \cdots FCH₃ in an Ar matrix. This is especially surprising since coordination to Li⁺ makes HOD more acidic, with a tendency to form stronger O–D \cdots F hydrogen bonds, than HOD molecules that are not coordinated to a metal ion.

The structures of Li(H₂O)₄(Al(OC(CF₃)₃)₄)⁶⁸ and Li(H₂O)(B(C₆H₃(CF₃)₂)₄)⁶⁹ were reported previously, and the FTIR spectra of the Li salt hydrates of the Li(H₂O)₄(Al(OC(CF₃)₃)₄)[–], Li(H₂O)(B(C₆H₃(CF₃)₂)₄)[–], and Ga(C₂H₅)[–] anions were first published by the author in ref. 36. These superweak^{33,82} anions, with a single negative charge and 36, 24, or 20 aliphatic C–F bonds for Li(HOD)(H₂O)₃(Al(OC(CF₃)₃)₄), Li(HOD)(B(3,5-C₆H₃(CF₃)₂)₄), and Li(HOD)(H₂O)_{*n*–1}(Ga(C₂F₅)₄), respectively, are significantly weaker hydrogen bond acceptors than fluoroanions with fewer F atoms and more polar M–F or E–F bonds (E = B, P, Si), including PF₆[–], SiF₆^{2–}, TiF₆^{2–}, SnF₆^{2–}, B₁₂F₁₂^{2–}, MnF₆^{3–}, and Mn(H₂O)₂F₄^{2–}. For Li(H₂O)_{1–4} salts, the O–H \cdots F hydrogen-bond acceptor strength decreases in the order TiF₆^{2–} > B₁₂F₁₂^{2–} > PF₆[–] >> Ga(C₂F₅)₄[–] > B(3,5-C₆H₃(CF₃)₂)₄[–] ~ Al(OC(CF₃)₃)₄[–]. For the two new Na(H₂O)_{1,2}⁺ salts that were studied, it was found that B₁₂F₁₂^{2–} and PF₆[–] have the same hydrogen-bond acceptor strength.

The polyfluoroalkoxyaluminate Al(OC(CF₃)₃)₄[–] anion was first reported in 2001.^{83–87} This anion is so weakly basic that Krossing and co-workers successfully used it to isolate and study many unique and interesting cations,^{34,82,87–91} including Ag(η²-P₄)₂⁺,⁸² Ag(P₄S₃)₂⁺,⁸⁸ and Li(H₂O)₄(Al(OC(CF₃)₃)₄)⁶⁸. The B(3,5-C₆H₃(CF₃)₂)₄[–] anion was first reported by Sonoda and Kobayashi in 1984,⁹² and has been used extensively for phase transfer catalysis,^{93–94} organometallic electrochemistry,⁹⁵ olefin and alkyne polymerization,^{96–97} and, most recently, nonoxidative catalytic dehydrogenation of alkanes⁹⁸ and the isolation and structural characterization of Li(H₂O)B(3,5-C₆H₃(CF₃)₂)₄.⁶⁹ The Ga(C₂F₅)₄[–] anion was recently reported by Hoge and co-workers and used to isolate and structurally characterize hydronium hydrate (H₅O₂)₂(H₂O)₂(Ga(C₂H₅)₄), which contains a cyclic, nearly planar [(H₃O)₂(H₂O)₂]²⁺ cluster.⁹⁹ It promises to be another superweak anion with which other interesting cations, perhaps including other metal salt hydrates, can be isolated and structurally characterized.

2.3.12 Asymmetric Hydrogen Bonding Environments in Hydrates

Figure 2.45, and the $\nu(\text{OD})$ frequencies listed in Tables 2.1 and 2.2, show that several salt hydrates of fluoroanions with a small percentage of HOD (i.e., with a single, uncoupled HOD molecule) have two or more $\nu(\text{OD})$ bands, indicating either different HOD orientations for the crystallographically unique HOD molecule (i.e., the HOD molecule is in an asymmetric hydrogen bonding environment), or more than one HOD positions in the $\text{M}(\text{HOD})(\text{H}_2\text{O})_{n-1}^{m+}$ coordination sphere, or both. The case of $\text{Cs}_2(\text{HOD})(\text{B}_{12}\text{F}_{12})$, was mentioned above in section 2.3.3. The structure of $\text{Cs}_2(\text{H}_2\text{O})(\text{B}_{12}\text{F}_{12})$ has a single unique H_2O molecule.⁶⁷ The two H atoms are in different hydrogen bonding environments, with $\text{O}(\text{H})\cdots\text{F}$ distances that differ by 0.106(6) Å (3.103(3) and 2.997(3) Å).⁶⁷ The spectrum in Figure 2.8 shows unequivocally that $\text{Cs}_2(\text{HOD})(\text{B}_{12}\text{F}_{12})$ has separate bands at 2669 and 2664 cm^{-1} , which result from the two orientations of the unique HOD molecule.

The two H_2O molecules in crystalline $\text{Rb}_2(\text{H}_2\text{O})(\text{B}_{12}\text{F}_{12})$ are symmetry related.⁶⁶ The two $\text{O}(\text{H})\cdots\text{F}$ distances for the two crystallographically unique O–H bonds are 2.931(2) and 2.857(2) Å,⁶⁶ a difference of only 0.074(4) Å. The FTIR spectrum of a sample of $\text{Rb}_2(\text{H}_2\text{O})_2(\text{B}_{12}\text{F}_{12})$ containing a small amount of $\text{Rb}_2(\text{HOD})(\text{H}_2\text{O})(\text{B}_{12}\text{F}_{12})$ has two $\nu(\text{OD})$ bands at 2668 and 2660 cm^{-1} and $\nu(\text{OH})$ bands at 3625 and 3614 cm^{-1} , as shown in Figure 2.15, which result from the two orientations of the crystallographically unique and uncoupled HOD molecule in the asymmetric hydrogen bonding environment.

FTIR spectra of a sample of $\text{Li}_2(\text{H}_2\text{O})_4(\text{B}_{12}\text{F}_{12})$ containing a small amount of $\text{Li}_2(\text{HOD})(\text{H}_2\text{O})_3(\text{B}_{12}\text{F}_{12})$, which is discussed in depth in Chapter 3 of this dissertation, (Figure 2.46) and a sample of $\text{Na}_2(\text{H}_2\text{O})_2(\text{B}_{12}\text{F}_{12})$ containing a small amount of $\text{Na}_2(\text{HOD})(\text{H}_2\text{O})(\text{B}_{12}\text{F}_{12})$ (Figure 2.22) also have two $\nu(\text{OD})$ bands, but with much larger separations than in the compounds discussed above (the four H_2O molecules in $\text{Li}_2(\text{H}_2\text{O})_4(\text{B}_{12}\text{F}_{12})$ are symmetry related so there is only one type of position in the formula unit;⁶⁶ see Figure 2.46). The two bands in the spectrum of a sample of $\text{Li}_2(\text{H}_2\text{O})_4(\text{B}_{12}\text{F}_{12})$ containing a small amount of $\text{Li}_2(\text{HOD})(\text{H}_2\text{O})_3(\text{B}_{12}\text{F}_{12})$ are at 2642 and 2518 cm^{-1} , a difference of 124 cm^{-1} . The large difference is because the two orientations of the

HOD ligand have different hydrogen bonding environments, with $\text{O(D)}\cdots\text{F} = 2.951(3) \text{ \AA}$ for one orientation and $\text{O(D)}\cdots\text{O} = 2.778(2)$ or $2.785(2) \text{ \AA}$ for the other orientation.⁶⁶ Note that the more red-shifted, lower wavenumber band, assigned to the $\text{O-D}\cdots\text{O}$ hydrogen bond, is significantly broader than the higher wavenumber band ($\text{FWHM} = 34$ vs 6 cm^{-1} , respectively) and has a significantly higher integrated intensity (by more than a factor of 2) than the higher wavenumber band. A greater redshift, increased FWHM, and increased integrated intensity are all indicative of stronger hydrogen bonding for the $\text{O-D}\cdots\text{O}$ hydrogen bond relative to the $\text{O-D}\cdots\text{F}$ hydrogen bond in $\text{Li(HOD)(H}_2\text{O)}_3(\text{B}_{12}\text{F}_{12})$.

The FTIR spectra of $\text{Na}_2(\text{H}_2\text{O})_2(\text{B}_{12}\text{F}_{12})$ and $\text{Na(H}_2\text{O)(PF}_6)$, shown in Figure 2.47, are in sharp contrast to the spectra of a sample of $\text{Na}_2(\text{H}_2\text{O})_2(\text{B}_{12}\text{F}_{12})$ containing a small amount of $\text{Na}_2(\text{HOD})(\text{H}_2\text{O})(\text{B}_{12}\text{F}_{12})$ and a sample of $\text{Na(H}_2\text{O)}_2(\text{PF}_6)$ containing a small amount of $\text{Na(HOD)(PF}_6)$, shown in Figure 2.48. Instead of the similar pairs of $\nu_{\text{asym}}(\text{OH})$ and $\nu_{\text{sym}}(\text{OH})$ in the spectra of $\text{Na}_2(\text{H}_2\text{O})_2(\text{B}_{12}\text{F}_{12})$ and $\text{Na(H}_2\text{O)(PF}_6)$ (i.e., similar peak positions and FWHM values), the spectra of $\text{Na}_2(\text{HOD})(\text{H}_2\text{O})(\text{B}_{12}\text{F}_{12})$ and $\text{Na(HOD)(PF}_6)$ are fundamentally different. The spectrum of $\text{Na(HOD)(PF}_6)$ has a single sharp $\nu(\text{OD})$ band at 2654 cm^{-1} ($\text{FWHM} = 6 \text{ cm}^{-1}$), approximately halfway between the $2704 \nu_{\text{asym}}(\text{OD})$ and the $2612 \nu_{\text{sym}}(\text{OD})$ bands for $\text{Na(HOD)(PF}_6)$, which is consistent with the symmetric H_2O hydrogen bonding environment shown in the $\text{Na(H}_2\text{O)(PF}_6)$ X-ray crystal structure shown in Figure 2.37. In contrast, the spectrum of $\text{Na}_2(\text{HOD})(\text{H}_2\text{O})(\text{B}_{12}\text{F}_{12})$ has two sharp $\nu(\text{OD})$ bands, at 2680 ($\text{FWHM} = 5 \text{ cm}^{-1}$) and 2628 cm^{-1} ($\text{FWHM} = 8 \text{ cm}^{-1}$), which are only $20\text{--}26 \text{ cm}^{-1}$ from the $2706 \nu_{\text{asym}}(\text{OD})$ and $2608 \nu_{\text{sym}}(\text{OD})$ values for $\text{Na}_2(\text{D}_2\text{O})(\text{B}_{12}\text{F}_{12})$. The structure of $\text{Na}_2(\text{H}_2\text{O})_2(\text{B}_{12}\text{F}_{12})$ is currently unknown. However, the spectrum of $\text{Na}_2(\text{H}_2\text{O})_2(\text{B}_{12}\text{F}_{12})$ suggests that there is one crystallographically unique H_2O molecule, and the spectrum of $\text{Na}_2(\text{HOD})(\text{H}_2\text{O})(\text{B}_{12}\text{F}_{12})$ suggests that the unique H_2O is in an asymmetric hydrogen bonding environment, either with significantly different $\text{O(H)}\cdots\text{F}$ distances of with one $\text{O-H}\cdots\text{F}$ hydrogen bond and one $\text{O-H}\cdots\text{O}$ hydrogen bond. Repeated attempts to grow crystals of $\text{Na}_2(\text{H}_2\text{O})_2(\text{B}_{12}\text{F}_{12})$ suitable for single-crystal X-ray diffraction have produced either $\text{Na}_2(\text{H}_2\text{O})_4(\text{B}_{12}\text{F}_{12})$,¹⁰⁰ $\text{Na}_2(\text{H}_2\text{O})_3(\text{B}_{12}\text{F}_{12})$,⁶⁶ or microcrystalline powders of $\text{Na}_2(\text{H}_2\text{O})_2(\text{B}_{12}\text{F}_{12})$.

Attempt to measure powder X-ray diffraction patterns for the microcrystalline powders of $\text{Na}_2(\text{H}_2\text{O})_2(\text{B}_{12}\text{F}_{12})$ have also proved unsuccessful. (Meaningful ATR-FTIR spectra of either $\text{Na}_2(\text{H}_2\text{O})_4(\text{B}_{12}\text{F}_{12})$ or $\text{Na}_2(\text{H}_2\text{O})_3(\text{B}_{12}\text{F}_{12})$ could not be obtained at room temperature because they rapidly undergo dehydration to $\text{Na}_2(\text{H}_2\text{O})_2(\text{B}_{12}\text{F}_{12})$, which is stable indefinitely to dehydration in air containing water vapor.)

The literature data listed in Table 2.2 show that FTIR spectra of some compounds with an isolated, uncoupled HOD ligand are significantly different O–D···F hydrogen bonds (depending on the position and/or orientation of the HOD ligand) can exhibit multiple $\nu(\text{OD})$ bands separated by 29 ($\text{K}(\text{HOD})_2\text{F}$), 55 ($\text{K}(\text{HOD})(\text{MnF}_4)$), 126 ($\text{Sr}(\text{HOD})(\text{H}_2\text{O})(\text{TiF}_6)$), or even 136 cm^{-1} ($\text{Zn}(\text{H}_2\text{O})_4\text{F}_2$). Portions of the structure and selected distances and angles for $\text{K}(\text{HOD})_2\text{F}$, $\text{K}(\text{HOD})(\text{MnF}_4)$, and $\text{Zn}(\text{H}_2\text{O})_4\text{F}_2$ are shown or listed in Figures 2.49–2.52 and Tables 2.3 and 2.4, respectively.

2.3.13 Correlations of $\nu(\text{OD})$ or $\nu(\text{OH})$ with $\text{O}\cdots\text{X}$ for $\text{HOH}\cdots\text{X}$ and $\text{HOD}\cdots\text{X}$ Hydrogen Bonds ($\text{X} = \text{F}, \text{O}$)

There have been many attempts to correlate $\nu(\text{OH})$ frequencies with $\text{O}(\text{H})\cdots\text{O}$ distances for compounds with intra- and intermolecular $\text{O}-\text{H}\cdots\text{O}$ hydrogen bonds. Some of the earliest and best known are by Nakamoto, Morgoshes, and Rundle,⁴⁶ Pimentel and Sederholm,⁴⁷ and Novak.² A graph made for ref. 36 with the data set in Novak's paper is shown in Figure 2.53. The average deviation of data points from the exponential regression curve is 158 cm^{-1} . A more recent paper by Libowitzky contained a $\nu(\text{OH})$ vs $\text{O}(\text{H})\cdots\text{O}$ graph with 124 data points for 65 materials.⁸ A graph made for ref. 36 from Libowitzky's data, to match the one made from the Novak data, is also shown in Figure 2.53. The average deviation of the data points from the exponential regression curve is 82 cm^{-1} .

Two papers, one by Berglund, Lindgren, and Tegenfeldt in 1978⁵ and one by Mikenda in 1986,⁴⁹ reported $\nu(\text{OD})$ vs $\text{O}(\text{H})\cdots\text{O}$ correlation curves for compounds with a single, uncoupled HOD molecule. A graph made for ref. 36 from the Berglund et al. data set is shown in Figure 2.54. The data was fit to an exponential regression curve with a fixed limit of 2720 cm^{-1} , and the R^2

value of the curve is 0.90. The average deviation of the 37 blue data points from the regression curve is 30 cm^{-1} .

An uncoupled $\nu(\text{OD})$ vs $\text{O}(\text{D})\cdots\text{F}$ correlation curve, the only one of its kind before the updated one published by the author in ref ³⁶, was published by Mikenda and Steinböck in 1994.⁶ The 28 data points were for salt hydrates of the fluoroanions *trans*- $\text{Mn}(\text{H}_2\text{O})_2\text{F}_4^-$, MnF_6^{3-} , FeF_6^{3-} , TiF_6^{2-} , SnF_6^{2-} , and F^- . The $\text{O}(\text{D})\cdots\text{F}$ values were $\text{O}(\text{H})\cdots\text{F}$ distances from the literature crystal structures. The $\nu(\text{OD})$ frequencies were from FTIR spectra recorded at 75 K by Mikenda and Steinböck. All of the $\nu(\text{OD})$ frequencies were less than 2600 cm^{-1} . As a result of the work presented in this chapter, and published in ref. 36, the author has added 25 data points for the 13 numbered compounds (one of the compounds, $\text{Co}(\text{HOD})(\text{H}_2\text{O})_5(\text{B}_{12}\text{F}_{12})$, is discussed in Chapter 4 of this dissertation) in Figure 2.53 to the Mikenda/Steinböck correlation, all but two of which have $\nu(\text{OD}) > 2600\text{ cm}^{-1}$. The data for this plot is listed in Table 2.2. The data was fitted to an exponential regression curve with a fixed limit of 2720 cm^{-1} , and the R^2 value of the curve is 0.88. This $\nu(\text{OD})$ vs $\text{O}(\text{D})\cdots\text{F}$ graph is shown in Figure 2.53. The average deviation of the 53 red data points from the regression curve is 27 cm^{-1} . The 53 points represents hydrates of 12 cations (Li^+ , Na^+ , K^+ , Rb^+ , Cs^+ , Mg^{2+} , Sr^{2+} , Mn^{2+} , Fe^{2+} , Co^{2+} , Ni^{2+} , and Zn^{2+}) and 12 fluoroanions ($\text{Al}(\text{OC}(\text{CF}_3)_3)_4^-$, $\text{B}(3,5\text{-C}_6\text{H}_3(\text{CF}_3)_2)_4^-$, $\text{Ga}(\text{C}_2\text{F}_5)_4^-$, PF_6^- , *trans*- $\text{Mn}(\text{H}_2\text{O})_2\text{F}_4^-$, MnF_6^{3-} , FeF_6^{3-} , SiF_6^- , TiF_6^{2-} , SnF_6^{2-} , $\text{B}_{12}\text{F}_{12}^{2-}$, and F^-).

The 28 Mikenda/Stienböck $\nu(\text{OD})$ values are from FTIR spectra recorded at 75 K⁶ and the six $\nu(\text{OD})$ values for $\text{Mg}(\text{HOD})(\text{H}_2\text{O})(\text{SiF}_6)$ are from a spectrum recorded at 93 K.¹⁰¹ The spectrum of $\text{HOD}\cdots\text{FCH}_3$ was recorded at 15 K in an Ar matrix. All of the $\nu(\text{OD})$ values from this chapter, and from Chapter 4, are from spectra recorded at room temperature. The temperature difference may affect $\nu(\text{OD})$ by ca. 5 cm^{-1} , which is the difference between the room temperature 2654 cm^{-1} $\nu(\text{OD})$ for $\text{Na}(\text{HOD})(\text{PF}_6)$ and Mikenda and Stienböck's 75 K 2649 cm^{-1} $\nu(\text{OD})$ for this compound. (The difference between the room temperature 2623 cm^{-1} $\nu(\text{OD})$ for $\text{Li}_2(\text{HOD})(\text{H}_2\text{O})(\text{TiF}_6)$ and Mikenda and Stienböck's 75 K 2620 cm^{-1} value is even less.) Mikenda and Stienböck reported the 75 K $\nu(\text{OD})$ for $\text{Na}(\text{HOD})(\text{PF}_6)$ in their paper⁶ but did not use it in their correlation because the

only structure of this compounds at the time was of poor quality. The author has chosen to use it in their correlation in Figure 2.54 because a good structure is now available.⁷¹

There is considerable scatter in all $\nu(\text{OD})$ or $\nu(\text{OH})$ vs $\text{O}\cdots\text{X}$ correlation plots ($\text{X} = \text{O}, \text{F}$). There are several possible causes. First, the O or F atoms in different molecules or anions do not necessarily have the same basicity or hydrogen-bond acceptor strength. Secondly, the $\text{O}-\text{H}\cdots\text{X}$ hydrogen bonds are generally not linear, and an $\text{O}\cdots\text{X}$ distance may not be as good an indication of hydrogen bond strength as a precise $\text{H}\cdots\text{X}$ distance, but very few precise $\text{H}\cdots\text{X}$ distances are available. Moreover, many hydrogen bonds are bifurcated, and there is no straightforward and standardized way to treat these when making a correlation curve.¹⁰² Finally, in some cases when an HOD molecule is in an asymmetric environment, only one $\nu(\text{OD})$ band was observed. The compound $\text{Li}(\text{H}_2\text{O})_4(\text{Al}(\text{OC}(\text{CF}_3)_3)_4)$ is an example of the last point. There is only one $\nu(\text{OD})$ band for $\text{Li}(\text{HOD})(\text{H}_2\text{O})_3(\text{Al}(\text{OC}(\text{CF}_3)_3)_4)$ (Figure 2.27) and only one $\nu(\text{OH})$ band for $\text{Li}(\text{HOD})(\text{D}_2\text{O})_3(\text{Al}(\text{OC}(\text{CF}_3)_3)_4)$ (Figure 2.25). Each of these bands is symmetric and can be fit with a single Lorentzian function. Nevertheless, the HOD molecule is in an asymmetric hydrogen bonding environment, with an $\text{O}(\text{H})\cdots\text{F}$ distance of 3.012(2) or 3.157(2) Å, and with an $\text{O}-\text{H}\cdots\text{F}$ angle of 134° or 146°, respectively.⁶⁸ Does the 3.157(2) Å $\text{O}(\text{H})\cdots\text{F}$ distance have the same effect on the $\text{O}-\text{D}$ oscillator in one orientation as the 3.012(2) Å $\text{O}(\text{H})\cdots\text{F}$ distance has on the $\text{O}-\text{D}$ oscillator in the other orientation because the $\text{O}-\text{H}\cdots\text{F}$ angles compensate for the difference in $\text{O}(\text{H})\cdots\text{F}$ distance? Any interpretation must be tempered by the fact that the H atoms positions are not precisely known as they would be in a neutron diffraction crystal structure, even though this is a very good X-ray crystal structure ($R = 0.0269$, $wR_2 = 0.0539$). The two $\text{O}-\text{H}$ distances are 0.68(5) and 0.70(5) Å and the $\text{H}-\text{O}-\text{H}$ angle is 102(5)°. What distance should be used for the $\nu(\text{OD})$ vs $\text{O}(\text{H})\cdots\text{F}$ correlation? The decision was to use the average value, 3.130 Å, as a compromise when making Figure 2.54.

Whatever the cause(s) of the scatter, it is sufficiently large that the correlation regression curves cannot be used to reliably predict a $\nu(\text{OD})$ frequency with even moderate accuracy. For example, in Figure 2.54 an $\text{O}(\text{D})\cdots\text{F}$ distance of 2.723 ± 0.001 Å is correlated with a $\nu(\text{OD})$

frequency as low as 2491 cm^{-1} (for $\text{Zn}(\text{HOD})(\text{H}_2\text{O})_3\text{F}_2$) or as high as 2633 cm^{-1} (for $\text{Mg}(\text{HOD})(\text{H}_2\text{O})_5(\text{B}_{12}\text{F}_{12})$). For $\nu(\text{OD}) = 2657 \pm 3\text{ cm}^{-1}$, $\text{O}(\text{D})\cdots\text{F}$ can be as short as $2.857(2)\text{ \AA}$ (for $\text{Rb}_2(\text{HOD})(\text{H}_2\text{O})(\text{B}_{12}\text{F}_{12})$) or as long as $3.170(6)\text{ \AA}$ (for $\text{Sr}(\text{HOD})(\text{H}_2\text{O})(\text{TiF}_6)$). Nevertheless, the scatter in the two correlation plots in Figure 2.54 notwithstanding, there is a clear difference between them. For a given $\nu(\text{OD})$ stretching frequency, the regression curves show that $\text{O}(\text{D})\cdots\text{R}$ is in general, $0.1\text{--}0.2\text{ \AA}$ shorter than $\text{O}(\text{D})\cdots\text{O}$, or for similar $\text{O}(\text{D})\cdots\text{X}$ distances, $\nu(\text{OD})$ for $\text{X} = \text{F}$ is significantly higher than $\nu(\text{OD})$ for $\text{X} = \text{O}$. This is in harmony with the lower basicity of F atoms vs O atoms in general and the smaller size of an F atom vs an O atom. Two examples are $\nu(\text{OD}) = 2636\text{ cm}^{-1}$ for $\text{Li}(\text{HOD})(\text{PF}_6)$ and 2619 cm^{-1} for $\text{Li}(\text{HOD})(\text{H}_2\text{O})_2(\text{ClO}_4)^{103}$ ($\text{O}(\text{D})\cdots\text{O} = 2.989(2)\text{ \AA}$; ¹⁰⁴ see Figure 2.55), and $\nu(\text{OD}) = 2654\text{ cm}^{-1}$ for $\text{Na}(\text{HOD})(\text{PF}_6)$ ($\text{O}(\text{D})\cdots\text{F} = 3.604(2)\text{ \AA}$ ⁷¹) and 2641 cm^{-1} for $\text{Na}(\text{HOD})(\text{ClO}_4)$ ($\text{O}(\text{D})\cdots\text{O} = 3.087(3)$ and $3.141(3)\text{ \AA}$; ¹⁰⁵ see Figure 2.56).

2.4 Conclusions and Future Work

2.4.1 Conclusion

It has been shown that hydrogen bonds between metal-coordinated H_2O , or HOD , and one, or more, aliphatic C–F bonds in three superweak *anions*, namely, $\text{Al}(\text{OC}(\text{CF}_3)_3)_4^-$, $\text{B}(3,5\text{-C}_6\text{H}_3(\text{CF}_3)_2)_4^-$, and $\text{Ga}(\text{C}_2\text{F}_5)_4^-$, gives rise to higher FTIR $\nu(\text{OH})$ and $\nu(\text{OD})$ frequencies, and are arguably weaker, than hydrogen bonds between H_2O or HOD and aliphatic C–F bonds in *neutral molecules*, namely polyvinylidene difluoride and CH_3F . The hydrogen bonds in $\text{Li}(\text{H}_2\text{O})_4(\text{Al}(\text{OC}(\text{CF}_3)_3)_4)$, $\text{Li}(\text{H}_2\text{O})(\text{B}(3,5\text{-C}_6\text{H}_3(\text{CF}_3)_2)_4)$, and $\text{Li}(\text{H}_2\text{O})_n(\text{Ga}(\text{C}_2\text{F}_5)_4)$ are among the weakest, if not the weakest, hydrogen bonds between an H_2O molecule and an F atom reported to date. However, as weak as they are, differences in $\text{O}\text{--}\text{H}\cdots\text{F}$ hydrogen bond strength within a given fluoroanion salt can be distinguished spectroscopically. Uncoupled HOD molecules in asymmetric $\text{F}\cdots\text{HOD}\cdots\text{F}'$ hydrogen bonding environments in four hydrates of $\text{B}_{12}\text{F}_{12}^{2-}$ gave rise to two observable $\nu(\text{OD})$ bands even if the two $\text{O}(\text{D})\cdots\text{F}$ distances differed by as little as $0.010(4)\text{ \AA}$. Finally, for solid hydrates, a $\nu(\text{OD})$ vs $\text{O}(\text{D})\cdots\text{F}$ graph with 53 data points, including 23 new data points with $\nu(\text{OD}) > 2600\text{ cm}^{-1}$, is displaced ca. $0.1\text{--}0.2\text{ \AA}$ to shorter distances relative to the $\nu(\text{OD})$

vs $\nu(\text{O(D)}\cdots\text{O})$ graph of Berglund, Lindgren, and Tegenfeldt,⁵ in harmony with the lower basicity and smaller size of F atoms vs O atoms.

2.4.2 Future Work

The logical next step would be to perform an in-depth neutron diffraction study of all the compounds studied in this chapter. A more accurate location of the H atom positions means that correlation of $\nu(\text{OD})$ vs $\text{H}\cdots\text{F}$ distance, and potentially $\text{O}-\text{H}\cdots\text{F}$ bond angle, will better inform on this relationship than current correlation curves, and likely greatly reduce scatter. Secondly, the salts studied in this chapter represent only a small fraction of the number of metal salt hydrates with WCAs. The family of $\text{Li}(\text{Al}(\text{OR}_f)_4)$ salts, to which $\text{Li}(\text{H}_2\text{O})_4(\text{Al}(\text{OC}(\text{CF}_3)_3)_4)$ belongs, contains numerous Li salts of WCAs that have yet to be explored spectroscopically, with the Na analogues further expanding the number of potential candidate materials worth studying. Thirdly, as will be discussed in Chapter 4 of this dissertation, this study is not limited to salts of monovalent cations. In the limit of this dissertation only monovalent cations and divalent cations (Chapter 4) have been explored. Synthesis of new salt hydrates of WCAs with M^{3+} cations will provide new materials that can be studied in this manner, and potentially reveal trends about the effect of $\text{M}^{m+}-\text{OH}_2$ coordination on the $\text{O}-\text{H}\cdots\text{X}$ hydrogen bonding. Additionally, this work is not restricted solely to fluoroanions. Preliminary investigation into the FTIR spectrum of $\text{Na}_2(\text{H}_2\text{O})_6(\text{B}_{12}\text{Cl}_{12})$ revealed that, like the fluoroanions discussed in this chapter, there are sharp, and resolvable, $\nu(\text{OH})$ peaks in the range of $3500\text{--}3650\text{ cm}^{-1}$ (Figure 2.57).³⁷ Looking at perchlorinated analogues, or new chlorinated WCAs, will allow for investigation into $\text{O}-\text{H}\cdots\text{X}$ hydrogen bonding as a function of the halogen participating in the bonding. Finally, looking at hydrogen bonding in the limit of the weakest hydrogen bonds is important, but it is only part of a greater effort to understand water–anion interactions in the solid state. Identification and study of materials with progressively stronger hydrogen bonding, up to the limit of coalescence of the $\nu_{\text{asym}}(\text{OH})$ and $\nu_{\text{sym}}(\text{OH})$ bands, will be important to achieve a more complete understanding of water–anion interactions.

References

1. Pimentel, G. C.; McClellan, A. L. *The Hydrogen Bond*; Dreeman: San Fransisco, Ca, 1960.
2. Novak, A. *Hydrogen Bonding in Solids. Correlation of Spectroscopic and Crystallographic Data Structure and Bonding* Springer: Berlin, 1974. *18*, 177–216.
3. Brown, I. D. On the Geometry of O–H···O Hydrogen Bonds. *Acta Crystallogr., Sect. A: Cryst. Phys., Diffr., Theor. Gen. Crystallogr.* **1976**, *A32*, 24–31.
4. Robertson, G. A. Theory of a Broadening of the Infrared Absorption Spectra of Hydrogen-Bonded Species. III. The Kinematic and Electronic Coupling Mechanisms. *Philos. Trans. R. Soc., A* **1977**, *286*, 25–53.
5. Berglund, B.; Lindgren, J.; Tegenfeldt, J. On the Correlation between Deuteron Quadrupole Coupling Constants, O–H and O–D Stretching Frequencies and Hydrogen-Bond Distances in Solid Hydrates. *J. Mol. Struct.* **1978**, *43*, 179–191.
6. Mikenda, W.; Steinböck, S. Stretching frequency versus bond distance correlation of O–D(H)···F hydrogen bonds in solid hydrates *Journal of Molecular Structure* **1994**, *326*, 123–130.
7. Iogansen, A. V. Direct proportionality of the hydrogen bonding energy and the intensification of the stretching $\nu(\text{XH})$ vibration in infrared spectra. *Spectrochim. Acta, Part A* **1999**, *55*, 1585–1612.
8. Libowitzky, E. Correlation of O–H Stretching Frequencies and O–H···O Hydrogen Bond Lengths in Minerals. *Monatsh. Chem.* **1999**, *130*, 1047–1059.
9. Steiner, T. The Hydrogen Bond in the Solid State. *Angew Chem Int Ed* **2002**, *41*, 48–76.
10. Georgiev, M.; Wildner, M.; Stoilova, D. Hydrogen bond strength in some beryllium salts, $\text{BeXO}_4 \cdot 4\text{H}_2\text{O}$ and $\text{Me}_2\text{Be}(\text{XO}_4)_2 \cdot 2\text{H}_2\text{O}$ ($\text{X} = \text{S}, \text{Se}$; $\text{Me} = \text{K}, \text{Rb}$): Correlation of structural data and infrared spectra. *Solid State Sci.* **2009**, *11*, 1358–1362.
11. Arunan, E.; Desiraju, G. R.; Klein, R. A.; Sadlej, J.; Scheiner, S.; Alkorta, I.; Clary, D. C.; Crabtree, R. H.; Dannenberg, J. J.; Hobza, P.; Kjaergaard, H. G.; Legon, A. C.; Mennucci, B.; Nesbitt, D. J. Definition of the hydrogen bond (IUPAC Recommendations 2011). *Pure Appl. Chem.* **2011**, *83*, 1637–1641.
12. Zhang, C.; Khaliullin, R. Z.; Bovi, D.; Guidoni, L.; Kühne, T. D. Vibrational Signature of Water Molecules in Asymmetric Hydrogen Bonding Environments. *The Journal of Physical Chemistry Letters* **2013**, *4*, 3245–3250.
13. Athokpam, B.; Ramesh, S. G.; McKenzie, R. H. Effect of hydrogen bonding on the infrared absorption intensity of OH stretch vibrations. *Chem. Phys.* **2017**, *488–489*, 43–54.

14. Boyer, M. A.; Marsalek, O.; Heindel, J. P.; Markland, T. E.; McCoy, A. B.; Xantheas, S. S. Beyond Badger's Rule: The Origins and Generality of the Structure-Spectra Relationship of Aqueous Hydrogen Bonds. *J. Phys. Chem. Lett.* **2019**, *10*, 918–924.
15. Fraley, P. E.; Rao, K. N. High Resolution Infrared Spectra of Water Vapor ν_1 and ν_3 Bands of H_2^{16}O . *Journal of Molecular Spectroscopy* **1969**, *29*, 348–364.
16. Mikuli, E.; Hetmanczyk, J.; Grad, B.; Kozak, A.; Wasicki, J. W.; Bilski, P.; Holderna-Natkaniec, K.; Medycki, W. The relationship between reorientational molecular motions and phase transitions in $[\text{Mg}(\text{H}_2\text{O})_6](\text{BF}_4)_2$, studied with the use of ^1H and ^{19}F NMR and FT-MIR. *J Chem Phys* **2015**, *142*, 069507.
17. Kuyanov, K. E.; Slipchenko, M. N.; Vilesov, A. F. Spectra of the ν_1 and ν_3 bands of water molecules in helium droplets. *Chem. Phys. Lett.* **2006**, *427*, 5–9.
18. Nelander, B. Infrared Spectrum of the Water Formaldehyde Complex in Solid Argon and Solid Nitrogen. *J. Chem. Phys.* **1980**, *72*, 77–84.
19. Yamakawa, K.; Ehara, N.; Ozawa, N.; Arakawa, I. Infrared spectroscopy of water clusters isolated in methane matrices: Effects of isotope substitution and annealing. *AIP Adv.* **2016**, *6*, 075302.
20. Stoyanov, E. S.; Kim, K. C.; Reed, C. A. An Infrared ν_{NH} Scale for Weakly Basic Anions. Implications for Single-Molecule Acidity and Superacidity. *J. Am. Chem. Soc.* **2006**, *128*, 8500.
21. Derendorf, J.; Kessler, M.; Knapp, C.; Ruhle, M.; Schulz, C. Alkali metal-sulfur dioxide complexes stabilized by halogenated *closo*-dodecaborate anions. *Dalton Trans* **2010**, *39*, 8671–8678.
22. Lacroix, M. R.; Bukovsky, E. V.; Lozinsek, M.; Folsom, T. C.; Newell, B. S.; Liu, Y.; Peryshkov, D. V.; Strauss, S. H. Manifestations of Weak O–H···F Hydrogen Bonding in $M(\text{H}_2\text{O})_n(\text{B}_{12}\text{F}_{12})$ Salt Hydrates: Unusually Sharp Fourier Transform Infrared $\nu(\text{OH})$ Bands and Latent Porosity ($M = \text{Mg–Ba, Co, Ni, Zn}$). *Inorg. Chem.* **2018**, *57*, 14983–15000.
23. Peter, S.; Suchanek, E.; Eßer, D.; Lutz, H. D. The Crystal Structure of Twinned $\text{Mg}(\text{BrO}_3)_2 \cdot 6\text{H}_2\text{O}$. *Z. Naturforsch* **1996**, *51*, 1072–1078.
24. Vijila Manonmoni, J.; Bhagavannarayana, G.; Ramasamy, G. M., S.; Amutha, M. Growth, structure and spectral studies of a novel mixed crystal potassium zinc manganese sulphate. *Spectrochim. Acta Part A* **2014**, *117*, 9–12.
25. Ghosh, S.; Oliveira, M.; Pacheco, T. S.; Perpétuo, G. J.; Franco, C. J. Growth and characterization of ammonium nickel-cobalt sulfate Tutton's salt for UV light applications. *J. Cryst. Growth* **2018**, *487*, 104–115.

26. Herzberg, G. Infrared and Raman Spectra of Polyatomic Molecules; *Molecular Spectra and Molecular Structure. II*. New York, NY, 1945.
27. Srinivasan, B. R.; Morajkar, S. M.; Khandolkar, S. S.; Näther, C.; Bensch, W. Synthesis, structure and properties of a hexarubidium heptamolybdate with bridging aqua ligands. *Indian J. Chem.* **2017**, *56A* 601–609.
28. Chen, W. j.; Long, L. S.; Huang, R. B.; Zheng, L. S. A Dihalide–Decahydrate Cluster of $[X_2(H_2O)_{10}]^{2-}$ in a Supramolecular Architecture of $\{[Na_2(H_2O)_6(H_2O@TMEQ[6])]\cdot 2(C_6H_5NO_3)\}-X_2(H_2O)_{10}$ (TMEQ[6] = $\alpha, \alpha', \delta, \delta'$ -Tetramethylcucurbit[6]uril; X = Cl, Br). *Cryst. Growth Des.* **2013**, *13*, 2507–2513.
29. Semerci, F.; Yeşilel, O. Z.; Ölmez, H.; Büyükgüngör, O. Supramolecular Assemblies of Copper(II)–pyridine-2,3-dicarboxylate Complexes with N-Donor Ligands and Clustered Water Molecules. *Inorg. Chim. Acta* **2014**, *409*, 407–417.
30. Falk, M.; Huang, C.-H.; Knop, O. Infrared Studies of Water in Crystalline Hydrates: Location of Hydrogen Atoms and Evidence for a Bifurcated Hydrogen Bond in $K_2SnCl_4 \cdot H_2O$. *Can. J. Chem.* **1974**, *52*, 2380–2388.
31. Miller, D. J.; Lisy, J. M. Hydrated Alkali-Metal Cations: Infrared Spectroscopy and ab Initio Calculations of $M^+(H_2O)_{x=2-5}$ Ar cluster ions for M= Li, Na, K, and Cs. *J Am Chem Soc* **2008**, *130*, 15381–15392.
32. Miller, D. J.; Lisy, J. M. Entropic Effects on Hydrated Alkali-Metal Cations: Infrared Spectroscopy and ab Initio Calculations of $M^+(H_2O)_{x=2-5}$ Cluster Ions for M = Li, Na, K, and Cs. *J Am Chem Soc* **2008**, *130*, 15393–15404.
33. Lupinetti, A. J.; Strauss, S. H. Superweak Anions – Chemistry and Catalysis: a Symposium Report. *Chemtracts-Inorg. Chem.* **1998**, *11*, 565–595.
34. Krossing, I.; Reisinger, A. Chemistry with weakly-coordinating fluorinated alkoxyaluminate anions: Gas phase cations in condensed phases? *Coordination Chemistry Reviews* **2006**, *250*, 2721–2744.
35. Krossing, I., 1.23 - Weakly Coordinating Anions: Fluorinated Alkoxyaluminates. In *Comprehensive Inorganic Chemistry II (Second Edition)*, Reedijk, J.; Poeppelemeier, K., Eds. Elsevier: Amsterdam, 2013; pp 681–705.
36. Lacroix, M. R.; Liu, Y.; Strauss, S. H. Hydrated Metal Ion Salts of the Weakly Coordinating Fluoroanions PF_6^- , TiF_6^{2-} , $B_{12}F_{12}^{2-}$, $Ga(C_2F_5)_4^-$, $B(3,5-C_6H_3(CF_3)_2)_4^-$, and $Al(OC(CF_3)_3)_4^-$. In Search of the Weakest $HOH \cdots F$ Hydrogen Bonds. *Inorg Chem* **2019**, *58*, 14900–14911.
37. Lacroix, M. R.; Gao, X.; Liu, Y.; Strauss, S. H. Unusually sharp FTIR $\nu(OH)$ bands and very weak $O \cdots H \cdots F$ hydrogen bonds in $M_2(H_2O)_{1,2}B_{12}F_{12}$ hydrates (M=Na–Cs). *Journal of Fluorine Chemistry* **2019**, *217*, 105–108.

38. Peryshkov, D. V.; Bukovsky, E. V.; Folsom, T. C.; Strauss, S. H. Solid-state solvation and anion packing patterns in X-ray structures of crystalline $K_2(\text{solv})_nB_{12}F_{12}$ (solv = $H_2O_2(\text{aq})$, CH_3OH , CH_3NO_2 , and CH_3CN). *Polyhedron* **2013**, *58*, 197–205.
39. Peryshkov, D. V.; Bukovsky, E. V.; Strauss, S. H. Efficient Preparation of $K_2B_{12}F_{12}$ in Neutral Acetonitrile; *Efficient Preparation of Fluorine Compounds* Wiley: New York, 2012.
40. Peryshkov, D. V.; Popov, A. A.; Strauss, S. H. Direct Perfluorination of $K_2B_{12}H_{12}$ in Acetonitrile Occurs at the Gas Bubble-Solution Interface and Is Inhibited by HF. Experimental and DFT Study of Inhibition by Protic Acids and Soft, Polarizable Anions. *J. Am. Chem. Soc.* **2009**, *131*, 18393–18403.
41. Bukovsky, E. V. Fluorinated Materials Synthesis and Characterization for Energy Storage and Energy Conversion Applications. Dissertation Colorado State University Fort Collins, Co, 2015.
42. Peryshkov, D. V. Direct Fluorination of $K_2B_{12}H_{12}$ and Synthesis and Characterization of Metal Salts of $B_{12}F_{12}^{2-}$. Dissertation, Colorado State University, Fort Collins, Co, 2011.
43. Zeng, G.; Holladay, S.; Langlois, D.; Zhang, Y.; Liu, Y. Kinetics of Heterogeneous Reaction of Ozone with Linoleic Acid and its Dependence on Temperature, Physical State, RH, and Ozone Concentration. *J. Phys. Chem. A* **2013**, *117*, 1963–1974.
44. Leng, C.; Hiltner, J.; Pham, H.; Kelley, J.; Mach, M.; Zhang, Y.; Liu, Y. Kinetics Study of Heterogeneous Reactions of Ozone with Erucic Acid Using an ATR-IR Flow Reactor. *Phys. Chem. Chem. Phys.* **2014**, *16*, 4350–4360.
45. Gao, X.; Zhang, Y.; Liu, Y. A Kinetics Study of the Heterogeneous Reaction of *n*-Butylamine with Succinic Acid Using an ATR-FTIR Flow Reactor. *Phys. Chem. Chem. Phys.* **2018**, *20*, 15464–15472.
46. Nakamoto, K.; Margoshes, M.; Rundle, R. E. Stretching Frequencies as a Function of Distances in Hydrogen Bonds. *J. Am. Chem. Soc.* **1955**, *77*, 6480–6486.
47. Pimentel, G. C.; Sederholm, C. H. Correlation of Infrared Stretching Frequencies and Hydrogen Bond Distances in Crystals. *J. Chem. Phys.* **1956**, *24*, 639–641.
48. Dearden, J. C. Rectilinear Correlation between –OH Stretching Frequency and O···O Distance in Intermolecularly and Intramolecularly Hydrogen Bonded Compounds. *Nature* **1965**, *206*, 1147–1148.
49. Mikenda, W. Stretching Frequency versus Bond Distance Correlation of OD(H)···Y (Y = N, O, S, Se, Cl, Br, I) Hydrogen Bonds in Solid Hydrates. *J. Mol. Struct.* **1986**, *147*, 1.
50. Ichikawa, M. Hydrogen-bond geometry and its isotope effect in crystals with OHO bonds—revisited. *J. Mol. Struct.* **2000**, *552*, 63–70 and references therein

51. Ikabata, Y.; Imamura, Y.; Nakai, H. Interpretation of Intermolecular Geometric Isotope Effect in Hydrogen Bonds: Nuclear Orbital plus Molecular Orbital Study. *J. Phys. Chem. A* **2011**, *115*, 1433 and references therein.
52. Ubbelohde, A. R.; Woodward, I. Isotope effect in potassium dihydrogen phosphate. *Nature* **1939**, *144*, 632.
53. Jin, T.; Zhang, W. Geometric H/D isotope effect in a series of organic salts involving short O–H···O hydrogen bonds between carboxyl and carboxylate groups. *CrystEngComm* **2019**, *21*, 4238–4242 and references therein.
54. Ahmed, F. R.; Cruickshank, D. W. J. A refinement of the crystal structure analyses of oxalic acid dihydrate. *Acta Crystallogr.* **1953**, *6*, 385–392.
55. Iwasaki, F. F.; Saito, Y. The crystal structure of deuterated oxalic acid dihydrate, (COOD)₂·2D₂O, by X-ray analysis. *Acta Crystallogr.* **1967**, *23*, 56–63.
56. Mootz, D.; Schilling, M. Trifluoroacetic Acid Tetrahydrate: A Unique Change from an Ionic to a Molecular Crystal Structure on Deuteration. *J. Am. Chem. Soc.* **1992**, *114*, 7435–7439.
57. Shipman, L. L.; Owicki, C.; Scheraga, H. A. Structure, Energetics, and Dynamics of Water Dimer. *J. Phys. Chem. A* **1974**, *78*, 2055–2060.
58. Engdahl, A.; Nelander, B. On the Relative Stabilities of H– and D– bonded Water Dimers. *J. Chem. Phys.* **1987**, *86*, 1819–1823.
59. Anick, D. J. Proton and Deuteron Position Preferences in Water Clusters: An Ab Initio Study. *J. Chem. Phys.* **2005**, *123*, 244309.
60. Futami, Y.; Kudoh, S.; Takayanagi, M.; Nakata, M. Structures of CH₃F···CH₃F and CH₃F···H₂O complexes in a supersonic jet studied by matrix-isolation infrared spectroscopy and density-functional-theory calculation. *Chem. Phys. Lett.* **2002**, *357*, 209–216.
61. Monat, J. E.; Toczyłowski, R. R.; Cybulski, S. M. Ab Initio Study of the CH₃F···H₂O Complex. *J. Phys. Chem. A* **2001**, *105*, 9004–9013.
62. Martins, J. B. L.; Politi, J. R. S.; Braga, A. D.; Gargano, R. Complexes of water with the fluoromethanes. *Chem. Phys. Lett.* **2006**, *431*, 51–55.
63. Caminati, W.; Melandri, S.; Rossi, I.; Favero, P. G. The C–F···H–O Hydrogen Bond in the Gas Phase. Rotational Spectrum and ab Initio Calculations of Difluoromethane-Water. *J. Am. Chem. Soc.* **1999**, *121*, 10098–10101.

64. Calabrese, C.; Li, W.; Prampolini, G.; Evangelisti, L.; Uriarte, I.; Cacelli, I.; Melandri, S.; Cocinero, E. J. A General Treatment to Study Molecular Complexes Stabilized by Hydrogen-, Halogen-, and Carbon-Bond Networks: Experiment and Theory of $(\text{CH}_2\text{F}_2)_n \cdots (\text{H}_2\text{O})_m$. *Angew. Chem., Int. Ed.* **2019**, *58*, 8437–8442.
65. Peryshkov, D. V.; Popov, A. A.; Strauss, S. H. Latent porosity in potassium dodecafluoro-*closo*-dodecaborate(2-). Structures and rapid room temperature interconversions of crystalline $\text{K}_2\text{B}_{12}\text{F}_{12}$, $\text{K}_2(\text{H}_2\text{O})_2\text{B}_{12}\text{F}_{12}$, and $\text{K}_2(\text{H}_2\text{O})_4\text{B}_{12}\text{F}_{12}$ in the presence of water vapor. *J Am Chem Soc* **2010**, *132*, 13902–13913.
66. Peryshkov, D. V.; Bukovsky, E. V.; Lacroix, M. R.; Wu, H.; Zhou, W.; Jones, W. M.; Lozinsek, M.; Folsom, T. C.; Heyliger, D. L.; Udovic, T. J.; Strauss, S. H. Latent Porosity in Alkali-Metal $\text{M}_2\text{B}_{12}\text{F}_{12}$ Salts: Structures and Rapid Room-Temperature Hydration/Dehydration Cycles. *Inorg. Chem.* **2017**, *56*, 12023–12041.
67. Peryshkov, D. V.; Strauss, S. H. $\text{K}_2\text{B}_{12}\text{F}_{12}$: A rare A_2X structure for an ionic compound at ambient conditions. *Journal of Fluorine Chemistry* **2010**, *131*, 1252–1256.
68. Raabe, I.; Wagner, K.; Santiso-Quiñones, G.; Krossing, I. Snapshots of the Hydrolysis of the Lithium Alkoxide $[\text{Li}\{\text{OC}(\text{CF}_3)_3\}]_4$. *Zeitschrift für anorganische und allgemeine Chemie* **2009**, *635*, 513–517.
69. Martínez-Martínez, A. J.; Weller, A. S. Solvent-free anhydrous Li^+ , Na^+ and K^+ salts of $[\text{B}(3,5\text{-}(\text{CF}_3)_2\text{C}_6\text{H}_3)_4]^-$, $[\text{BAr}^{\text{F}_4}]^-$. Improved synthesis and solid-state structures. *Dalton Trans* **2019**, *48*, 3551–3554.
70. Marseglia, E. A.; Brown, I. D. Lithium Hexafluorotitanate Dihydrate and Lithium Hexafluorostannate Dihydrate. *Acta Crystallogr., Sect. B: Struct. Crystallogr. Cryst. Chem.* **1973**, *B29*, 1352–1354.
71. Guzei, I. A.; Langenham, J. M. The correct space group of $\text{NaPF}_6 \cdot \text{H}_2\text{O}$. *Acta Crystallogr., Sect. C: Cryst. Struct. Commun.* **2003**, *59*, i95–i96.
72. Himmelspach, A.; Zähres, M.; Finze, M. Salts of the Lewis-Acidic Dianion $[\text{Hg}(\textit{closo}\text{-}1\text{-CB}_{11}\text{F}_{11})_2]_2$: Coordination of Acetonitrile and Water. *Inorg. Chem.* **2011**, *50*, 3186–3188.
73. Mierzwicki, K.; Mielke, Z.; Sałdyka, M.; Coussan, S.; Roubin, P. Structure, spectra and stability of a tetrafluoromethane-water complex. *Phys. Chem. Chem. Phys.* **2008**, *10*, 1292–1297 and references therein.
74. Rosenberg, R. E. Does Fluoromethane Form a Hydrogen Bond with Water? *J. Phys. Chem. A* **2012**, *116*, 10842–10849.
75. Kusanagi, H. Infrared Spectrum of Water Isotopes (H_2O , HOD , and D_2O Molecules) in Hydrophobic Poly(vinylidene fluoride) *Chemistry Letters* **1997**, *26*, 683–684.

76. Ayers, G. P.; Pullin, A. D. E. The I.R. Spectra of Matrix Isolated Water Species – I. Assignment of Bands to $(\text{H}_2\text{O})_2$, $(\text{D}_2\text{O})_2$, and HDO Dimer Species in Argon Matrices. *Spectrochim. Acta, Part A* **1976**, *32A*, 1629–1639.
77. Bentwood, R. M.; Barnes, A. J.; Orville-Thomas, W. J. Studies of Intermolecular interactions by Matrix Isolation Vibrational Spectroscopy. Self-association of Water. *J. Mol. Spectrosc.* **1980**, *84*, 391–404.
78. Engdahl, A.; Nelander, B. Water in Krypton Matrices. *J. Mol. Struct.* **1989**, *193*, 101–109.
79. Barker, E. F.; Sleator, W. W. The Infrared Spectrum of Heavy Water. *J. Chem. Phys.* **1935**, *3*, 660–663.
80. Benedict, W. W.; Gailar, N.; Plyler, E. K. Rotation-Vibration Spectra of Deuterated Water Vapor. *J. Chem. Phys.* **1956**, *24*, 1139–1165.
81. Rank, D. H.; Larsen, K. D.; Bordner, E. B. The Raman Spectrum of Heavy Water Vapor. *J. Chem. Phys.* **1934**, *2*, 464–467.
82. Krossing, I.; Van Wullen, L. Superweak complexes of tetrahedral P_4 molecules with the silver cation of weakly coordinating anions. *Chem. - Eur. J.* **2002**, *8*, 700–711.
83. Krossing, I. The Facile Preparation of Weakly Coordinating Anions: Structure and Characterisation of Silver Polyfluoroalkoxyaluminates $\text{AgAl}(\text{OR}_F)_4$, Calculation of the Alkoxide Ion Affinity. *Chem. Eur. J.* **2001**, *7*, 490–502.
84. Krossing, I.; Brands, H.; Feuerhake, R.; Koenig, S. New Reagents to Introduce Weakly Coordinating Anions to Type $\text{Al}(\text{OR}_F)_4^-$: Synthesis, Structure, and characterization of Cs and Trityl salts. *Journal of Fluorine Chemistry* **2001**, *112*, 83–90.
85. Ivanova, S. M.; Nolan, B. G.; Kobayashi, Y.; Miller, S. M.; Anderson, O. P.; Strauss, S. H. Relative Lewis Basicities of Six $\text{Al}(\text{OR}_F)_4^-$ superweak anions and the structures of $\text{LiAl}\{\text{OCH}(\text{CF}_3)_2\}_4$ and $[\text{1-Et-3-Me-1,3-C}_3\text{H}_3\text{N}_2][\text{Li}\{\text{Al}\{\text{OCH}(\text{CF}_3)_2\}_4\}_2]$. *Chem. Eur. J.* **2001**, *7*, 503–510.
86. Strauss, S. H.; Nolan, B. G.; Barbarich, T. J.; Rockwell, J. J. *Weakly Coordinating Anions Containing Perfluoroalkoxide Ligands*, U. S. Patent 6,221,941 B1 (April 24, 2001).
87. Krossing, I. Weakly Coordinating Anions: Fluorinated Alkoxyaluminates; *Comprehensive Inorganic Chemistry II 2nd ed* Elsevier Amsterdam 2013. 681–705 and references therein.
88. Adolf, A.; Gonsior, M.; Krossing, I. Extending the Coordination Chemistry of Molecular P_4S_3 : The Polymeric $\text{Ag}(\text{P}_4\text{S}_3)^+$ and $\text{Ag}(\text{P}_4\text{S}_3)_2^+$ Cations. *J. Am. Chem. Soc.* **2002**, *124*, 7111–7116.
89. Krossing, I.; Raabe, I. Non Coordinating Anions K Fact or Fiction? A Survey of Likely Candidates. *Angew. Chem., Int. Ed.* **2004**, *43*, 2066–2090 and references therein.

90. Engesser, T. A.; Lichtenthaler, M. R.; Schleep, M.; Krossing, I. Reactive p-block cations stabilized by weakly coordinating anions. *Chem Soc Rev* **2016**, *45*, 789–899.
91. Riddlestone, I. M.; Kraft, A.; Schaefer, J.; Krossing, I. Taming the Cationic Beast: Novel Developments in the Synthesis and Application of Weakly Coordinating Anions. *Angew. Chem., Int. Ed.* **2018**, *57*, 13982–14024.
92. Nishida, H.; Takata, N.; Yoshimura, M.; Sonoda, T.; Kobayashi, H. Tetrakis(3,5-bis(trifluoromethyl)phenyl)borate. Highly Lipophilic Stable Anionic Agent for Solvent-Extraction of Cations. *Bull. Chem. Soc. Jpn.* **1984**, *57*, 2600–2604.
93. Kobayashi, H. Weakly Coordinating Bulky Anions Designed by Efficient use of Polyfluoro-substitution. *J. Fluorine Chem.* **2000**, *105*, 201–203.
94. Luongo, C. A.; Bu, J.; Burke, N. L.; Gilbert, J. D.; Prentice, B. M.; Cummings, S.; Reed, C. A.; McLuckey, S. A. Selective Removal of Alkali Metal Cations from Multiply-Charged Ions via Gas-Phase Ion/Ion Reactions Using Weakly Coordinating Anions. *J. Am. Soc. Mass Spectrom.* **2015**, *26*, 404–414.
95. Geiger, W. E.; Barrière, F. Organometallic Electrochemistry Based on Electrolytes Containing Weakly-Coordinating Fluoroarylborate Anions. *Acc. Chem. Res.* **2010**, *43*, 1030–1039.
96. Zou, W.; Pang, W.; Chen, C. Redox control in palladium catalyzed norbornene and alkyne polymerization. *Inorg. Chem. Front.* **2017**, *4*, 795–800.
97. Hong, C.; Sui, X.; Li, Z.; Pang, W.; M, C. Phosphine phosphonic amide nickel catalyzed ethylene polymerization and copolymerization with polar monomers. *Dalton Trans* **2018**, *47*, 8264–8267.
98. McKay, A. I.; Bukvic, A. J.; Tegner, B. E.; Burnage, A. L.; Martínez-Martínez, A. J.; Rees, N. H.; Macgregor, S. A.; Weller, A. S. Room Temperature Acceptorless Alkane Dehydrogenation from Molecular σ -Alkane Complexes. *J. Am. Chem. Soc.* **2019**, *141*, 11700–11712.
99. Niemann, M.; Neumann, B.; Stammeler, H. G.; Hoge, B. Synthesis, Properties, and Application of Tetrakis(pentafluoroethyl)gallate, $[\text{Ga}(\text{C}_2\text{F}_5)_4]^-$. *Angew. Chem., Int. Ed.* **2019**, *58*, 8938–8942.
100. Bukovsky, E. V.; Peryshkov, D. V.; Wu, H.; Zhou, W.; Tang, W. S.; Jones, W. M.; Stavila, V.; Udovic, T. J.; Strauss, S. H. Comparison of the Coordination of $\text{B}_{12}\text{F}_{12}^{2-}$, $\text{B}_{12}\text{Cl}_{12}^{2-}$, and $\text{B}_{12}\text{H}_{12}^{2-}$ to Na^+ in the Solid State: Crystal Structures and Thermal Behavior of $\text{Na}_2(\text{B}_{12}\text{F}_{12})$, $\text{Na}_2(\text{H}_2\text{O})_4(\text{B}_{12}\text{F}_{12})$, $\text{Na}_2(\text{B}_{12}\text{Cl}_{12})$, and $\text{Na}_2(\text{H}_2\text{O})_6(\text{B}_{12}\text{Cl}_{12})$. *Inorg Chem* **2017**, *56*, 4369–4379.
101. Guillermet, J.; Novak, A.; Foglizzo, E. Étude par spectroscopie infrarouge de la structure du cation $\text{Mg}(\text{H}_2\text{O})_6^{2+}$ dans quelques sels de magnésium hydratés. *J. Mol. Struct.* **1973**, *17*, 91–104.

102. Lutz, H. D.; Jung, C.; Trömel, M.; Lösel, J. Brown's bond valences, a measure of the strength of hydrogen bonds. *J. Mol. Struct.* **1995**, *351*, 205–209.
103. Berglund, B.; Lindgren, J.; Tegenfeldt, J. O–H and O–D Stretching Vibrations in Isotopically Dilute HDO Molecules in Some Solid Hydrates. *J. Mol. Struct.* **1978**, *43*, 169–177.
104. Lundgren, J. O.; Liminga, R.; Tellgren, R. Neutron Diffraction Refinement of Pyroelectric Lithium Perchlorate Trihydrate. *Acta Crystallogr., Sect. B: Struct. Crystallogr. Cryst. Chem.* **1982**, *38*, 15–20.
105. Berglund, B.; Tellgren, R.; Thomas, J. O. Hydrogen bond studies. CXVI A neutron diffraction study of the structure of sodium perchlorate monohydrate, $\text{NaClO}_4 \cdot \text{H}_2\text{O}$, at 298 K. *Acta Crystallogr., Sect. B: Struct. Crystallogr. Cryst. Chem.* **1976**, *32*, 2444–2449.
106. Lacroix, M. R.; Liu, Y.; Strauss, S. H. Room-Temperature FTIR Spectra of the Cyclic S_4 $(\text{H}_2\text{O})_4$ Cluster in Crystalline $\text{Li}_2(\text{H}_2\text{O})_4(\text{B}_{12}\text{F}_{12})$: Observation of B and E $\nu(\text{OH})$ Bands and Coupling of Strong O–H–O and Weak O–H–F Vibrations. *The Journal of Physical Chemistry A* **2019**, *123*, 9781–9790.
107. Preisinger, A.; Zottl, M.; Mereiter, K.; Mikenda, W. S., S.; Dufek, P.; Schwarz, K.; Blaha, P. Hydrogen Bonding in Potassium Fluoride Dihydrate: A Crystallographic, Spectroscopic, and Theoretical Study. *Inorg. Chem.* **1994**, *33*, 4774–4780.
108. Palacio, F.; Andres, M.; Esteban Calderon, C.; Martinez Ripoll, M.; Garcíablancó, S. Crystal-Structure and Magnetic-Properties of Linear-Chain Potassium Aquotetrafluoromanganate(III). *Journal of Solid State Chemistry* **1988**, *76*, 33–39.
109. Bukvetsky, B. V.; Muradyan, M. A.; Simonov, M. A.; Simonov, V. I. Refinement of the Crystal Structure of Strontium Dihydrate Hexafluorotitanate, $\text{SrTiF}_6 \cdot 2\text{H}_2\text{O}$. *Kristallografiya* **1979**, *24*, 29–37.
110. Brink, G.; Falk, M. Infrared studies of water in crystalline hydrates: $\text{NaClO}_4 \cdot \text{H}_2\text{O}$, $\text{LiClO}_4 \cdot 3\text{H}_2\text{O}$, and $\text{Ba}(\text{ClO}_4)_2 \cdot 3\text{H}_2\text{O}$. *Can. J. Chem.* **1970**, *48*, 2096–2103.
111. Roisnel, T.; Nunez, P.; Tressaud, A.; Molins, E.; Rodriguez Carvajal, J. Investigation of $\text{K}_2\text{MnF}_5 \cdot \text{H}_2\text{O}$ by neutron diffraction. *J. Solid State Chem.* **2000**, *150*, 104–111.
112. Bukovec, P. K., V. Synthesis and crystal structure of cesium diaquatetrafluoromanganate(III). *J. Chem. Soc. Dalton Trans.* **1977**, 945–947.
113. Cherkasova, T. G.; Tatarinova, E. S.; Cherkasova, E. V. Crystal Structure of Hexaaquamagnesium Hexfluorosilicate *Russian Journal of Inorganic Chemistry* **2004**, *49*, 1064–1067.
114. Massa, W.; Burk, V. Erdalkali-Fluoromanganate(III): $\text{BaMnF}_5 \cdot \text{H}_2\text{O}$ und $\text{SrMnF}_5 \cdot \text{H}_2\text{O}$. *Z. Anorg. Allg. Chem.* **1984**, *516*, 119–126.

115. Laligant, Y.; Pannetier, J.; Leblanc, M.; Labbe, P.; Heger, G.; Ferey, G. Crystal structure refinement of the inverse weberite $\text{MnFeF}_5(\text{H}_2\text{O})_2$. *Zeitschrift Fur Kristallographie* **1987**, *181*, 1–10.
116. Benghalem, A.; Leblanc, M. C., Y. Room-Temperature Structure of Iron(II) Hexafluorostannate(IV) Hexahydrate. *Acta Cryst.* **1990**, *C46*, 2453–2454.
117. Mikenda, W.; Pertlik, F.; Steinböck, S. Crystal Structures and Vibrational Spectra of $M\text{SnF}_6 \cdot 6\text{H}_2\text{O}$ ($M = \text{Fe, Co, Ni}$). *Monatshefte für Chemie* **1995**, *126*, 61–66.
118. Prince, E. Configuration of the Water Molecule in Cupric Fluoride Dihydrate at 298 K. *J. Chem. Phys.* **1972**, *56*, 4352–4355.
119. Bukvetskii, B. V. N., Y. Z.; Fykin, L. E.; Polishchuk, S. A.; Laptash, N. M. Neutron-diffraction study of the atomic structure of $\text{ZnF}_2(\text{H}_2\text{O})_4$. *Koord. Khim.* **1977**, *3*, 1594–1599.

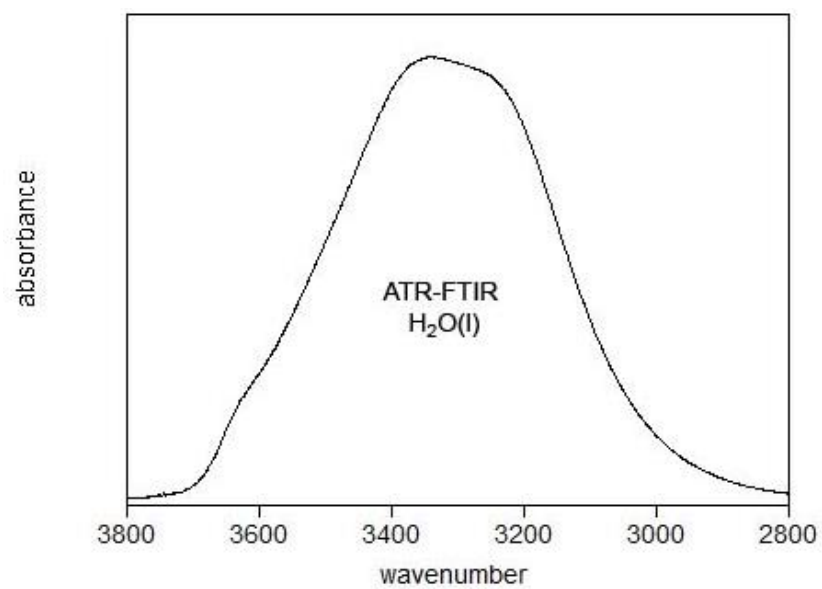


Figure 2.1. ATR-FTIR spectrum of H₂O(*l*) deposited on a ZnSe ATR crystal collected at room temperature. The band is centered ca. 3300 cm⁻¹ with a FWHM > 400 cm⁻¹.

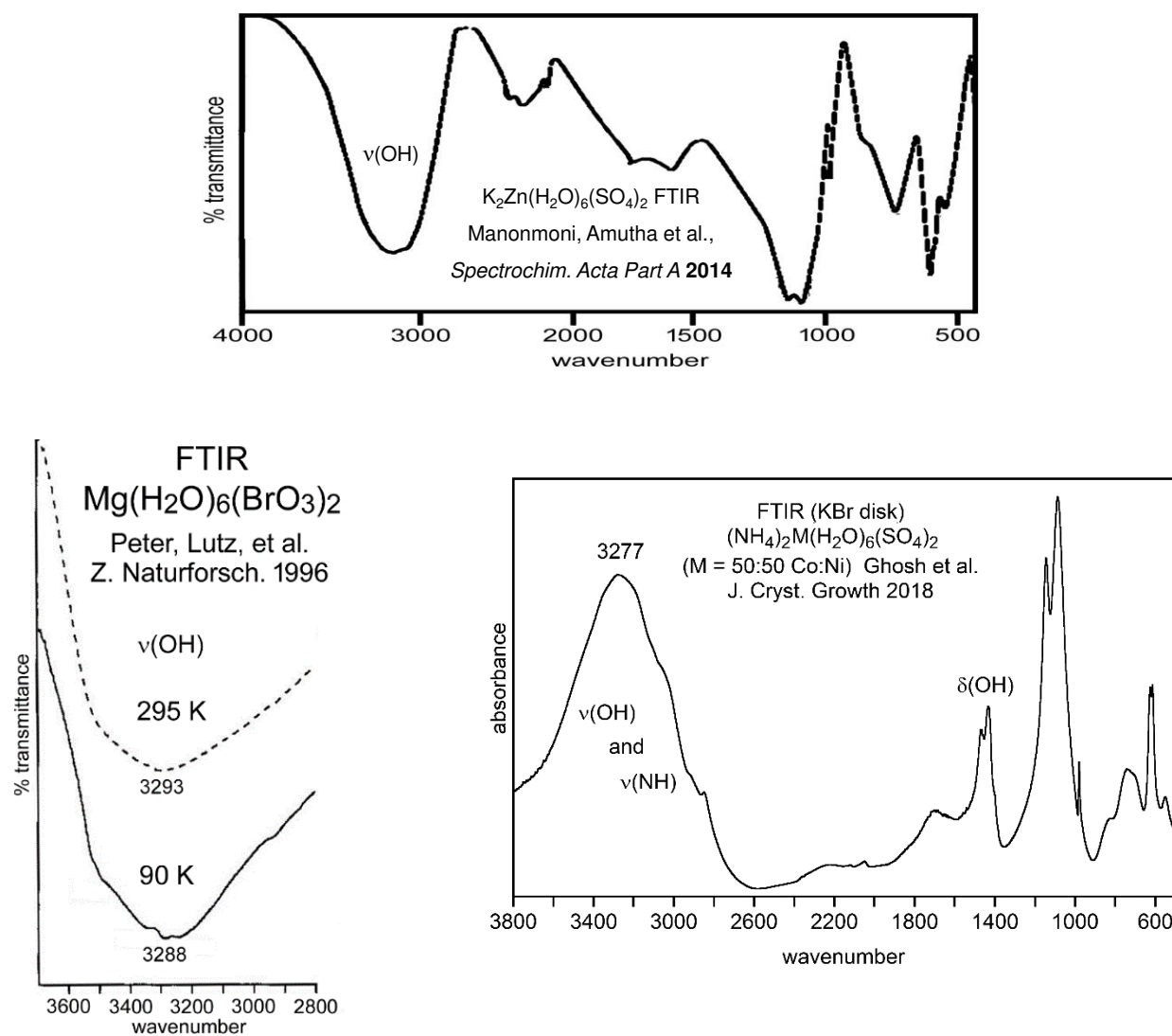


Figure 2.2. FTIR spectra of $Mg(H_2O)_6(BrO_3)_2$ (ref. 23), the Tutton salt $K_2Zn(H_2O)_6(SO_4)_2$ (ref. 24), and $(NH_4)_2M(H_2O)_6(SO_4)_2$ (ref. 25; M = 50:50 Co:Ni). The $\nu(OH)$ bands at 3000–3300 cm^{-1} are significantly redshifted relative to $\nu_{asym}(OH)$ and $\nu_{sym}(OH)$ for $H_2O(g)$ (3756 and 3655 cm^{-1} , respectively²⁶). The first two figures were adapted from figures in the respective references. The author thanks Prof. Santunu Ghosh for kindly supplying a digital data file with which the spectrum of $(NH_4)_2M(H_2O)_6(SO_4)_2$ was prepared.

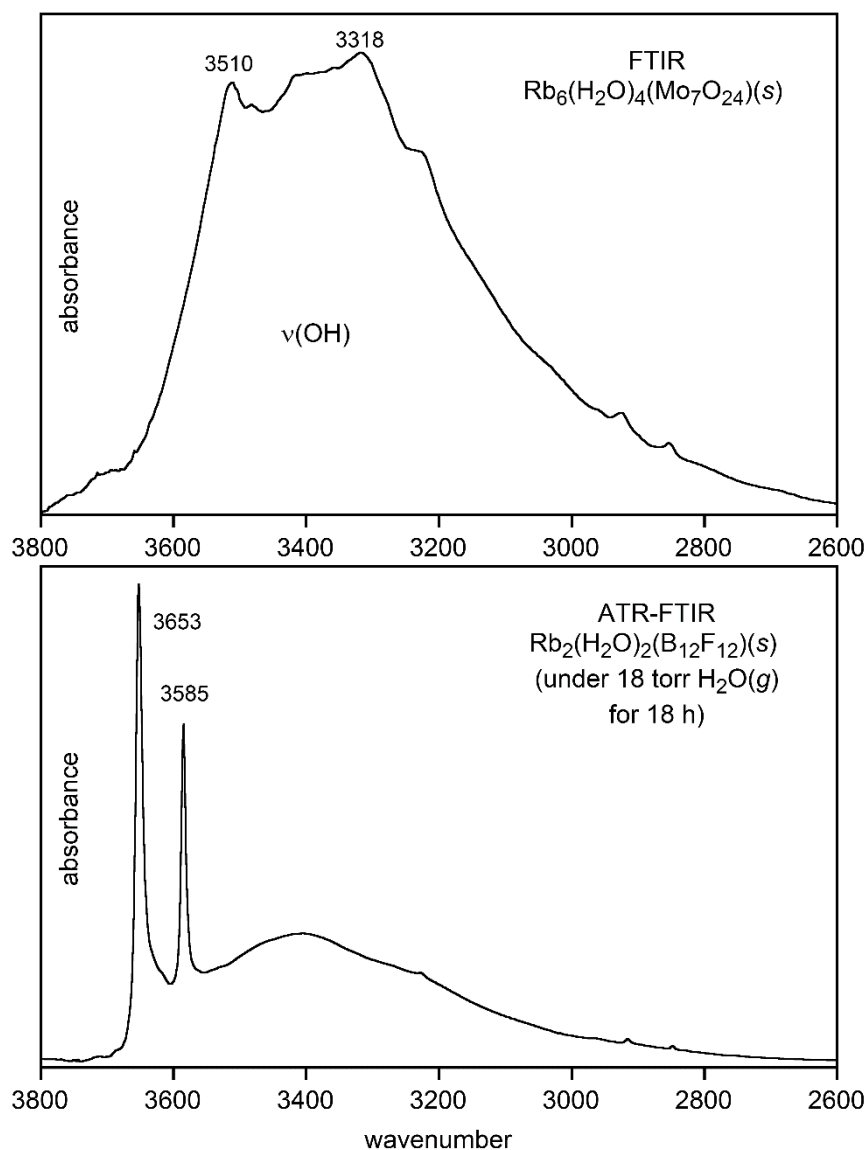


Figure 2.3. FTIR spectra of $\text{Rb}_6(\text{H}_2\text{O})_4(\text{Mo}_7\text{O}_{24})$ (top; ref. 27; Nujol mull) and $\text{Rb}_2(\text{H}_2\text{O})_2(\text{B}_{12}\text{F}_{12})$ (bottom; originally published in ref. 37) at 22 °C. The broad band centered at ca. 3400 cm^{-1} in the spectrum of $\text{Rb}_2(\text{H}_2\text{O})_2(\text{Z})$ is due to H_2O on the surface of the microcrystalline particles. The sharp bands at 3653 and 3585 cm^{-1} are assigned to $\nu_{\text{asym}}(\text{OH})$ and $\nu_{\text{sym}}(\text{OH})$ for the symmetry-related coordinated H_2O molecules and have FWHMs of 9 and 8 cm^{-1} , respectively. The top figure was adapted from a figure in ref. 27.

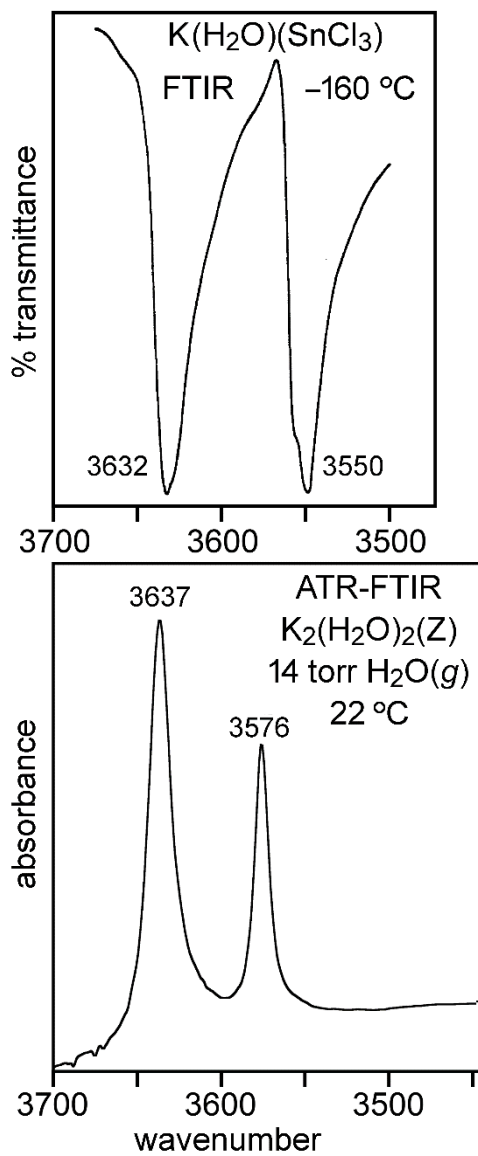


Figure 2.4. The $\nu(\text{OH})$ regions in the FTIR spectra of $\text{K}(\text{H}_2\text{O})(\text{SnCl}_3)$ (top; ref. 30; $-160\text{ }^\circ\text{C}$) and $\text{K}_2(\text{H}_2\text{O})_2(\text{B}_{12}\text{F}_{12})$ (bottom; this work). The $\nu(\text{OH})$ peaks for $\text{K}(\text{H}_2\text{O})(\text{SnCl}_3)$ at $30\text{ }^\circ\text{C}$ are 3618 and 3538 cm^{-1} , and it is not known how much broader they are relative to the $-160\text{ }^\circ\text{C}$ spectrum shown here. The top figure was adapted from a figure in ref. 30.

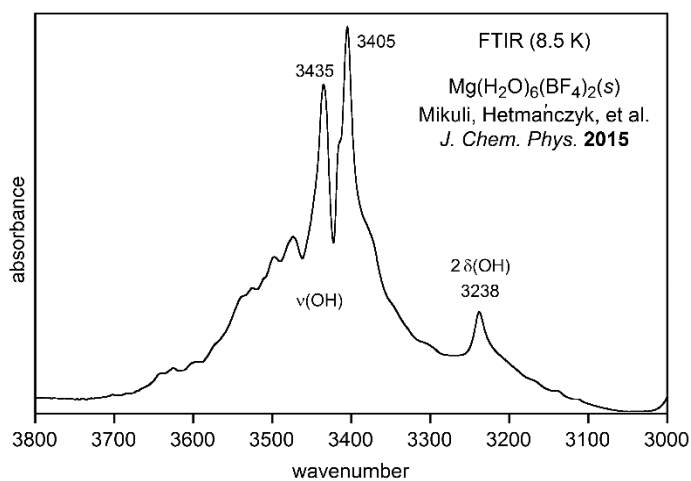
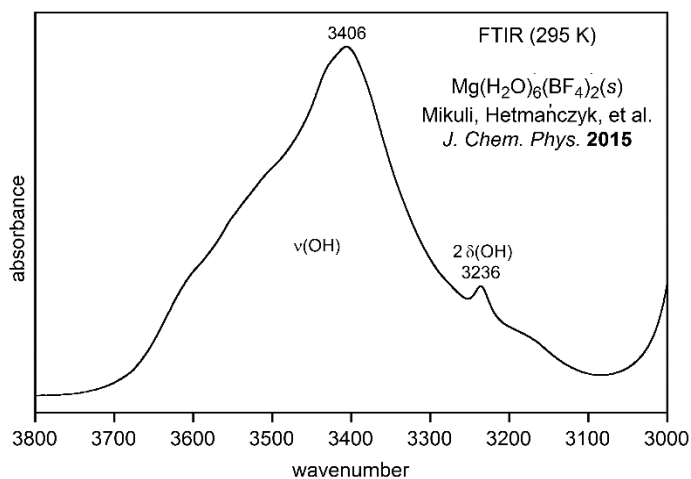


Figure 2.5. The $\nu(\text{OH})$ regions of FTIR spectra of $\text{Mg}(\text{H}_2\text{O})_6(\text{BF}_4)_2$ at 295 K (top) and 8.5 K (bottom). Peak positions in cm^{-1} and their assignments are shown. Different versions of these spectra were first published in ref. 16. The author thanks Dr. Joanna Hetmańczyk for providing digital copies from which the spectra shown in this figure were made.

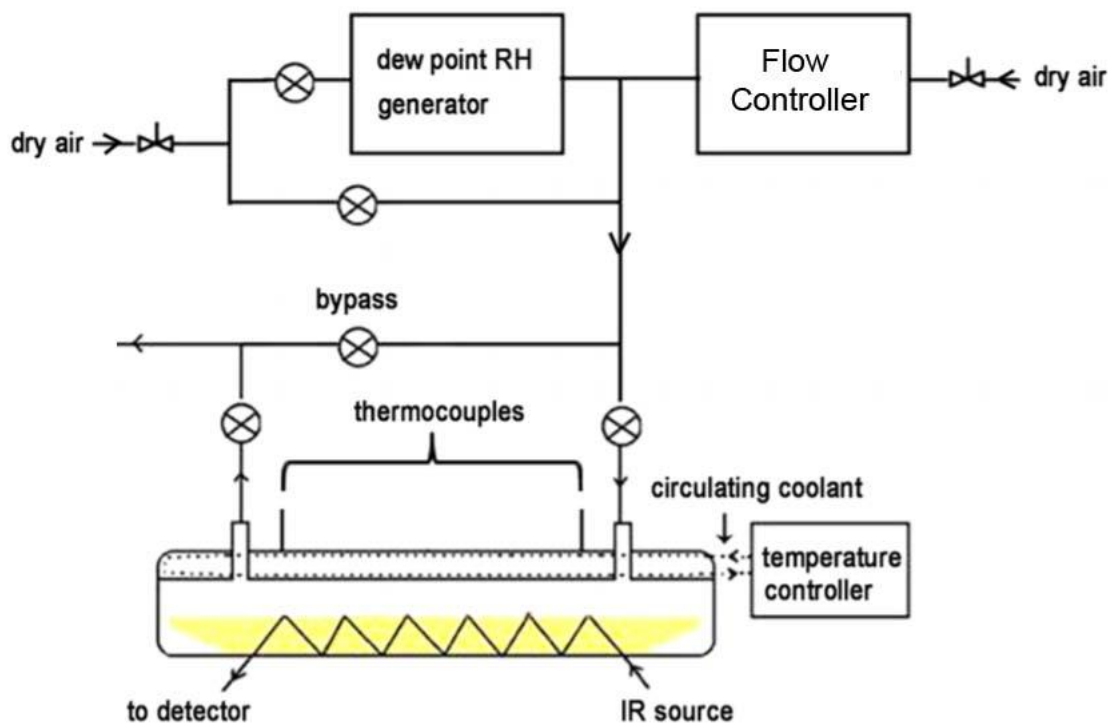


Figure 2.6. Schematic diagram of the instrumental set up adapted from Figure 1 in ref. 43. The three primary differences in this set up for the work discussed in this dissertation are (i) an Alicat Scientific flowmeter (flow controller) replaces the ozone generator, and allows for control of the dry gas (N_2) flow at rates between $1\text{--}1000\text{ mL min}^{-1}$; (ii) the ozone monitor has been removed as no ozone was added in any of the work in this dissertation; and (iii) the temperature controller was not utilized in any of the room temperature work.

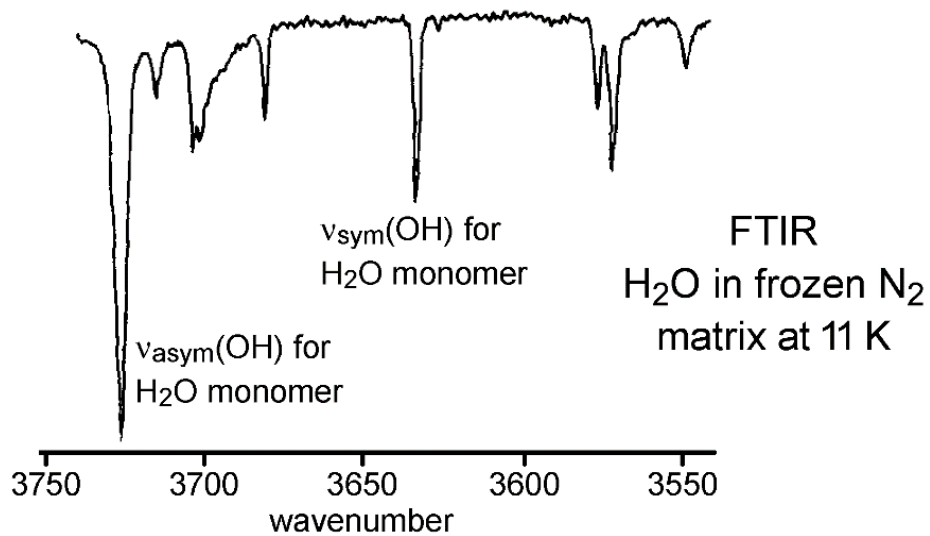


Figure 2.7. ATR-FTIR spectrum of H₂O in a frozen N₂ matrix at 11 K (ref. 18). The bands labelled as $\nu_{\text{asym}}(\text{OH})$ and $\nu_{\text{sym}}(\text{OH})$ are due to monomeric H₂O molecules. The other bands are due to dimers and higher oligomers. This figure was adapted from a figure in ref. 18.

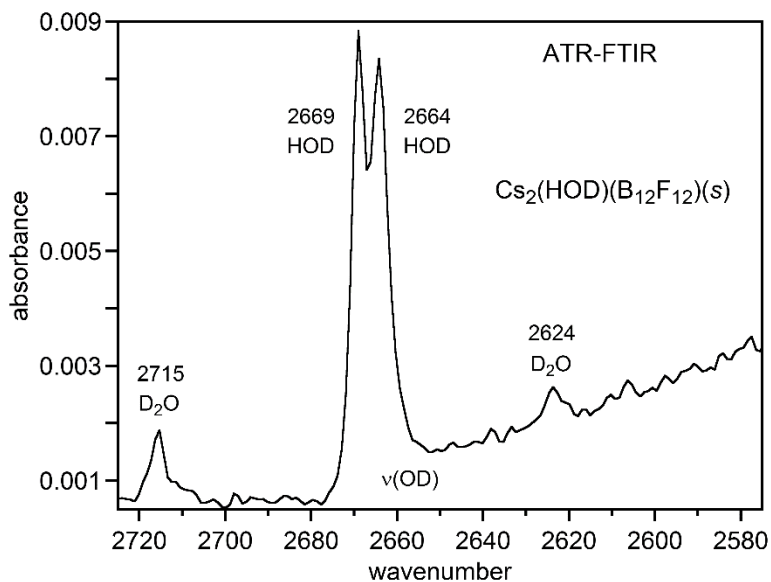
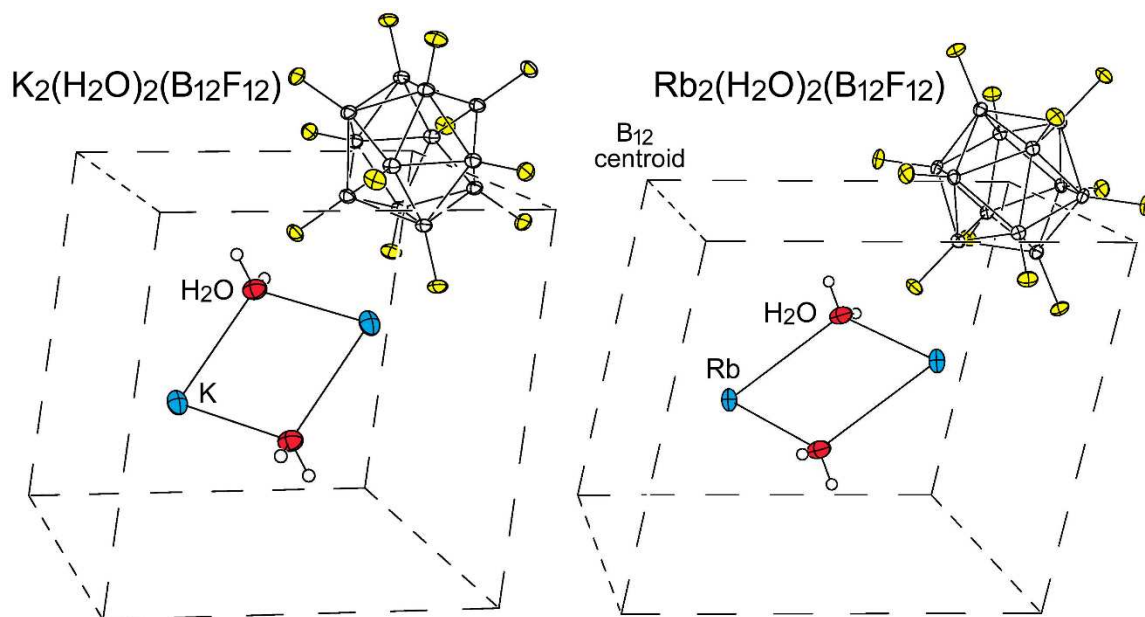


Figure 2.8. ATR-FTIR spectrum of a microcrystalline sample containing a small amount of $\text{Cs}_2(\text{HOD})(\text{B}_{12}\text{F}_{12})$ and $\text{Cs}_2(\text{D}_2\text{O})(\text{B}_{12}\text{F}_{12})$ evaporated on a ZnSe crystal from aqueous solution originally containing ca. 10% D_2O . Peak positions in cm^{-1} and their assignments are shown. The two bands at 2669 and 2664 cm^{-1} in the spectrum are due to the different $\text{O}(\text{D})\cdots\text{F}$ environments (the $\text{O}(\text{D})\cdots\text{F}$ distances are 2.997(3) and 3.103(3) Å (ref. 67)). The peaks at 2715 and 2624 cm^{-1} are assigned to the $\nu_{\text{asym}}(\text{OD})$ and $\nu_{\text{asym}}(\text{OD})$ stretching vibrations, respectively, for the small amount of $\text{Cs}_2(\text{D}_2\text{O})(\text{B}_{12}\text{F}_{12})$ present in the sample.



M–O	2.7698(6), 2.7726(6) Å	2.857(1), 2.915(1) Å
M–F	6 @ 2.598(1)–3.159(1) Å (ave. 2.857 Å)	8 @ 2.909(1)–3.237(1) Å (ave. 3.100 Å)
O(H)⋯F	2.978(1); 2.972(1), 2.978(1)	2.857(2); 2.859(2), 2.931(2)
⊙⋯⊙	7.276 × 2, 7.295 Å	7.166 × 2, 7.851 Å
acute ⊙⋯⊙⋯⊙	78.7, 81.3°	77.0, 88.4°

Figure 2.9. Comparison of the isomorphous $P2_1/c$, $Z = 2$, X-ray crystals structures of $K_2(H_2O)_2(B_{12}F_{12})$ ($T = 110(2)$ K; formula unit volume = 367.9 \AA^3) and $Rb_2(H_2O)_2(B_{12}F_{12})$ ($T = 120(2)$ K; formula unit volume = 381.6 \AA^3). The symbol \odot represents a B_{12} centroid. The structure of $K_2(H_2O)_2(B_{12}F_{12})$ was reported in ref. 65. The structure of $Rb_2(H_2O)_2(B_{12}F_{12})$ was reported in ref. 66.

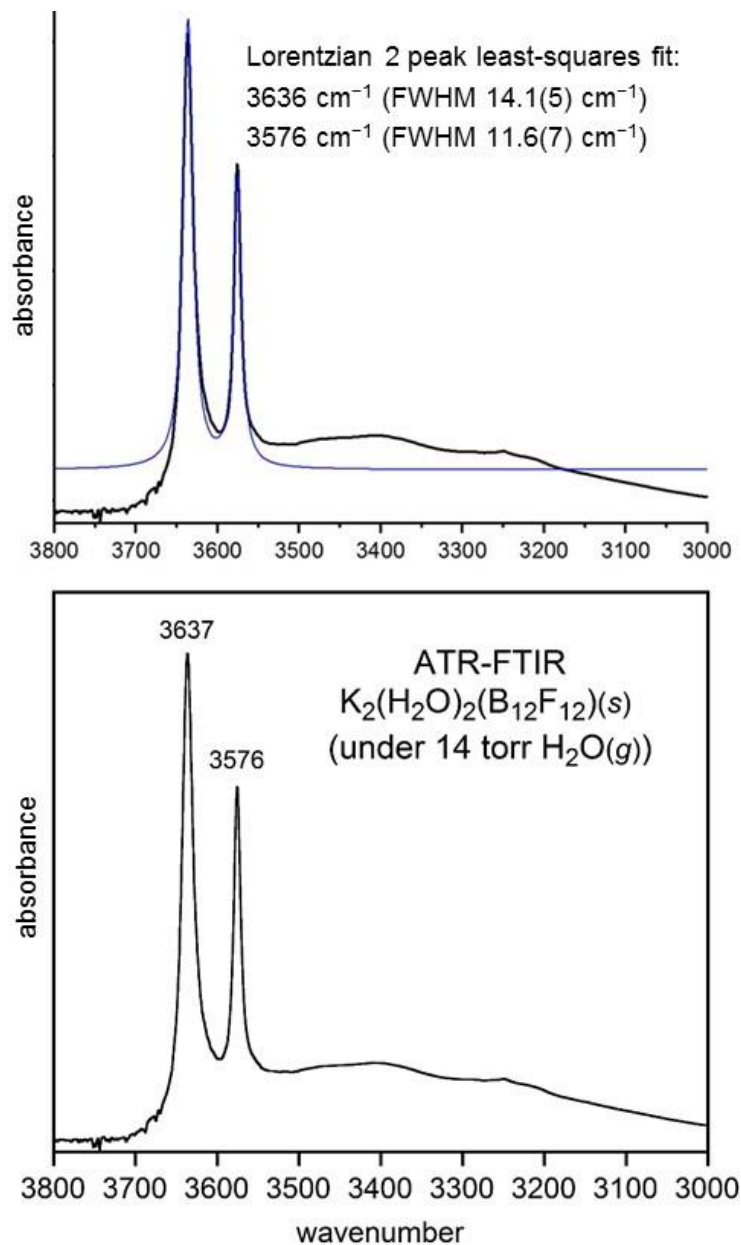


Figure 2.10. Lorentzian least-squares fit to the $\nu(\text{OH})$ bands in the ATR-FTIR spectrum of $\text{K}_2(\text{H}_2\text{O})_2(\text{B}_{12}\text{F}_{12})(s)$ evaporated on the ZnSe ATR crystal from an aqueous solution and then held under 14 torr $\text{H}_2\text{O}(g)$. Only the two sharp peaks were fit to Lorentzian peaks, not the broad surface H_2O band at ca. 3400 cm^{-1} . The blue trace is the sum of the two peak fit.

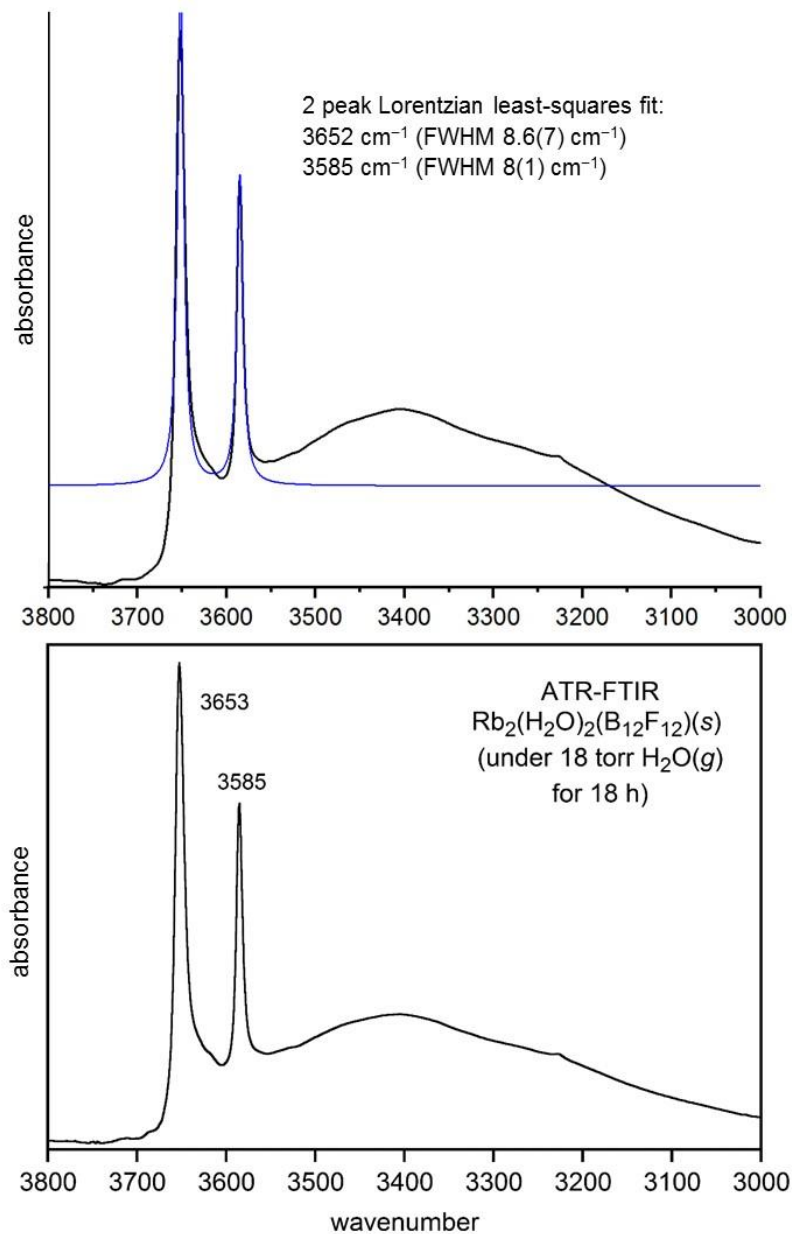


Figure 2.11. Lorentzian least-squares fit to the $\nu(\text{OH})$ bands in the FTIR spectrum of $\text{Rb}_2(\text{H}_2\text{O})_2(\text{B}_{12}\text{F}_{12})(s)$ evaporated on the ZnSe ATR crystal from an aqueous solution and then held under 18 torr $\text{H}_2\text{O}(g)$ for 18 h. Only the two sharp peaks were fit to Lorentzian peaks, not the broad surface H_2O band at ca. 3400 cm^{-1} . The blue trace is the sum of the two peak fit.

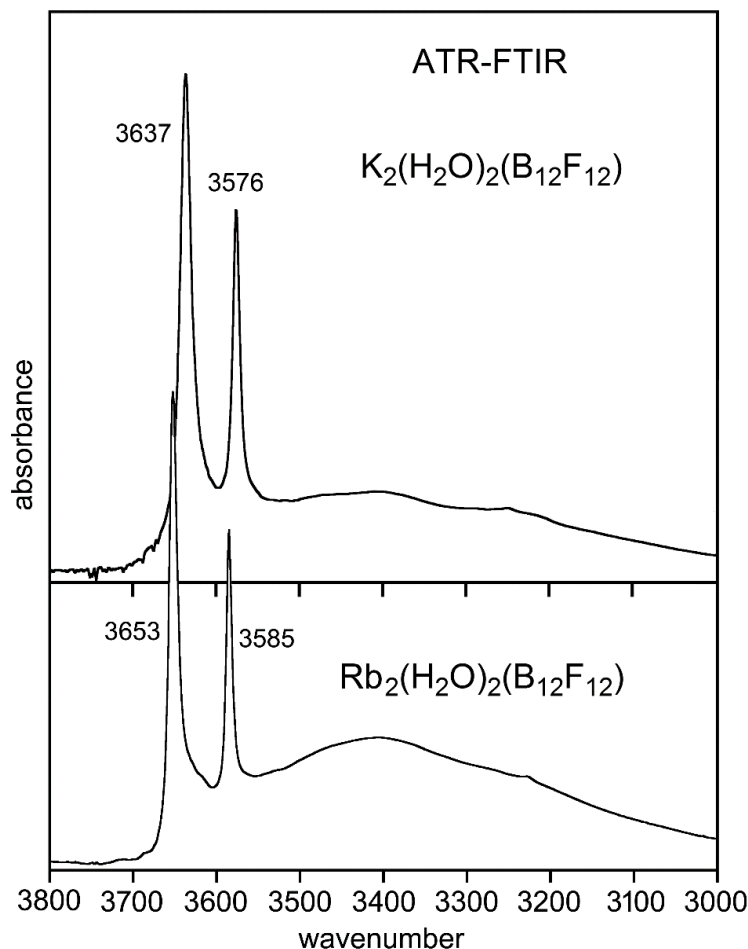


Figure 2.12. ATR-FTIR spectra ($\nu(\text{OH})$ regions) of thin films of microcrystalline $\text{K}_2(\text{H}_2\text{O})_2(\text{B}_{12}\text{F}_{12})$ and $\text{Rb}_2(\text{H}_2\text{O})_2(\text{B}_{12}\text{F}_{12})$ evaporated on a ZnSe crystal from aqueous solutions. Peak positions in cm^{-1} are shown. The higher wavenumber and more narrow $\nu(\text{OH})$ bands for the coordinated H_2O molecules in $\text{Rb}_2(\text{H}_2\text{O})_2(\text{B}_{12}\text{F}_{12})$ indicate weaker hydrogen bonding to the $\text{B}_{12}\text{F}_{12}^{2-}$ anion than in $\text{K}_2(\text{H}_2\text{O})_2(\text{B}_{12}\text{F}_{12})$. This is probably due to the weaker Brønsted acidity of $\text{H}_2\text{O}-\text{Rb}^+$ moieties relative to $\text{H}_2\text{O}-\text{K}^+$ moieties. This comparison is valid because the two compounds have nearly identical solid-state structures, as shown in Figure 2.9. These spectra were first published in ref. 37.

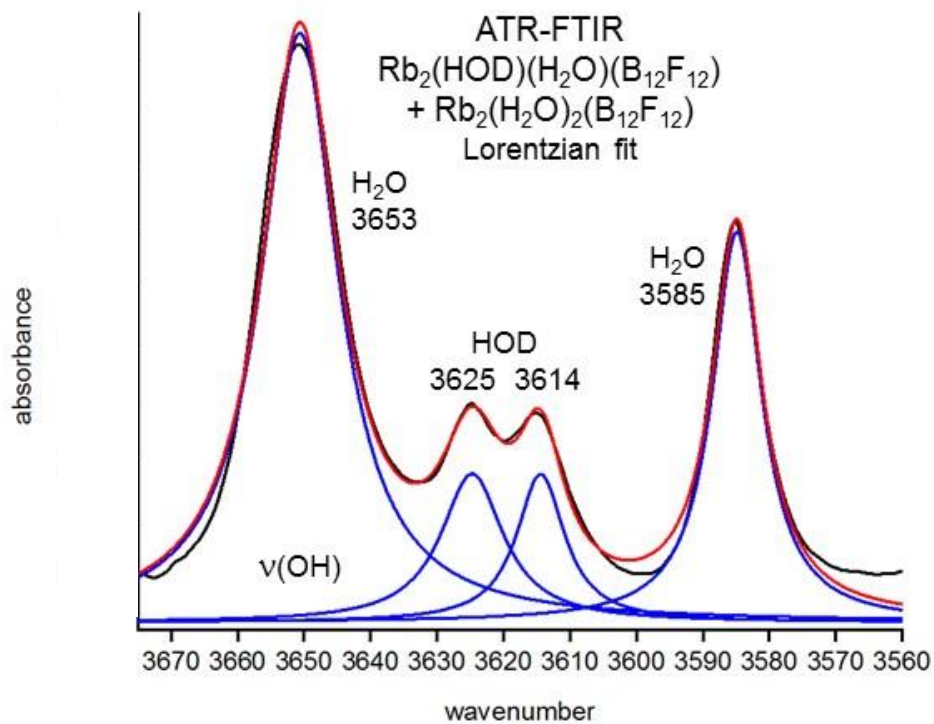


Figure 2.13. The $\nu(\text{OH})$ ATR-FTIR region of a spectrum for a microcrystalline sample containing $\text{Rb}_2(\text{H}_2\text{O})_2(\text{B}_{12}\text{F}_{12})$ and $\text{Rb}_2(\text{HOD})(\text{H}_2\text{O})(\text{B}_{12}\text{F}_{12})$ evaporated on the ZnSe ATR crystal from a 90:10 $\text{H}_2\text{O}:\text{D}_2\text{O}$ solution. Peak positions in cm^{-1} and their assignments are shown. The black trace is the experimental spectrum. The red trace is the sum of the Lorentzian fitted blue traces for the spectrum.

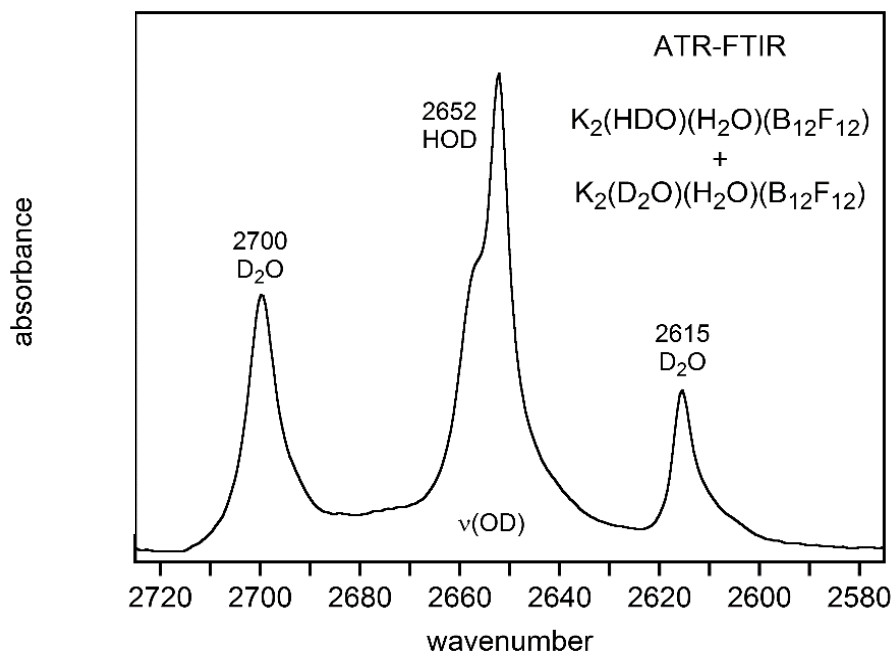


Figure 2.14. ATR-FTIR spectra of microcrystalline samples containing $K_2(\text{HOD})(\text{H}_2\text{O})(\text{B}_{12}\text{F}_{12})$ evaporated on a ZnSe crystal from aqueous solutions containing ca. 10% D_2O . Peak positions in cm^{-1} and their assignments are shown. The samples also contain smaller amounts of $K_2(\text{D}_2\text{O})(\text{H}_2\text{O})(\text{B}_{12}\text{F}_{12})$. The shoulder on the 2652 cm^{-1} band in the spectrum of $K_2(\text{HOD})(\text{H}_2\text{O})(\text{B}_{12}\text{F}_{12})$ indicates that there may be two narrow peaks that are not resolved.

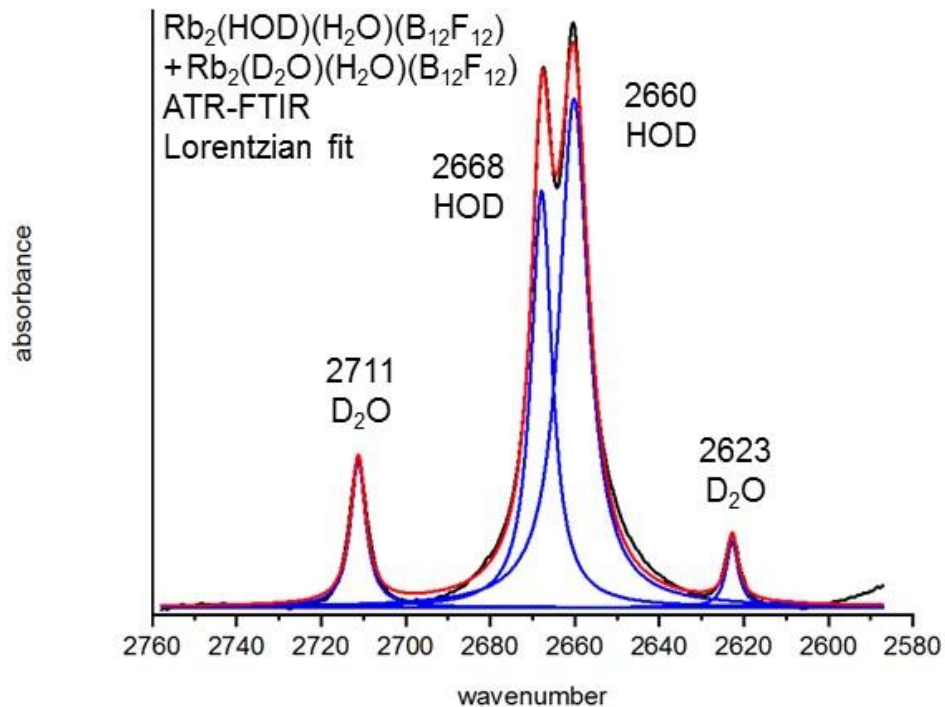


Figure 2.15. The $\nu(\text{OD})$ ATR-FTIR region of a spectrum for a microcrystalline sample containing $\text{Rb}_2(\text{HOD})(\text{H}_2\text{O})(\text{B}_{12}\text{F}_{12})$ and $\text{Rb}_2(\text{D}_2\text{O})(\text{H}_2\text{O})(\text{B}_{12}\text{F}_{12})$ evaporated on the ZnSe ATR crystal from a 90:10 $\text{H}_2\text{O}:\text{D}_2\text{O}$ solution. Peak positions in cm^{-1} and their assignments are shown. The black trace is the experimental spectrum. The red trace is the sum of the Lorentzian fitted blue traces for the spectrum.

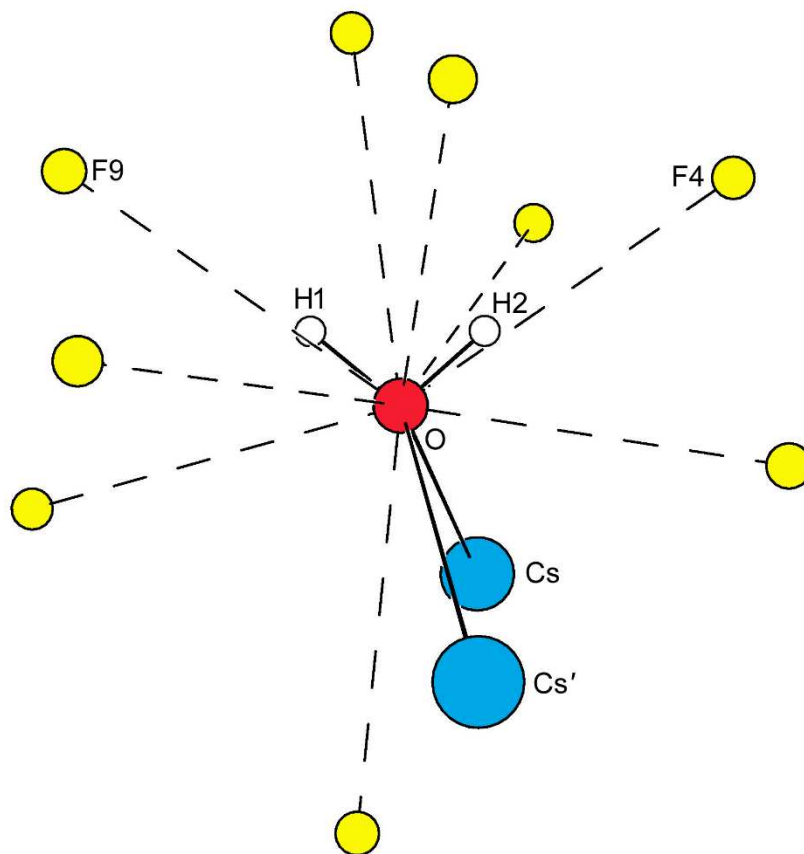


Figure 2.16. A portion of the X-ray crystal structure of $\text{Cs}_2(\text{H}_2\text{O})(\text{B}_{12}\text{F}_{12})$, reported in ref. 67. Selected distances (Å) and angles: Cs–O, 3.137(2) Å; Cs'–O, 3.310(2) Å; O–F4, 3.103(3) Å; O–F9, 2.997(3) Å; O–H2···F4, 148°; O–H1···F9, 157°.

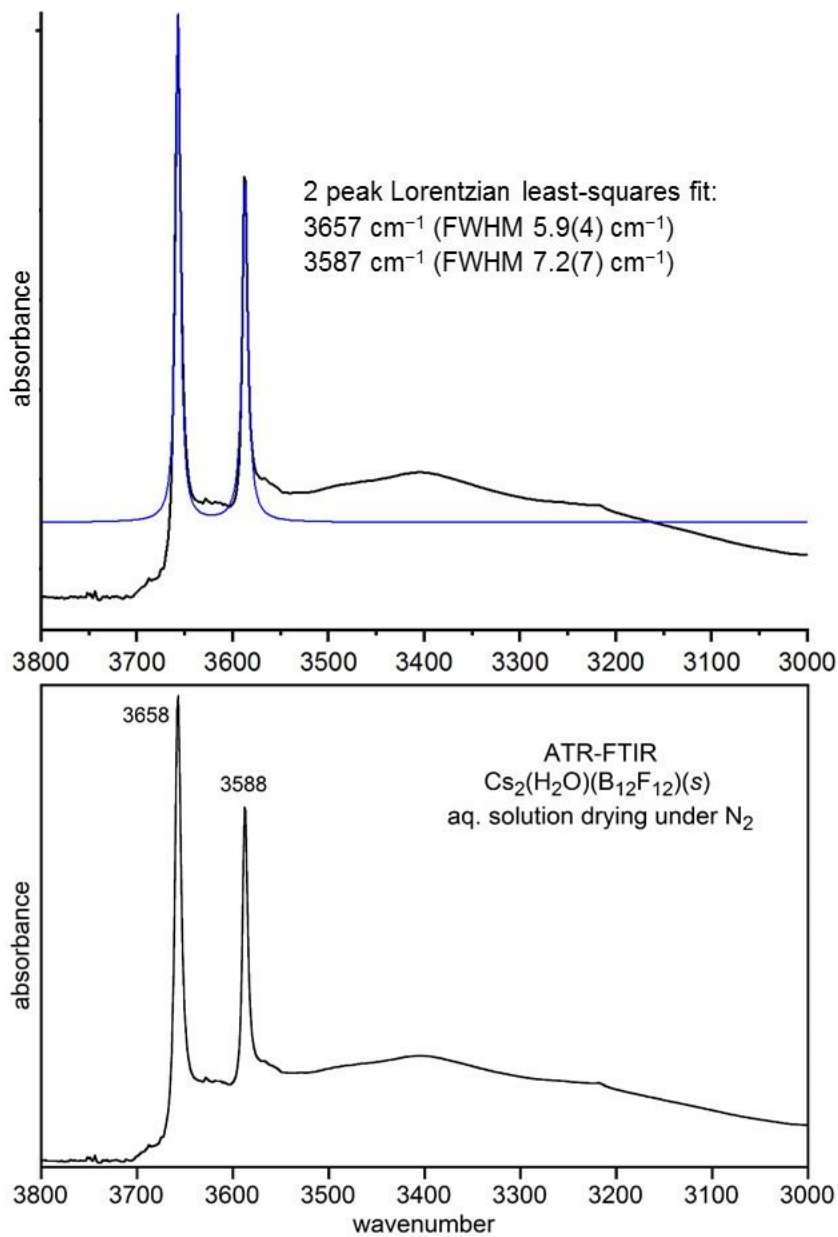


Figure 2.17. Lorentzian least-squares fit to the $\nu(\text{OH})$ bands in the ATR-FTIR spectrum of $\text{Cs}_2(\text{H}_2\text{O})(\text{B}_{12}\text{F}_{12})$. Peak positions in cm^{-1} and their assignments are shown. The spectrum was collected during drying of an aqueous solution under a flow $\text{N}_2(\text{g})$. Only the two sharp peaks were fit to Lorentzian peaks, not the broad surface H_2O band at ca. 3400 cm^{-1} . The blue trace is the sum of the two peak fit.

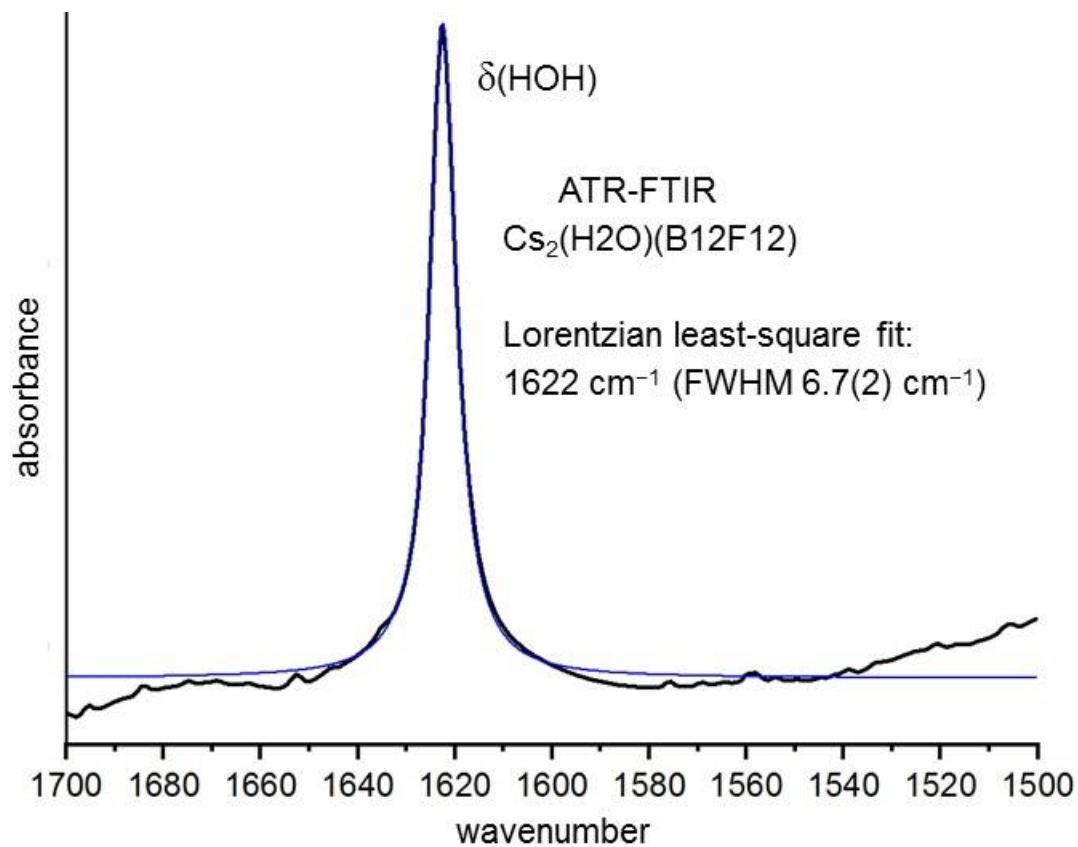


Figure 2.18. Lorentzian least-squares fit to the $\delta(\text{HOH})$ band in the FTIR spectrum of $\text{Cs}_2(\text{H}_2\text{O})(\text{Z})(s)$ while it was evaporating on the ZnSe ATR crystal from an aqueous solution. The blue trace is the fit of the single peak.

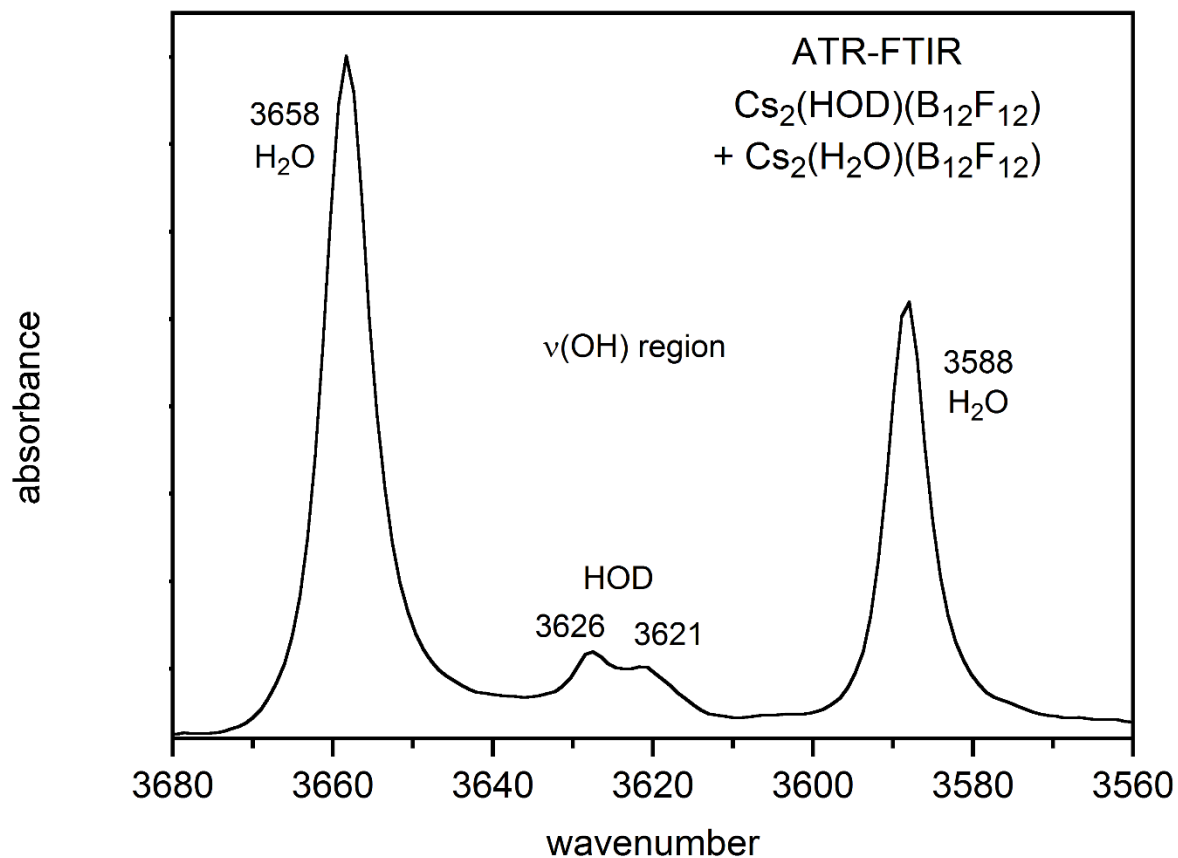


Figure 2.19. ATR-FTIR spectra of a microcrystalline sample containing $\text{Cs}_2(\text{HOD})(\text{B}_{12}\text{F}_{12})$ and $\text{Cs}_2(\text{H}_2\text{O})(\text{B}_{12}\text{F}_{12})$ evaporated on the ZnSe crystal. Peak positions in cm^{-1} and their assignments are shown. The two bands at 3626 and 3621 cm^{-1} assigned to $\text{Cs}_2(\text{HOD})(\text{B}_{12}\text{F}_{12})$ are due to the different $\text{O}(\text{H})\cdots\text{F}$ environments (the $\text{O}(\text{H})\cdots\text{F}$ distances are 2.997(3) and 3.103(3) Å (ref. 67; see Figure 2.16)).

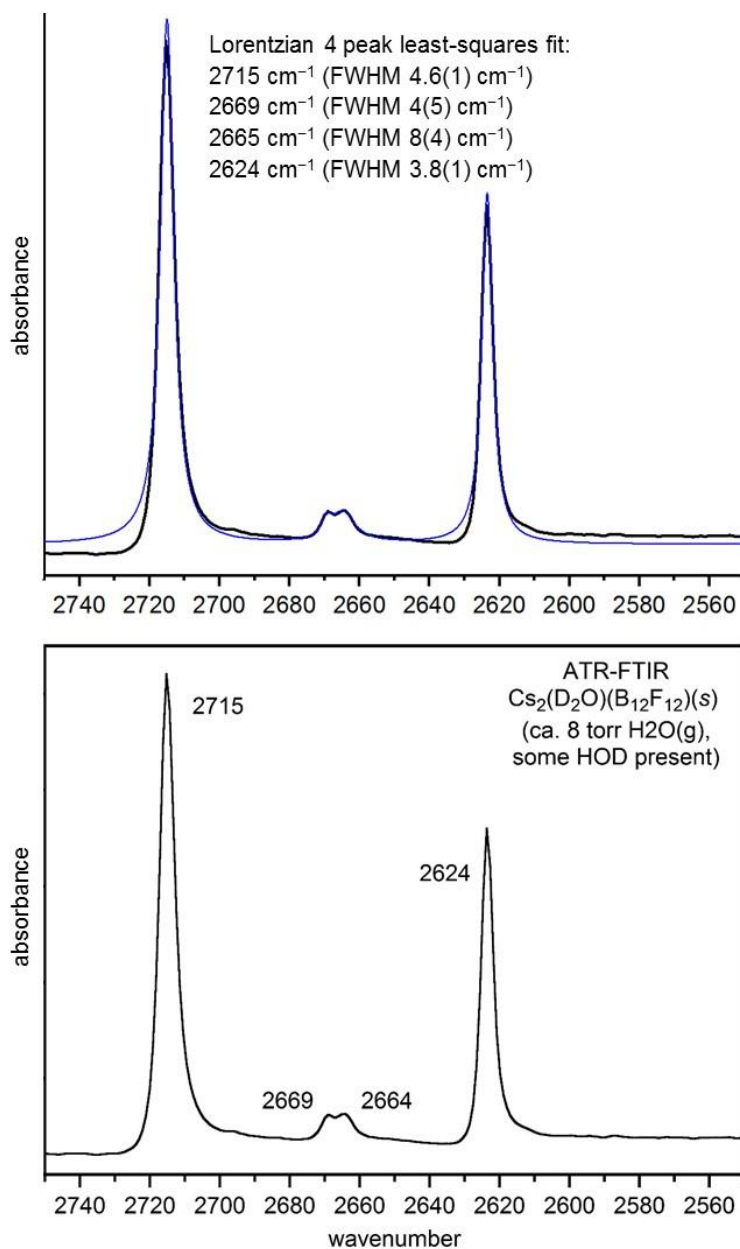


Figure 2.20. Lorentzian least-squares fit to the four $\nu(\text{OD})$ peaks in the FTIR spectrum of $\text{Cs}_2(\text{D}_2\text{O})(\text{Z})(\text{s})$ evaporated on the ZnSe ATR crystal from a D_2O solution and then held under 8 torr $\text{H}_2\text{O}(\text{g})$. Some coordinated HOD appeared during the $\text{H}_2\text{O}/\text{D}_2\text{O}$ exchange, leading to the two weak $\nu(\text{OD})$ peaks at 2669 and 2664 cm^{-1} . The blue trace is the sum of the four peak fit.

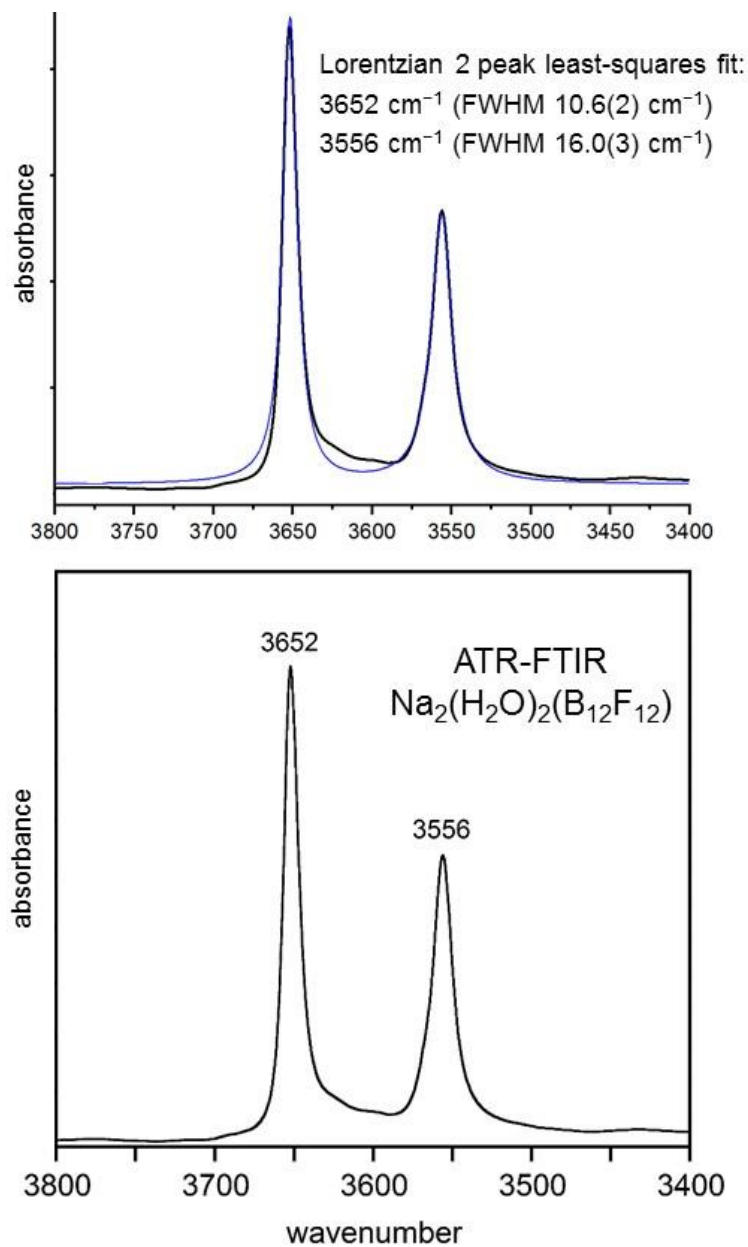


Figure 2.21. Lorentzian least-

squares fit to the $\nu(\text{OH})$ bands in the ATR-FTIR spectrum of $\text{Na}_2(\text{H}_2\text{O})_2(\text{Z})(s)$ evaporated on the ZnSe ATR crystal from an aqueous solution and then held under dry N_2 . The blue trace is the sum of the two peak fit.

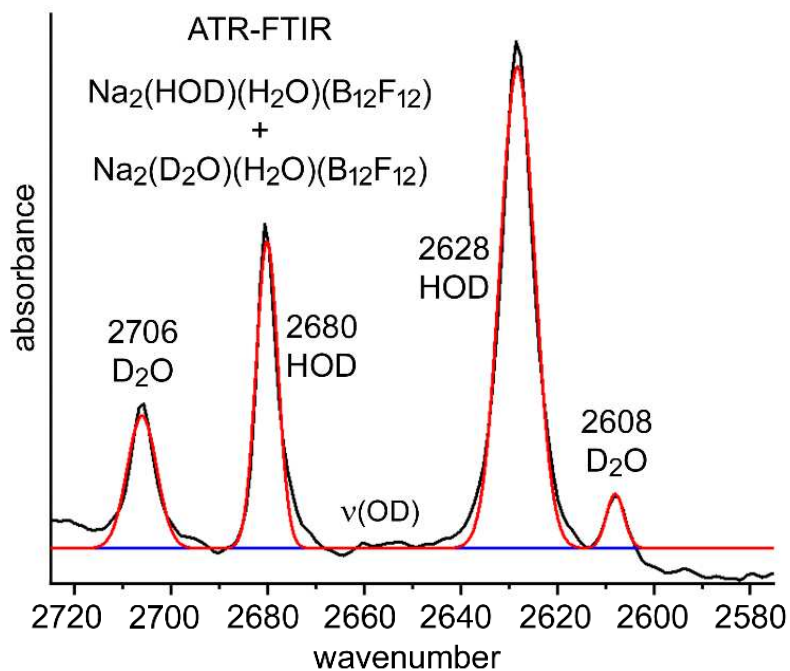


Figure 2.22. ATR-FTIR spectrum (black trace) of a sample containing $\text{Na}_2(\text{HOD})(\text{H}_2\text{O})(\text{B}_{12}\text{F}_{12})$ and $\text{Na}_2(\text{D}_2\text{O})(\text{H}_2\text{O})(\text{B}_{12}\text{F}_{12})$ evaporated on a ZnSe ATR crystal (the predominant species in the sample was $\text{Na}_2(\text{H}_2\text{O})_2(\text{B}_{12}\text{F}_{12})$). Peak positions in cm^{-1} and their assignments (HOD or D_2O) are shown. The red traces are the sums of the four blue Lorentzian fitted peaks.

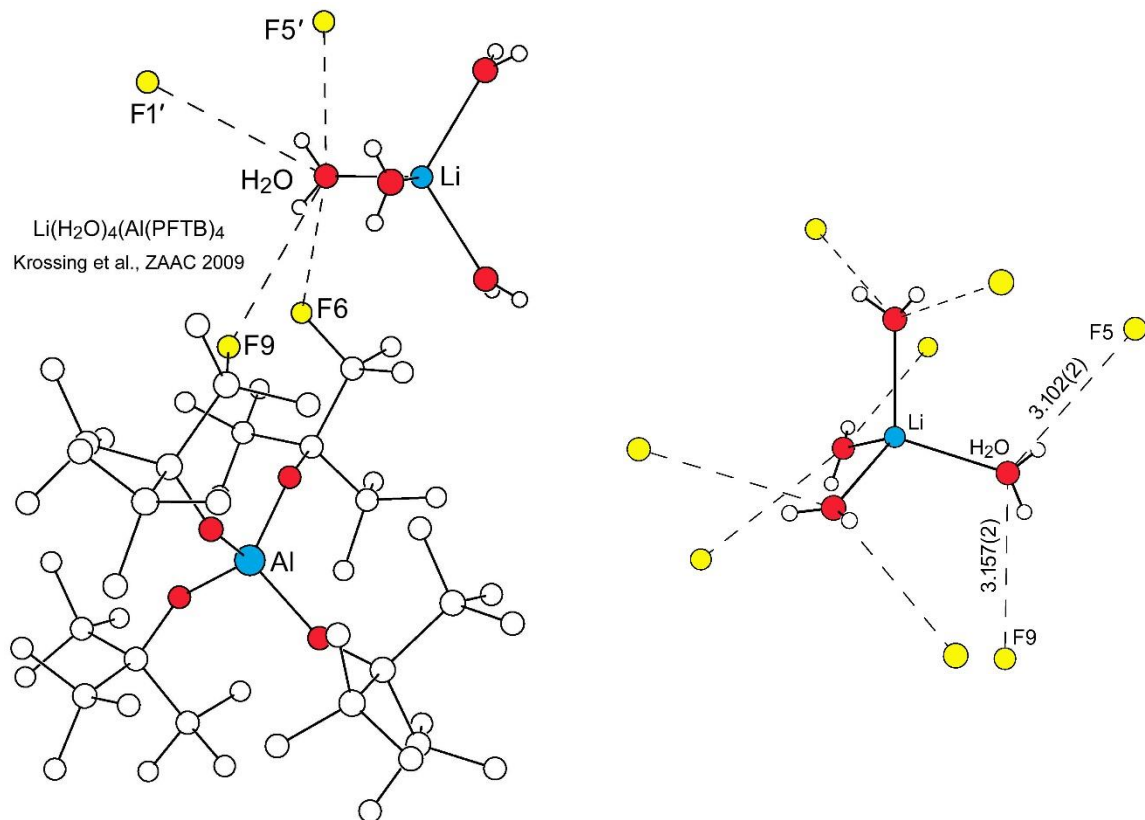


Figure 2.23. Two portions of the X-ray crystal structure of $\text{Li}(\text{H}_2\text{O})_4(\text{Al}(\text{OC}(\text{CF}_3)_3)_4)$, which was published in 2009 in ref. 68. The two $\text{O}(\text{H})\cdots\text{F}$ distances for each of the four symmetry-related coordinated H_2O molecules are 3.102(2) and 3.157(2) Å ($\text{O}-\text{H}\cdots\text{F} = 130$ and 148° , respectively). The left drawing shows that each H_2O molecule has two additional, very weak, $\text{O}(\text{H})\cdots\text{F}$ bonds with distances of 3.296(2) and 3.297(2) Å ($\text{O}-\text{H}\cdots\text{F} = 134$ and 146° , respectively). Therefore, each $\text{O}-\text{H}$ moiety can be thought of as participating in pairs of bifurcated $\text{O}(\text{H})\cdots\text{F}$ hydrogen bonds. By several criteria, including the $\nu(\text{OD})$ value of 2706 cm^{-1} for $\text{Li}(\text{HOD})(\text{H}_2\text{O})_3(\text{Al}(\text{OC}(\text{CF}_3)_3)_4)$, these appear to be the weakest $\text{O}(\text{H})\cdots\text{F}$ hydrogen bonds between an H_2O molecule and an F atom.

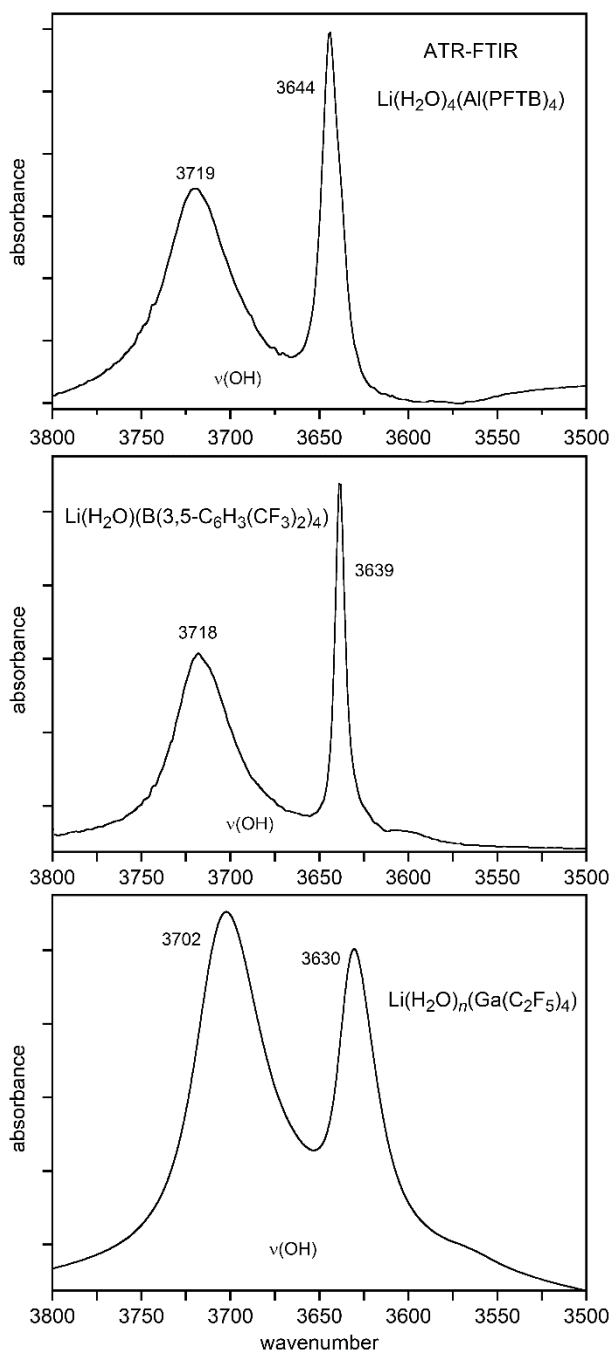


Figure 2.24. ATR-FTIR spectra of microcrystalline samples of $\text{Li}(\text{H}_2\text{O})_4(\text{Al}(\text{OC}(\text{CF}_3)_3)_4)$, $\text{Li}(\text{H}_2\text{O})(\text{B}(3,5\text{-C}_6\text{H}_3(\text{CF}_3)_2)_4)$, and $\text{Li}(\text{H}_2\text{O})_n(\text{Ga}(\text{C}_2\text{F}_5)_4)$. Peak positions in cm^{-1} and their assignments are shown (FWHM values are listed in Table 2.1). The wavenumber (cm^{-1}) ranges are the same and the wavenumber scales are aligned.

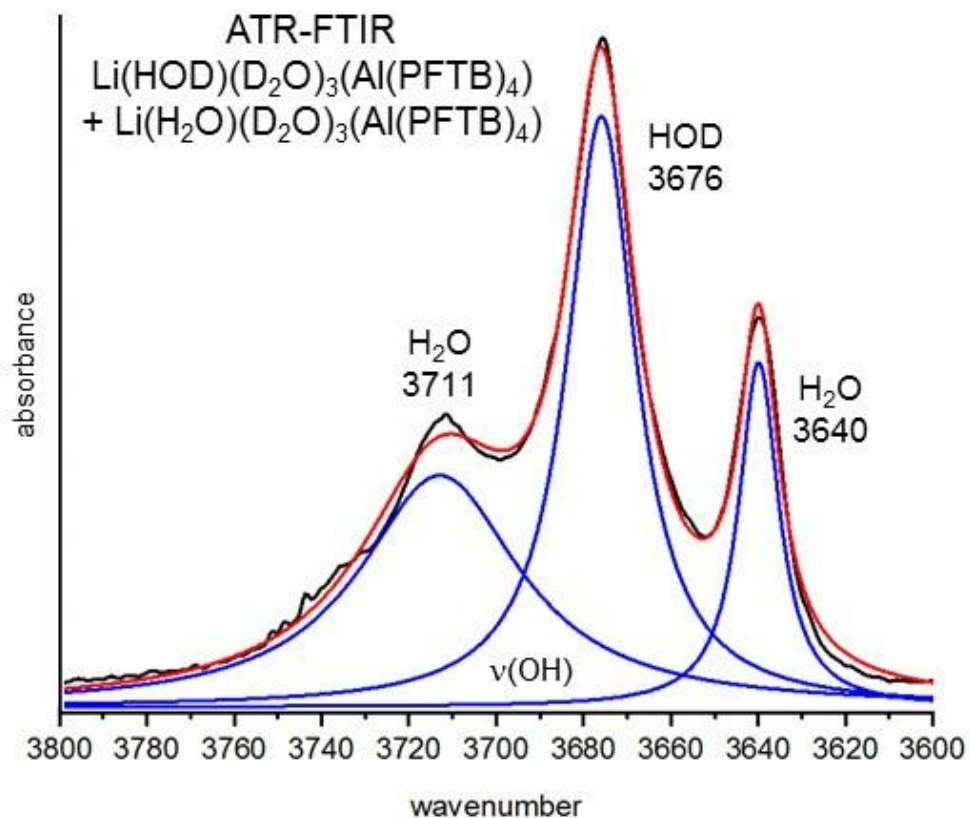


Figure 2.25. The $\nu(\text{OH})$ region of the ATR-FTIR spectrum of a microcrystalline sample containing $\text{Li}(\text{HOD})(\text{D}_2\text{O})_3(\text{Al}(\text{PFTB})_4)$ and $\text{Li}(\text{H}_2\text{O})(\text{D}_2\text{O})_3(\text{Al}(\text{PFTB})_4)$. Peak positions in cm^{-1} and their assignments are shown. The black trace is the experimental spectrum. The red trace is the sum of the Lorentzian fitted blue traces for the spectrum. The FWHM value for the central band at 3676 cm^{-1} is 20 cm^{-1} .

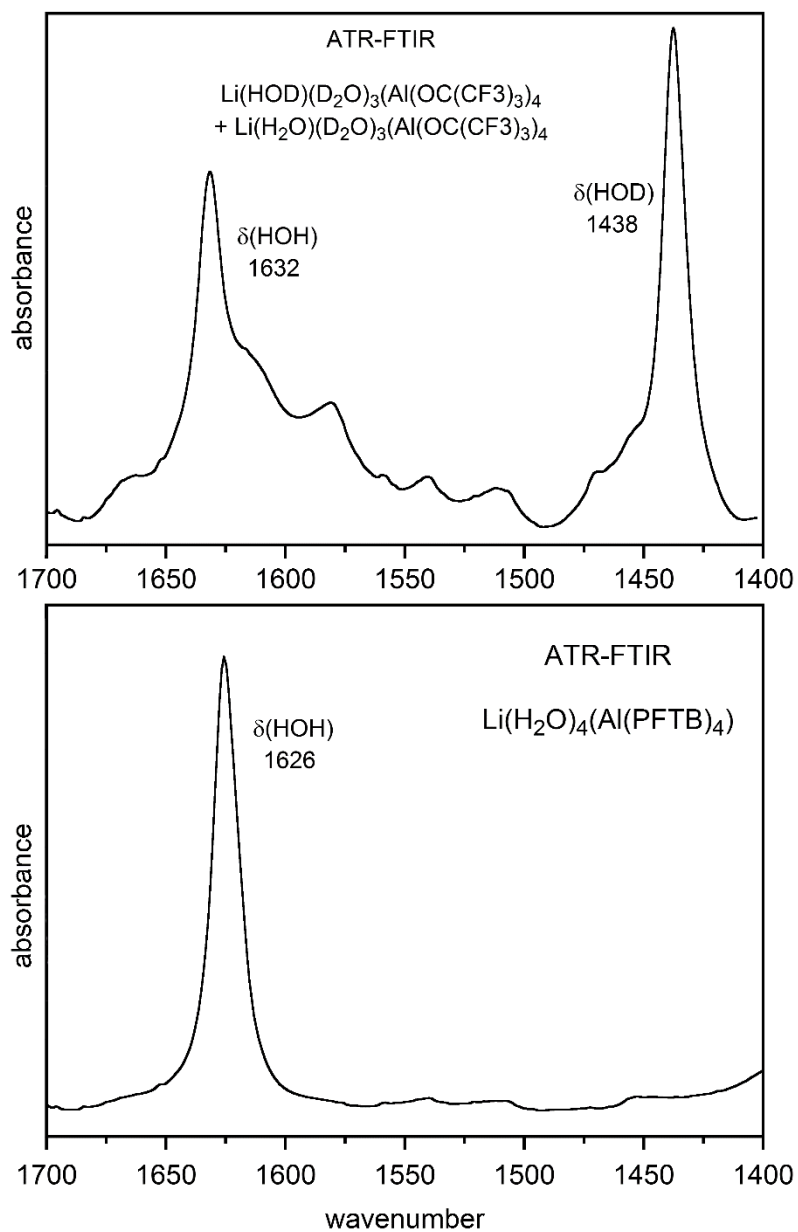


Figure 2.26. The $\delta(\text{HOH})/\delta(\text{HOD})$ regions of ATR-FTIR spectra of microcrystalline samples of a mixture of $\text{Li(HOD)(D}_2\text{O)}_3\text{(Al(PFTB)}_4)$ and $\text{Li(H}_2\text{O)(D}_2\text{O)}_3\text{(Al(PFTB)}_4)$ (top) and $\text{Li(H}_2\text{O)}_4\text{(Al(PFTB)}_4)$ (bottom). Peak positions in cm^{-1} and their assignments are shown.

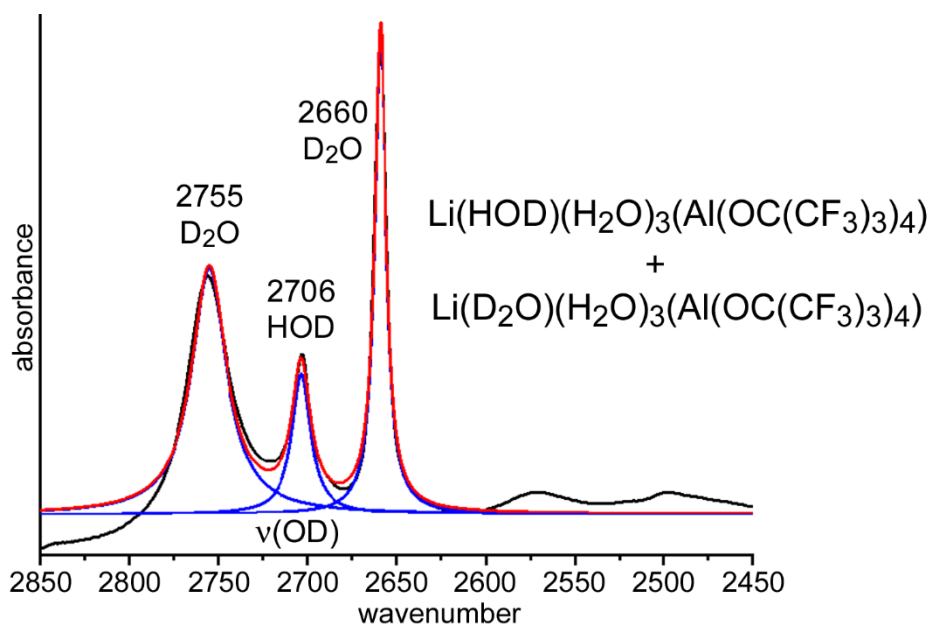


Figure 2.27. ATR-FTIR spectra (black traces) of a sample containing $\text{Li}(\text{HOD})(\text{H}_2\text{O})_3(\text{Al}(\text{OC}(\text{CF}_3)_3)_4)$ and $\text{Li}(\text{D}_2\text{O})(\text{H}_2\text{O})_3(\text{Al}(\text{OC}(\text{CF}_3)_3)_4)$. Peak positions in cm^{-1} and their assignments (HOD or D_2O) are shown (FWHM values are listed in Table 2.1). The red traces are the sums of three blue Lorentzian fitted bands.

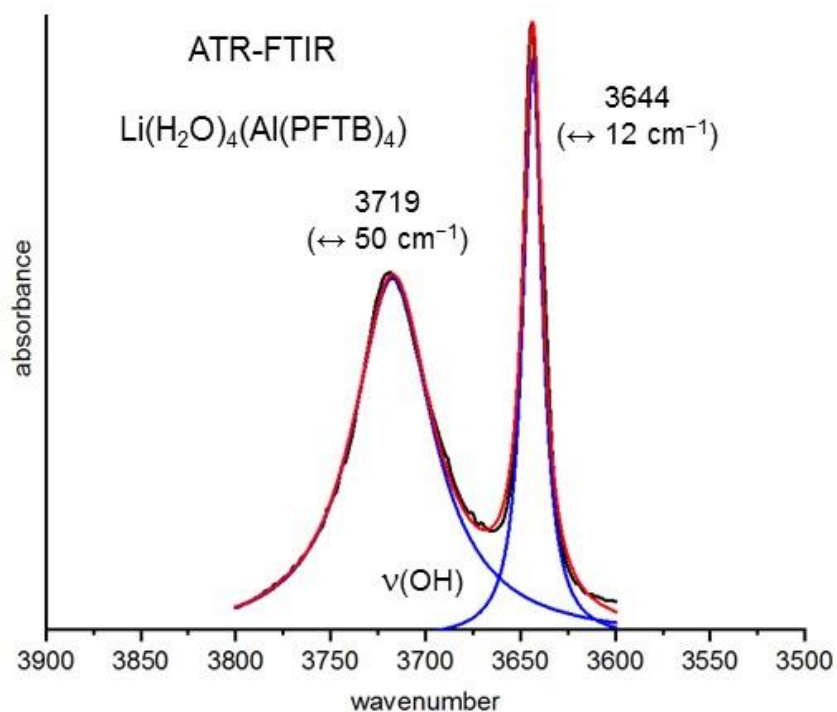


Figure 2.28. The $\nu(\text{OH})$ regions of ATR-FTIR spectra for microcrystalline samples of $\text{Li}(\text{H}_2\text{O})_4(\text{Al}(\text{PFTB})_4)$ on the ZnSe ATR crystal. The black traces are the experimental spectra. The red traces are the sums of the two Lorentzian fitted bands. The band positions and FWHM values (\leftrightarrow) in cm^{-1} are shown.

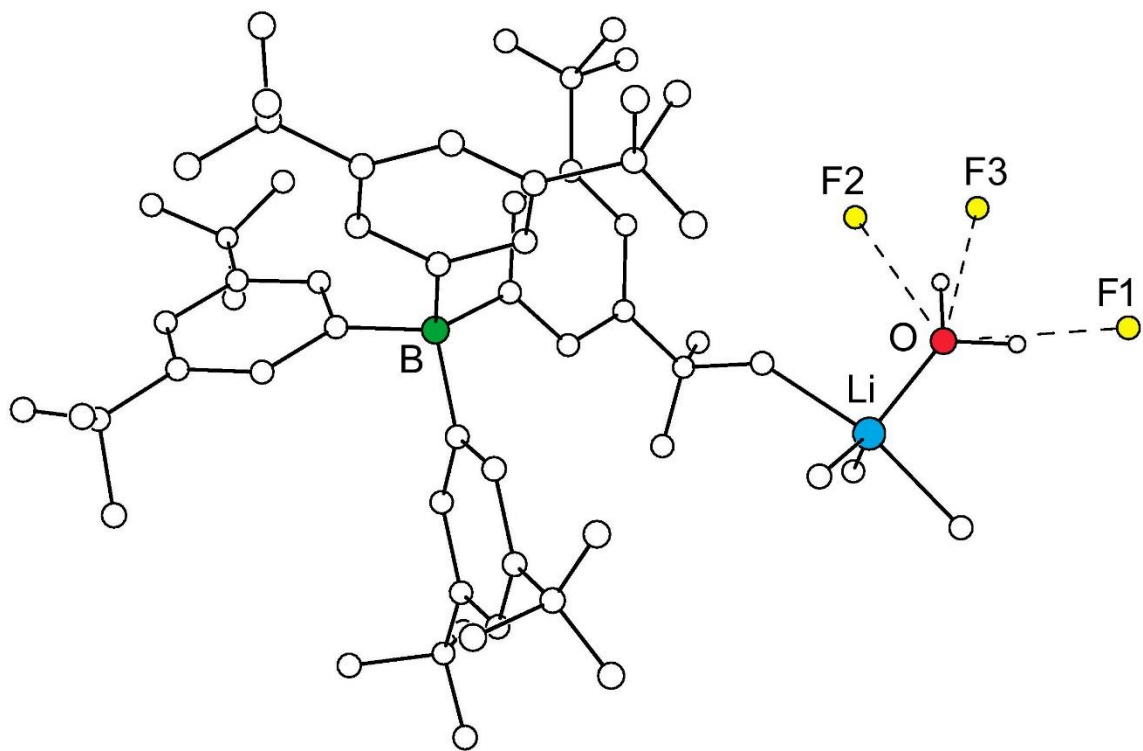


Figure 2.29. A portion of the single-crystal X-ray structure of $\text{Li}(\text{H}_2\text{O})(\text{B}(3,5\text{-C}_6\text{H}_3(\text{CF}_3)_2)_4)$, published in 2019 in ref. 69. The $\text{O}(\text{H})\cdots\text{F}$ distances for the bifurcated hydrogen bond are 2.995(6) and 3.077(6) Å ($\text{O-H}\cdots\text{F} = 140$ and 157° , respectively). The other $\text{O}(\text{H})\cdots\text{F}$ distance is 2.995(6) Å ($\text{O-H}\cdots\text{F} = 167^\circ$).

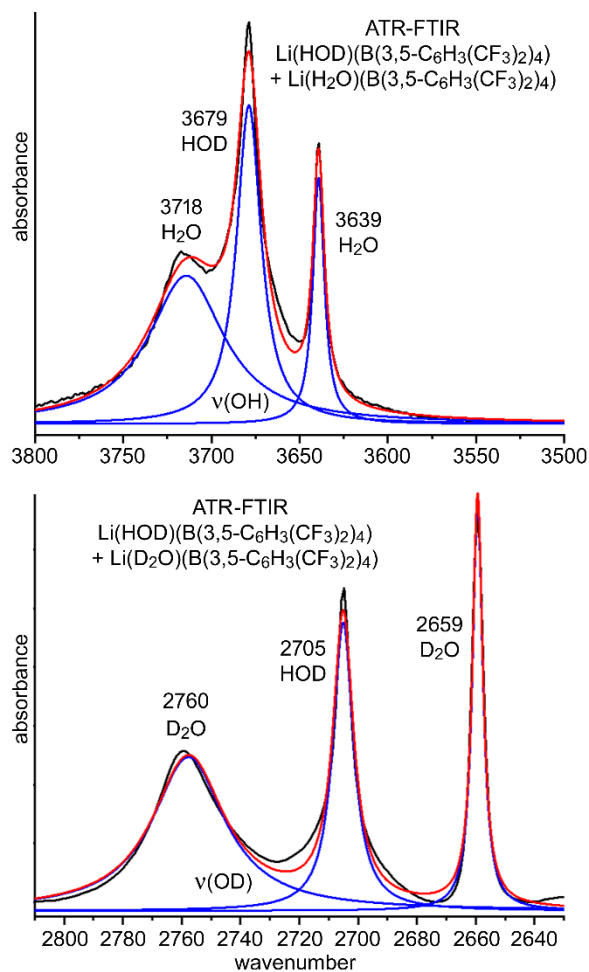


Figure 2.30. ATR-FTIR spectra (black traces; 2 cm^{-1} resolution) of the $\nu(\text{OH})$ region of a microcrystalline sample containing $\text{Li}(\text{HOD})(\text{B}(3,5\text{-C}_6\text{H}_3(\text{CF}_3)_2)_4)$ and $\text{Li}(\text{H}_2\text{O})(\text{B}(3,5\text{-C}_6\text{H}_3(\text{CF}_3)_2)_4)$ pressed onto the ZnSe ATR crystal (top) and the $\nu(\text{OD})$ region of a microcrystalline sample containing $\text{Li}(\text{HOD})(\text{B}(3,5\text{-C}_6\text{H}_3(\text{CF}_3)_2)_4)$ and $\text{Li}(\text{D}_2\text{O})(\text{B}(3,5\text{-C}_6\text{H}_3(\text{CF}_3)_2)_4)$ pressed onto the ZnSe ATR crystal (bottom). Peak positions in cm^{-1} and their assignments (HOD , H_2O , or D_2O) are shown (FWHM values are listed in Table 2.1). The red traces are the sums of the three blue Lorentzian fitted peaks. Full-widths at half-maximum absorbance are listed in Table 2.1.

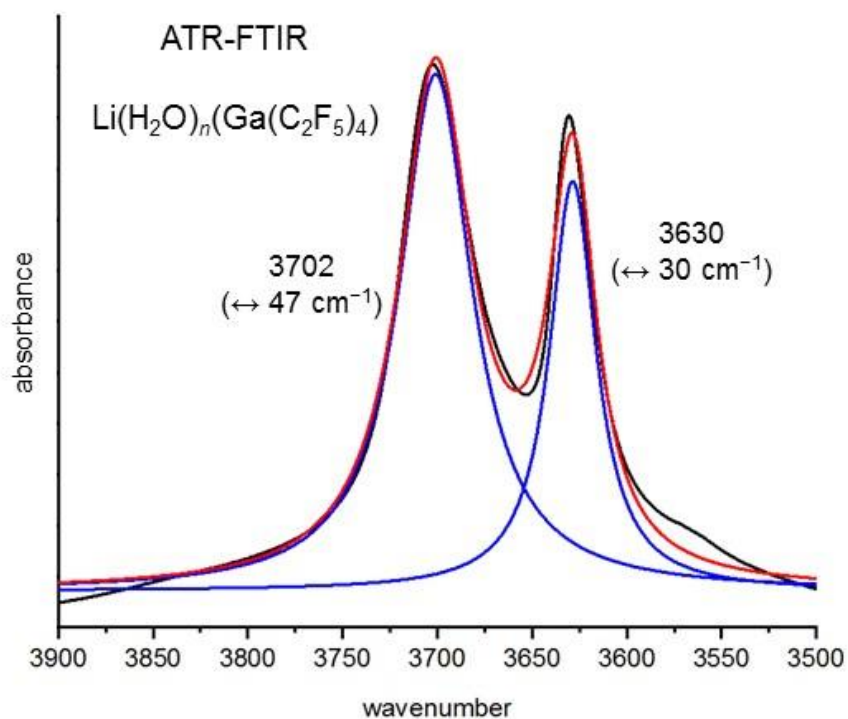


Figure 2.31. The $\nu(\text{OH})$ regions of ATR-FTIR spectra for microcrystalline sample of $\text{Li}(\text{H}_2\text{O})_n(\text{Ga}(\text{C}_2\text{F}_5)_4)$ (bottom) on the ZnSe ATR crystal. The black traces are the experimental spectra. The red traces are the sums of the two Lorentzian fitted bands. The band positions and FWHM values (\leftrightarrow) in cm^{-1} are shown.

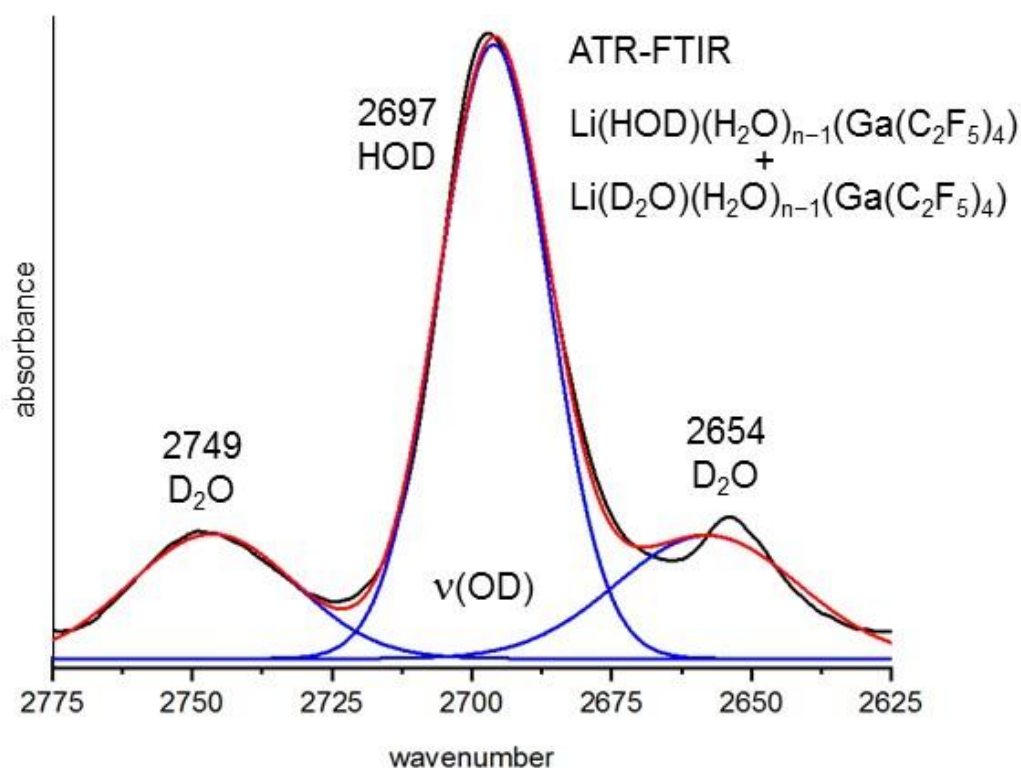


Figure 2.32. ATR-FTIR spectrum of the $\nu(\text{OD})$ region of a microcrystalline sample containing $\text{Li}(\text{HOD})(\text{H}_2\text{O})_{n-1}(\text{Ga}(\text{C}_2\text{F}_5)_4)$ and $\text{Li}(\text{D}_2\text{O})(\text{H}_2\text{O})_{n-1}(\text{Ga}(\text{C}_2\text{F}_5)_4)$ that was evaporated on the ZnSe ATR crystal from an 90:10 $\text{H}_2\text{O}:\text{D}_2\text{O}$ solution (the majority species was $\text{Li}(\text{H}_2\text{O})_n(\text{Ga}(\text{C}_2\text{F}_5)_4)$). Peak positions in cm^{-1} and their assignments are shown. The black trace is the experimental spectrum. The red trace is the sum of the three Gaussian fitted bands (for this spectrum the Gaussian fit was significantly better than the Lorentzian fit). The FWHM for the central 2697 cm^{-1} band is 24 cm^{-1} .

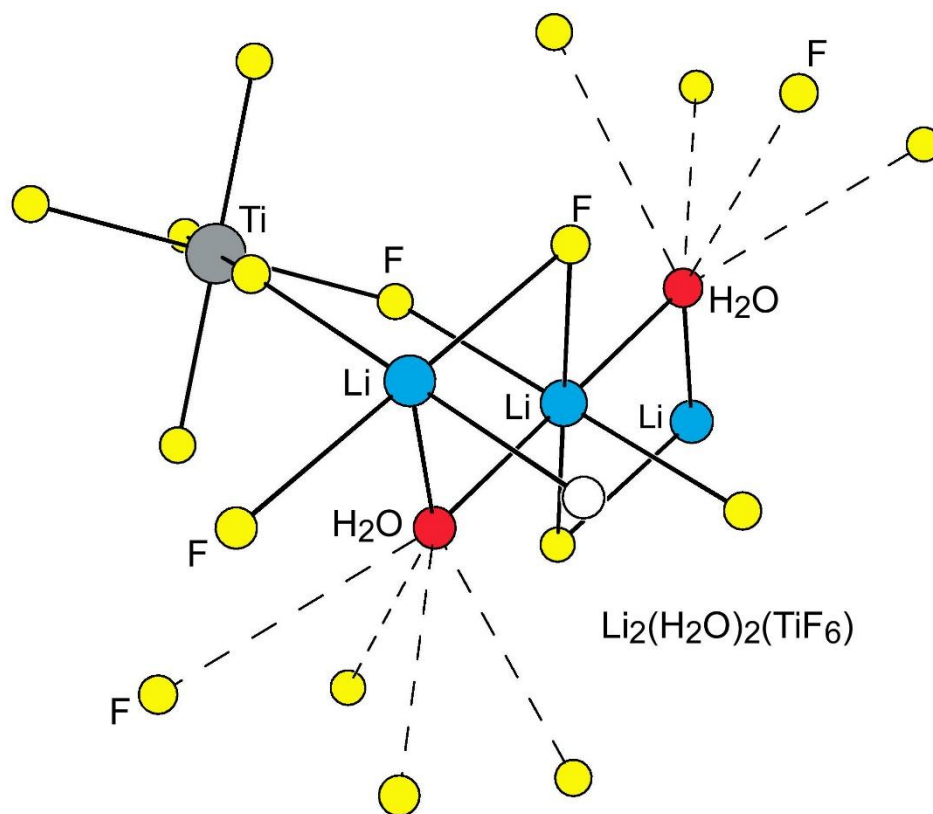


Figure 2.33. A portion of the X-ray crystal structure of $\text{Li}_2(\text{H}_2\text{O})_2(\text{TiF}_6)$ (ref. 70; the H atoms were not located). The $\text{O}(\text{H})\cdots\text{F}$ distances for each of the symmetry related H_2O molecules are $3.007(6) \times 2$ and $3.048(6) \text{ \AA} \times 2$ (presumably both O–H bonds participate in bifurcated hydrogen bonds).

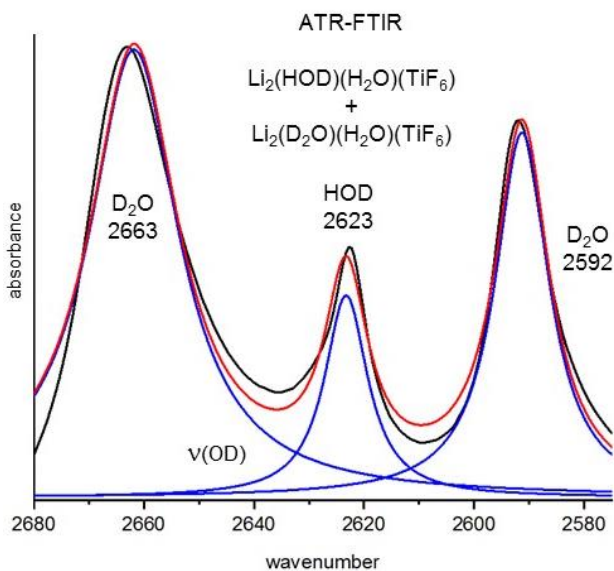
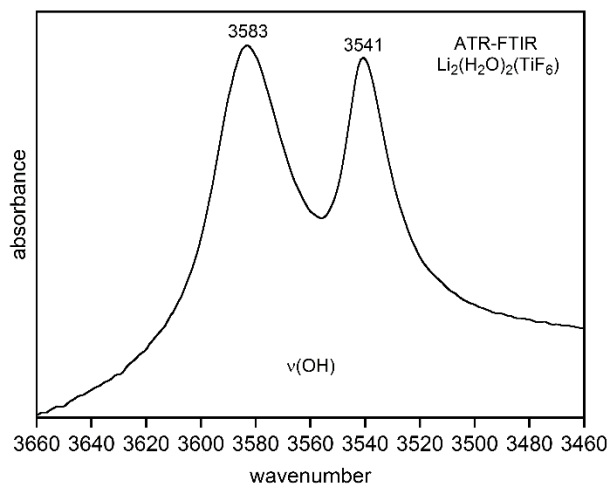


Figure 2.34. FTIR $\nu(\text{OH})$ region for a sample of $\text{Li}_2(\text{H}_2\text{O})_2(\text{TiF}_6)$ (top) and FTIR $\nu(\text{OD})$ region for a sample containing $\text{Li}_2(\text{HOD})(\text{H}_2\text{O})(\text{TiF}_6)$ and $\text{Li}_2(\text{D}_2\text{O})(\text{H}_2\text{O})(\text{TiF}_6)$ (bottom; the predominant species in the sample was $\text{Li}_2(\text{H}_2\text{O})_2(\text{TiF}_6)$). Peak positions in cm^{-1} and their assignments are shown.

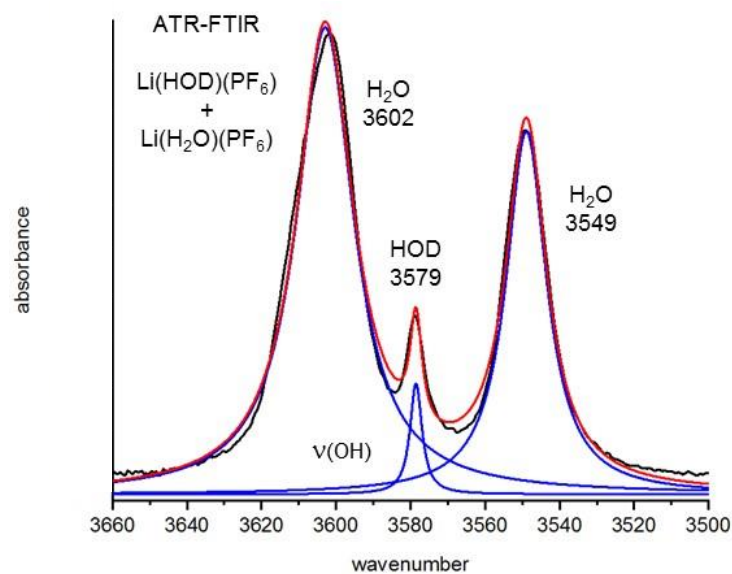
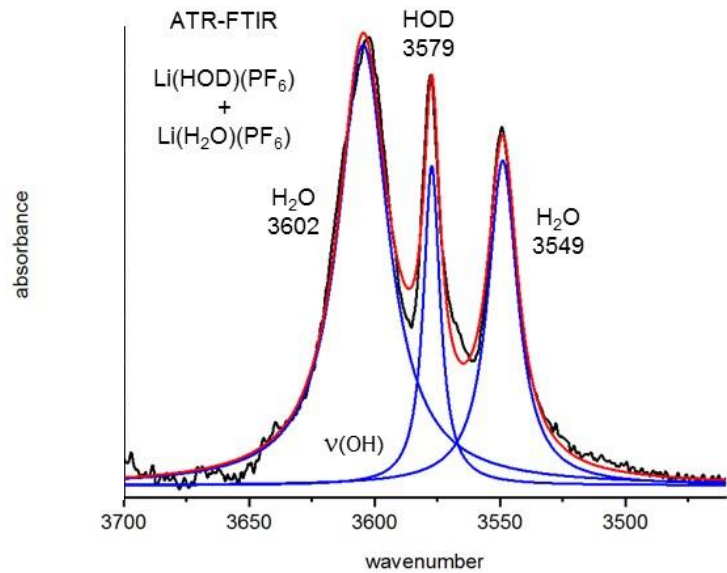


Figure 2.35. The $\nu(\text{OH})$ regions for two samples containing different amounts of $\text{Li}(\text{HOD})(\text{PF}_6)$ and $\text{Li}(\text{H}_2\text{O})(\text{PF}_6)$. Peak positions in cm^{-1} and their assignments are shown. The wavenumber ranges are not equal and the spectra are not aligned.

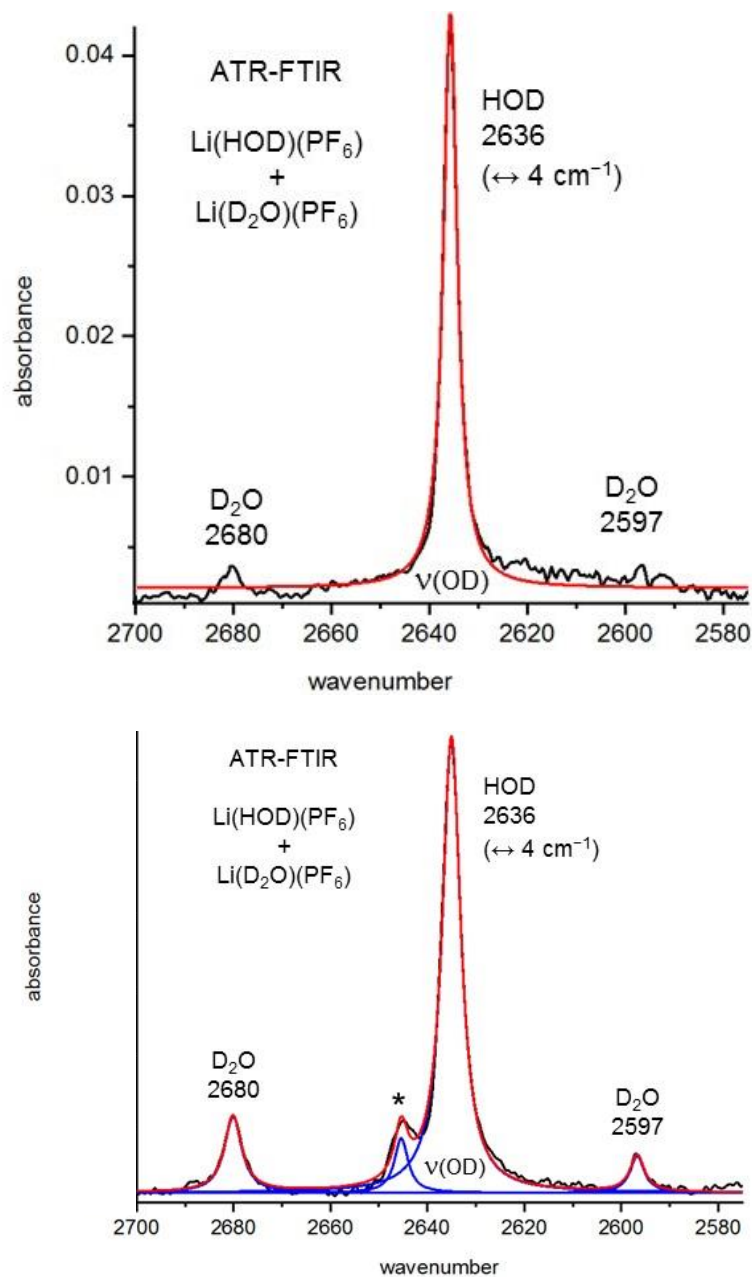


Figure 2.36. FTIR $\nu(\text{OD})$ regions for two samples containing different amounts of $\text{Li}(\text{HOD})(\text{PF}_6)$ and $\text{Li}(\text{H}_2\text{O})(\text{PF}_6)$. Peak positions in cm^{-1} and their assignments are shown. The wavenumber ranges are equal, and the spectra are aligned. The small band at ca. 2645 cm^{-1} in the bottom spectrum is due to an impurity. The FWHM (\leftrightarrow) for the central 2636 cm^{-1} band is 4 cm^{-1} .

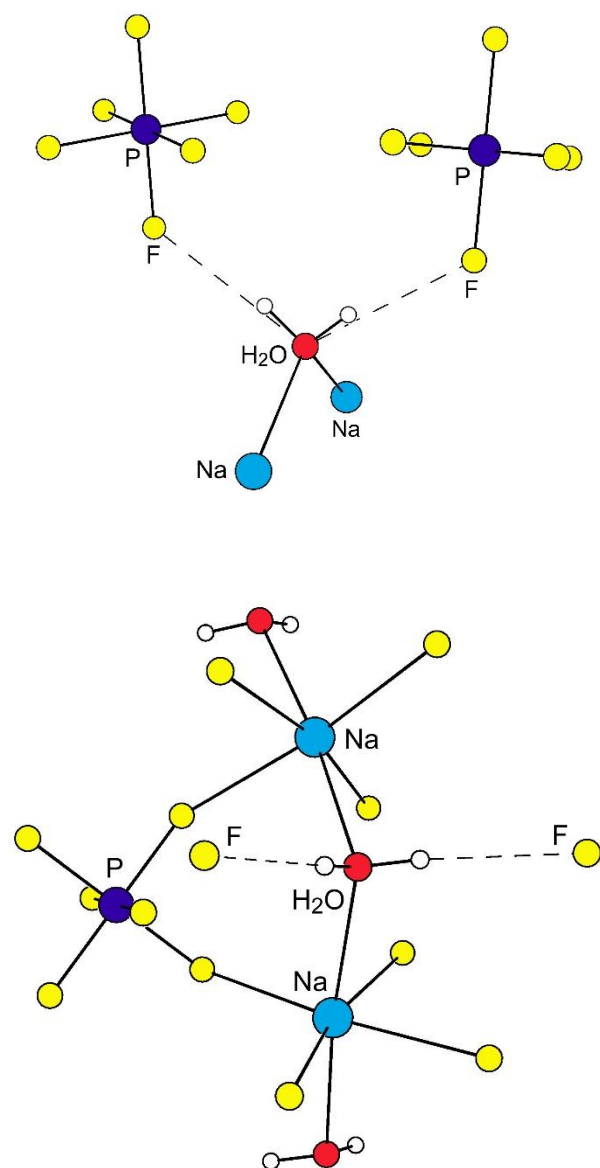


Figure 2.37. Portions of the single-crystal X-ray structure of $\text{Na}(\text{H}_2\text{O})(\text{PF}_6)$, published in 2003 in ref. 71. The Na^+ ions and H_2O molecules are arranged on infinite $[-\text{Na}-\mu-\text{H}_2\text{O}-\text{Na}-\mu-\text{H}_2\text{O}-]_\infty$ chains. The symmetry related $\text{O}(\text{H})\cdots\text{F}$ distances are $3.064(2)$ Å.

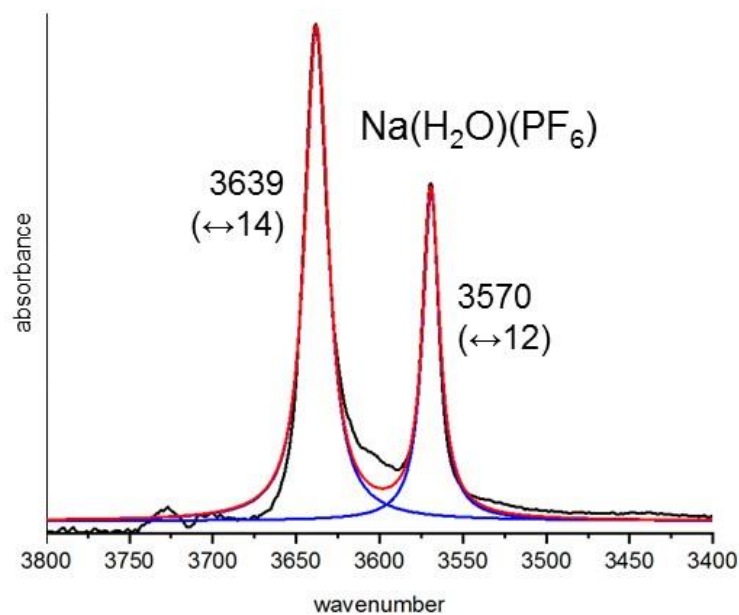


Figure 2.38. ATR-FTIR spectra of microcrystalline sample of $\text{Na}(\text{H}_2\text{O})(\text{PF}_6)$ on the ZnSe ATR crystal. Peak positions and FWHM values (in square brackets) in cm^{-1} are shown.

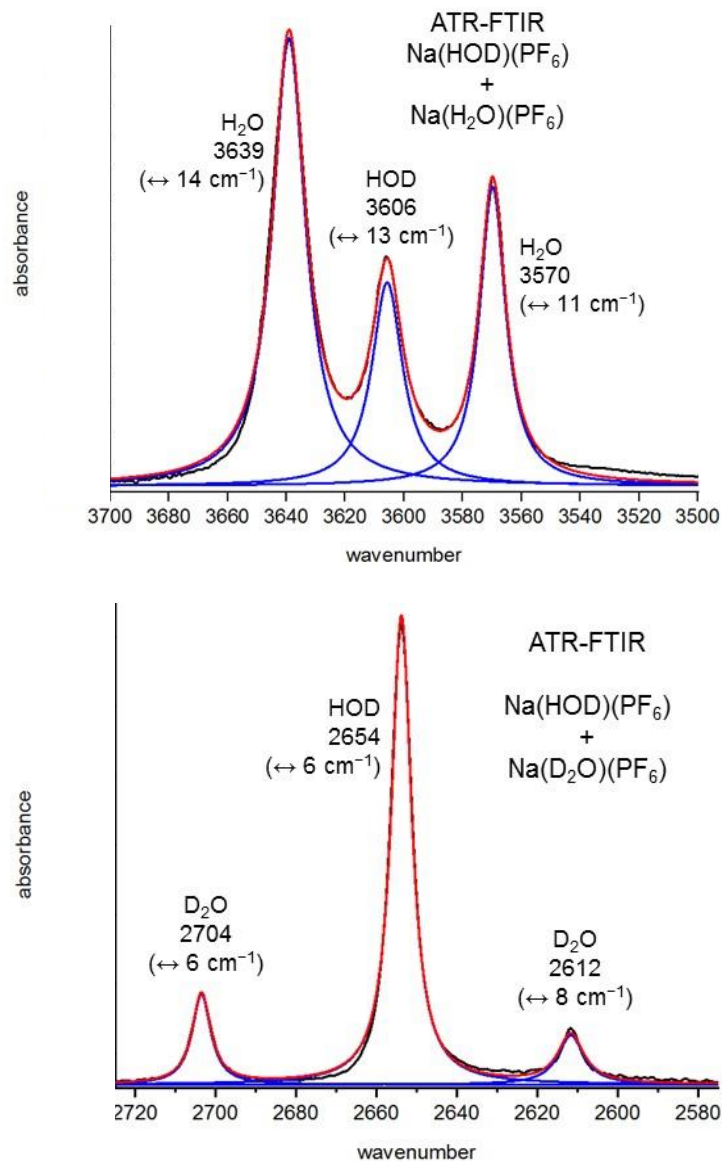


Figure 2.39. The $\nu(\text{OH})$ and $\nu(\text{OD})$ regions of the ATR-FTIR spectrum of a microcrystalline sample containing $\text{Na}(\text{HOD})(\text{PF}_6)$, $\text{Na}(\text{D}_2\text{O})(\text{PF}_6)$, and $\text{Na}(\text{H}_2\text{O})(\text{PF}_6)$. The sample was prepared by exposing anhydrous NaPF_6 to the $\text{H}_2\text{O}/\text{HOD}/\text{D}_2\text{O}$ vapor above a 50:50 $\text{H}_2\text{O}:\text{D}_2\text{O}$ mixture and pressing the resulting solid on the ZnSe ATR crystal of the ATR-FTIR spectrometer. Note that the spectra are not aligned and have different wavenumber ranges. Peak positions and FWHM values (\leftrightarrow) in cm^{-1} are shown. Exchange with atmospheric $\text{H}_2\text{O}(g)$ between the time the sample was removed from the $\text{H}_2\text{O}/\text{HOD}/\text{D}_2\text{O}$ affected the relative intensities of the bands for the $\text{Na}(\text{HOD})(\text{PF}_6)$, $\text{Na}(\text{D}_2\text{O})(\text{PF}_6)$, and $\text{Na}(\text{H}_2\text{O})(\text{PF}_6)$ isotopologs.

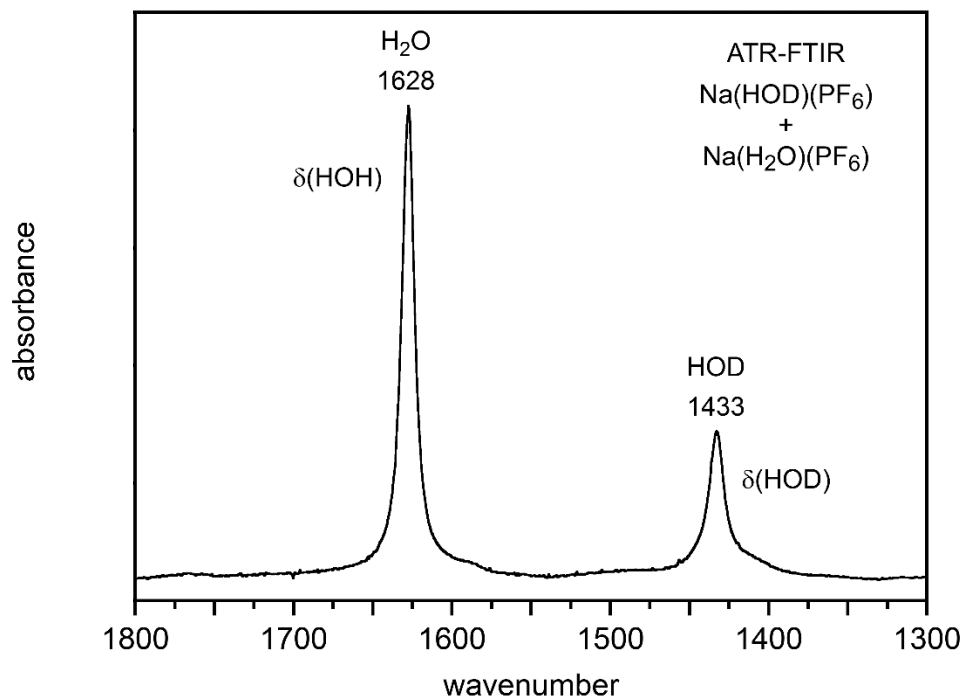


Figure 2.40. The $\delta(\text{HOH})$ and $\delta(\text{HOD})$ region of the ATR-FTIR spectrum of a microcrystalline sample containing $\text{Na}(\text{HOD})(\text{PF}_6)$ and $\text{Na}(\text{H}_2\text{O})(\text{PF}_6)$. The sample was prepared by exposing anhydrous NaPF_6 to the $\text{H}_2\text{O}/\text{HOD}/\text{D}_2\text{O}$ vapor above a 50:50 $\text{H}_2\text{O}:\text{D}_2\text{O}$ mixture and pressing the resulting solid on the ZnSe ATR crystal of the ATR-FTIR spectrometer. Peak positions in cm^{-1} and their assignments are shown. The position of the $\delta(\text{DOD})$ band, at ca. 1200 cm^{-1} , could not be determined precisely because of the overlap of other bands in the spectrum.

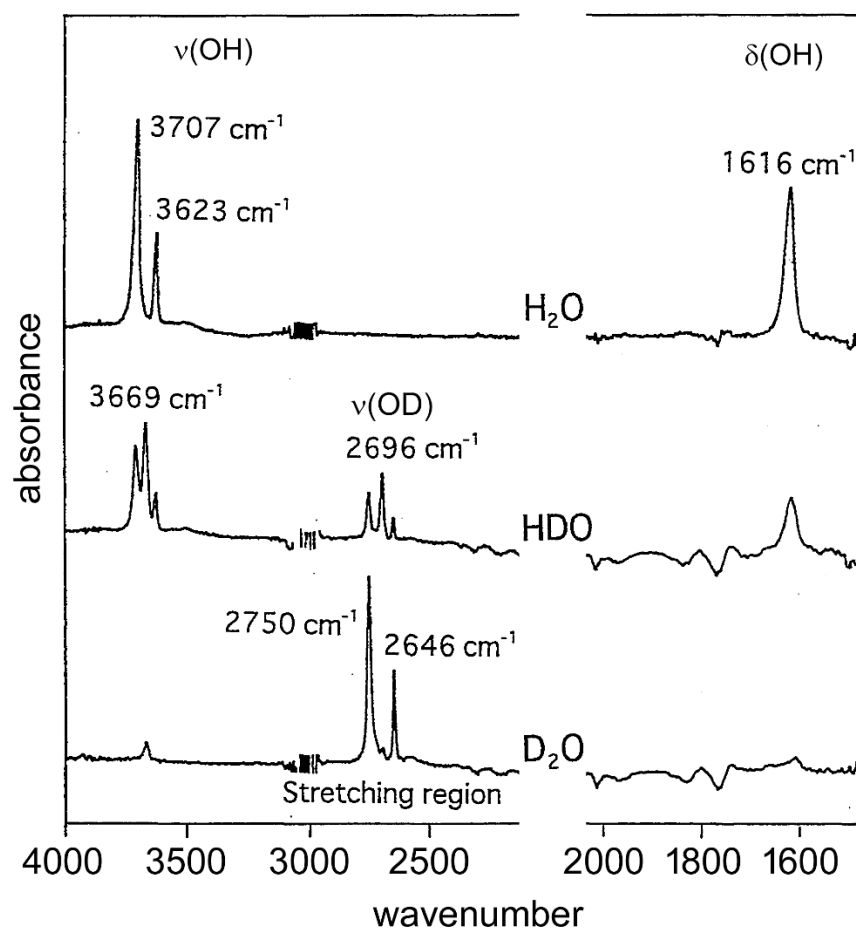


Figure 2.41. FTIR spectra, reported by Kusanagi in ref. 75, of monomeric H₂O, HOD, and D₂O absorbed in polyvinylidene difluoride. Peak positions in cm⁻¹ and their assignments are shown. This figure is adapted from a figure in the cited reference.

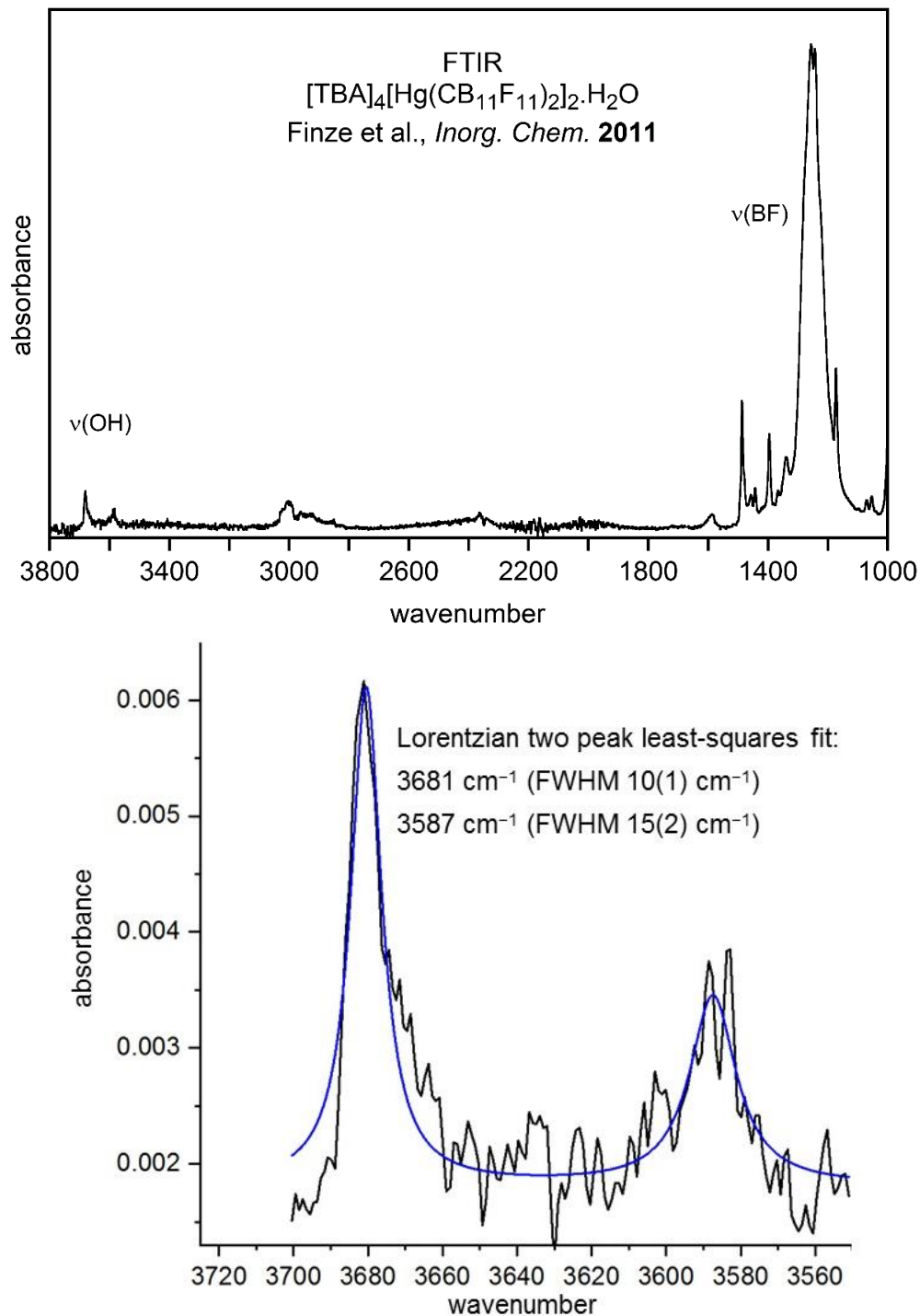


Figure 2.42. The FTIR spectrum of $[\text{NEt}_4]_4[\text{Hg}(\text{CB}_{11}\text{F}_{11})_2]_2 \cdot \text{H}_2\text{O}$ (top; supporting information in ref. 72) and a Lorentzian least-squares fit to the two $\nu(\text{OH})$ bands (bottom; this work). The author thanks Prof. Maik Finze for alerting Professor Steve Strauss to the existence of this spectrum and for providing a digital copy so it could be plotted in absorbance rather than %transmittance.

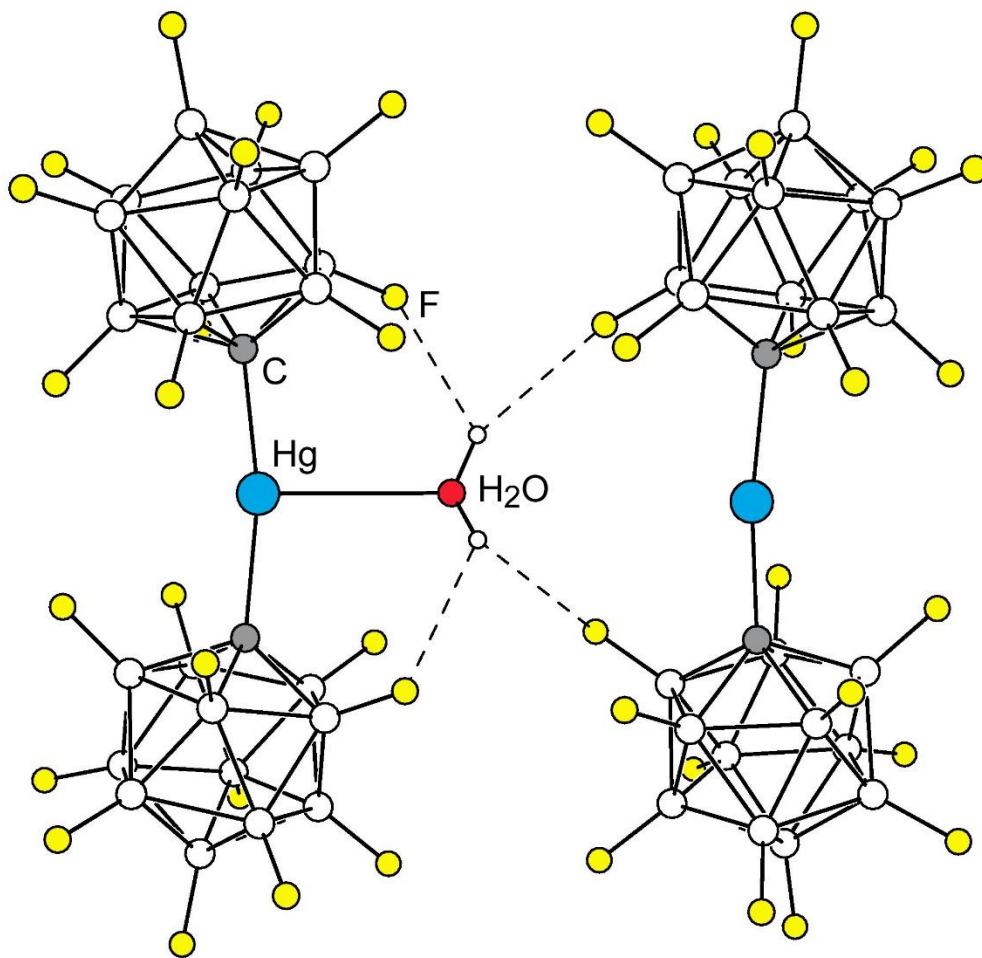


Figure 2.43. Portion of the X-ray crystal structure of $[\text{NEt}_4]_2[\text{Hg}(\text{H}_2\text{O})(\text{CB}_{11}\text{F}_{11})_2]$, published in 2011 in ref. 72. This figure is adapted from a figure in the cited reference.

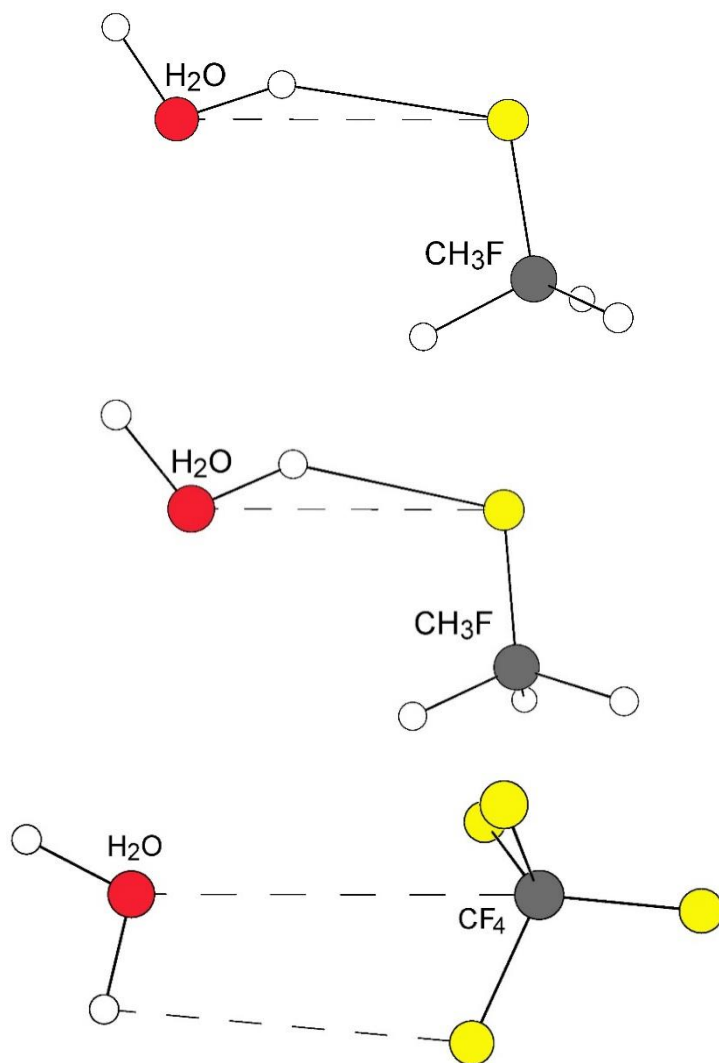


Figure 2.44. The calculated structures of $\text{HOH}\cdots\text{FCH}_3$ and the $\text{H}_2\text{O}-\text{CF}_4$ van der Waals complex. The top drawing is the DFT optimized structure of $\text{HOH}\cdots\text{FCH}_3$ published in ref. 60, with $R(\text{O}\cdots\text{F}) = 2.89 \text{ \AA}$, $R(\text{H}\cdots\text{F}) = 2.00 \text{ \AA}$, and $\text{O}-\text{H}\cdots\text{F} = 153^\circ$. We thank Prof. Yoshisuke Futami for the DFT optimized coordinates for $\text{HOH}\cdots\text{FCH}_3$. The middle drawing is the MP2/aug-cc-pVQZ optimized structure of $\text{HOH}\cdots\text{FCH}_3$ published in ref. 74, with $R(\text{O}\cdots\text{F}) = 2.58 \text{ \AA}$, $R(\text{H}\cdots\text{F}) = 1.99 \text{ \AA}$, and $\text{O}-\text{H}\cdots\text{F} = 146^\circ$. The bottom drawing is the MP2/aug-cc-pVTZ optimized structure of the lowest energy conformation of the $\text{H}_2\text{O}-\text{CF}_4$ van der Waals complex published in ref. 73. This complex does not have an $\text{O}-\text{H}\cdots\text{F}$ hydrogen bond. The author thanks Prof. Krzysztof Mierzwicki for the MP2 optimized coordinates for the $\text{H}_2\text{O}-\text{CF}_4$ complex.

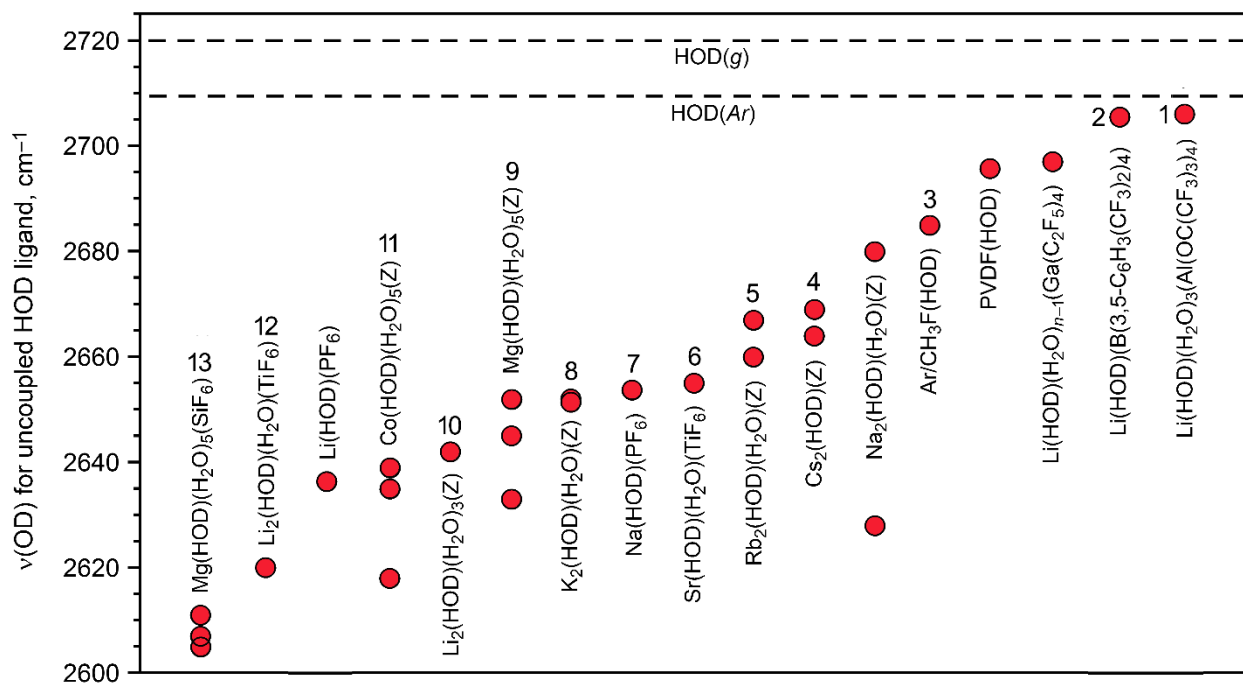


Figure 2.45. Plot of $\nu(\text{OD})$ values in ascending order from left to right for compounds with one HOD molecule per formula unit and $\nu(\text{OD}) > 2600 \text{ cm}^{-1}$ ($Z^{2-} = \text{B}_{12}\text{F}_{12}^{2-}$). The dashed lines are $\nu(\text{OD})$ values for HOD(g) (2720 cm^{-1} , refs. 54–56) and for HOD in an Ar matrix at 17 K (2709 cm^{-1} , refs. ⁷⁶ and ⁷⁸). See Table 2.1 for references.

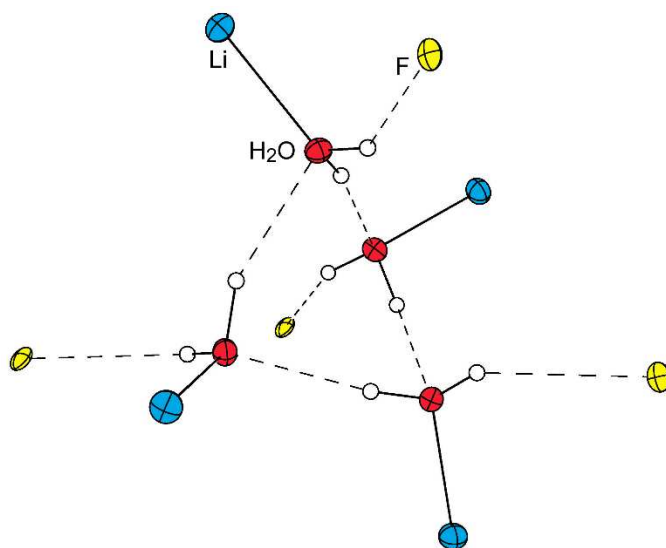
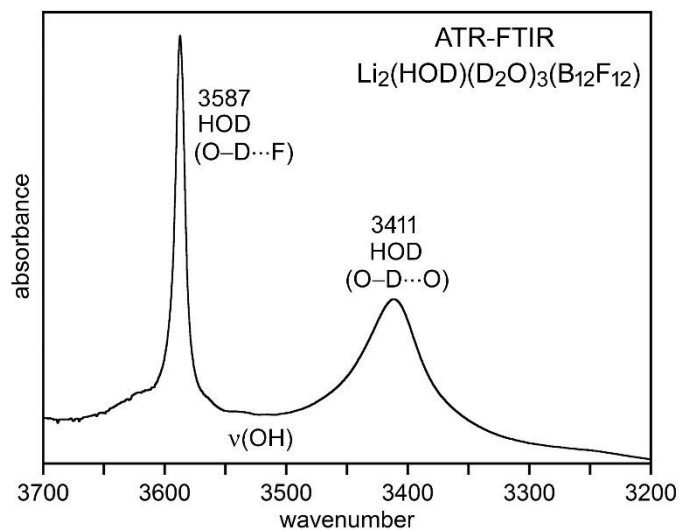


Figure 2.46. The FTIR $\nu(\text{OH})$ region for $\text{Li}_2(\text{HOD})(\text{D}_2\text{O})_3(\text{B}_{12}\text{F}_{12})$ (top; this work and ref. 106; peak positions in cm^{-1} and their assignments are shown) and a portion of the X-ray crystal structure of $\text{Li}_2(\text{H}_2\text{O})_4(\text{B}_{12}\text{F}_{12})$ (bottom; ref. 66; 50% probability ellipsoids except for H atoms). The $\text{O}(\text{H})\cdots\text{F}$ distance for the $\text{O}-\text{H}\cdots\text{F}$ hydrogen bonds is $2.951(3)$ Å. The two $\text{O}(\text{H})\cdots\text{O}$ distances for the $\text{O}-\text{H}\cdots\text{O}$ hydrogen bonds are $2.778(2)$ and $2.785(2)$ Å.

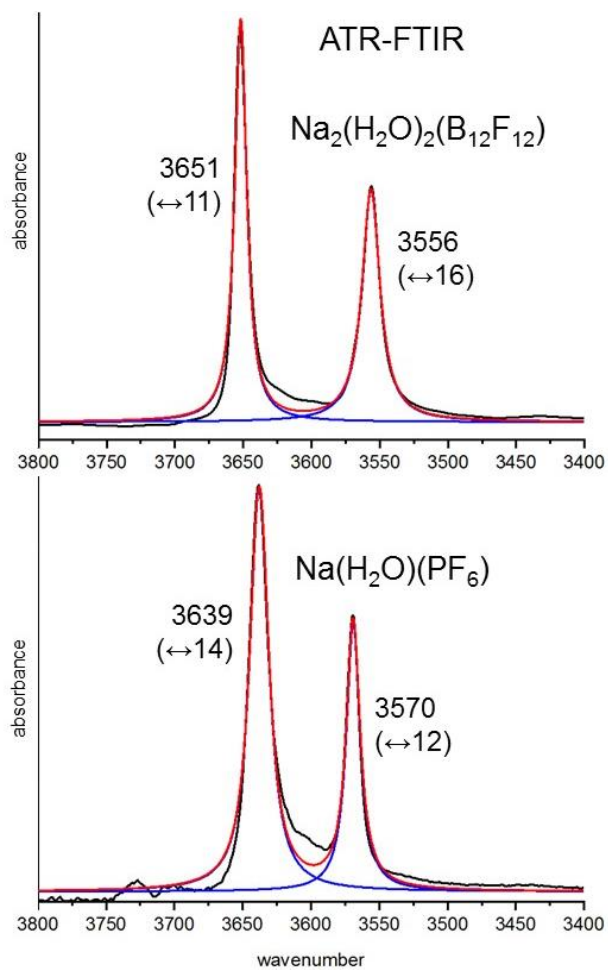


Figure 2.47. ATR-FTIR spectra of microcrystalline samples of $\text{Na}_2(\text{H}_2\text{O})_2(\text{B}_{12}\text{F}_{12})$ (top) and $\text{Na}(\text{H}_2\text{O})(\text{PF}_6)$ (bottom) on the ZnSe ATR crystal. Peak positions and FWHM values (\leftrightarrow) in cm^{-1} are shown. The spectrum of $\text{Na}_2(\text{H}_2\text{O})_2(\text{B}_{12}\text{F}_{12})$ was first reported in ref. 37.

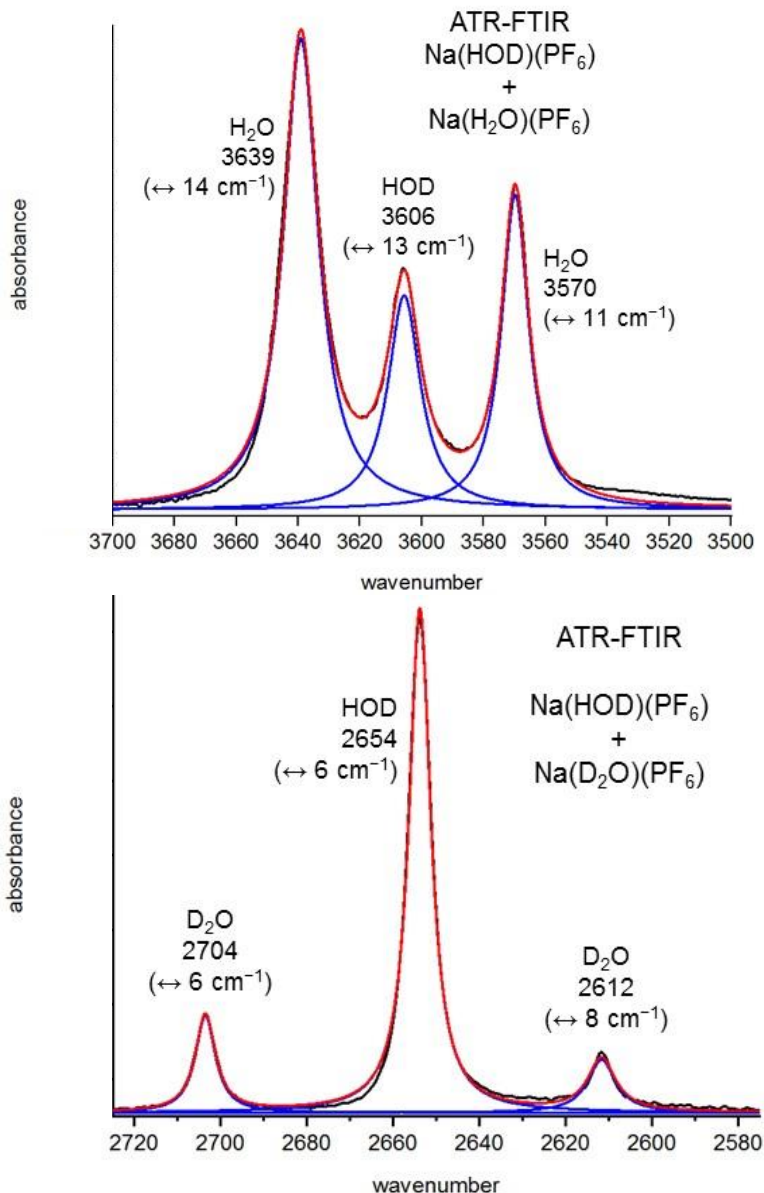
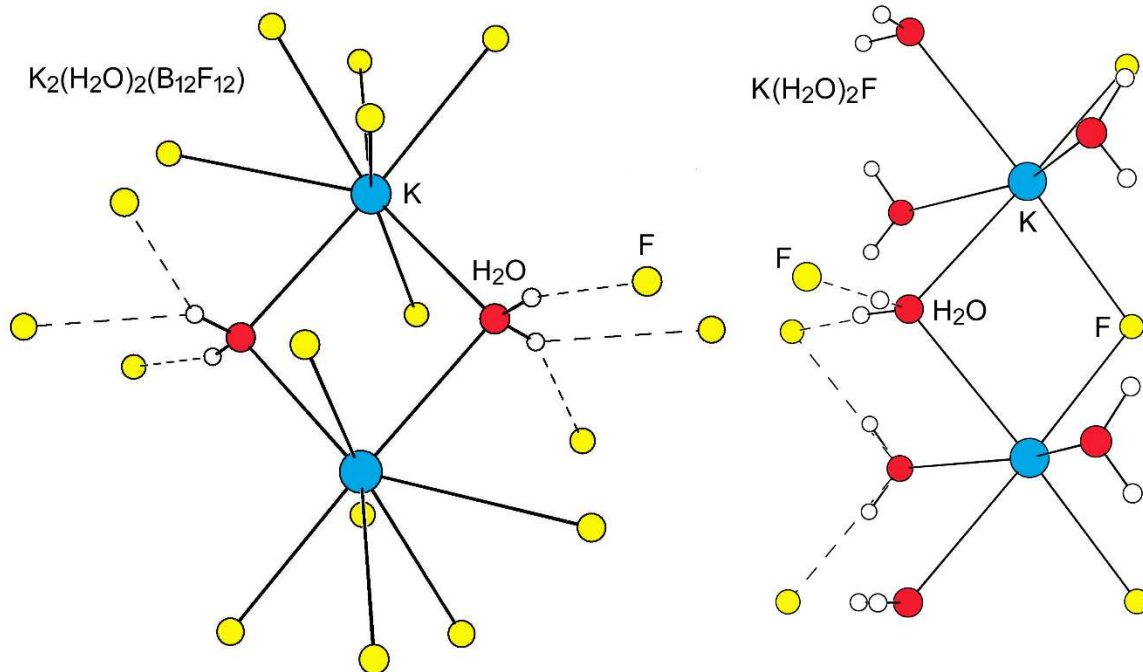


Figure 2.48. The $\nu(\text{OH})$ and $\nu(\text{OD})$ regions of the ATR-FTIR spectrum of a microcrystalline sample containing $\text{Na}(\text{HOD})(\text{PF}_6)$, $\text{Na}(\text{D}_2\text{O})(\text{PF}_6)$, and $\text{Na}(\text{H}_2\text{O})(\text{PF}_6)$. The sample was prepared by exposing anhydrous NaPF_6 to the $\text{H}_2\text{O}/\text{HOD}/\text{D}_2\text{O}$ vapor above a 50:50 $\text{H}_2\text{O}:\text{D}_2\text{O}$ mixture and pressing the resulting solid on the ZnSe ATR crystal of the ATR-FTIR spectrometer. Note that the spectra are not aligned and have different wavenumber ranges. Peak positions and FWHM values (\leftrightarrow) in cm^{-1} are shown. Exchange with atmospheric $\text{H}_2\text{O}(\text{g})$ between the time the sample was removed from the $\text{H}_2\text{O}/\text{HOD}/\text{D}_2\text{O}$ affected the relative intensities of the bands for the $\text{Na}(\text{HOD})(\text{PF}_6)$, $\text{Na}(\text{D}_2\text{O})(\text{PF}_6)$, and $\text{Na}(\text{H}_2\text{O})(\text{PF}_6)$ isotopologs.



M–O	2.7698(6), 2.7726(6) Å	2.714(1), 2.794(1) Å (O1); 2.762(1) Å × 2 (O2)
M–F	6 @ 2.598(1)–3.159(1) Å (ave. 2.857 Å)	2.703(1) Å × 2
O(H)⋯F	2.978(1); 2.972(1), 2.978(1)	2.711 (1) Å × 2 (O1); 2.720(1), 2.741(1) Å (O2)

Figure 2.49. Comparison of portions of the single-crystal X-ray structures of $\text{K}_2(\text{H}_2\text{O})_2(\text{B}_{12}\text{F}_{12})$ (data collection at 110(2) K, ref. 65) and $\text{K}(\text{H}_2\text{O})_2\text{F}$ (data collection at 120 K, ref. 107). The two H_2O molecules in $\text{K}_2(\text{H}_2\text{O})_2(\text{B}_{12}\text{F}_{12})$ are symmetry related. There are two types of H_2O molecules in $\text{K}(\text{H}_2\text{O})_2\text{F}$, those that are *trans* to H_2O (O1) and those that are *trans* to F (O2).

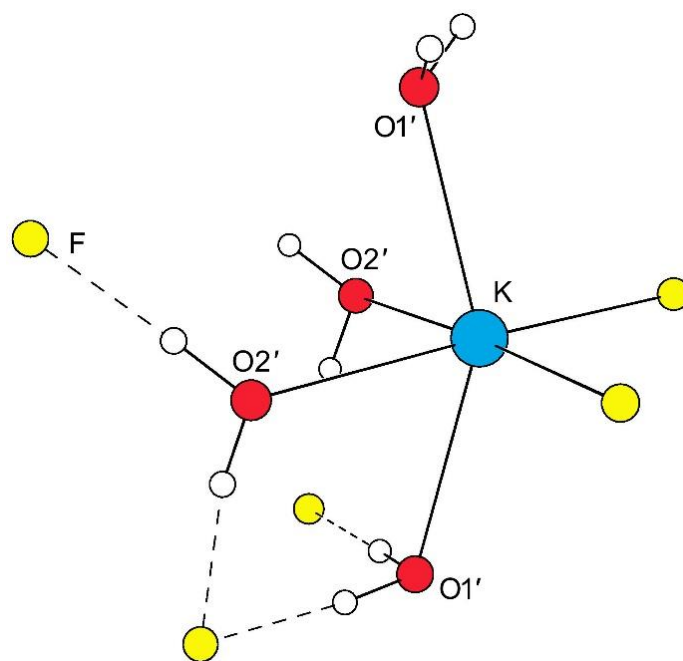


Figure 2.50. A portion of the neutron diffraction structure of $\text{K}(\text{H}_2\text{O})_2\text{F}$ (ref. 107). The dashed lines connect O with either O or F atoms. Selected distances and angles, including those involving the H atoms in the neutron diffraction structure, are listed in Table 2.3, below.

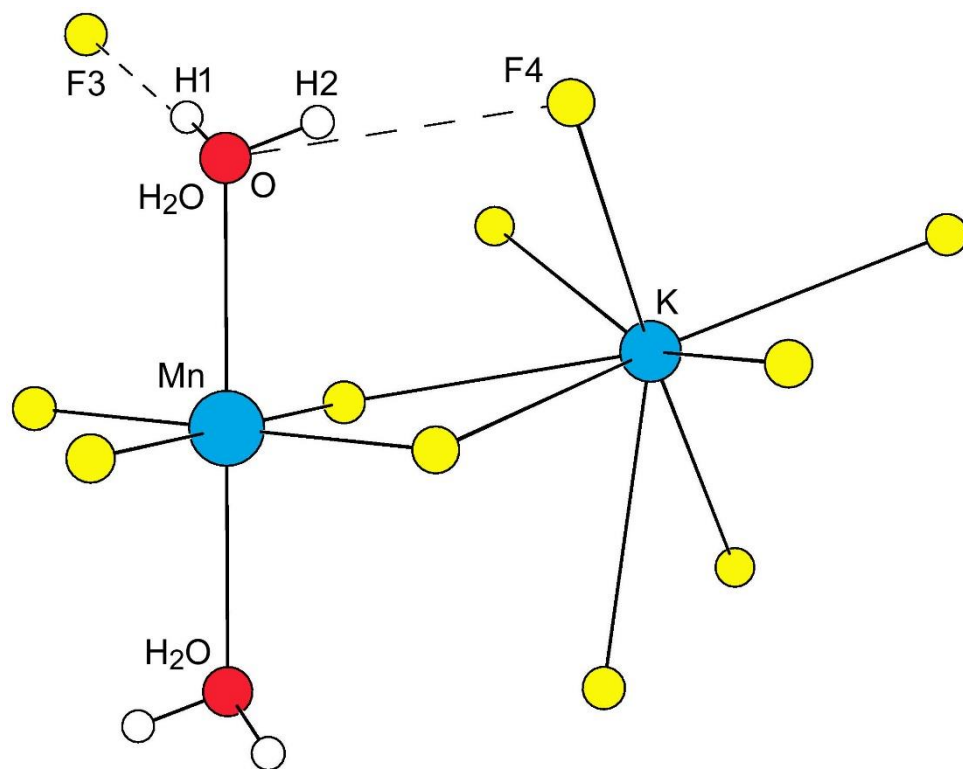


Figure 2.51. A portion of the X-ray crystal structure of $\text{K}(\text{H}_2\text{O})(\text{MnF}_4)$ (ref. 108). Selected distances and angles: $\text{O}\cdots\text{F}_3$, 2.682(3) Å; $\text{O}\cdots\text{F}_4$, 2.820(2) Å; $\text{O}-\text{H}_1\cdots\text{F}_3$, 168°; $\text{O}-\text{H}_2\cdots\text{F}_4$, 154°. Only one of the two unique Mn atoms is shown (the other Mn atom is not coordinated to H_2O molecules).

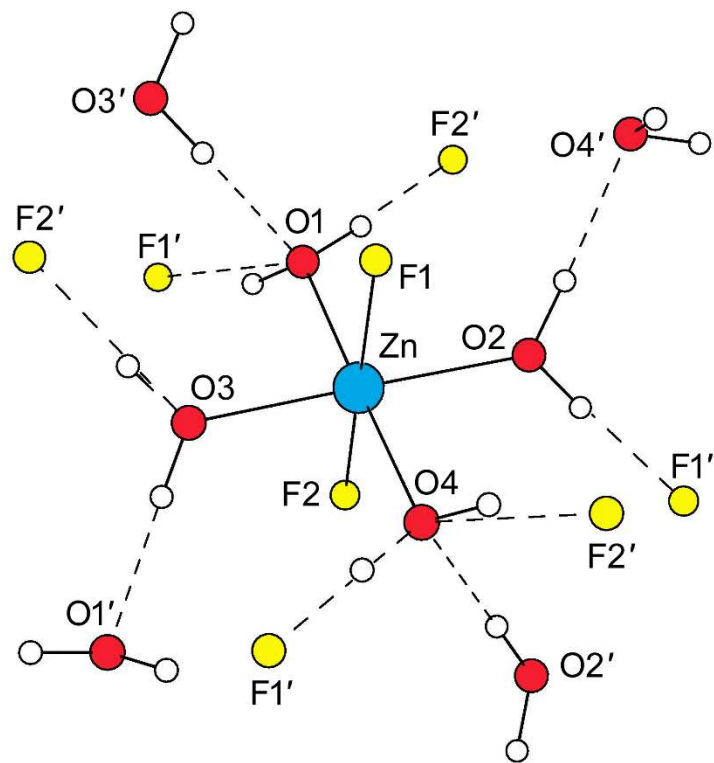


Figure 2.52. A portion of the neutron diffraction crystal structure of $\text{Zn}(\text{H}_2\text{O})_4\text{F}_2$ (ref. 109). Selected The dashed lines connect O with either O or F atoms. Distances and angles involving H atoms are listed in Table 2.4, below.

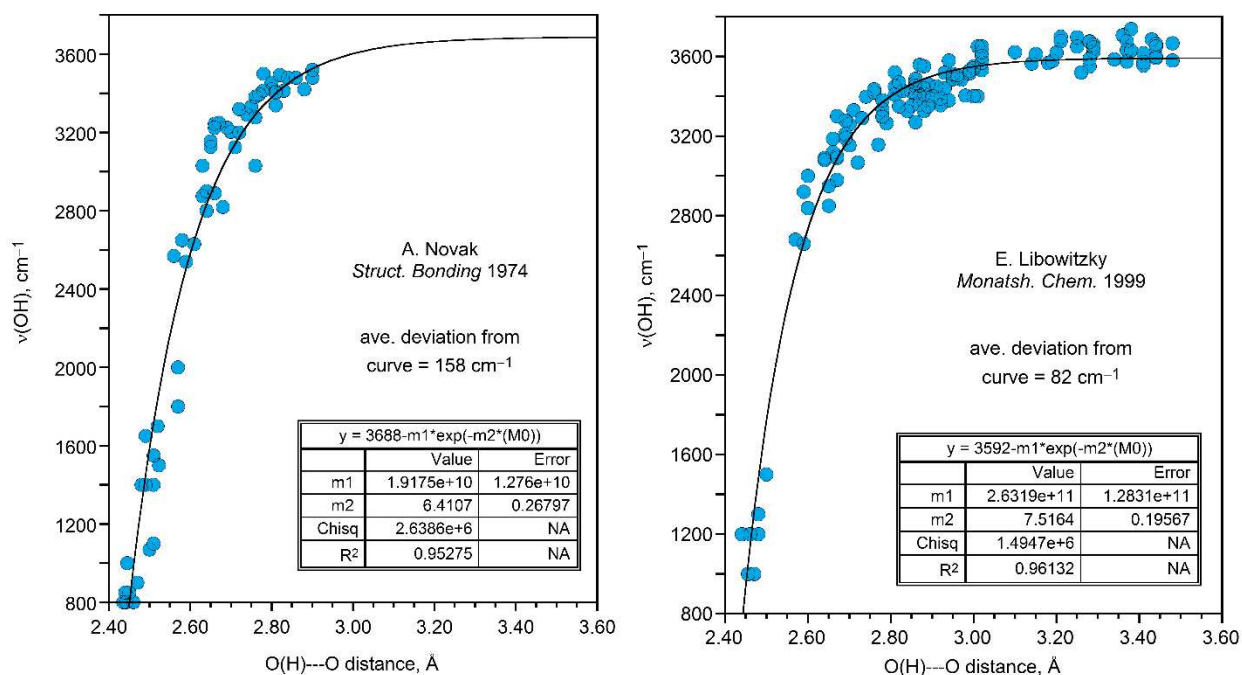


Figure 2.53. Two $\nu(\text{OH})$ vs. $R(\text{O(H)}\cdots\text{O})$ hydrogen-bond correlation curves. The Novak curve on the left was prepared from data in ref. 2. The Libowitzky curve on the right, for 65 minerals, was prepared from data discussed but not listed explicitly in ref. 8. The author thanks Prof. Eugen Libowitzky for a copy of the data sheet from which the curve on the right was made. As of August 2019, ref. 8 has been cited more than 780 times since 1999, including 25 times during the first half of 2019.

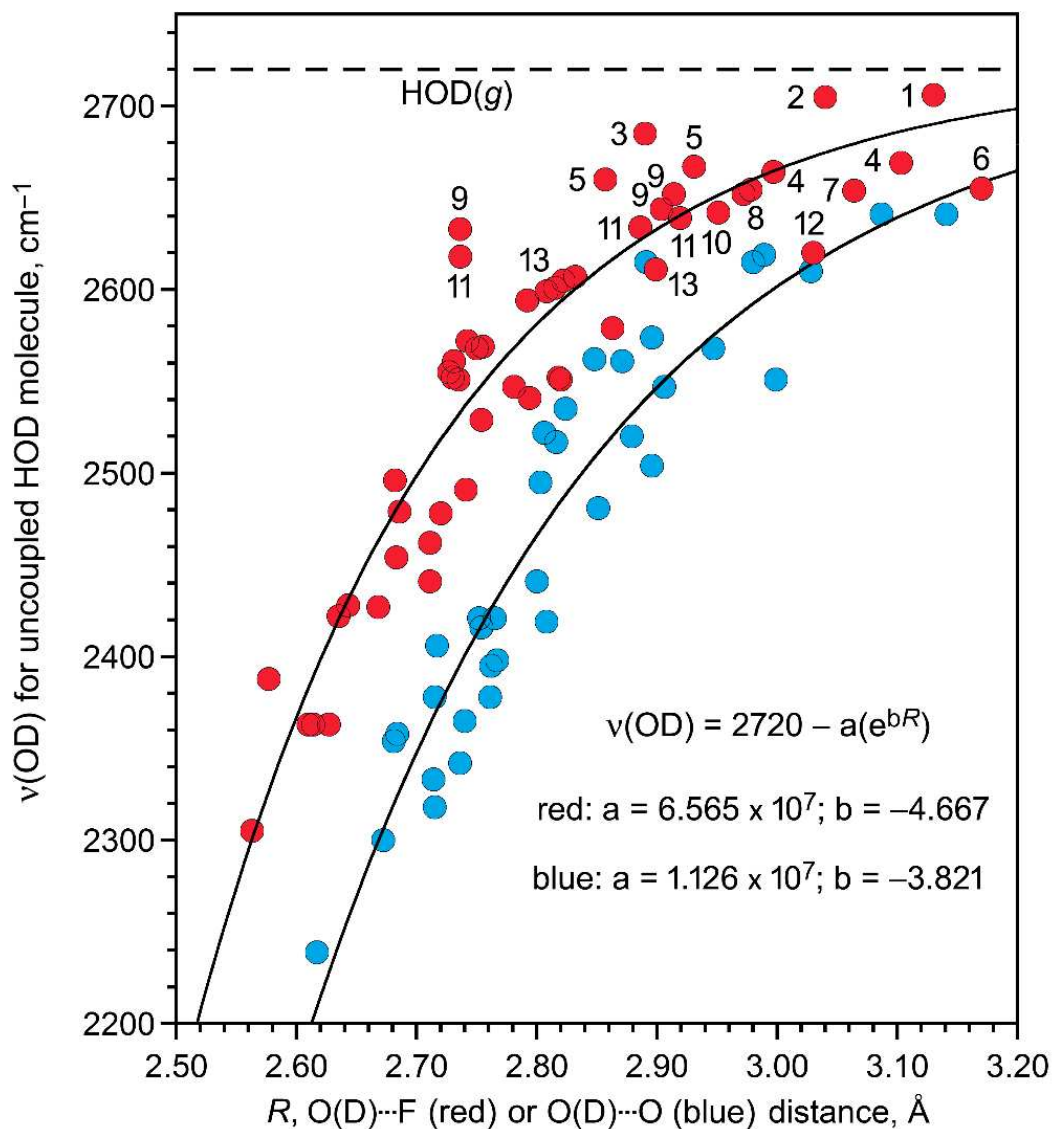


Figure 2.54. Plots of (i) $\nu(\text{OD})$ vs. $\text{O}(\text{H})\cdots\text{F}$ distance for fluoroanion salt hydrates containing a single HOD ligand coordinated to a metal cation (red circles) and (ii) $\nu(\text{OD})$ vs. $\text{O}(\text{D})\cdots\text{O}$ distance for oxoanion salt hydrates containing a single HOD ligand coordinated to a metal cation (blue circles). The red data points are from this work and refs. 6 and ²². These data are listed in Table 2.2. The blue data points are from ref. 5. The dashed line indicates the 2720 cm^{-1} $\nu(\text{OD})$ value for $\text{HOD}(g)$. The numbers 1–13 next to some red data points refer to the numbered compounds in Figure 2.45.

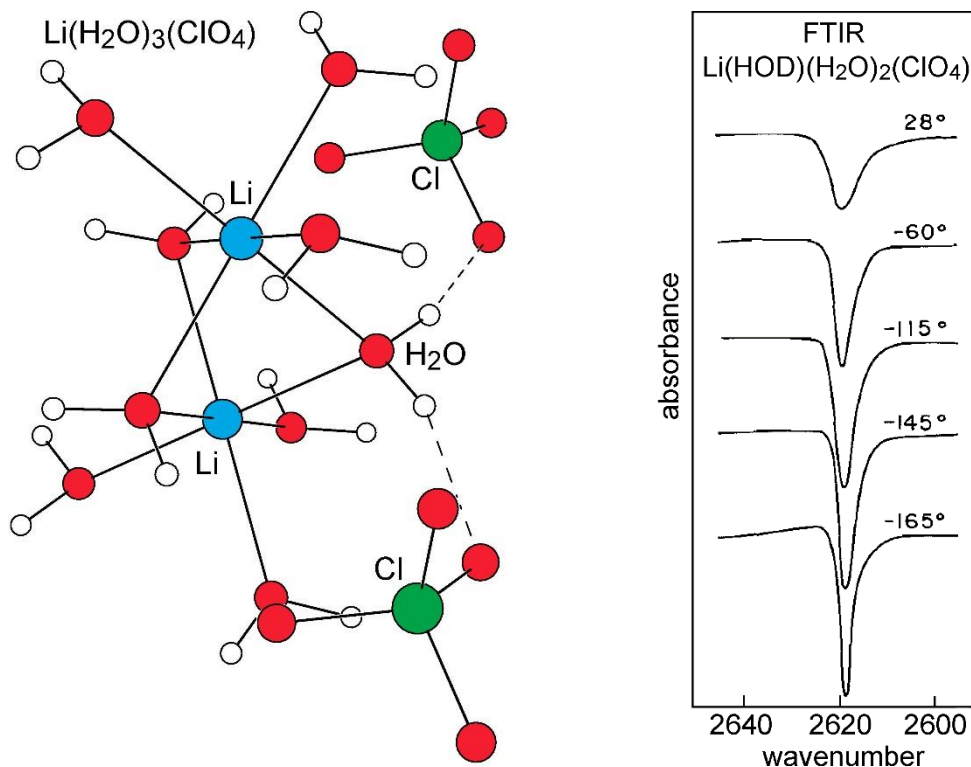


Figure 2.55. A portion of the neutron diffraction crystal structure of $\text{Li}(\text{H}_2\text{O})_3(\text{ClO}_4)$ (ref. 104) and variable temperature FTIR spectra of $\text{Li}(\text{HOD})(\text{H}_2\text{O})_2(\text{ClO}_4)$ (ref. 110; the temperatures shown are in °C). The sharp $\nu(\text{OD})$ stretching frequency at -165°C is 2619 cm^{-1} . All of the H_2O molecules are symmetry related and are in symmetric hydrogen bonding environments. The unique $\text{O}(\text{H})\cdots\text{O}$ distance and $\text{O}-\text{H}\cdots\text{O}$ angle are $2.889(2)\text{ \AA}$ and 162° , respectively. This figure is adapted from figures in the referenced citation.

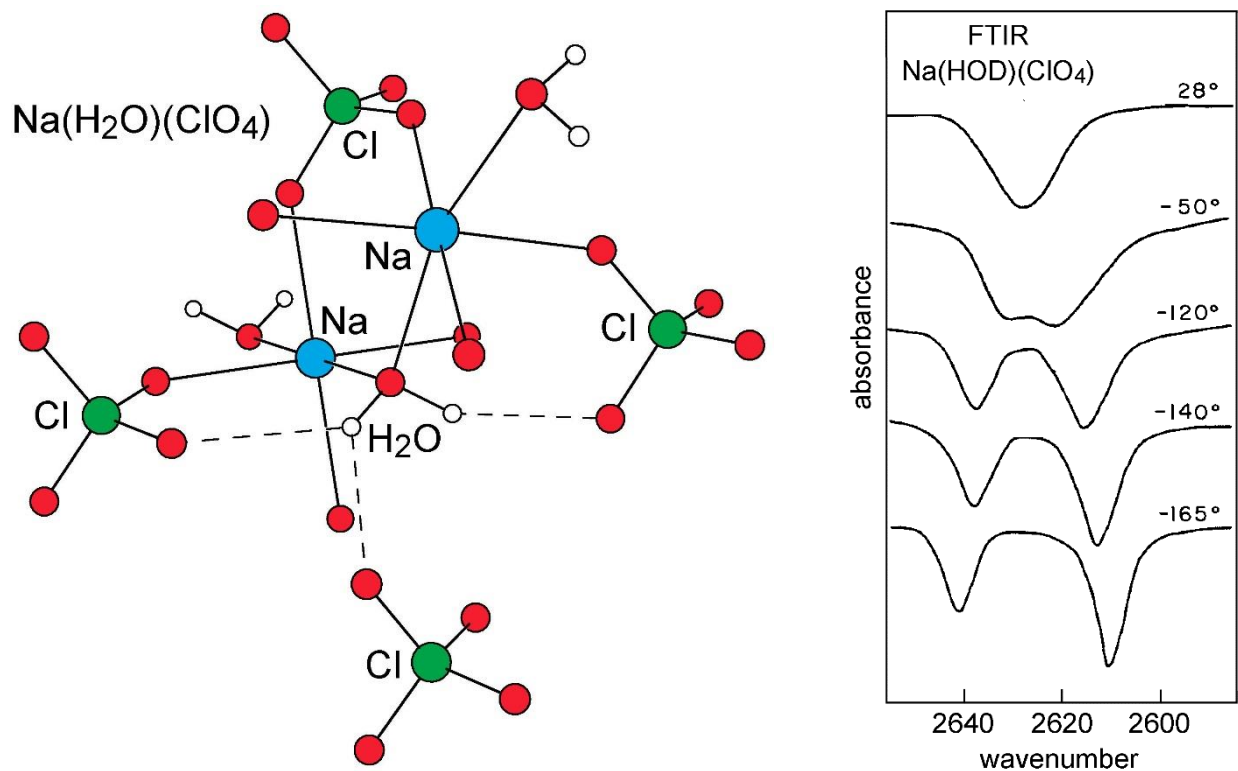


Figure 2.56. A portion of the neutron diffraction crystal structure of Na(H₂O)(ClO₄) (ref. 105) and variable temperature FTIR spectra of Na(HOD)(ClO₄) (ref. 110; the temperatures shown are in °C). The $\nu(\text{OD})$ stretching frequencies in the -165°C spectrum are at 2641 and 2610 cm^{-1} . The $\text{O}(\text{H})\cdots\text{O}$ distances for the bifurcated hydrogen bond involving the H₂O molecule are $3.087(3)$ and $3.141(3)\text{ \AA}$, and the $\text{O}-\text{H}\cdots\text{O}$ angles are 140 and 135° , respectively. The other $\text{O}(\text{H})\cdots\text{O}$ distance and $\text{O}-\text{H}\cdots\text{O}$ angle are $3.028(3)\text{ \AA}$ and 156° , respectively. This figure is adapted from figures in the referenced citation.

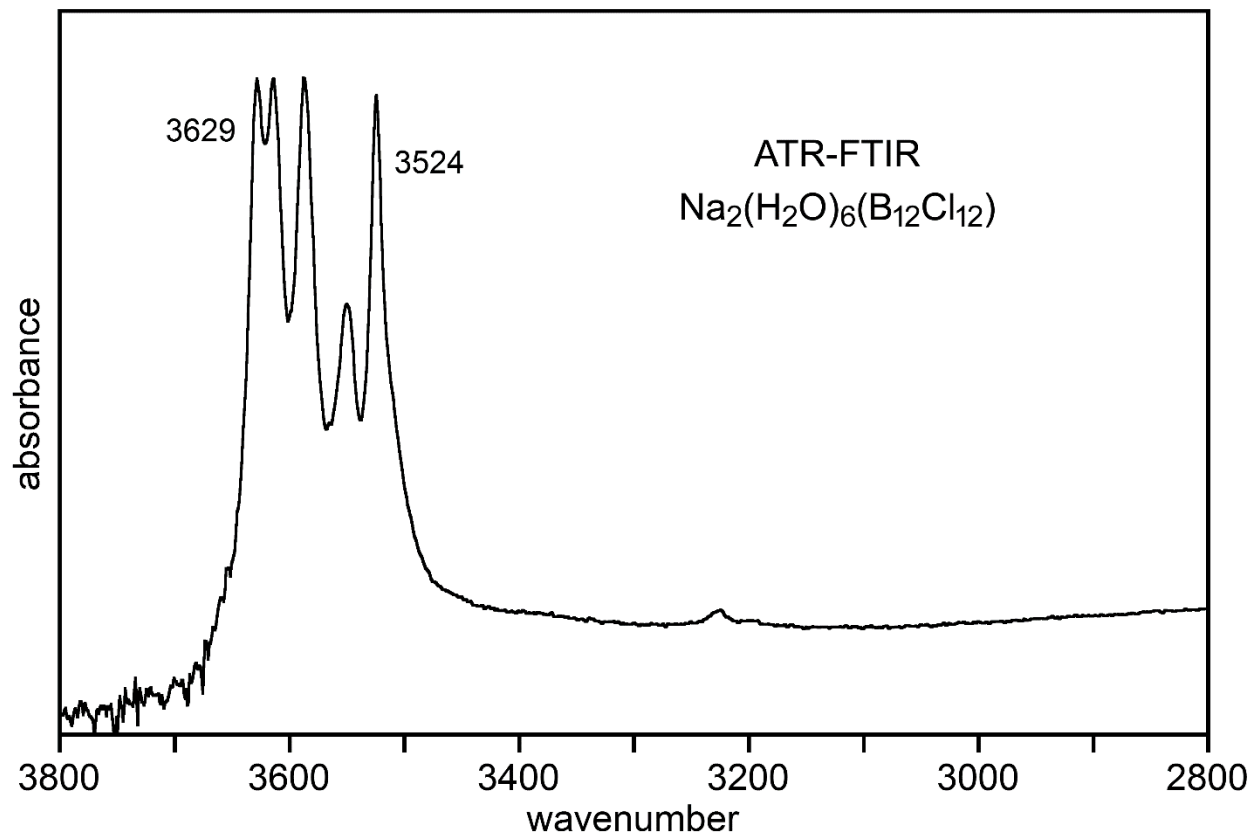


Figure 2.57. FTIR spectrum of $\text{Na}_2(\text{H}_2\text{O})_6(\text{B}_{12}\text{Cl}_{12})$ at 22 °C. The sample of was prepared by allowing an aqueous solution of $\text{Na}_2(\text{B}_{12}\text{Cl}_{12})$ to evaporate on the ATR crystal. It is possible that some H_2O may have evaporated from the sample while the spectrum was recorded.

Table 2.1. FTIR $\nu(\text{OH})$ and $\nu(\text{OD})$ frequencies with full-widths at half-maximum absorbance (FWHM) and X-ray diffraction O(H/D)···F distances^a

compound	$\nu_{\text{asym}}(\text{OH})$ or $\nu_{\text{asym}}(\text{OD})$ [FWHM], cm^{-1}	$\nu_{\text{sym}}(\text{OH})$ or $\nu_{\text{sym}}(\text{OD})$ [FWHM], cm^{-1}	$\nu(\text{OD})$ for unique HOD [FWHM], cm^{-1}	O(H/D)···F distance(s), \AA
$\text{Li}(\text{H}_2\text{O})_4(\text{Al}(\text{OC}(\text{CF}_3)_3)_4)$	3719 [50] ^b	3644 [12] ^b	—	—
$\text{Li}(\text{D}_2\text{O})_4(\text{Al}(\text{OC}(\text{CF}_3)_3)_4)$	2755 [24] ^c	2660 [9] ^c	—	—
$\text{Li}(\text{HOD})(\text{H}_2\text{O})_3(\text{Al}(\text{OC}(\text{CF}_3)_3)_4)$	—	—	2706 [15] ^c	3.102(2), 3.157(2) ^d
$\text{Li}(\text{H}_2\text{O})(\text{B}(3,5\text{-C}_6\text{H}_3(\text{CF}_3)_2)_4)$	3718 [41] ^e	3639 [7] ^e	—	—
$\text{Li}(\text{D}_2\text{O})(\text{B}(3,5\text{-C}_6\text{H}_3(\text{CF}_3)_2)_4)$	2760 [30] ^e	2659 [5] ^e	—	—
$\text{Li}(\text{HOD})(\text{B}(3,5\text{-C}_6\text{H}_3(\text{CF}_3)_2)_4)$	—	—	2705 [9] ^e	$2.995(6) \times 2^f$
$\text{Li}(\text{H}_2\text{O})_n(\text{Ga}(\text{C}_2\text{F}_5)_4)$	3702 [46] ^b	3630 [30] ^b	—	—
$\text{Li}(\text{D}_2\text{O})(\text{H}_2\text{O})_{n-1}(\text{Ga}(\text{C}_2\text{F}_5)_4)$	2749 ^g	2654 ^g	—	—
$\text{Li}(\text{HOD})(\text{H}_2\text{O})_{n-1}(\text{Ga}(\text{C}_2\text{F}_5)_4)$	—	—	2697 [24] ^g	—
$\text{Li}(\text{H}_2\text{O})(\text{PF}_6)$	3602 [20] ^h	3549 [14] ^h	—	—
$\text{Li}(\text{D}_2\text{O})(\text{PF}_6)$	2680 ^h	ca. 2590 ^h	—	—
$\text{Li}(\text{HOD})(\text{PF}_6)$	—	—	2636 [4] ^{h,i}	—
$\text{Li}_2(\text{H}_2\text{O})_2(\text{TiF}_6)$	3583 [33] ^j	3541 [< 33] ^j	—	—

$\text{Li}_2(\text{D}_2\text{O})_2(\text{TiF}_6)$	2663 [20] ^j	2592 [12] ^j	—	—
$\text{Li}_2(\text{HOD})(\text{H}_2\text{O})(\text{TiF}_6)$			2623 [10] ^{j,k}	3.007(8), 3.048(9) ^l
$\text{Li}_2(\text{H}_2\text{O})_4(\text{B}_{12}\text{F}_{12})$	3596 [7], 3583 [26] ^{m,n}	3441 [44], 3401 [67] ^{m,n}	—	—
$\text{Li}_2(\text{D}_2\text{O})_4(\text{B}_{12}\text{F}_{12})$	2651 [25] ^m	2511 [48] ^m	—	—
$\text{Li}_2(\text{HOD})(\text{H}_2\text{O})_3(\text{B}_{12}\text{F}_{12})$	—	—	2642 [6] ⁿ	2.951(3) ^o
$\text{Na}(\text{H}_2\text{O})(\text{PF}_6)$	3639 [14] ^{p,q}	3570 [11] ^{p,q}	—	—
$\text{Na}(\text{D}_2\text{O})(\text{PF}_6)$	2704 [6] ^q	2612 [8] ^q	—	—
$\text{Na}(\text{HOD})(\text{PF}_6)$	—	—	2654 [6] ^q	3.064(2) × 2 ^r
$\text{Na}_2(\text{H}_2\text{O})_2(\text{B}_{12}\text{F}_{12})$	3651 [11] ^p	3556 [16] ^p	—	—
$\text{Na}_2(\text{D}_2\text{O})_2(\text{B}_{12}\text{F}_{12})$	2706 [7] ^q	2608 [4] ^q	—	—
$\text{Na}_2(\text{HOD})(\text{H}_2\text{O})(\text{B}_{12}\text{F}_{12})$	—	—	2680 [5], 2628 [8] ^q	—
$\text{K}_2(\text{H}_2\text{O})_2(\text{B}_{12}\text{F}_{12})$	3637 [14] ^{s,t}	3576 [12] ^{s,t}	—	—
$\text{K}_2(\text{D}_2\text{O})_2(\text{B}_{12}\text{F}_{12})$	2700 [7] ^u	2615 [6] ^u	—	—
$\text{K}_2(\text{HOD})(\text{H}_2\text{O})(\text{B}_{12}\text{F}_{12})$	—	—	2652 [16] ^u	2.978(1); 2.972(1), 2.978(1) ^{v,w}
$\text{Rb}_2(\text{H}_2\text{O})_2(\text{B}_{12}\text{F}_{12})$	3653 [9] ^s	3585 [8] ^s	—	—
$\text{Rb}_2(\text{D}_2\text{O})_2(\text{B}_{12}\text{F}_{12})$	2711 [5] ^x	2623 [4] ^x	—	—
$\text{Rb}_2(\text{HOD})(\text{H}_2\text{O})(\text{B}_{12}\text{F}_{12})$	—	—	2667 [6]; 2660 [9] ^x	2.857(2); 2.859(2), 2.931(2) ^{o,w}
$\text{Cs}_2(\text{H}_2\text{O})(\text{B}_{12}\text{F}_{12})$	3658 [6] ^s	3588 [7] ^s	—	—
$\text{Cs}_2(\text{D}_2\text{O})(\text{B}_{12}\text{F}_{12})$	2715 [5] ^u	2624 [4] ^u	—	—

$\text{Cs}_2(\text{HOD})(\text{B}_{12}\text{F}_{12})$	—	—	2669 [3]; 2664 [6] ^u	3.103(3); 2.997(3) ^y
$[\text{NEt}_4]_2[\text{Hg}(\text{H}_2\text{O})(\text{CB}_{11}\text{F}_{11})_2]$	3681 [10] ^z	3587 [15] ^z	—	—

^a All results from this work unless otherwise indicated. All FTIR spectra recorded at room temperature. Abbreviation: $\text{B}(\text{C}_6\text{H}_3(\text{CF}_3)_2)_4 = \text{B}(3,5\text{-C}_6\text{H}_3(\text{CF}_3)_2)_4$. ^b See Figures 2.23, 2.24, and 2.31. ^c See Figure 2.26. ^d ref. 68; identical bifurcated $\text{O}(\text{D})\cdots\text{F}$ hydrogen bonds in either orientation of the HOD ligand, with two additional $\text{O}(\text{D})\cdots\text{F}$ distances of 3.296(2) and 3.297(2) Å not listed in this table; see Figure 2.28. ^e See Figures 2.23 and 2.29. ^f ref. 69. ^g See Figure 2.31. ^h See Figures 2.34 and 2.35. ⁱ $\nu(\text{OH}) = 3579 \text{ cm}^{-1}$ (FWHM = 4 cm^{-1}); see Figure 2.35. ^j See Figure 2.33; $\nu(\text{OH})$ for $\text{Li}_2(\text{HOD})(\text{D}_2\text{O})(\text{TiF}_6)$ is 3558 cm^{-1} . ^k 75 K literature value = 2620 cm^{-1} ; ref. 6. ^l ref. 70; see Figure 2.32. ^m ref. 106. ⁿ The $\nu(\text{OD})$ frequency for the $\text{O}-\text{D}\cdots\text{O}$ hydrogen bond in $\text{Li}_2(\text{HOD})(\text{H}_2\text{O})_3(\text{Z})$ is 2518 cm^{-1} ; see Figure 2.45. ^o ref. 66; see Figure 2.45. ^p ref. 37; see Figure 2.46. ^q See Figures 2.38 and 2.47. ^r ref. 71; see Figure 2.36. ^s ref. 37; see Figure 2.12. ^t The $\nu(\text{OH})$ values for $\text{K}_2(\text{H}_2^{18}\text{O})_2(\text{B}_{12}\text{F}_{12})$, 3624 and 3569 cm^{-1} , were reported in ref. 65. ^u See Figure 2.19. ^v ref. 65. ^w See Figure 2.9. ^x See Figures 2.8 and 2.14. ^y ref. 67. ^z ref. 37 (see also ref. 72).

Table 2.2. $\nu(\text{OD})$ frequencies and $R(\text{O}\cdots\text{F})$ distances for structurally-characterized compounds with an uncoupled HOD molecule coordinated to the metal ion that makes one or more $\text{O}-\text{D}\cdots\text{F}$ hydrogen bonds^a

compound	data point on Figures 2.52 and 2.53	$\nu(\text{OD})$, cm^{-1}	$\nu(\text{OD})$ ref.	$R(\text{O}\cdots\text{F})$ distance, Å	$R(\text{O}\cdots\text{F})$ ref.
$\text{Li}(\text{HOD})(\text{H}_2\text{O})_3(\text{Al}(\text{OC}(\text{CF}_3)_3)_4)$	1	2706	this work	3.102(3)	68
$\text{Li}(\text{HOD})(\text{B}(3,5\text{-C}_6\text{H}_3(\text{CF}_3)_2)_4)$	2	2705	this work	2.995(6);	69
$\text{Li}_2(\text{HOD})(\text{H}_2\text{O})_3(\text{B}_{12}\text{F}_{12})$	10	2642	this work	2.951(3)	66
$\text{Li}_2(\text{H}_2\text{O})_2(\text{TiF}_6)$	12	2623 ^b	this work	3.007(8), 3.048(9)	70
$\text{Na}(\text{HOD})(\text{PF}_6)$	7	2654 ^c	6	3.064(3)	71
$\text{K}_2(\text{HOD})(\text{H}_2\text{O})(\text{B}_{12}\text{F}_{12})$	8	2653, 2652	this work	2.978(1), 2.972(1)	65
$\text{K}(\text{HOD})(\text{MnF}_4)$		2551; 2496	6	2.820(4); 2.682(4)	108
$\text{K}_2(\text{HOD})(\text{MnF}_5)$		2551	6	2.735(6)	111
$\text{K}(\text{H}_2\text{O})_2\text{F}$		2491; 2478; 2462	6	2.741(1); 2.720(1); 2.711(1) \times 2	107
$\text{Rb}_2(\text{HOD})(\text{H}_2\text{O})(\text{B}_{12}\text{F}_{12})$	5	2667; 2660	this work	2.931(2); 2.857(2)	66
$\text{Cs}_2(\text{HOD})(\text{B}_{12}\text{F}_{12})$	4	2669; 2664	this work; ³⁷	3.103(3); 2.997(3)	67
$\text{Cs}(\text{HOD})(\text{H}_2\text{O})(\text{MnF}_4)$		2479; 2454; 2422; 2388	6	2.686(4); 2.683(4); 2.635(4); 2.577(4)	112
$\text{Mg}(\text{HOD})(\text{H}_2\text{O})_5(\text{B}_{12}\text{F}_{12})$	9	2652; 2644; 2633	this work ^d 22	2.914(2); 2.904(2); 2.749(2), 2.723(2)	22
$\text{Mg}(\text{HOD})(\text{H}_2\text{O})_5(\text{SiF}_6)$	13	2611; 2607; 2605; 2601 2599; 2594	101	2.899(3); 2.832(3) 2.822(3); 2.815(3) 2.808(3); 2.792(3)	113
$\text{Sr}(\text{HOD})(\text{MnF}_5)$		2552	6	2.82(2)	114
$\text{Sr}(\text{HOD})(\text{H}_2\text{O})(\text{TiF}_6)$	6	2655; 2547; 2529	6	3.170(6); 2.781(6); 2.754(6)	109
$\text{Ba}(\text{HOD})(\text{MnF}_5)$		2541	6	2.794(9)	114
$\text{Mn}(\text{HOD})(\text{H}_2\text{O})(\text{FeF}_5)$		2579	6	2.86(2)	115
$\text{Fe}(\text{HOD})(\text{H}_2\text{O})_5(\text{SnF}_6)$		2572; 2561	6	2.742(6); 2.731(6)	116
$\text{Co}(\text{HOD})(\text{H}_2\text{O})_5(\text{SnF}_6)$		2569; 2555	6	2.755(9); 2.727(9)	117
$\text{Co}(\text{HOD})(\text{H}_2\text{O})_5(\text{B}_{12}\text{F}_{12})$	11	2639; 2634 2618	this work ^d 22	2.919(1); 2.886(1) 2.739(1); 2.734(1)	22
$\text{Ni}(\text{HOD})(\text{H}_2\text{O})_5(\text{SnF}_6)$		2568; 2552	6	2.750(9); 2.730(9)	117
$\text{Cu}(\text{H}_2\text{O})_2\text{F}_2$		2428	6	2.643(3)	118

Table 2.2. $\nu(\text{OD})$ frequencies and $R(\text{O}\cdots\text{F})$ distances for structurally-characterized compounds with an uncoupled HOD molecule coordinated to the metal ion that makes one or more $\text{O}-\text{D}\cdots\text{F}$ hydrogen bonds^a (continued)

$\text{Zn}(\text{H}_2\text{O})_4\text{F}_2$		2441; 2427; 2363; 2363; 2363; 2305	6	2.711(14); 2.668(14); 2.627(14); 2.614(14); 2.610(14); 2.563(14)	¹¹⁹
$\text{HOD}\cdots\text{FCH}_3$	3	2685	⁶⁰	2.89	— ^e

^a All $\nu(\text{OD})$ values from spectra recorded at 295 K except $\nu(\text{OD})$ values from refs. 6 and ¹⁰¹, which are from spectra recorded at 75 and 93 K, respectively. These 53 $\nu(\text{OD})$, $R(\text{O}(\text{D})\cdots\text{F})$ data sets are represented by the red data points in Figure 2.53. ^b A $\nu(\text{OD})$ value of 2620 cm^{-1} at 75 K was reported for this compound in ref. 6. ^c A $\nu(\text{OD})$ value of 2649 cm^{-1} at 75 K was reported for this compound in ref. 6. ^d The deconvolution of these peaks into two $\nu(\text{OD})$ values is reported here for the first time. Only a combined peak was reported in ref. 22. ^e DFT calculated distance; Prof. Yoshisuke Futami, personal communication, 2019.

Table 2.3. Selected distances and angles for the three structures of $\text{K}(\text{H}_2\text{O})_2\text{F}$ in ref. 107^a

bond	neutron diffraction	X-ray diffraction	X-ray diffraction	$\nu(\text{OD})$ of $\text{K}(\text{HOD})(\text{H}_2\text{O})\text{F}$, cm^{-1} (ref. 6)
	at 295 K, Å	at 298 K, Å	at 120 K, Å ^b	
K–F	$2.716(2) \times 2^c$	$2.716(1) \times 2$	$2.703(1) \times 2$	
K–O1	2.726(2)	2.727(1)	2.714(1)	
K–O1'	2.822(2)	2.817(1)	2.794(1)	
K–O2	$2.784(2) \times 2$	$2.781(1) \times 2$	$2.762(1) \times 2$	
O1(H)⋯F	2.719(2)	2.722(1)	$2.711(1) \times 2$	2462
O2(H)⋯F	2.734(2)	2.733 (1)	2.720(1)	2478
O2'(H)⋯F	2.753(2)	2.758(1)	2.741(1)	2491
O1–H	0.97×2			
O2–H	0.97; 0.97			
(O1)H⋯F	1.75×2			
O1–H⋯F (angle)	174°			
(O2)H⋯F	1.76; 1.80			
O2–H⋯F (angle)	178°; 170°			

Table 2.4. Selected distances and angles for the neutron diffraction structure of $\text{Zn}(\text{H}_2\text{O})_4\text{F}_2^{\text{a}}$

moiety	$R(\text{O}(\text{H})\cdots\text{F}/\text{O}), \text{Å}$	$\nu(\text{OD}), \text{cm}^{-1}$	$R(\text{O}-\text{H}), \text{Å}$	$R(\text{H}\cdots\text{O})/\text{F}, \text{Å}$	$R(\text{O}-\text{H}\cdots\text{O}/\text{F}), \text{deg}$
O1–H \cdots F1'	2.610(14)	2363	0.96	1.69	160
O1–H \cdots F2'	2.563(14)	2305	0.95	1.61	175
O2–H \cdots F1'	2.668(14)	2427	0.93	1.74	173
O2–H \cdots O4'	2.921(14)	—	0.99	1.93	178
O3–H \cdots F2'	2.711(14)	2441	0.98	1.75	169
O3–H \cdots O1'	2.813(14)	—	0.92	1.90	176
O4–H \cdots F1'	2.614(14)	2363	0.99	1.66	165
O4–H \cdots F2'	2.627(14)	2363	0.99	1.62	175

^a Distances and angles from ref. 119. $\nu(\text{OD})$ frequencies from ref. 6.

CHAPTER 3 OBSERVATION OF B AND E $\nu(\text{OH})$ FTIR BANDS AND COUPLING OF STRONG O–H \cdots O AND WEAK O–H \cdots F VIBRATIONS IN THE CYCLIC S4 (H₂O)₄ CLUSTERS IN CRYSTALLINE Li₂(H₂O)₄(B₁₂F₁₂)

3.1 Introduction and Relevant Literature

Chemists and physicists have studied small water clusters for decades.¹⁻⁵ This includes calculations of their structures, stabilities, and vibrational spectra by theorists and experimental vibrational spectroscopic studies of (H₂O)_n clusters in low-temperature matrices, generated by cold jet expansion, or confined in metal–organic frameworks or crystalline organic or inorganic compounds.²⁻³³ Reasons for studying (H₂O)_n clusters range from understanding cloud and ice formation as well as other atmospheric phenomena (including the radiation balance of the earth),¹⁴ a variety of biochemical processes, as a bridge from the gas phase to condensed phases, as a bridge from single-molecule adsorption to monolayer and bilayer adsorption of H₂O to solid surfaces,³⁴⁻³⁵ as models for bulk phenomena such as proton transport and solvation,³⁶ and as an easily accessible experimental platform for studying isotope effects.⁴

The most important physicochemical methods for studying (H₂O)_n and M(H₂O)_n^{m+} clusters are vibrational spectroscopies, including Fourier transform infrared (FTIR), Raman, infrared molecular beam depletion, infrared sum frequency generation, infrared cavity ringdown, and terahertz laser vibration–rotation spectroscopies.^{11,22,32,37-42} The number of $\nu(\text{OH})$ bands, their red shifts from H₂O(g), and their relative intensities, bandshapes, and bandwidths can suggest the value of *n* and provide information about the network of O–H \cdots O hydrogen bonds in the cluster. Even when an unambiguous assignment is not possible, FTIR spectra can generally rule out some compositions and/or structures.³¹

Low-temperature matrix and cold jet expansion experiments cannot produce neutral (H₂O)_n clusters with a single value of *n*, so typical FTIR spectra in these experiments contain $\nu(\text{OH})$ bands due to a mixture of neutral (H₂O)_n clusters with, for example, *n* = 3–6. Five examples of spectra from the literature are shown in Figures 3.1–3.4.^{14,28,31-32,43} The assignment of bands to particular (H₂O)_n clusters is generally based on experimental vs. calculated $\nu(\text{OH})$ band positions, relative intensities as a function of H₂O content, bandshapes, and bandwidths (many of the experimental papers include calculated fundamental vibrational

frequencies).^{11,14,17-18,22-23,28,31-32} It is also possible that more than one water cluster isomer is present for some values of n (see, for example, Figure 3.1)

When a $(\text{H}_2\text{O})_n$ cluster is observed in a crystalline hydrate, it is generally not possible to obtain meaningful vibrational spectra of it, and in many cases vibrational spectra of the $\nu(\text{OH})$ region are not reported for new solid state compounds containing water clusters when their X-ray/neutron diffraction data are published. Consider the cyclic $(\text{H}_2\text{O})_4$ tetramer, also known as the R4 cluster.^{5,8,44} The X-ray structure of $[\text{Na}_2(\text{H}_2\text{O}@\text{TMEQ}[6])]\cdot 2(\text{C}_6\text{H}_5\text{NO}_3)\text{Cl}_2(\text{H}_2\text{O})_{10}$ contains an R4 cluster, but there are so many other H_2O molecules in the lattice that the vibrational spectra were not reported (TMEq[6] = $\alpha, \alpha', \delta, \delta'$ -tetramethylcucurbit[6]uril).¹⁶ Copper(II) pyridine-2,3-dicarboxylates crystalized with the R4 clusters hydrogen bonded to other H_2O molecules.²¹ The analysis of the $\nu(\text{OH})$ region of the FTIR spectra consisted of one sentence: “The IR spectra of complexes show strong bands between 3386 and 3142 cm^{-1} due to the O–H stretching vibrations of the H_2O molecules.”²¹ The X-ray structure of $\text{Cu}(\text{abit})(\text{NO}_3)\cdot 5\text{H}_2\text{O}$ contains a “water tape” of R4 tetramers and R6 hexamers (Habit = 4-amino-3,5-bis(imidazole-1-ylmethyl)-1,2,4-triazol).¹³ No vibrational spectra were reported. The X-ray structure of $\text{Cu}(3\text{-amino-methylpyridine})\cdot (\text{H}_2\text{O})(\text{oxalate})\cdot 2\text{H}_2\text{O}$ contains an R4 cluster, but also contains H_2O coordinated to Cu^{2+} .^{15,26} The FTIR spectrum has a broad and uninformative $\nu(\text{OH})$ region, as shown in Figure 3.5.¹⁵ Some of the $\nu(\text{OH})$ bands in the Raman spectrum were also broad, as shown in Figure 3.6.²⁶ The compound $[\text{Fe}_3(\mu^3\text{-O})(\mu^2\text{-CH}_3\text{COO})_6(\text{C}_5\text{H}_5\text{NO})_2(\text{H}_2\text{O})]\text{ClO}_4\cdot 4\text{H}_2\text{O}$ is another example of a complex containing an R4 cluster. The FTIR spectrum also has a broad and uninformative $\nu(\text{OH})$ region, as shown in Figure 3.7.⁴⁵ There are other examples of R4 clusters in crystalline compounds,⁸ including several in which the H_2O molecules are coordinated to alkali metals.⁴⁶⁻⁴⁸ However none of these papers reported vibrational spectra that can be interpreted unambiguously.

The Stauss–Boltalina research group previously reported the synthesis and X-ray structure of the lithium salt hydrate $\text{Li}_2(\text{H}_2\text{O})_4(\text{B}_{12}\text{F}_{12})$ in 2017.⁴⁹ The four H_2O molecules form a cyclic $(\text{H}_2\text{O})_4$ cluster with four O–H \cdots O hydrogen bonds with an effective (not crystallographic) S_4 symmetry, as show in Figure 3.8. This cyclic $(\text{H}_2\text{O})_4$ cluster of waters makes $\text{Li}_2(\text{H}_2\text{O})_4(\text{B}_{12}\text{F}_{12})$ distinct from the other stable room-temperature salt hydrates of $\text{B}_{12}\text{F}_{12}^{2-}$ discussed in the previous chapter. Previously all deviations in the $\nu(\text{OH})$ band

positions from $\text{H}_2\text{O}(\text{g})$ were due to the formation of weak $\text{O}-\text{H}\cdots\text{F}$ hydrogen bonds, but the H_2O molecules in $\text{Li}_2(\text{H}_2\text{O})_4(\text{B}_{12}\text{F}_{12})$ participate in both $\text{O}-\text{H}\cdots\text{F}$ and $\text{O}-\text{H}\cdots\text{O}$ hydrogen bonds, which adds a new layer of complexity when studying the spectra of $\text{Li}_2(\text{H}_2\text{O})_4(\text{B}_{12}\text{F}_{12})$ and its deuterated isotopologs. The four so-called “dangling” or “free” $\text{O}-\text{H}$ bonds not participating in the $\text{O}-\text{H}\cdots\text{O}$ hydrogen bonding responsible for holding the cluster together each form the previously mentioned $\text{O}-\text{H}\cdots\text{F}$ hydrogen bonds with the weakly coordinating⁵⁰ $\text{B}_{12}\text{F}_{12}^{2-}$ anion. The $\text{O}(\text{H})\cdots\text{F}$ distance is 2.951(2) Å. As shown in the previous chapter, the weak $\text{O}-\text{H}\cdots\text{F}$ hydrogen bonds between water and the weakly coordinating $\text{B}_{12}\text{F}_{12}^{2-}$ anion allow for resolution of $\nu(\text{OH})$ bands not normally resolvable when crystallographic waters form stronger hydrogen bonds with nonfluorinated anions. This, combined with the fact that $\text{Li}_2(\text{H}_2\text{O})_4(\text{B}_{12}\text{F}_{12})$ has no IR bands above 1500 cm^{-1} other than bands associated with H_2O molecules [viz. $\nu(\text{OH})$ and $\delta(\text{HOH})$ vibrations], makes it an ideal structural and spectroscopic model for the putative cyclic S_4 $(\text{H}_2\text{O})_4$ cluster that is, in part, the subject of many research papers.^{2-4,11-12,14,17,19-20,22-25,27-28,31,33,40-41,43,51-53}

All of the work presented in this chapter has been published as a paper in the *Journal of Physical Chemistry A* titled *Room-Temperature FTIR Spectra of the Cyclic S_4 $(\text{H}_2\text{O})_4$ Cluster in Crystalline $\text{Li}_2(\text{H}_2\text{O})_4(\text{B}_{12}\text{F}_{12})$: Observation of B and E $\nu(\text{OH})$ Bands and Coupling of Strong $\text{O}-\text{H}\cdots\text{O}$ and Weak $\text{O}-\text{H}\cdots\text{F}$ Vibrations*. The author of this dissertation is the first author and only graduate student or postdoc author of this paper. The structures presented in this chapter were collected and determined by previous Strauss group members.

3.2 Experimental

3.2.1 Reagents and General Procedures

Deuterium oxide (D_2O , Cambridge Isotopes, 99.9%) was used as received. Distilled H_2O was deionized with a Barstead Nanopure system. The deionized distilled water (dd- H_2O) had a resistivity greater than or equal to 18 MΩ. All references to H_2O used in this chapter correspond to dd- H_2O . The compounds $\text{K}_2(\text{H}_2\text{O})_2(\text{B}_{12}\text{F}_{12})$ ⁵⁴ and $\text{Li}_2(\text{H}_2\text{O})_4(\text{B}_{12}\text{F}_{12})$ ⁴⁹ were prepared as previously described in sections 2.2.2 and 2.2.6, respectively, in Chapter 2 of this dissertation.

3.2.2 FTIR Spectroscopy

All ATR-FTIR spectra were collected by the author with a Nicolet 6700 FTIR spectrometer equipped with a stainless-steel Harrick Horizon ATR flow reactor described in detail in previous publications⁵⁵⁻⁵⁷ (and discussed in section 2.2.10). In a typical experiment, an aliquot of dilute aqueous solution of $\text{Li}_2(\text{H}_2\text{O})_4(\text{B}_{12}\text{F}_{12})$ was deposited on a $5 \text{ cm} \times 1 \text{ cm} \times 0.2 \text{ cm}$ ZnSe ATR crystal (New Era Enterprise) and sealed in the flow reactor, where it was allowed to evaporate to insipient dryness with a purge of N_2 (typically 1 L min^{-1}). No attempt was made to control the size or distribution of the microcrystalline particles formed on the crystal. The IR beam was directed into the ATR crystal at an incident angle of 45° by mirrors after leaving the interferometer, and the reflected light was returned to a liquid N_2 cooled mercury cadmium telluride detector. All spectra were collected using 128 scans and 1 cm^{-1} resolution unless otherwise indicated.

Samples of microcrystalline $\text{Li}_2(\text{D}_2\text{O})_4(\text{B}_{12}\text{F}_{12})$ were prepared by first dissolving a sample of $\text{Li}_2(\text{H}_2\text{O})_4(\text{B}_{12}\text{F}_{12})$ in 99.9% D_2O and evaporated to dryness three times. The resulting solid of $\text{Li}_2(\text{D}_2\text{O})_4(\text{B}_{12}\text{F}_{12})$ was dissolved in 99.9% D_2O a fourth time, and an aliquot was deposited on the ATR crystal (after the crystal, and chamber, had been seasoned with D_2O) and allowed to evaporate to dryness as described above.

Samples containing microcrystalline $\text{Li}_2(\text{HOD})(\text{H}_2\text{O})_3(\text{B}_{12}\text{F}_{12})$ and $\text{Li}_2(\text{HOD})(\text{D}_2\text{O})_3(\text{B}_{12}\text{F}_{12})$ were prepared by dissolving $\text{Li}_2(\text{H}_2\text{O})_4(\text{B}_{12}\text{F}_{12})$ in either 95:5 (v:v) $\text{H}_2\text{O}:\text{D}_2\text{O}$ or 5:95 (v:v) $\text{H}_2\text{O}:\text{D}_2\text{O}$, respectively, and depositing and drying aliquots on the ATR crystal as described above. As a result, the sample referred to as “ $\text{Li}_2(\text{HOD})(\text{H}_2\text{O})_3(\text{B}_{12}\text{F}_{12})$ ” in fact only contains a small amount of $\text{Li}_2(\text{HOD})(\text{H}_2\text{O})_3(\text{B}_{12}\text{F}_{12})$, with most of the sample being $\text{Li}_2(\text{H}_2\text{O})_4(\text{B}_{12}\text{F}_{12})$. The sample contained only a negligible amount of $\text{Li}_2(\text{D}_2\text{O})(\text{H}_2\text{O})_3(\text{B}_{12}\text{F}_{12})$ or $\text{Li}_2(\text{HOD})_2(\text{H}_2\text{O})_2(\text{B}_{12}\text{F}_{12})$. Therefore, as far as the $\nu(\text{OD})$ region of the FTIR spectrum is concerned, this sample was $\text{Li}_2(\text{HOD})(\text{H}_2\text{O})_3(\text{B}_{12}\text{F}_{12})$ and will be referred to as such.

3.3 Results and Discussion

3.3.1 Spectroscopic data

The $\nu(\text{OH})$ regions of the ATR-FTIR spectra of microcrystalline samples of $\text{Li}_2(\text{H}_2\text{O})_4(\text{B}_{12}\text{F}_{12})$ and $\text{Li}_2(\text{HOD})(\text{D}_2\text{O})_3(\text{B}_{12}\text{F}_{12})$ evaporated on the ZnSe ATR crystal are shown in Figure 3.9. A complete IR spectrum for a sample of $\text{Li}_2(\text{H}_2\text{O})_4(\text{B}_{12}\text{F}_{12})$, from 650 to 4000 cm^{-1} , is shown in Figure 3.10. The inset drawing

is of the $\text{Li}_4(\text{H}_2\text{O})_4^{4+}$ cluster taken from the X-ray structure. All bands in the 1500–4000 cm^{-1} region of the spectrum are due only to vibrations of the H_2O molecules. The small feature at 3200 cm^{-1} is due to the $2\delta(\text{HOH})$ overtone.⁵⁸ The two $\nu(\text{OH})$ peaks in spectrum of $\text{Li}_2(\text{HOD})(\text{D}_2\text{O})_3(\text{B}_{12}\text{F}_{12})$ are due to the H in the HOD molecule existing in one of two different hydrogen bonding environments based on the orientation of the HOD molecule. In the $[(\text{HOD})(\text{D}_2\text{O})_3]$ cluster the HOD molecule can form an $\text{O}-\text{H}\cdots\text{F}$ and $\text{O}-\text{D}\cdots\text{O}$ pair of hydrogen bonds, or it can form a $\text{O}-\text{H}\cdots\text{O}$ and $\text{O}-\text{D}\cdots\text{F}$ pair of hydrogen bonds. The broader band, at 3401 cm^{-1} in the $\text{Li}_2(\text{H}_2\text{O})_4(\text{B}_{12}\text{F}_{12})$ spectrum and 3411 cm^{-1} in the $\text{Li}_2(\text{HOD})(\text{D}_2\text{O})_3(\text{B}_{12}\text{F}_{12})$ spectrum, is assigned to the $\text{O}-\text{H}$ oscillator participating in $\text{O}-\text{H}\cdots\text{O}$ hydrogen bonding. The broader peak, at 3583 cm^{-1} in the $\text{Li}_2(\text{H}_2\text{O})_4(\text{B}_{12}\text{F}_{12})$ spectrum and 3587 cm^{-1} in the $\text{Li}_2(\text{HOD})(\text{D}_2\text{O})_3(\text{B}_{12}\text{F}_{12})$ spectrum, is assigned to the $\text{O}-\text{H}$ oscillator participating in $\text{O}-\text{H}\cdots\text{F}$ hydrogen bonding. Note that in this sample is ca. 5–10% $\text{Li}_2(\text{HOD})(\text{D}_2\text{O})_3(\text{B}_{12}\text{F}_{12})$ and 90–95% $\text{Li}_2(\text{D}_2\text{O})_4(\text{B}_{12}\text{F}_{12})$.

The ATR-FTIR spectra of the $\nu(\text{OD})$ region (2400–2750 cm^{-1}) for microcrystalline samples of $\text{Li}_2(\text{D}_2\text{O})_4(\text{B}_{12}\text{F}_{12})$ and $\text{Li}_2(\text{HOD})(\text{H}_2\text{O})_3(\text{B}_{12}\text{F}_{12})$ evaporated on the ZnSe ATR crystal are shown in Figure 3.11. The spectrum of $\text{Li}_2(\text{D}_2\text{O})_4(\text{B}_{12}\text{F}_{12})$ contained a larger amount of an impurity than was present in the batch of $\text{Li}_2(\text{H}_2\text{O})_4(\text{B}_{12}\text{F}_{12})$ used to prepare the aqueous solutions of $\text{Li}_2(\text{D}_2\text{O})_4(\text{B}_{12}\text{F}_{12})$ and ca. 5–10% $\text{Li}_2(\text{HOD})(\text{H}_2\text{O})_3(\text{B}_{12}\text{F}_{12})$ in 90–95% $\text{Li}_2(\text{H}_2\text{O})_4(\text{B}_{12}\text{F}_{12})$. These impurity peaks are indicated with asterisks in Figure 3.11. The two $\nu(\text{OD})$ peaks present in this region are due to the two possible environments the $\text{O}-\text{D}$ oscillator can occupy, with the broader peak at lower wavenumbers assigned to the $\text{O}-\text{D}\cdots\text{O}$ hydrogen bonding environment and the narrow peak at higher wavenumbers assigned to the a $\text{O}-\text{D}\cdots\text{F}$ hydrogen bonding environment.

Lorentzian fits of the $\nu(\text{OH})$ peak assigned to the $\text{O}-\text{H}\cdots\text{O}$ environment and the $\nu(\text{OD})$ peak assigned to the $\text{O}-\text{D}\cdots\text{O}$ environment for the spectra of $\text{Li}_2(\text{H}_2\text{O})_4(\text{B}_{12}\text{F}_{12})$, $\text{Li}_2(\text{HOD})(\text{D}_2\text{O})_3(\text{B}_{12}\text{F}_{12})$, $\text{Li}_2(\text{D}_2\text{O})_4(\text{B}_{12}\text{F}_{12})$, and $\text{Li}_2(\text{HOD})(\text{H}_2\text{O})_3(\text{B}_{12}\text{F}_{12})$ are shown in Figure 3.12. A four-peak Lorentzian fit of the entire $\nu(\text{OH})$ region of the spectrum of $\text{Li}_2(\text{H}_2\text{O})_4(\text{B}_{12}\text{F}_{12})$ is shown in Figure 3.13.

The $\delta(\text{HOH})$ bending region of the ATR-FTIR spectrum for samples of $\text{Li}_2(\text{H}_2\text{O})_4(\text{B}_{12}\text{F}_{12})$ or $\text{K}_2(\text{H}_2\text{O})_2(\text{B}_{12}\text{F}_{12})$ evaporated on the ZnSe ATR crystal are shown in Figure 3.14. Lorentzian fits of the $\delta(\text{HOH})$ band(s) for both of the $\text{Li}_2(\text{H}_2\text{O})_4(\text{B}_{12}\text{F}_{12})$ and $\text{K}_2(\text{H}_2\text{O})_2(\text{B}_{12}\text{F}_{12})$ samples are shown in Figure 3.15

along with portions of the X-ray crystal structure for each compound depicting the cation–water interaction environment. The $\delta(\text{DOD})$ band is clearly visible in the spectrum of $\text{Li}_2(\text{D}_2\text{O})_4(\text{B}_{12}\text{F}_{12})$, but it was not analyzed by peak fitting due to overlap with the $\nu(\text{BF})$ band (Figure 3.16).

3.3.2 Structure of $\text{Li}_2(\text{H}_2\text{O})_4(\text{B}_{12}\text{F}_{12})$

Drawings of the $\text{Li}_2(\text{H}_2\text{O})_4(\text{B}_{12}\text{F}_{12})$ structure, which were first published in 2017,⁴⁹ are shown in Figure 3.8 and 3.13. The $\text{B}_{12}\text{F}_{12}^{2-}$ anions form a tetragonal polyhedron with $\odot \cdots \odot$ distances of 6.767, 7.287, and 7.287 Å and $\odot \cdots \odot \cdots \odot$ angles of 90° ($\odot = \text{B}_{12}$ centroid). There is only one unique H_2O molecule. The four symmetry-related H_2O molecules form a skew quadrilateral $(\text{H}_2\text{O})_4$ cluster with S_4 symmetry held together by four $\text{O}-\text{H} \cdots \text{O}$ hydrogen bonds. The two $\text{O}(\text{H}) \cdots \text{O}$ distances for each H_2O molecule in the cluster, at 2.778(2) and 2.785(2) Å, are the same to within $\pm 3\sigma$. The four H atoms in the $\text{O}-\text{H} \cdots \text{O}$ hydrogen bonds are disordered, producing two equivalent sets of hydrogen bonds that undoubtedly interconvert, as suggested by the mirror-image drawings in Figure 3.17.

The $(\text{H}_2\text{O})_4$ cluster is held in the center of the $[\text{B}_{12}\text{F}_{12}^{2-}]_8$ polyhedron by coordination to four Li^+ ions centered on four of the six $[\text{B}_{12}\text{F}_{12}^{2-}]_8$ faces [$\text{Li}-\text{O} = 1.995(1)$ Å] and by four relatively weak $\text{O}-\text{H} \cdots \text{F}$ hydrogen bonds [$\text{O}(\text{H}) \cdots \text{F} = 2.951(2)$ Å]. The calculated most stable structure for an isolated $(\text{H}_2\text{O})_4$ cluster is cyclic and has S_4 symmetry,^{14,25,32} but the four O atoms in the calculated structure are coplanar. In contrast, the calculated structure of the cyclic $(\text{H}_2\text{O})_4$ cluster adsorbed to the $\text{NaCl}(001)$ surface only has C_2 symmetry, as shown in Figure 3.18.⁵⁹ The cluster is distorted from S_4 symmetry because two of the four H_2O molecules are coordinated to surface Na^+ ions and the other two form $\text{O}-\text{H} \cdots \text{Cl}$ hydrogen bonds to surface Cl^- ions. The CCSD(T)/aVQZ calculated cyclic structure of S_4 $(\text{H}_2\text{O})_4$ ²⁵ and the $\text{M}_4(\text{H}_2\text{O})_4$ clusters in $\text{Rb}_2[\text{Pt}_2(\text{POP})_4] \cdot 4\text{H}_2\text{O}$ ($\text{pop}^{2-} = \text{HOOPOPOOH}^{2-}$),⁴⁸ $\text{Na}_4[\text{Mo}_{12}\text{O}_{46}(\text{AsC}_6\text{H}_4-4\text{-OH-3-NO}_2)_4] \cdot 8\text{H}_2\text{O}$,⁴⁷ and $\text{Li}_2(\text{H}_2\text{O})_4(\text{B}_{12}\text{F}_{12})$ are compared in Figure 3.19. The structural parameters of these cyclic $(\text{H}_2\text{O})_4$ clusters and several others are listed in Table 3.1.

The terminology used for the cyclic $(\text{H}_2\text{O})_n$ clusters is that there are “bound” and free (or dangling) $\text{O}-\text{H}_b$ and $\text{O}-\text{H}_f$ bonds, respectively. The bound $\text{O}-\text{H}_b$ bonds are the ones that form the $\text{O}-\text{H} \cdots \text{O}$ hydrogen bonds that hold the cluster together. The $\text{O}-\text{H}_f$ bonds in the crystalline compounds with $(\text{H}_2\text{O})_n$ clusters are rarely free. The ones listed in Table 3.1 engage in weak $\text{O}-\text{H} \cdots \text{F}$ hydrogen bonds in $\text{Li}_2(\text{H}_2\text{O})_4(\text{B}_{12}\text{F}_{12})$ or $\text{O}-$

H \cdots N and/or O–H \cdots O hydrogen bonds in the other compounds, in some cases forming shorter hydrogen bonds than those formed by the O–H_b bonds.

With one exception, the structural parameters of the R4 (H₂O)₄ clusters, shown in Figure 3.19 and listed in Table 3.1, are similar. The major difference is the perpendicular displacement of the O atoms from their least-squares plane. The planar calculated clusters, and the three hydrates of copper and zinc coordination compounds all have the smallest displacement, 0 Å, from their respective least-squares plane. The largest displacements are for Li₂(H₂O)₄(B₁₂F₁₂) (± 0.633 Å)⁴⁹ and for (H₂O)₄ on NaCl(001) (± 0.374 Å).⁵⁹ The symmetry of a cyclic (H₂O)₄ cluster can only be S₄ if the four H₂O molecules are identical crystallographically and the O–H_f bonds are arranged up-down-up-down around the cluster, as in Na₄[Mo₁₂O₄₆(AsC₆H₄-4-OH-3-NO₂)₄] \cdot 8H₂O,⁴⁷ and (NMe₄)MnCo(CN)₆ \cdot 8H₂O,⁶⁰ even when there are two different O(H) \cdots O distances for the symmetry-related H₂O molecules, as in Li₂(H₂O)₄(B₁₂F₁₂). If there are two pairs of unique H₂O molecules in the cluster, the highest possible symmetries are C₂, as in Rb₂[Pt₂(POP)₄I] \cdot 4H₂O,⁴⁸ and (H₂O)₄ on NaCl(001),⁵⁹ or C_i, as in Zn[(bdc)(bim)] \cdot 2H₂O,⁶¹ Cu(3-amp)(C₂O₄) \cdot 3H₂O,¹⁵ and Cu₂(pyrdc)₂(1,2-Me₂Im)₄ \cdot 6H₂O²¹ (see Table 3.1 for abbreviation definitions).

3.3.3 Structure and FTIR Spectrum of the K₂(H₂O)₂(B₁₂F₁₂)

To appreciate the significance of the FTIR spectra of Li₂(H₂O)₄(B₁₂F₁₂) and its deuterated isotopologs, it is important to compare them to the structures and FTIR spectra of the alkali metal B₁₂F₁₂²⁻ salt hydrates, presented and discussed in Chapter 2 of this dissertation. Specifically Li₂(H₂O)₄(B₁₂F₁₂) will be compared to K₂(H₂O)₂(B₁₂F₁₂), whose structure and FTIR spectrum are shown in Figure 3.20. This particular salt hydrate is representative of, and the most well studied of, the family of alkali metal salt hydrates of the B₁₂F₁₂²⁻ anion. Unlike Li₂(H₂O)₄(B₁₂F₁₂), K₂(H₂O)₂(B₁₂F₁₂) does not have any O(H) \cdots O hydrogen bonds. The O(H) \cdots F distance for K₂(H₂O)₂(B₁₂F₁₂) is 2.972(2) Å, and is comparable to the 2.951(3) Å O(H) \cdots F distance for Li₂(H₂O)₄(B₁₂F₁₂). The O–H bonds for the one unique water molecule in K₂(H₂O)₂(B₁₂F₁₂) have nearly identical O–H \cdots F hydrogen bonding environments, and the O–H oscillators of the H₂O molecule are strongly coupled (as in H₂O(g)) to produce two ν (OH) bands at 3636 and 3576.³⁸ (The corresponding bands for H₂O(g) are 3756 and 3576 cm⁻¹.⁶²) Significantly, the O–H oscillator of the two H₂O molecules in the K₂(H₂O)₂ quadrilateral are not coupled. Finally, the isotopolog K₂(HOD)(D₂O)(B₁₂F₁₂) exhibits a single

$\nu(\text{OH})$ band at 3604 cm^{-1} , halfway between 3636 and 3576 cm^{-1} . This is indicative of a single unique O–H \cdots F hydrogen bonding environment, in $\text{K}_2(\text{H}_2\text{O})_2(\text{B}_{12}\text{F}_{12})$

3.3.4 ATR-FTIR Spectra of $\text{Li}_2(\text{H}_2\text{O})_4(\text{B}_{12}\text{F}_{12})$ and Its Deuterated Isotopologs

The spectrum of $\text{Li}_2(\text{H}_2\text{O})_4(\text{B}_{12}\text{F}_{12})$, shown in Figure 3.9 and 3.10, is fundamentally different than the spectrum of $\text{K}_2(\text{H}_2\text{O})_2(\text{B}_{12}\text{F}_{12})$ and the other alkali metal $\text{B}_{12}\text{F}_{12}^{2-}$ salt hydrates. In the spectrum of $\text{Li}_2(\text{H}_2\text{O})_4(\text{B}_{12}\text{F}_{12})$ the two $\nu(\text{OH})$ bands, at 3583 and 3401 cm^{-1} , are much broader and significantly more red-shifted than the $\text{K}_2(\text{H}_2\text{O})_2(\text{B}_{12}\text{F}_{12})$ $\nu(\text{OH})$ bands at 3636 and 3576 cm^{-1} . Furthermore, the $\text{Li}_2(\text{H}_2\text{O})_4(\text{B}_{12}\text{F}_{12})$ $\nu(\text{OH})$ bands are separated by 183 cm^{-1} , three times greater than the separation of the $\text{K}_2(\text{H}_2\text{O})_2(\text{B}_{12}\text{F}_{12})$ $\nu(\text{OH})$ bands (60 cm^{-1}). This is because the O–H bonds on each H_2O molecule in $\text{Li}_2(\text{H}_2\text{O})_4(\text{B}_{12}\text{F}_{12})$ are in substantially different environments.

The spectrum of $\text{Li}_2(\text{HOD})(\text{D}_2\text{O})_3(\text{B}_{12}\text{F}_{12})$ is also shown in Figure 3.9. There are two $\nu(\text{OH})$ bands only slightly shifted from the $\nu(\text{OH})$ band position for $\text{Li}_2(\text{H}_2\text{O})_4(\text{B}_{12}\text{F}_{12})$. Significantly, the $\nu(\text{OH})$ bands for $\text{Li}_2(\text{HOD})(\text{D}_2\text{O})_3(\text{B}_{12}\text{F}_{12})$ are narrower and more symmetric than the $\nu(\text{OH})$ bands for $\text{Li}_2(\text{H}_2\text{O})_4(\text{B}_{12}\text{F}_{12})$. Several conclusions can be drawn from these observations. First, the coupling of the O–H_f and O–H_b oscillators on each H_2O molecule in $\text{Li}_2(\text{H}_2\text{O})_4(\text{B}_{12}\text{F}_{12})$ is not as strong as in $\text{K}_2(\text{H}_2\text{O})_2(\text{B}_{12}\text{F}_{12})$, undoubtedly because the O–H \cdots F and O–H \cdots O stretching vibrations in $\text{Li}_2(\text{H}_2\text{O})_4(\text{B}_{12}\text{F}_{12})$ have significantly different energies. When only one O–H bond per water cluster is present in either type of $\text{Li}_2(\text{HOD})(\text{D}_2\text{O})_3(\text{B}_{12}\text{F}_{12})$ formula unit, independent $\nu(\text{O–H}\cdots\text{F})$ and $\nu(\text{O–H}\cdots\text{O})$ bands are observed at 3587 and 3411 cm^{-1} , respectively. Therefore, coupling of the O–H \cdots F and O–H \cdots O stretches in each $\text{Li}_2(\text{H}_2\text{O})_4(\text{B}_{12}\text{F}_{12})$ formula unit, albeit weak, may have resulted in shifts of the $\nu(\text{OH})$ bands from 3587 and 3411 cm^{-1} in $\text{Li}_2(\text{HOD})(\text{D}_2\text{O})_3(\text{B}_{12}\text{F}_{12})$ to 3583 and 3401 cm^{-1} respectively, in $\text{Li}_2(\text{H}_2\text{O})_4(\text{B}_{12}\text{F}_{12})$. If true, these observations represent the first experimental evidence that the bond-stretching normal modes for O–H_b and O–H_f bonds in a cyclic $(\text{H}_2\text{O})_n$ cluster are not independent. They may be weakly coupled. An alternative explanation, suggested by a reviewer of the author's paper *Room-Temperature FTIR Spectra of the Cyclic S_4 $(\text{H}_2\text{O})_4$ Cluster in Crystalline $\text{Li}_2(\text{H}_2\text{O})_4(\text{B}_{12}\text{F}_{12})$: Observation of B and E $\nu(\text{OH})$ Bands and Coupling of Strong O–H \cdots O and Weak O–H \cdots F Vibrations*,⁶³ which the work in this chapter is based on, is that the shifts may be due

to “the loss of E mode opposite-side OH coupling rather than the loss of O–H_f to O–H_b coupling.” However, my tentative conclusion is that the first explanation is the more likely explanation.

The FTIR spectra of Li₂(D₂O)₄(B₁₂F₁₂) and Li₂(HOD)(H₂O)₃(B₁₂F₁₂) tell the same story. The independent $\nu(\text{O–D}\cdots\text{F})$ and $\nu(\text{O–D}\cdots\text{O})$ bands for different Li₂(HOD)(H₂O)₃(B₁₂F₁₂) formula units are at 2642 and 2518 cm⁻¹ respectively [$\Delta\nu(\text{OD}) = 124 \text{ cm}^{-1}$]. For Li₂(D₂O)₄(B₁₂F₁₂), weak coupling of the O–D \cdots F and O–D \cdots O stretching vibrations results in $\nu(\text{OD})$ bands that are broader, not as symmetric, and shifted, in opposite directions, by only 9 and 5 cm⁻¹, respectively, to 2651 and 2513 cm⁻¹.

The weak coupling notwithstanding, the bands at 3401 and 2513 cm⁻¹ in the spectra of Li₂(H₂O)₄(B₁₂F₁₂) and Li₂(D₂O)₄(B₁₂F₁₂), respectively, are primarily due to the O–H \cdots O bond stretching in Li₂(H₂O)₄(B₁₂F₁₂) and O–D \cdots O bond stretching in Li₂(D₂O)₄(B₁₂F₁₂). The shoulders on these bands suggest the presence of an additional unresolved band. The 3401 and 2513 cm⁻¹ bands could not be fit by with a single Lorentzian function, but were successfully fit by a pair of Lorentzian functions, as shown in Figure 3.12. In contrast, the $\nu(\text{OH})$ band at 3411 cm⁻¹ in the spectrum of Li₂(HOD)(D₂O)₃(B₁₂F₁₂) and the $\nu(\text{OD})$ band at 2518 cm⁻¹ in the spectrum of Li₂(HOD)(H₂O)₃(B₁₂F₁₂) were successfully fit with a single Lorentzian function, as also shown in Figure 3.12.

The $\nu(\text{OH})$ and $\nu(\text{OD})$ stretching frequencies for Li₂(H₂O)₄(B₁₂F₁₂) and isotopomers of its deuterated isotopologs are listed in Table 3.2, which also includes experimental $\nu(\text{OH})$ and $\nu(\text{OD})$ values assigned to cyclic (H₂O)₄ and (D₂O)₄ clusters in the gas phase, in liquid He droplets, and in noble gas matrices; these values come from spectra presented in Figure 3.1–3.4.^{9,11,14,31–32,41,43} It appears that the coordination of the (H₂O)₄ tetramers to the Li⁺ ions in Li₂(H₂O)₄(B₁₂F₁₂) and Li₂(D₂O)₄(B₁₂F₁₂) does not significantly affect $\nu(\text{OH}_b)$ and $\nu(\text{OD}_b)$, respectively, relative to the gas phase or matrix isolated (H₂O)₄ clusters. The main 3401 cm⁻¹ $\nu(\text{OH}_b)$ band for Li₂(H₂O)₄(B₁₂F₁₂) (FWHM 67 cm⁻¹) is between the 3416 $\nu(\text{OH}_b)$ band for gas phase (H₂O)₄ (FWHM 58 cm⁻¹) and the 3383 $\nu(\text{OH}_b)$ band for (H₂O)₄ in a Ne matrix at 9 K. The main 2513 cm⁻¹ $\nu(\text{OD}_b)$ band for Li₂(D₂O)₄(B₁₂F₁₂) is within 12 cm⁻¹ of the 2501 $\nu(\text{OD}_b)$ band for gas phase (D₂O)₄ and 21 cm⁻¹ of the 2492 $\nu(\text{OD}_b)$ band for (D₂O)₄ in a Ne matrix at 7K. There has been only one mixed-isotope cyclic water tetramer studied by IR spectroscopy prior to this work.¹⁴ The 3374 $\nu(\text{OH}_b)$ band for [(HOD)(H₂O)₃] in a Ne matrix at 9 K is red-shifted 9 cm⁻¹ from the 3383 $\nu(\text{OH}_b)$ band for (H₂O)₄ under the same conditions.

For comparison, the 3411 $\nu(\text{OH}_b)$ band for $\text{Li}_2(\text{HOD})(\text{D}_2\text{O})_3(\text{B}_{12}\text{F}_{12})$ is blue-shifted by 10 cm^{-1} from the 3401 $\nu(\text{OH}_b)$ band for $\text{Li}_2(\text{H}_2\text{O})_4(\text{B}_{12}\text{F}_{12})$.

On the other hand, the main 3583 cm^{-1} $\nu(\text{OH}_f)$ band for $\text{Li}_2(\text{H}_2\text{O})_4(\text{B}_{12}\text{F}_{12})$ is more than 100 cm^{-1} lower than the 3714 $\nu(\text{OH}_f)$ band for gas phase $(\text{H}_2\text{O})_4$ or the 3695 $\nu(\text{OH}_f)$ band for $(\text{H}_2\text{O})_4$ in an Ar matrix at 30 K. The corresponding $\nu(\text{OD}_f)$ differences for $\text{Li}_2(\text{D}_2\text{O})_4(\text{B}_{12}\text{F}_{12})$ vs. $(\text{D}_2\text{O})_4$ in a Ne matrix at 9 K is also more than 100 cm^{-1} . These differences are undoubtedly due to the O–H \cdots F and O–D \cdots F hydrogen bonds in the lithium compounds. Similarly, the 3658 and 3588 cm^{-1} $\nu(\text{OH})$ values for crystalline $\text{Cs}_2(\text{H}_2\text{O})(\text{B}_{12}\text{F}_{12})$, in which the coordinated monomeric H_2O molecule participates in two O–H \cdots F hydrogen bonds, are 98 and 67 cm^{-1} lower than the 3756 and 3657 $\nu(\text{OH})$ values for monomeric $\text{H}_2\text{O}(\text{g})$, respectively.³⁸

Therefore, even weak O–H \cdots F hydrogen bonding has a significantly larger effect on the H_2O $\nu(\text{OH})$ values than does coordination of H_2O to Li^+ in $\text{Li}_2(\text{H}_2\text{O})_4(\text{B}_{12}\text{F}_{12})$. However, coordination of a single H_2O molecule to Li^+ in the gas phase, in the absence of any hydrogen binding, is predicted to lower $\nu_{\text{asym}}(\text{OH})$ by 85 cm^{-1} and $\nu_{\text{sym}}(\text{OH})$ by 27 cm^{-1} .⁶⁴ Experimentally, the IR spectrum of the evaporatively cooled gas-phase $[\text{Ar-Na-OH}_2]^+$ cation exhibited $\nu_{\text{asym}}(\text{OH})$ and $\nu_{\text{sym}}(\text{OH})$ bands that were 49 and 23 cm^{-1} lower, respectively, than the corresponding values for $\text{H}_2\text{O}(\text{g})$.⁶⁵ The reason why the $\nu(\text{OH}_b)$ shift is so small for $\text{Li}_2(\text{H}_2\text{O})_4(\text{B}_{12}\text{F}_{12})$ is probably because of the coordination of Li^+ to two H_2O molecules and four F atoms in $\text{Li}_2(\text{H}_2\text{O})_4(\text{B}_{12}\text{F}_{12})$ significantly lowers its Lewis acidity and/or polarizing ability relative to a bare Li^+ ion.

The spectra in Figure 3.14, 3.15, and 3.16 show the 1637 and 1656 cm^{-1} $\delta(\text{HOH})$ bands for $\text{Li}_2(\text{H}_2\text{O})_4(\text{B}_{12}\text{F}_{12})$ and the 1202 cm^{-1} $\delta(\text{DOD})$ band for $\text{Li}_2(\text{D}_2\text{O})_4(\text{B}_{12}\text{F}_{12})$. These values are compared with the corresponding values for $\text{H}_2\text{O}(\text{g})$ and both calculated and matrix isolated $(\text{H}_2\text{O})_4$ clusters in Table 3.3. In all but one of the reports of experimental FTIR result, two $\delta(\text{HOH})$ bands were observed, one at 1608–1637 cm^{-1} and one at 1624–1660 cm^{-1} , with separations of the two band positions of 12–21 cm^{-1} (the separation in the spectrum of $\text{Li}_2(\text{H}_2\text{O})_4(\text{B}_{12}\text{F}_{12})$ is 19 cm^{-1} (1656–1637 cm^{-1} = 19 cm^{-1})). The two broad, overlapped $\delta(\text{HOH})$ bands observed at 1629 and 1641 cm^{-1} for the presumed S_4 $(\text{H}_2\text{O})_4$ cluster in liquid He droplets are shown in Figure 3.21.

It has long been known that hydrogen bonds involving D are more stable than those involving H, all other things being equal.^{4,66-70} A consequence of the ca. 60 cm^{-1} (ca. 0.72 kJ mol^{-1}) energy difference between

the HO–D···OH₂ and DO–H···OH₂ water dimer isotopomers is that only the former deuterium-bonded structure (which will be abbreviated [(H_fOD_b)(H₂O)]) was observed in an Ar matrix below 10 K.⁶⁷⁻⁶⁹ Anick calculated virtually the same energy difference for the *S*₄ water tetramer isotopomers [(H_fOD_b)(H₂O)₃] and [(D_fOH_b)(H₂O)₃].⁴ With such a small energy difference, it is not surprising that there are two ν(OH) bands in the room temperature spectrum of Li₂(HOD)(D₂O)₃(B₁₂F₁₂) and two ν(OD) bands in the room temperature spectrum of Li₂(HOD)(H₂O)₃(B₁₂F₁₂).

3.3.5 Assignment of O–H Stretching and H–O–H Bending Normal Modes to Bands in Vibrational Spectra of Cyclic *S*₄ (H₂O)₄ Clusters.

The 12 O–H_f, O–H_b, and H_f–O–H_b normal modes for *S*₄ (H₂O)₄ cluster are shown in Figure 3.22. The letter designation are the symmetries (the irreducible representation) for each mode. The individual drawings are simplifications of the relative motions of the atoms during the indicated vibration. This is justified because the mixing of modes of the same symmetry will be small if the vibrations are separated by hundreds of wavenumbers (e.g., for gas phase *S*₄ (H₂O)₄,⁴¹ δ(HOH) = 1629 cm⁻¹, ν(OH_b) = 3416 cm⁻¹, and ν(OH_f) = 3714 cm⁻¹). Even when ν(OH_b) and ν(OH_f) are only separated by 182 cm⁻¹, as in Li₂(H₂O)₄(B₁₂F₁₂), the mixing of these modes only resulted in band position shifts of 5–10 cm⁻¹. Additionally, The A normal modes can be ignored because they are not infrared active.

DFT calculations by Ceponkus, Uvdal, and Nelander in 2012 predicted B and E fundamental ν(OH_b) frequencies for an isolated *S*₄ (H₂O)₄ cluster to be 3484 and 3445 cm⁻¹, respectively.¹⁴ DFT calculations by Vasylieva, Doroshenko, et al. in 2019 predicted the B and E ν(OH_b) frequencies to be 3331 and 3288 cm⁻¹, respectively.³² CCSD(T)/aug-cc-pVDZ calculations by Miliordos, Aprà, and Xantheas in 2013 predicted B and E ν(OH_b) frequencies to be 3385 and 3357 cm⁻¹, respectively.¹⁹ In these three studies, the separation of the E ν(OH_b) band from the higher wavenumber B band was 28-43 cm⁻¹. In all three cases, the higher wavenumber B normal mode is predicted to give rise to a less intense band than the band for the combined E normal modes. Ceponkus, Uvdal, and Nelander hypothesize that the doubly degenerate E band, with be significantly more intense than the B band.¹⁴ Vasylieva, Doroshenko, et al. calculated the integrated intensity of the 3331 (B) and 3288 (E) cm⁻¹ bands as 29.1 and 1467 arb. units, respectively, for vacuum and 29.7 and 1549.5 arb. units, respectively, for an argon matrix. The ratio of these two bands (E/B) are 50.4 and 52.2,

respectively. The integrated intensities for the proposed B and E bands at 3596 and 3583 cm^{-1} , respectively, in Figure 3.13 are 0.2417 and 8.4753 arb. units resulting in a E/B ratio of 35.07. This ratio is consistent with the hypothesis by Ceponkus, Uvdal, and Nelander that the E band will be significantly more intense than the B band, and while the observed ratio is not as large as the calculated ratios by Vasylieva, Doroshenko, et al., deviations between experimental and computational models are not uncommon, coupled with fact that the environments are significantly different (O–H \cdots F hydrogen bond vs O–H \cdots Ar induced dipole) can potentially account for this difference.

The author's interpretation of the lower intensity band at 3441 and 2538 cm^{-1} in the two-peak Lorentzian fitted spectra in Figure 3.12 is that they represent the B normal mode for the four coupled O–H \cdots O hydrogen bonds in $\text{Li}_2(\text{H}_2\text{O})_4(\text{B}_{12}\text{F}_{12})$ and the four coupled O–D \cdots O hydrogen bonds in $\text{Li}_2(\text{D}_2\text{O})_4(\text{B}_{12}\text{F}_{12})$, respectively, while the much more intense bands at 3401 and 2513 cm^{-1} represent the corresponding E normal modes. Figure 3.13 shows that the $\nu(\text{O–H}\cdots\text{O})$ and $\nu(\text{O–H}\cdots\text{F})$ bands in the spectrum of $\text{Li}_2(\text{H}_2\text{O})_4(\text{B}_{12}\text{F}_{12})$ may both have an unresolved, lower-intensity B symmetry band at higher wavenumbers. The shoulder on the higher-wavenumber side of the 3583 cm^{-1} $\nu(\text{OH}_f)$ band is not as pronounced as the shoulder on the higher-wavenumber side of the 3401 cm^{-1} $\nu(\text{OH}_b)$ band. Nevertheless, fitting the 3583 cm^{-1} band with two Lorentzian functions resulted in a better fit than with a single Lorentzian function. In some studies, higher-wavenumber shoulders can be seen on $\nu(\text{OH}_b)$ or $\nu(\text{OD}_b)$ bands assigned to S_4 $(\text{H}_2\text{O})_4$ or $(\text{D}_2\text{O})_4$ clusters in noble gas matrices or in the gas phase. Some examples are shown in Figure 3.1, 3.3, and 3.4.^{14,31,43} Only in the cases of the gas phase IR cavity ringdown spectra of $(\text{D}_2\text{O})_4$ (Figure 3.4) and $(\text{H}_2\text{O})_4$ (Figure 3.23) were the shoulders explicitly attributed to $\nu(\text{OD}_b)$ or $\nu(\text{OH}_b)$ band splitting.⁴³ However, the shoulder in the spectrum of $(\text{D}_2\text{O})_4$ was estimated to represent a band only 4 cm^{-1} higher than the main $\nu(\text{OD}_b)$ band, not ca. 25 cm^{-1} as in the spectrum of $\text{Li}_2(\text{D}_2\text{O})_4(\text{B}_{12}\text{F}_{12})$. In contrast, the shoulder was estimated to be 26 cm^{-1} higher in energy in the IR cavity ringdown spectrum of $(\text{H}_2\text{O})_4$, as shown in Figure 3.23.⁴³ The $\nu(\text{OD}_b)$ band in the spectrum of $(\text{D}_2\text{O})_4$ in a Ne matrix at 9 K was split into three bands with very small separations, at 2489, 2492, and 2494 cm^{-1} , although only “a smooth symmetric band at 3383 cm^{-1} ” was observed in the spectrum of $(\text{H}_2\text{O})_4$ under the same conditions (this was the verbatim description of the 3383 cm^{-1} band in the spectrum shown in Figure 3.1).¹⁴

Figure 3.14 and 3.12 show that a higher-wavenumber shoulder on the $\delta(\text{HOH})$ band at 1637 cm^{-1} in the spectrum of $\text{Li}_2(\text{H}_2\text{O})_4(\text{B}_{12}\text{F}_{12})$ can be resolved to reveal a low-intensity band at 1656 cm^{-1} . I tentatively attribute this band to the $\delta(\text{HOH})$ B vibration. However, that assignment must remain tentative because the $\delta(\text{HOH})$ B vibration is predicted to be lower in energy than the $\delta(\text{HOH})$ E vibration in all of the theoretical papers cited in Table 3.3. It is possible that the lower-intensity, lower-wavenumber band is the E band and the higher-energy, higher-wavenumber band is the B band.

3.4 Conclusions and Future Work

3.4.1 Conclusions

ATR-FTIR spectra of crystalline samples that contain only one structurally well-characterized water cluster, either $S_4(\text{H}_2\text{O})_4$ or $S_4(\text{D}_2\text{O})_4$, or a mixture of $S_4(\text{H}_2\text{O})_4$ and a small percentage of $[(\text{HOD})(\text{D}_2\text{O})_3]$, or a mixture of $S_4(\text{D}_2\text{O})_4$ and a small percentage of $[(\text{HOD})(\text{H}_2\text{O})_3]$, suggest that (i) B and E normal modes gave rise to distinguishable $\nu(\text{OH}_b)$, $\nu(\text{OH}_f)$, and $\delta(\text{HOH})$ bands separated by 42, 13, and 19 cm^{-1} , respectively, in the room-temperature FTIR spectrum of $\text{Li}_2(\text{H}_2\text{O})_4(\text{B}_{12}\text{F}_{12})$; (ii) B and E normal modes gave rise to distinguishable $\nu(\text{OD}_b)$ bands separated by 20 cm^{-1} in the room-temperature FTIR spectrum of $\text{Li}_2(\text{D}_2\text{O})_4(\text{B}_{12}\text{F}_{12})$; (iii) coupling between the $\nu(\text{OD}_b)$ and $\nu(\text{OD}_f)$ normal modes, albeit weak, may be responsible for the observed shifts of $4\text{--}10\text{ cm}^{-1}$ for the respective bands in the spectra of $\text{Li}_2(\text{H}_2\text{O})_4(\text{B}_{12}\text{F}_{12})$ vs $\text{Li}_2(\text{HOD})(\text{D}_2\text{O})_3(\text{B}_{12}\text{F}_{12})$ or the spectra of $\text{Li}_2(\text{D}_2\text{O})_4(\text{B}_{12}\text{F}_{12})$ vs $\text{Li}_2(\text{HOD})(\text{H}_2\text{O})_3(\text{B}_{12}\text{F}_{12})$; and (iv) a $\delta(\text{DOD})$ band for an $S_4(\text{D}_2\text{O})_4$ cluster was observed for the first time at ca. 1202 cm^{-1} . In addition, the FTIR spectra of samples containing $[(\text{HOD})(\text{H}_2\text{O})_3]$ or $[(\text{HOD})(\text{D}_2\text{O})_3]$ clusters are the first examples in which bands that can be unambiguously assigned to both $\text{HO}\text{--}\text{D}\cdots\text{O}$ and $\text{DO}\text{--}\text{H}\cdots\text{O}$ hydrogen bonds in the same sample have been observed for R4 water tetramers.

3.4.2 Future Work

Based on the results presented in this chapter there are multiple avenues for continuation of this work. With access to an ATR-FTIR instrument with a sample chamber capable of reaching cryogenic temperatures investigation of the intensity ratios of the $\nu(\text{OH})$ and $\nu(\text{OD})$ bands corresponding to the $[(\text{H}_f\text{OD}_b)(\text{H}_2\text{O})_3]$ and $[(\text{D}_f\text{OH}_b)(\text{H}_2\text{O})_3]$ structures discussed in Section 3.3.5 can be performed. The hypothesis to be tested would be that “at cryogenic temperatures, the integrated intensity of the 3587 cm^{-1} band should increase relative to

the lower-wavenumber 3411 cm^{-1} band in the spectrum of $\text{Li}_2(\text{HOD})(\text{D}_2\text{O})_3(\text{B}_{12}\text{F}_{12})$, and the integrated intensity of the 2642 cm^{-1} band should decrease relative to the lower-wavenumber 2518 cm^{-1} band in the spectrum of $\text{Li}_2(\text{HOD})(\text{H}_2\text{O})_3(\text{B}_{12}\text{F}_{12})$.⁶³ This would represent the disappearance of the $\text{DO}-\text{H}\cdots\text{O}$ hydrogen bonds as the temperature decreased in favor of the more stable $\text{HO}-\text{D}\cdots\text{O}$ hydrogen bonds, allowing connection of the observed results in my room-temperature spectra of $\text{Li}_2(\text{HOD})(\text{H}_2\text{O})_3(\text{B}_{12}\text{F}_{12})$ and $\text{Li}_2(\text{HOD})(\text{D}_2\text{O})_3(\text{B}_{12}\text{F}_{12})$ to the cryogenic temperature results showing only the presence of $\text{HO}-\text{D}\cdots\text{O}$ hydrogen bonds.

Computational simulations of the IR spectra of $\text{Li}_2(\text{H}_2\text{O})_4(\text{B}_{12}\text{F}_{12})$, and the deuterated isotopologs covered in this chapter, by a theorist would complement the experimental work performed and allow for further testing of the conclusions drawn from the experimental data; specifically the apparent intramolecular coupling of the $\text{O}-\text{H}_b$ and $\text{O}-\text{H}_f$ oscillators in $\text{Li}_2(\text{H}_2\text{O})_4(\text{B}_{12}\text{F}_{12})$. By simulating the spectrum with and without coupling, the band position of $\nu(\text{O}-\text{H}_f)$ and $\nu(\text{O}-\text{H}_b)$ for both scenarios can be compared to the respective band position in $\text{Li}_2(\text{H}_2\text{O})_4(\text{B}_{12}\text{F}_{12})$ and $\text{Li}_2(\text{HOD})(\text{D}_2\text{O})_3(\text{B}_{12}\text{F}_{12})$. A similar study can also be performed for the $\text{O}-\text{D}_b$ and $\text{O}-\text{D}_f$ oscillators as well. Simulations may also help address the alternative explanation presented by the reviewer of the paper based on the work presented in this chapter.⁶³ By simulating the IR spectrum of the system after removing “E mode opposite-side OH coupling” their explanation can be tested as well.

Finally, as new compounds containing $(\text{H}_2\text{O})_n$ clusters are published, an effort to study those that also possess fluoroanions via similar experiments should be undertaken. Much of the ambiguity in the widely accepted low temperature matrix experiments has to do with the fact that multiple values of n are generated and studied simultaneously. Thus, while theory may assist in assignment of $\nu(\text{OH})$ and $\nu(\text{OD})$ bands, definitive assignment and determination of environmental effects on the $\nu(\text{OH})$ and $\nu(\text{OD})$ bands will have to come from compounds like $\text{Li}_2(\text{H}_2\text{O})_4(\text{B}_{12}\text{F}_{12})$ and its deuterated isotopologs. In part due to the very weak $\text{O}-\text{H}\cdots\text{F}$ hydrogen bonding allowing for resolution of the $\nu(\text{OH})$ bands at room temperature as discussed in the previous chapter of this dissertation.

References

1. Van Thiel, M.; Becker, E. D.; Pimentel, G. C. Infrared Studies of Hydrogen Bonding of Water by the Matrix Isolation Method. *J. Chem. Phys.* **1957**, *27*, 486–490.
2. Honegger, E.; Leutwyler, S. Intramolecular Vibrations of Small Water Clusters. *J. Chem. Phys.* **1988**, *88*, 2582–2595.
3. Xantheas, S. S.; Dunning, T. H. Ab Initio Studies of Cyclic Water Clusters (H₂O)_n, n = 1–6. I. Optimal Structures and Vibrational Spectra. *J. Chem. Phys.* **1993**, *99*, 8774–8792.
4. Anick, D. J. Proton and Deuteron Position Preferences in Water Clusters: An Ab Initio Study. *J. Chem. Phys.* **2005**, *123*, 244309.
5. Mascali, M.; Infantes, L.; Chisholm, J. Water oligomers in crystal hydrates--what's news and what isn't? *Angew. Chem. Int. Ed. Engl.* **2006**, *45*, 32–36.
6. Ludwig, R. Water: From Clusters to the Bulk *Angew. Chem. Int. Ed.* **2001**, *40*, 1808–1827.
7. Maheshwary, S.; Patel, N.; Sathyamurthy, N.; Kulkarni, A. D.; Gadre, S. R. Structure and Stability of Water Clusters (H₂O)_n, n = 8–20: An Ab Initio Investigation. *J. Phys. Chem. A* **2001**, *105*, 10525–10537.
8. Infantes, L.; Motherwell, S. Water Clusters in Organic Molecular Crystals. *CrystEngComm* **2002**, *4*, 454–461.
9. Burnham, C. J.; Xantheas, S. S.; Miller, M. A.; Applegate, B. E.; Miller, R. E. The Formation of Cyclic Water Complexes by Sequential Ring Insertion: Experiment and Theory. *J. Chem. Phys.* **2002**, *117*, 1109–1122.
10. Ewing, G. E. H₂O on NaCl: From Single Molecule, to Clusters, to Monolayer, to Thin Film, To Deliquescence *Struct. Bond.* Springer-Verlag: Berlin, 2005. *116*,
11. Hirabayashi, S.; Yamada, K. M. T. Infrared Spectra and Structure of Water Clusters Trapped in Argon and Krypton Matrices. *J. Mol. Struct.* **2006**, *795*, 78–83.
12. Qian, P.; Lu, L. N.; Song, W.; Yang, Z. Z. Study of Water Clusters in the n = 2–34 Size Regime, Based on the ABEEM/MM Model. *Theor. Chem. Acc.* **2009**, *123*, 487–500.
13. Zhu, X.; Feng, Y. F.; Li, M.; Li, M. L.; Zhang, Y. A Novel T4(1)6(1) Water Tape Encapsulated in a (3,3)-Connected 2D Copper Metal–Organic Framework. *CrystEngComm* **2012**, *14*, 79–89.

14. Ceponkus, J.; Uvdal, P.; Nelander, B. Water Tetramer, Pentamer, and Hexamer in Inert Matrices. *J. Phys. Chem. A* **2012**, *116*, 4842–4850.
15. Shukla, M.; Kharediya, B.; Srivastava, N.; Saha, S.; Sunkari, S. Water square (uudd) in novel Cu^{II} framework structures built from isomeric (aminomethyl)pyridines and oxalate: Synthesis, structure, spectral and DFT studies. *Polyhedron* **2013**, *54*, 164–172.
16. Chen, W. j.; Long, L. S.; Huang, R. B.; Zheng, L. S. A Dihalide–Decahydrate Cluster of [X₂(H₂O)₁₀]²⁻ in a Supramolecular Architecture of {[Na₂(H₂O)₆(H₂O@TMEQ[6])] \cdot 2(C₆H₅NO₃)} \cdot X₂(H₂O)₁₀ (TMEQ[6] = $\alpha,\alpha',\delta,\delta'$ -Tetramethylcucurbit[6]uril; X = Cl, Br). *Cryst. Growth Des.* **2013**, *13*, 2507–2513.
17. Ceponkus, J.; Engdahl, A.; Uvdal, P.; Nelander, B. Structure and Dynamics of Small Water Clusters, Trapped in Inert Matrices. *Chem. Phys. Lett.* **2013**, *581*, 1–9.
18. Nijem, N.; Canepa, P.; Kaipa, U.; Tan, K.; Roodenko, K.; Tekarli, S.; Halbert, J.; Oswald, W. H.; Arvapally, R. K.; Yang, C. Water Cluster Confinement and Methane Adsorption in the Hydrophobic Cavities of a Fluorinated Metal–Organic Framework. *J. Am. Chem. Soc.* **2013**, *135*, 12615–12626.
19. Miliordos, E.; Aprà, E.; Xantheas, S. S. Optimal Geometries and Harmonic Vibrational Frequencies of the Global Minima of Water Clusters (H₂O)_n, n = 2–6, and Several Hexamer Local Minima at the CCSD(T) Level of Theory. *J. Chem. Phys.* **2013**, *139*, 114302.
20. Howard, J. C.; Tschumper, G. S. Wavefunction Methods for the Accurate Characterization of Water Clusters. *WIREs Comput. Mol. Sci.* **2014**, *4*, 199–224.
21. Semerci, F.; Yeşilel, O. Z.; Ölmez, H.; Büyükgüngör, O. Supramolecular Assemblies of Copper(II)–pyridine-2,3-dicarboxylate Complexes with N-Donor Ligands and Clustered Water Molecules. *Inorg. Chim. Acta* **2014**, *409*, 407–417.
22. Otto, K. E.; Xue, Z.; Zielke, P.; Suhm, M. A. The Raman Spectrum of Isolated Water Clusters. *Phys. Chem. Chem. Phys.* **2014**, *16*, 9849–9858.
23. Zischang, J.; Suhm, M. A. The OH Stretching Spectrum of Warm Water Clusters. *J. Chem. Phys.* **2014**, *140*, 064312.
24. Howard, J. C.; Tschumper, G. S. Benchmark Structures and Harmonic Vibrational Frequencies Near the CCSD(T) Complete Basis Set Limit for Small Water Clusters: (H₂O)_n = 2, 3, 4, 5, 6. *J. Chem. Theory Comput.* **2015**, *11*, 2126–2136.
25. Miliordos, E.; Xantheas, S. S. An Accurate and Efficient Computational Protocol for Obtaining the Complete Basis Set Limits of the Binding Energies of Water Clusters at the MP2

- and CCSD(T) Levels of Theory: Application to $(\text{H}_2\text{O})_m$, $m = 2-6, 8, 11, 16$, and 17. *J. Chem. Phys.* **2015**, *142*, 234303.
26. Shukla, M. Raman Spectroscopic Study of Water Tetramer in $[\text{Cu}(\text{3-aminomethyl})\text{pyridine} \text{OH}2\text{oxalate} \cdot 2\text{H}_2\text{O}]_n$. *Polyhedron* **2016**, *105*, 200–204.
27. Wang, Y.; Bowman, J. M. Calculations of the IR Spectra of Bend Fundamentals of $(\text{H}_2\text{O})_n=3,4,5$ Using the WHBB_2 Potential and Dipole Moment Surfaces. *Phys. Chem. Chem. Phys.* **2016**, *18*, 24057–24062.
28. Pogorelov, V. Y.; Doroshenko, I. Y. Vibrational spectra of water clusters, trapped in low temperature matrices. *Low Temp. Phys.* **2016**, *42*, 1163–1166.
29. Douberly, G. E.; Miller, R. E.; Xantheas, S. S. Formation of Exotic Networks of Water Clusters in Helium Droplets Facilitated by the Presence of Neon Atoms. *J. Am. Chem. Soc.* **2017**, *139*, 4152–4156.
30. Ahmed, F.; Datta, J.; Sarkar, S.; Dutta, B.; Jana, A. D.; Ray, P. P.; Mir, M. H. Water Tetramer Confinement and Photosensitive Schottky Behavior of a 2D Coordination Polymer. *ChemistrySelect* **2018**, *3*, 6985–6991.
31. Shimazaki, Y.; Arakawa, I.; Yamakawa, K. D_2O Clusters Isolated in Rare-Gas Solids: Dependence of Infrared Spectrum on Concentration, Deposition Rate, Heating Temperature, and Matrix Material. *AIP Adv.* **2018**, *8*, No. 045313.
32. Vasylieva, A.; Doroshenko, I.; Doroshenko, O.; Pogorelov, V. Effect of Argon Environment on Small Water Clusters in Matrix Isolation. *Low Temp. Phys.* **2019**, *45*, 736–743.
33. Aida, M.; Akase, D. Hydrogen-Bond Pattern to Characterize Water Network. *Pure Appl. Chem.* **2019**, *91*, 301–316.
34. Schaefer, A.; Lanzilotto, V.; Cappel, U. B.; Uvdal, P.; Borg, A.; Sandell, A. Defect-Induced Water Bilayer Growth on Anatase $\text{TiO}_2(101)$. *Langmuir* **2018**, *34*, 10856–10864.
35. Anick, D. J. Static Density Functional Study of Graphene–Hexagonal Bilayer Ice Interaction. *J. Phys. Chem. A* **2014**, *118*, 7498–7506.
36. Anick, D. J. Zero Point Energy of Polyhedral Water Clusters. *J. Phys. Chem. A* **2005**, *109*, 5596–5601.
37. Lacroix, M. R.; Bukovsky, E. V.; Lozinsek, M.; Folsom, T. C.; Newell, B. S.; Liu, Y.; Peryshkov, D. V.; Strauss, S. H. Manifestations of Weak $\text{O}\cdots\text{H}\cdots\text{F}$ Hydrogen Bonding in

M(H₂O)_n(B₁₂F₁₂) Salt Hydrates: Unusually Sharp Fourier Transform Infrared ν (OH) Bands and Latent Porosity (M = Mg–Ba, Co, Ni, Zn). *Inorg. Chem.* **2018**, *57*, 14983–15000.

38. Lacroix, M. R.; Gao, X.; Liu, Y.; Strauss, S. H. Unusually sharp FTIR ν (OH) bands and very weak O–H···F hydrogen bonds in M₂(H₂O)_{1,2}B₁₂F₁₂ hydrates (M=Na–Cs). *J. Fluorine Chem.* **2019**, *217*, 105–108.

39. Yang, N.; Duong, C. H.; Kelleher, P. J.; McCoy, A. B.; Johnson, M. A. Deconstructing Water's Diffuse OH Stretching Vibrational Spectrum with Cold Clusters. *Science* **2019**, *364*, 275–278.

40. Fröchtenicht, R.; Kaloudis, M.; Koch, M.; Huisken, F. Vibrational Spectroscopy of Small Water Complexes Embedded in Large Liquid Helium Clusters. *J. Chem. Phys.* **1996**, *105*, 6128–6140.

41. Huisken, F.; Kaloudis, M.; Kulcke, A. Infrared Spectroscopy of Small Size-Selected Water Clusters. *J. Chem. Phys.* **1996**, *104*, 17–25.

42. Paul, J. B.; Collier, C. P.; Saykally, R. J.; Scherer, J. J.; O'Keefe, A. Direct Measurement of Water Cluster Concentrations by Infrared Cavity Ringdown Laser Absorption Spectroscopy. *J. Phys. Chem. A* **1997**, *101*, 5211–5214.

43. Paul, J. B.; Provencal, R. A.; Chapo, C.; Petterson, A.; Saykally, R. J. Infrared Cavity Ringdown Spectroscopy of Water Clusters: O–D Stretching Bands. *J. Chem. Phys.* **1998**, *109*, 10201–10206.

44. Infantes, L.; Chisholm, J.; Motherwell, S. Extended Motifs from Water and Chemical Functional Groups in Organic Molecular Crystals. *CrystEngComm* **2003**, *5*, 480–486.

45. Supriya, S.; Das, S. K. A Cyclic (H₂O)₄ Cluster Characterized in the Solid State Disappears on Heating and Regenerates from Water Vapor: A Supramolecular Reversible Gas–Solid Reaction. *New J. Chem.* **2003**, *27*, 1568–1574.

46. Fitzgerald, L. J.; Gallucci, J. C.; Gerken, R. E. Structures of Tetrapotassium, Tetrarubidium and Tetraesium 1,4,5,8-Naphthalenetetracarboxylate Hexahydrates. *Acta Crystallogr., Sect. C: Cryst. Struct. Commun.* **1993**, *49*, 1287–1294.

47. Johnson, B. J. S.; Schroden, R. C.; Zhu, C.; Stein, A. Synthesis and Characterization of 2D and 3D Structures from Organic Derivatives of Polyoxometalate Clusters: Role of Organic Moiety, Counterion, and Solvent. *Inorg. Chem.* **2001**, *40*, 5972–5978.

48. Iguchi, H.; Takaishi, S.; Breedlove, B. K.; Yamashita, M.; Matsuzaki, H.; Okamoto, H. Controlling the Electronic States and Physical Properties of MMXType Diplatinum-Iodide Chain Complexes via Binary Counteranions. *Inorg. Chem.* **2012**, *51*, 9967–9977.
49. Peryshkov, D. V.; Bukovsky, E. V.; Lacroix, M. R.; Wu, H.; Zhou, W.; Jones, W. M.; Lozinsek, M.; Folsom, T. C.; Heyliger, D. L.; Udovic, T. J.; Strauss, S. H. Latent Porosity in Alkali-Metal $M_2B_{12}F_{12}$ Salts: Structures and Rapid Room-Temperature Hydration/Dehydration Cycles. *Inorg. Chem.* **2017**, *56*, 12023–12041.
50. Lupinetti, A. J.; Strauss, S. H. Superweak Anions – Chemistry and Catalysis: a Symposium Report. *Chemtracts-Inorg. Chem.* **1998**, *11*, 565–595.
51. Cruzan, J. D.; Viant, M. R.; Brown, M. G.; Saykally, R. J. Tetrahertz LaserVibration–Rotation Tunneling Spectroscopy of the Water Tetramer. *J. Phys. Chem. A* **1997**, *101*, 9022–9031.
52. Schwan, R.; Kaufman, M.; Leicht, D.; Schwaab, G.; Havenith, M. Infrared Spectroscopy of the ν_2 Band of the Water Monomer and Small Water Clusters $(H_2O)_n=2,3,4$ in Helium Droplets. *Phys. Chem. Chem. Phys.* **2016**, *18*, 24063–24069.
53. Yang, Y.; Wang, E. G. Water on NaCl Surface: Adsorption, Diffusion, Dissolution, and Nucleation. *J. Comput. Theor. Nanosci.* **2008**, *5*, 247–268.
54. Peryshkov, D. V.; Popov, A. A.; Strauss, S. H. Latent porosity in potassium dodecafluoro-closo-dodecaborate(2-). Structures and rapid room temperature interconversions of crystalline $K_2B_{12}F_{12}$, $K_2(H_2O)_2B_{12}F_{12}$, and $K_2(H_2O)_4B_{12}F_{12}$ in the presence of water vapor. *J. Am. Chem. Soc.* **2010**, *132*, 13902–13913.
55. Zeng, G.; Holladay, S.; Langlois, D.; Zhang, Y.; Liu, Y. Kinetics of Heterogeneous Reaction of Ozone with Linoleic Acid and its Dependence on Temperature, Physical State, RH, and Ozone Concentration. *J. Phys. Chem. A* **2013**, *117*, 1963–1974.
56. Leng, C.; Hiltner, J.; Pham, H.; Kelley, J.; Mach, M.; Zhang, Y.; Liu, Y. Kinetics Study of Heterogeneous Reactions of Ozone with Erucic Acid Using an ATR-IR Flow Reactor. *Phys. Chem. Chem. Phys.* **2014**, *16*, 4350–4360.
57. Gao, X.; Zhang, Y.; Liu, Y. A Kinetics Study of the Heterogeneous Reaction of *n*-Butylamine with Succinic Acid Using an ATR-FTIR Flow Reactor. *Phys. Chem. Chem. Phys.* **2018**, *20*, 15464–15472.
58. Wang, Y.; Bowman, J. M. IR Spectra of the Water Hexamer: Theory, with Inclusion of the Monomer Bend Overtone, and Experiment Are in Agreement. *J. Phys. Chem. Lett.* **2013**, *4*, 1104–1108.

59. Yang, Y.; Meng, S.; Wang, E. G. Water Adsorption on a NaCl (001) Surface: A Density Functional Theory Study. *Phys. Rev. B* **2006**, *74*, 245409.
60. Ziegler, B.; Witzel, M.; Schwarten, M.; Babel, D. Neutron and X-ray Diffraction Studies on Powders and Single Crystals of Compounds Structurally Related to Prussian Blue: $(\text{CsMn}^{\text{II}}\text{Cr}^{\text{III}})(\text{CN})_6 \cdot \text{D}_2\text{O}$, $\text{NMe}_4\text{Mn}^{\text{II}}(\text{Cr}_{0,06}\text{Mn}_{0,94})^{\text{III}}(\text{CN})_6 \cdot 8\text{H}_2\text{O}$, $\text{NMe}_4\text{Mn}^{\text{II}}\text{Co}^{\text{III}}(\text{CN})_6 \cdot 8\text{H}_2\text{O}$, $\text{Mn}_3^{\text{II}}[\text{Mn}^{\text{III}}(\text{CN})_6]_2 \cdot 15\text{H}_2\text{O}$ and $\text{Cd}_3[\text{Fe}^{\text{III}}(\text{CN})_6]_2 \cdot 15\text{H}_2\text{O}$. *Z. Naturforsch. B: Chem. Sci.* **1999**, *54*, 870–876.
61. Zhao, J.; Dong, W. W.; Li, C.; Mou, Y. Q.; Mu, Z. H.; Li, D. S. Encapsulation of Discrete $(\text{H}_2\text{O})_4$ Clusters in a 1D Tube-Like Metal-Organic Coordination Polymer. *Synth. React. Inorg., Met.-Org., Nano-Met. Chem.* **2006**, *42*, 628–633.
62. Fraley, P. E.; Rao, K. N. High Resolution Infrared Spectra of Water Vapor ν_1 and ν_3 Bands of H_2^{16}O . *J. Mol. Spectrosc.* **1969**, *29*, 348–364.
63. Lacroix, M. R.; Liu, Y.; Strauss, S. H. Room-Temperature FTIR Spectra of the Cyclic S_4 $(\text{H}_2\text{O})_4$ Cluster in Crystalline $\text{Li}_2(\text{H}_2\text{O})_4(\text{B}_{12}\text{F}_{12})$: Observation of B and E $\nu(\text{OH})$ Bands and Coupling of Strong $\text{O}-\text{H}\cdots\text{O}$ and Weak $\text{O}-\text{H}\cdots\text{F}$ Vibrations. *The Journal of Physical Chemistry A* **2019**, *123*, 9781–9790.
64. Riera, M.; Brown, S. E.; Paesani, F. Isomeric Equilibria, Nuclear Quantum Effects, and Vibrational Spectra of $\text{M}^+(\text{H}_2\text{O})_n=1-3$ Clusters, with $\text{M} = \text{Li}, \text{Na}, \text{K}, \text{Rb},$ and Cs , through Many-Body Representations. *J. Phys. Chem. A* **2018**, *122*, 5811–5821.
65. Vaden, T. D.; Weinheimer, C. J.; Lisy, J. M. Evaporatively Cooled $\text{M}^+(\text{H}_2\text{O})\text{Ar}$ Cluster Ions: Infrared Spectroscopy and Internal Energy Conversion. *J. Chem. Phys.* **2004**, *121*, 3102–3107.
66. Shipman, L. L.; Owicki, C.; Scheraga, H. A. Structure, Energetics, and Dynamics of Water Dimer. *J. Phys. Chem. A* **1974**, *78*, 2055–2060.
67. Ayers, G. P.; Pullin, A. D. E. The I.R. Spectra of Matrix Isolated Water Species – I. Assignment of Bands to $(\text{H}_2\text{O})_2$, $(\text{D}_2\text{O})_2$, and HDO Dimer Species in Argon Matrices. *Spectrochim. Acta, Part A* **1976**, *32A*, 1629–1639.
68. Ayers, G. P.; Pullin, A. D. E. The I.R. Spectra of Matrix Isolated Water Species–IV. The Configuration of the Water Dimer in Argon Matrices. *Spectrochim. Acta, Part A* **1976**, *32A*, 1695–1704.
69. Engdahl, A.; Nelander, B. On the Relative Stabilities of H– and D– bonded Water Dimers. *J. Chem. Phys.* **1987**, *86*, 1819–1823.
70. Engdahl, A.; Nelander, B. Water in Krypton Matrices. *J. Mol. Struct.* **1989**, *193*, 101–109.

71. Paul, J. B.; Provencal, R. A.; Chapo, C.; Roth, K.; Casaes, R.; Saykally, R. J. Infrared Cavity Ringdown Spectroscopy of the Water Cluster Bending Vibrations. *J. Phys. Chem. A* **1999**, *103*, 2972-2974.
72. Watanade, Y.; Maeda, S.; Ohno, K. Intramolecular Vibrational Frequencies of Water Clusters $(\text{H}_2\text{O})_n$ ($n = 2-5$): Anharmonic Analyses Using Potential Functions Based on the Scaled Hypersphere Search Method. *J. Chem. Phys.* **2008**, *129*, No. 074315.

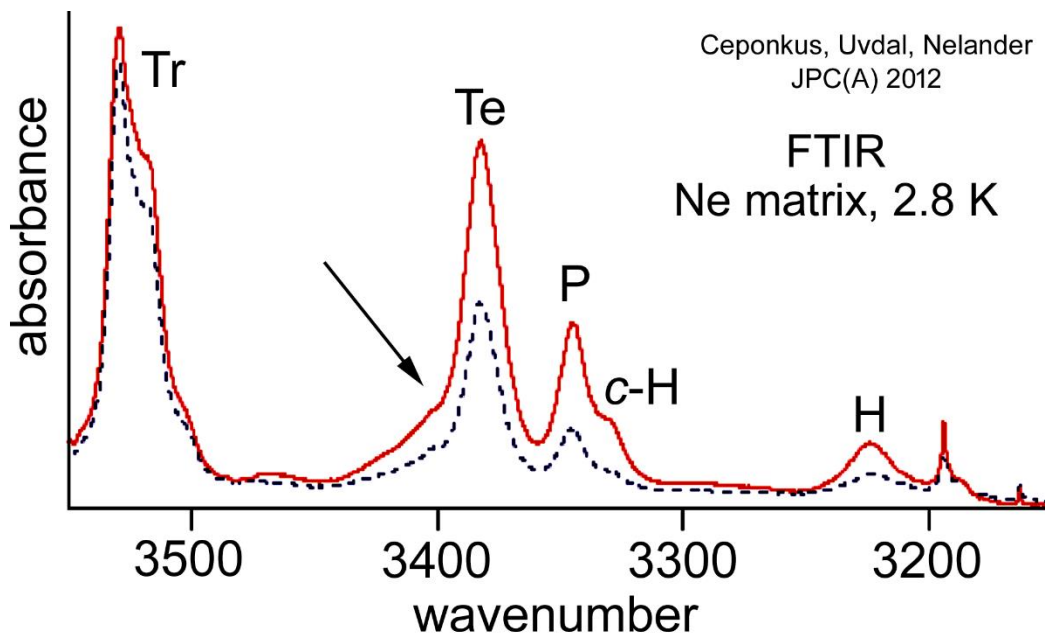


Figure 3.1. The $\nu(\text{OH}_b)$ region of a neon matrix with $(\text{H}_2\text{O})_n$ clusters ($n = 3-6$) ($\nu(\text{OH}_b)$ is an abbreviation for $\nu(\text{O}-\text{H}\cdots\text{O})$). This figure was modified from Figure 1 in ref 14. Abbreviations: Tr, trimer; Te, tetramer; P, pentamer; *c*-H, cyclic hexamer; H, hexamer. The dotted line spectrum was recorded first at 2.8 K. The solid red line spectrum was recorded at 2.8 K after warming to 8 K. The arrow, which has been added to the modified figure, points to a shoulder on the higher-wavenumber side of the peak assigned to the cyclic $(\text{H}_2\text{O})_4$ tetramer.

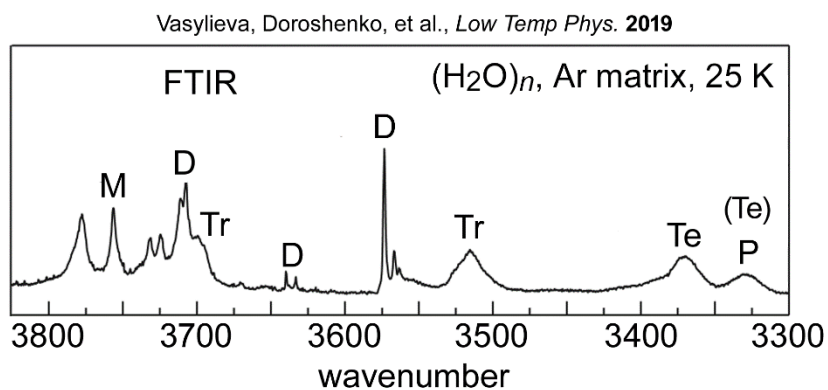
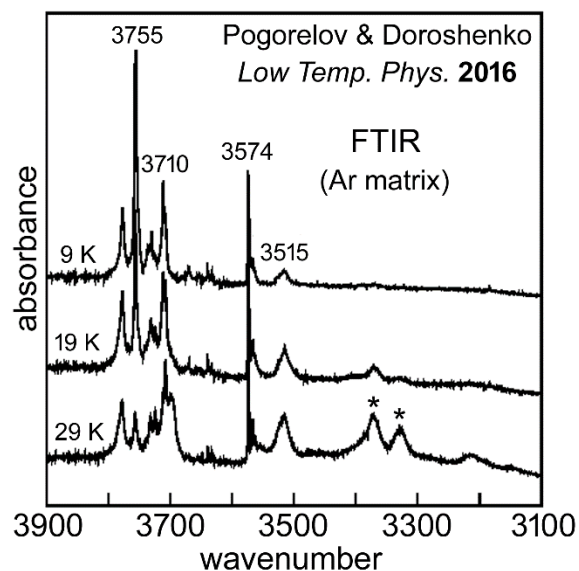


Figure 3.2. FTIR spectra of the $\nu(\text{OH})$ regions of argon matrices containing $(\text{H}_2\text{O})_n$ clusters ($n = 2\text{--}5$). The upper set of spectra was modified from Figure 4 in ref 28. The lower spectrum was adapted from Figure 4 in ref 32 (abbreviations: D, dimer; Tr, trimer; Te, tetramer; P, pentamer). In the 29 K spectrum in the upper set of spectra, the peaks marked with asterisks were assigned to a $(\text{H}_2\text{O})_4$ tetramer in Table 1 of ref 28 (the asterisks have been added to the modified figure for this work). In the lower spectrum, the peak marked with P, for pentamer, in the published spectrum, is now believed to belong to the tetramer (Prof. Iryna Doroshenko, personal communication to Professor Steve Strauss, July 2019). The label (Te) was added to the modified figure to represent the change in the assignment.

$(D_2O)_n$ in Ar at 5.3 K

Shimazaki, Arakawa, Yamakawa, *AIP Adv.* 2018

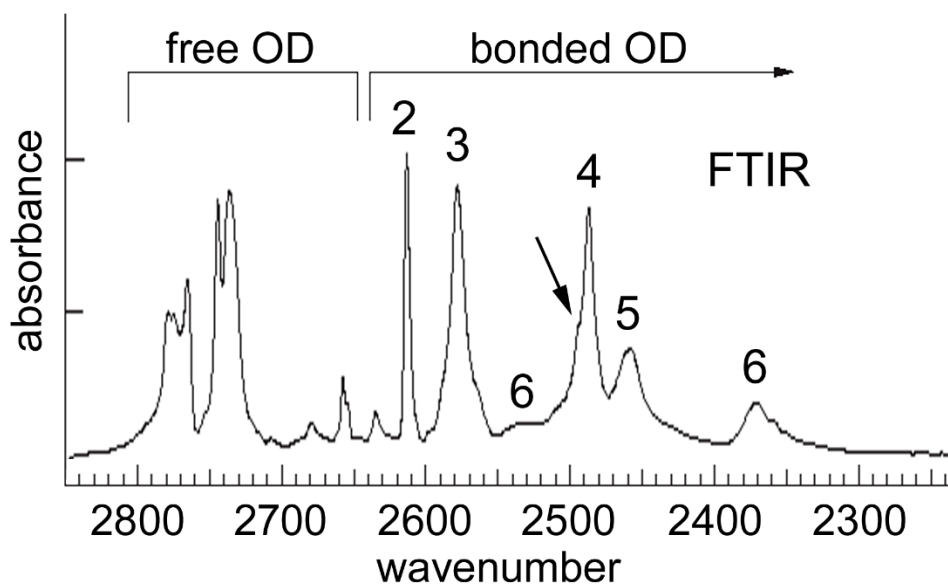


Figure 3.3. FTIR spectrum of $(D_2O)_n$ clusters in a frozen Ar matrix at 5.3 K ($Ar/D_2O = 400$). This figure was modified from Figure 1 in ref 3. The arrow, which has been added to the modified figure, points to a shoulder on the higher-wavenumber side of the peak assigned to the cyclic $(H_2O)_4$ tetramer.

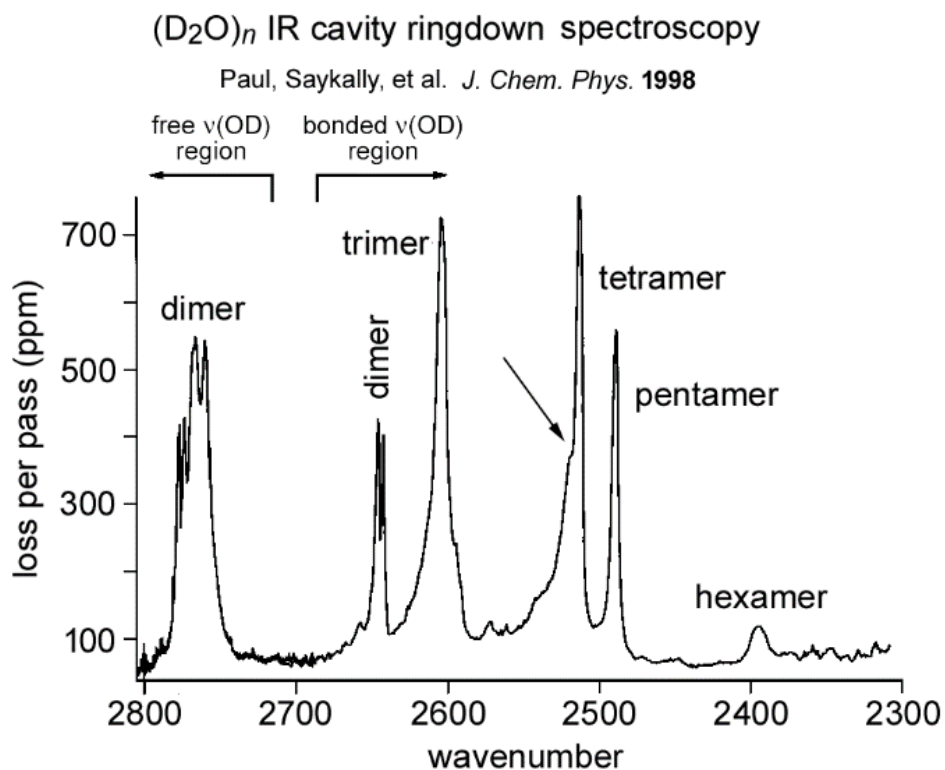


Figure 3.4. IR cavity ringdown spectrum in the $\nu(\text{OD})$ region of fully deuterated water clusters taken under expansion conditions favoring small clusters ($n \leq 6$). This figure was modified from Figure 1 in ref 43. The arrow, which has been added to the modified figure, points to a shoulder on the higher-wavenumber side of the peak assigned to the cyclic $(\text{H}_2\text{O})_4$ tetramer. The significance of this shoulder was discussed in ref 43.

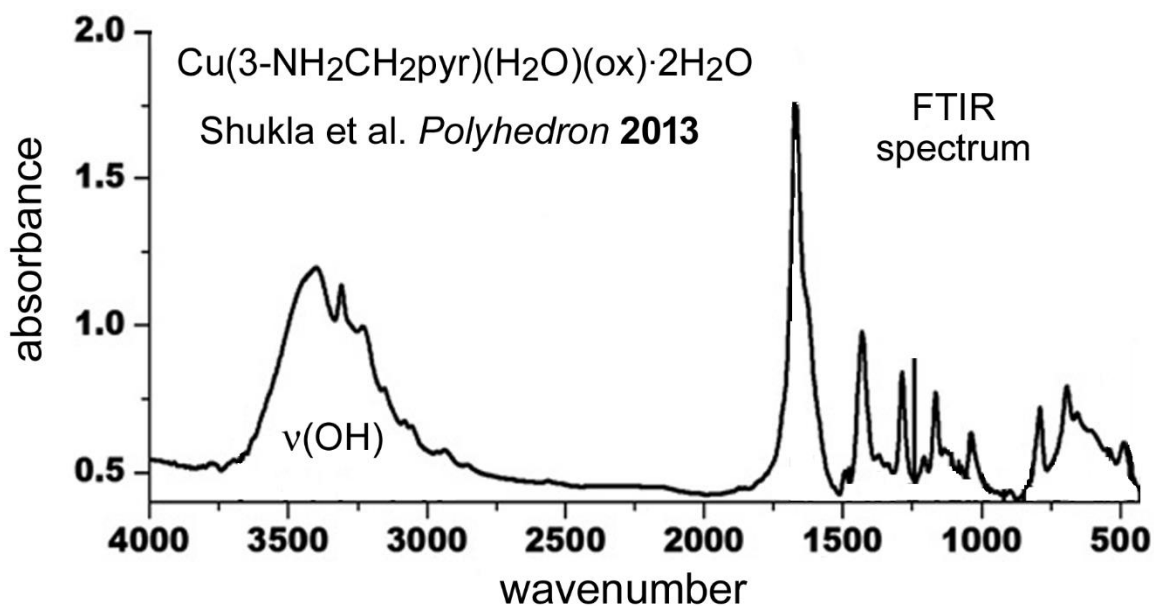


Figure 3.5. FTIR spectrum of $\nu(\text{OH})$ region of $\text{Cu}(3\text{-aminomethylpyridine})(\text{H}_2\text{O})(\text{oxalate}) \cdot 2\text{H}_2\text{O}$, which contains a cyclic $(\text{H}_2\text{O})_4$ tetramer as well as H_2O molecules coordinated to the Cu^{2+} ion. This figure was modified for this work from Figure 7 in ref 15.

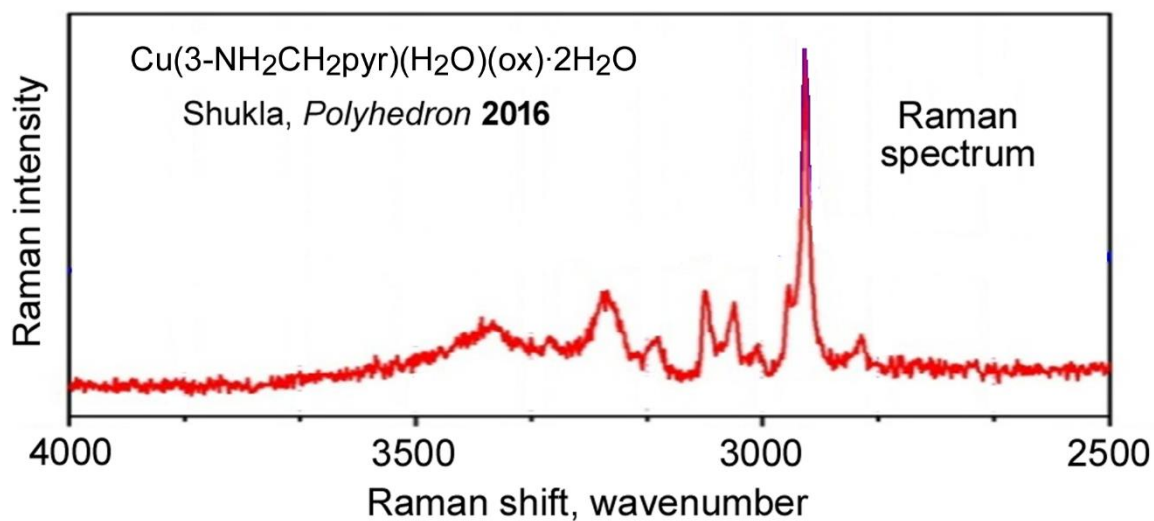
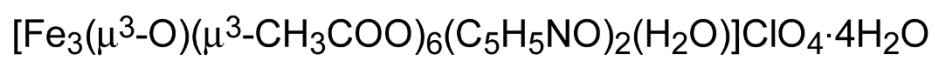


Figure 3.6. Raman spectrum of $\nu(\text{OH})$ region of $\text{Cu}(3\text{-aminomethylpyridine})(\text{OH}_2\text{oxalate})\cdot 2\text{H}_2\text{O}$, which contains a cyclic $(\text{H}_2\text{O})_4$ tetramer as well as H_2O molecules coordinated to the Cu^{2+} ion. This figure was modified for this work from Figure 3 in ref 26. The author listed $\nu(\text{OH})$ bands at 3388 and 3227 cm^{-1} as belonging to the $(\text{H}_2\text{O})_4$ tetramer and bands at 3306 and 3149 cm^{-1} as belonging to the coordinated H_2O molecule. Given the quality of the spectrum, these band positions must be considered approximate at best.



Supriya and Das, *New J. Chem.* **2003**

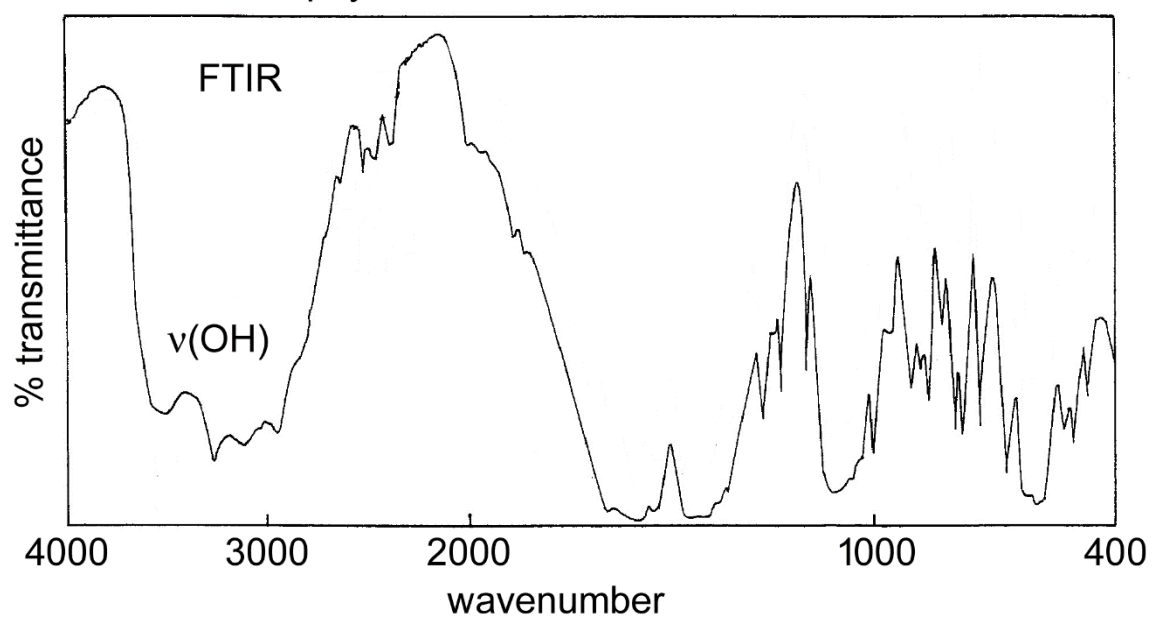


Figure 3.7. FTIR spectrum of $[\text{Fe}_3(\mu^3\text{-O})(\mu^2\text{-CH}_3\text{COO})_6(\text{C}_5\text{H}_5\text{NO})_2(\text{H}_2\text{O})]\text{ClO}_4 \cdot 4\text{H}_2\text{O}$. This figure was modified from Figure 5 in ref 45.

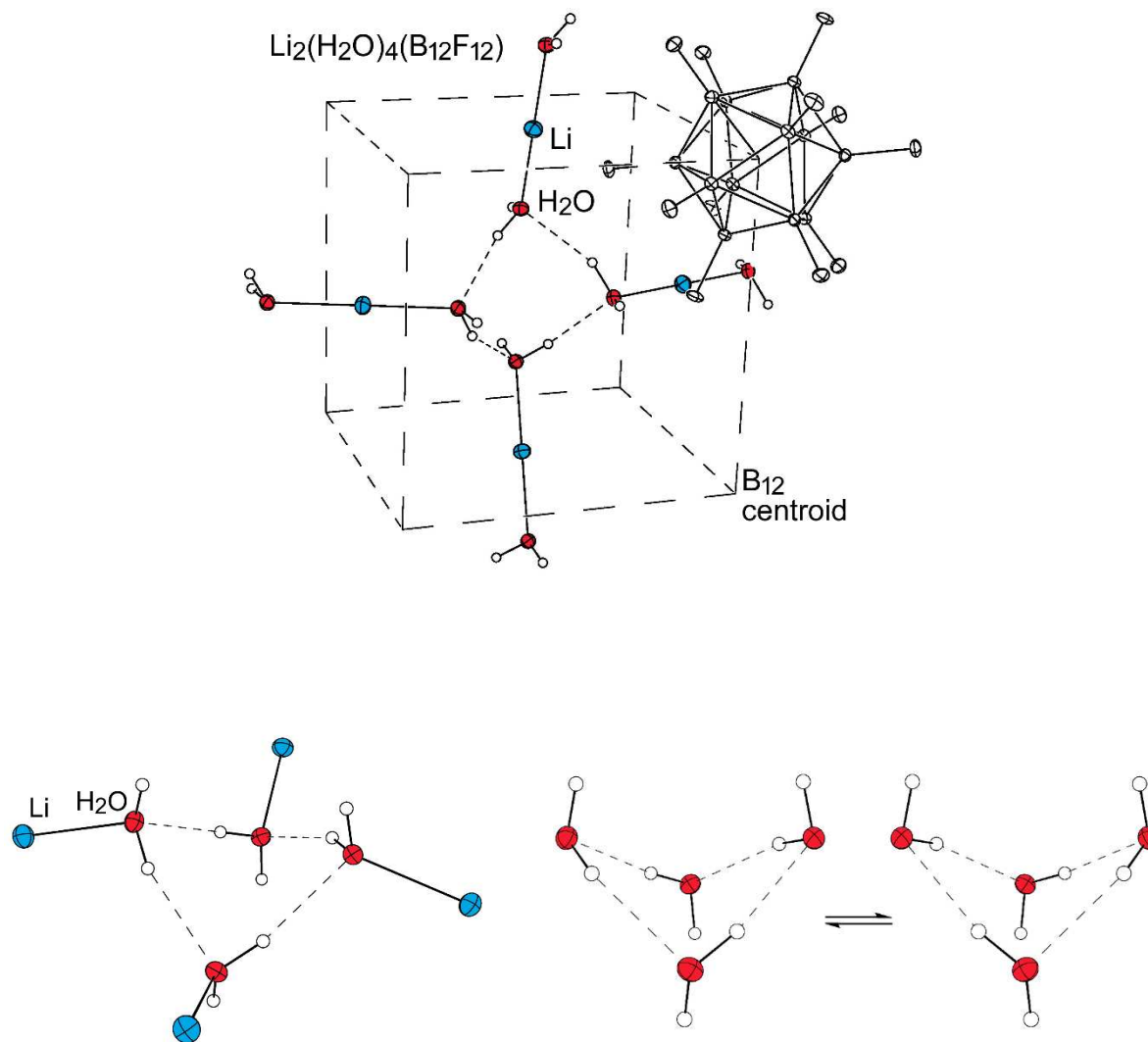


Figure 3.8. The X-ray crystal structure of $\text{Li}_2(\text{H}_2\text{O})_4(\text{B}_{12}\text{F}_{12})$ (50% probability ellipsoids except for H atoms; ref 49). The H_2O molecules are symmetry related. Ignoring the disorder of the H atoms that form the $\text{O}-\text{H}\cdots\text{O}$ hydrogen bonds (lower right), the $(\text{H}_2\text{O})_4$ cluster has S_4 point symmetry (the crystallographic symmetry is D_2). Each H_2O molecule participates in two $\text{O}-\text{H}\cdots\text{O}$ hydrogen bonds with $\text{O}(\text{H})\cdots\text{O}$ distances of 2.778(2) and 2.785(2) Å. The perpendicular displacements of the O atoms from the O_4 least-squares plane are ± 0.633 Å.

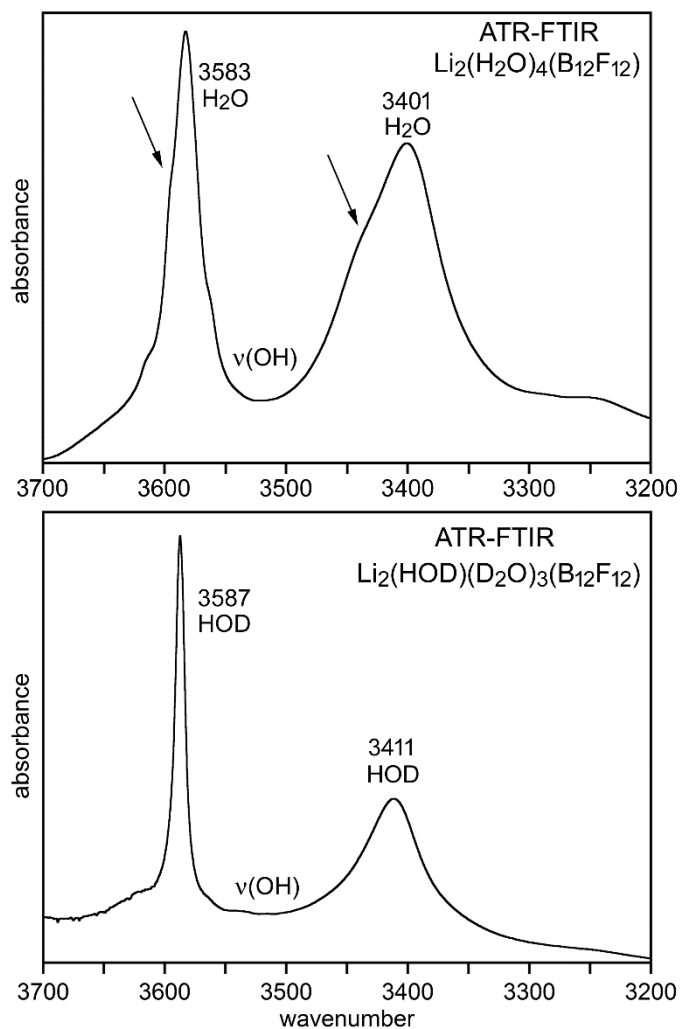


Figure 3.9. The ATR-FTIR $\nu(\text{OH})$ stretching region of microcrystalline samples of $\text{Li}_2(\text{H}_2\text{O})_4(\text{B}_{12}\text{F}_{12})$ (top) and $\text{Li}_2(\text{HOD})(\text{D}_2\text{O})_3(\text{B}_{12}\text{F}_{12})$ (bottom). The samples were prepared by evaporating aqueous solutions on the ZnSe ATR crystal. The solution for the sample of $\text{Li}_2(\text{HOD})(\text{D}_2\text{O})_3(\text{B}_{12}\text{F}_{12})$ was ca. 5–10% HOD and 90–95% D_2O . The majority species in that sample was $\text{Li}_2(\text{D}_2\text{O})_4(\text{B}_{12}\text{F}_{12})$. The arrows in the top spectrum point to shoulders that indicate an additional unresolved band under both of the main bands.

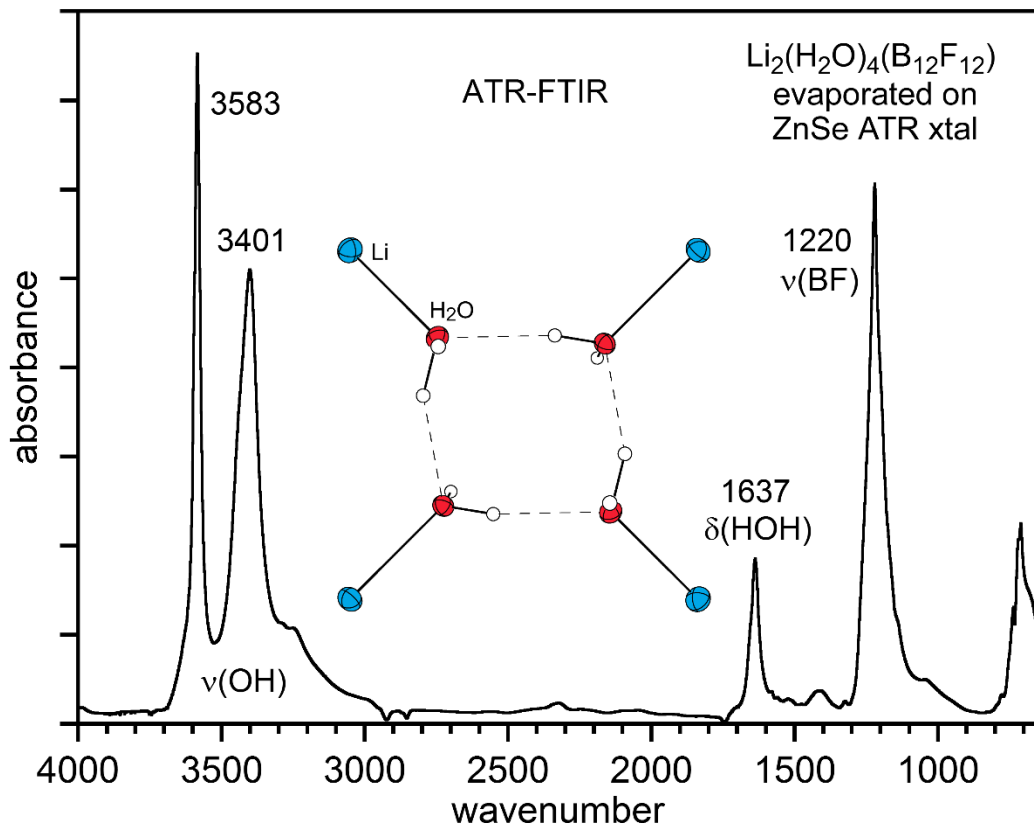


Figure 3.10. The entire ATR-FTIR spectrum of a microcrystalline sample of $\text{Li}_2(\text{H}_2\text{O})_4(\text{B}_{12}\text{F}_{12})$. The sample was prepared by evaporating an aqueous solution (100% H_2O) on the ZnSe ATR crystal. The inset shows the $(\text{H}_2\text{O})_4$ cluster with effective S_4 symmetry coordinated to four equivalent Li^+ ions. The least-squares plane of the four O atoms is in the plane of the page, and pairs of O atoms on opposite corners of the tetramer are displaced $\pm 0.663 \text{ \AA}$ from that plane.

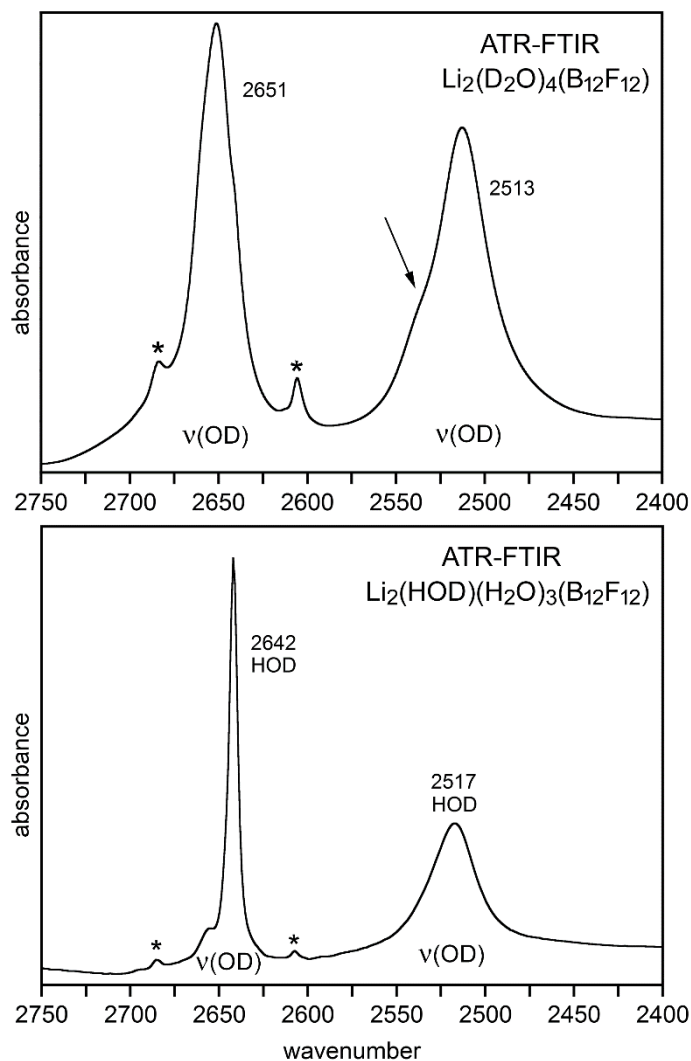


Figure 3.11. The ATR-FTIR $\nu(\text{OD})$ stretching region of microcrystalline samples of $\text{Li}_2(\text{D}_2\text{O})_4(\text{B}_{12}\text{F}_{12})$ (top) and $\text{Li}_2(\text{HOD})(\text{H}_2\text{O})_3(\text{B}_{12}\text{F}_{12})$ (bottom). The bands marked with asterisks are due to an impurity. The samples were prepared by evaporating aqueous solutions on the ZnSe ATR crystal. The solution for the sample of $\text{Li}_2(\text{HOD})(\text{H}_2\text{O})_3(\text{B}_{12}\text{F}_{12})$ was ca. 5–10% HOD and 90–95% H_2O . The majority species in that sample was $\text{Li}_2(\text{H}_2\text{O})_4(\text{B}_{12}\text{F}_{12})$. The arrow in the top spectrum point to a shoulder that indicates an additional unresolved band is present under the main band.

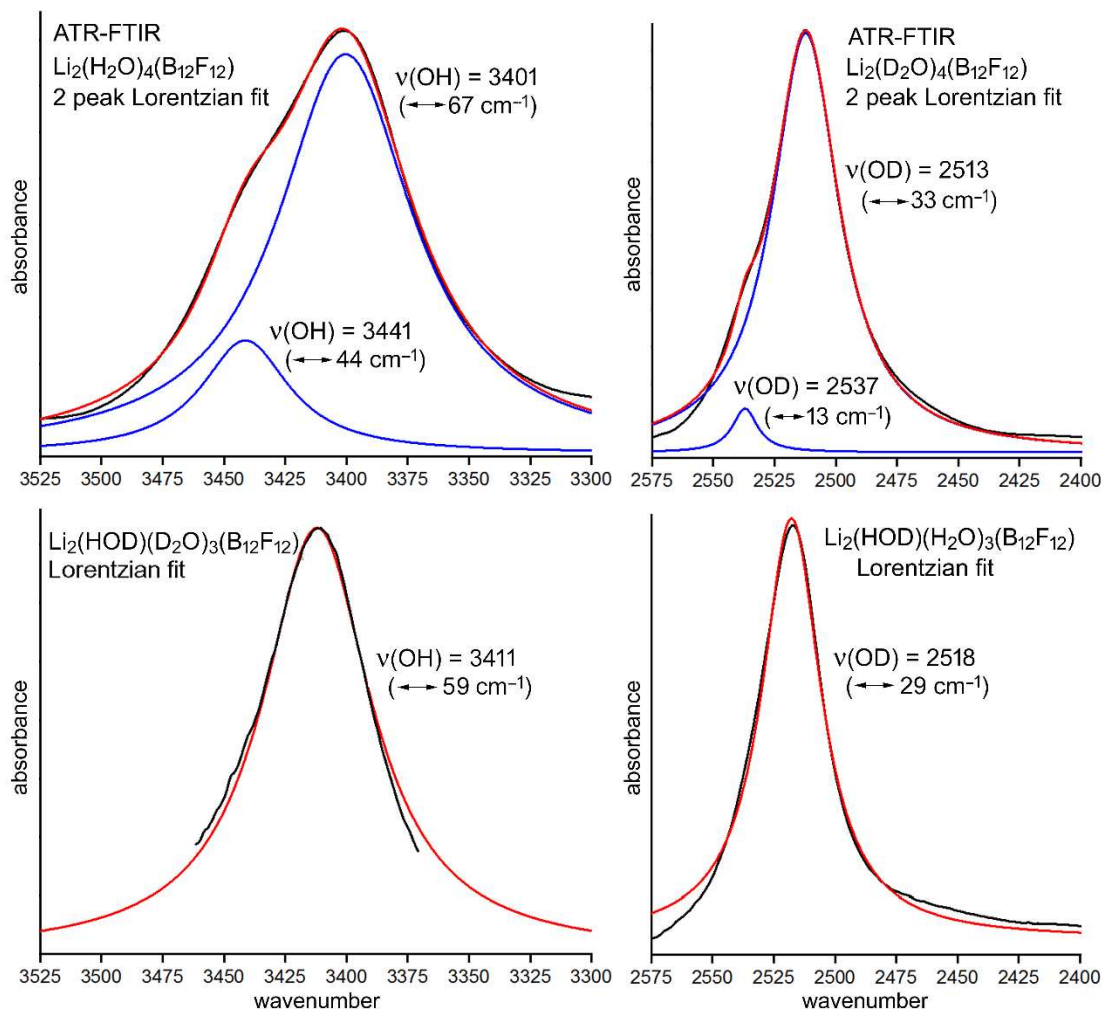


Figure 3.12. Lorentzian fits to the $\nu(\text{OH})$ bands for the O–H \cdots O hydrogen bonds in ATR-FTIR spectra of $\text{Li}_2(\text{H}_2\text{O})_4(\text{B}_{12}\text{F}_{12})$ (upper left) and $\text{Li}_2(\text{HOD})(\text{D}_2\text{O})_3(\text{B}_{12}\text{F}_{12})$ (lower left) and Lorentzian fits to the $\nu(\text{OD})$ bands for the O–D \cdots O hydrogen bonds in ATR-FTIR spectra of $\text{Li}_2(\text{D}_2\text{O})_4(\text{B}_{12}\text{F}_{12})$ (upper right) and $\text{Li}_2(\text{HOD})(\text{H}_2\text{O})_3(\text{B}_{12}\text{F}_{12})$ (lower right). The fitted band positions are shown above the FWHM values (\leftrightarrow = FWHM) in parentheses. The ratio of integrated intensities of the 3441 and 3401 cm^{-1} bands in the upper left spectrum is 0.14. The ratio of integrated intensities of the 2537 and 2513 cm^{-1} bands in the upper right spectrum is 0.04.

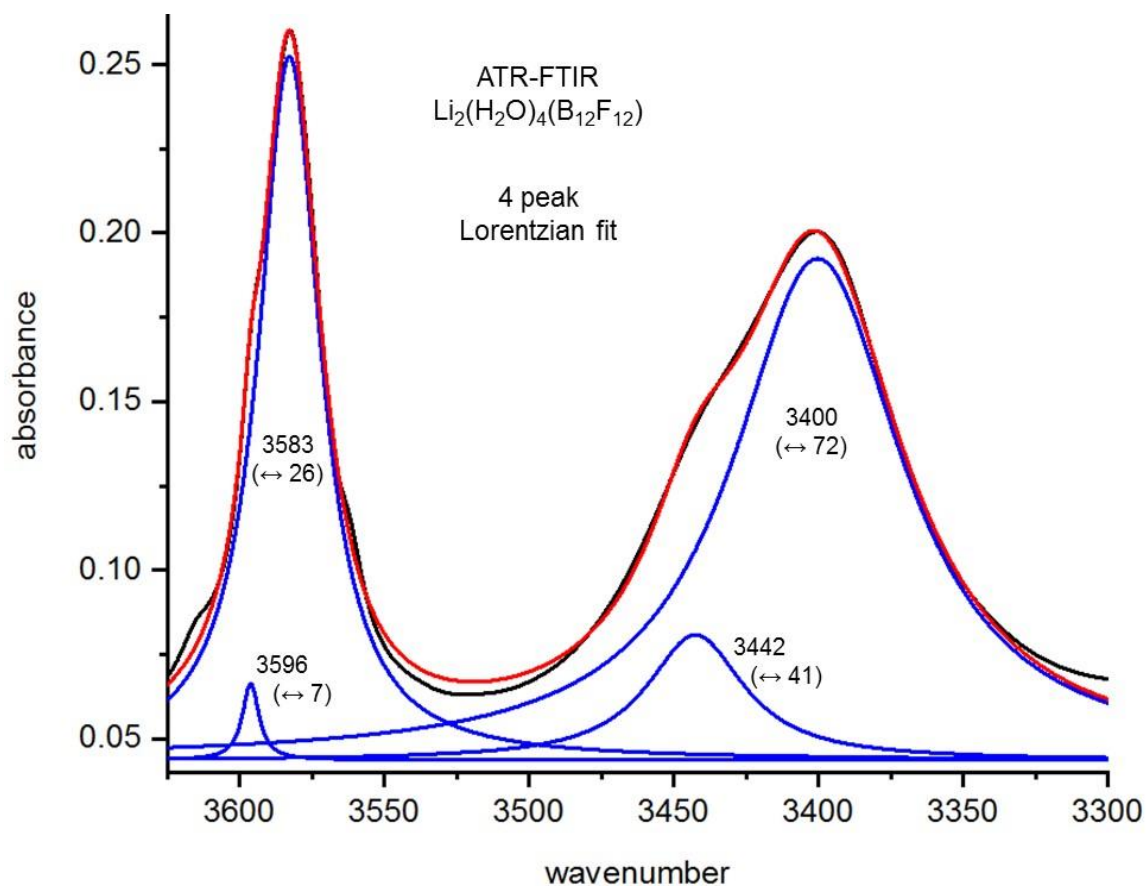


Figure 3.13. Four-peak Lorentzian fit to the entire $\nu(\text{OH})$ region of the ATR-FTIR spectrum of microcrystalline $\text{Li}_2(\text{H}_2\text{O})_4(\text{B}_{12}\text{F}_{12})$. The Lorentzian fit peak positions in cm^{-1} are shown above the FWHM values in cm^{-1} in parentheses (\leftrightarrow = FWHM). The fit parameters are slightly different than the fit parameters for just the $\nu(\text{OH})$ envelope at ca. 3401 cm^{-1} in Figure 3.12 ($3441 (\leftrightarrow 44)$; $3401 (\leftrightarrow 67)$). The ratio of integrated intensities of the 3596 and 3583 cm^{-1} bands is 0.03 . The ratio of integrated intensities of the 3442 and 3400 cm^{-1} bands is 0.14 .

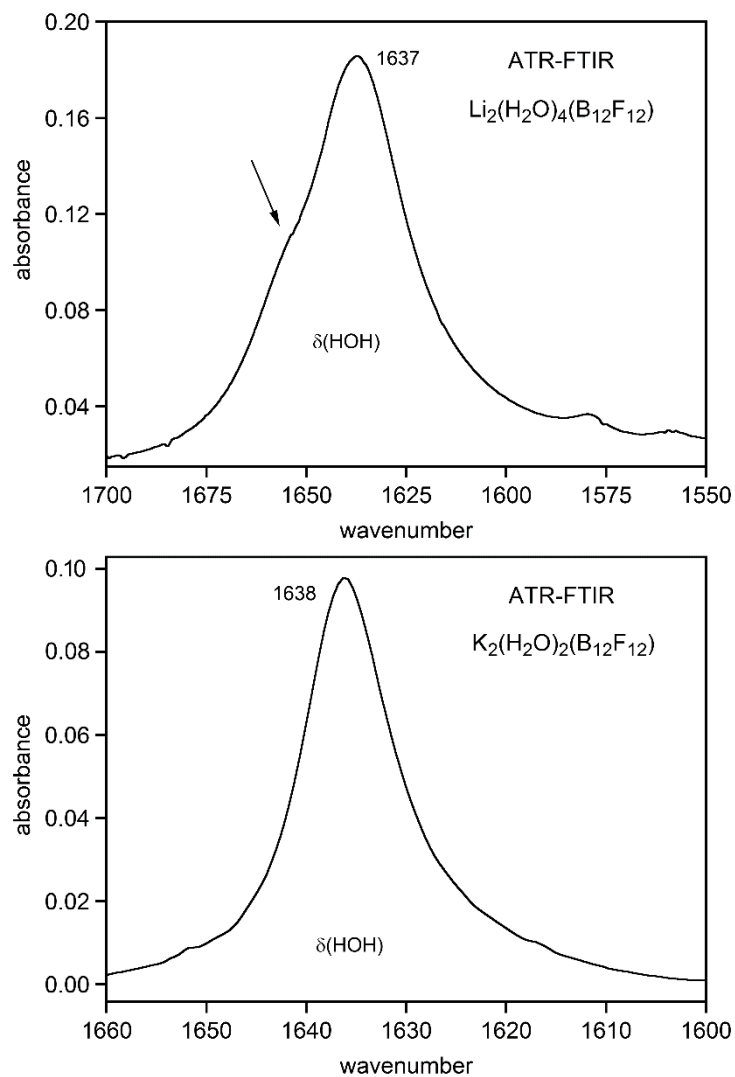


Figure 3.14. ATR-FTIR spectra in the $\delta(\text{HOH})$ bending region of microcrystalline samples of $\text{Li}_2(\text{H}_2\text{O})_4(\text{B}_{12}\text{F}_{12})$ (above) and $\text{K}_2(\text{H}_2\text{O})_2(\text{B}_{12}\text{F}_{12})$ (below). The samples were prepared by evaporating aqueous solutions (100% H_2O) on the ZnSe crystal. The arrow in the top spectrum points to a shoulder that indicates an additional unresolved band is present.

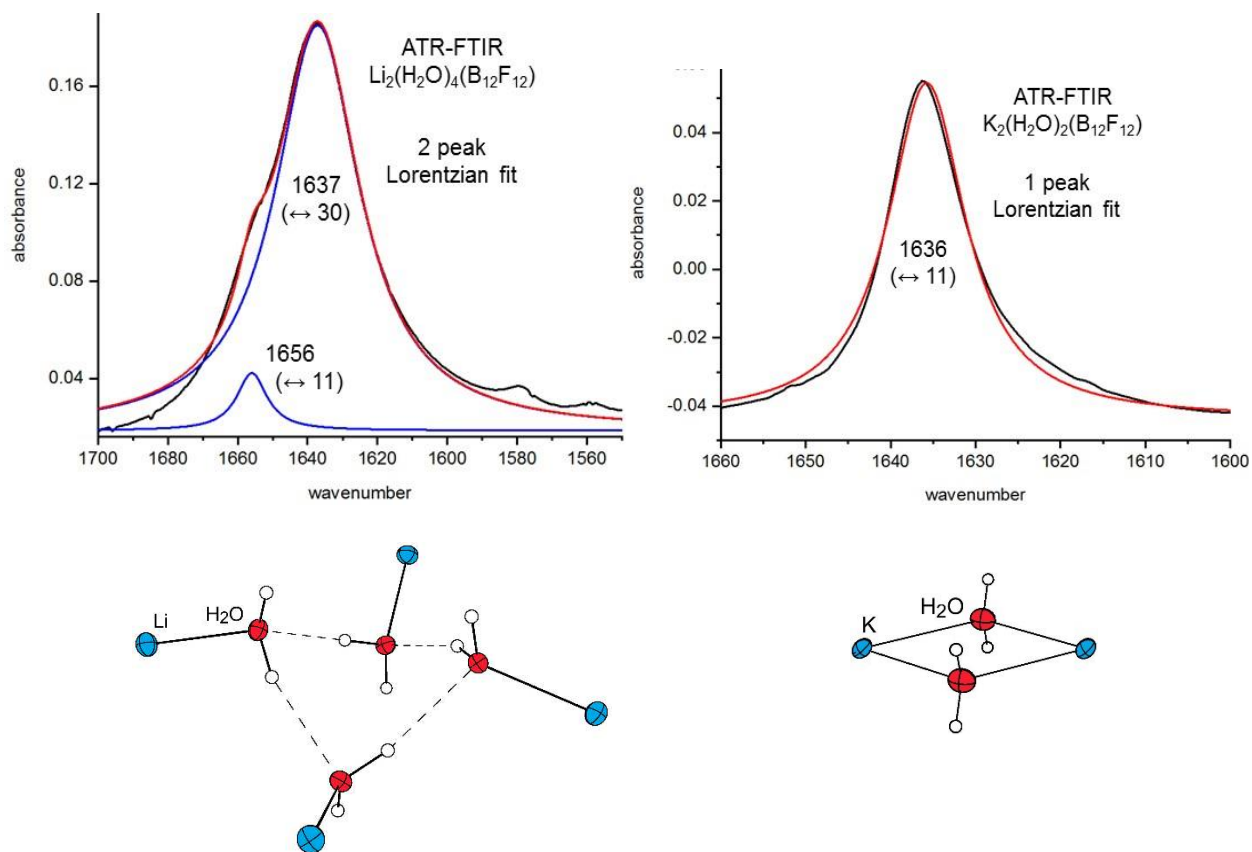


Figure 3.15. Lorentzian fits to $\delta(\text{HOH})$ peaks in the ATR-FTIR spectra of $\text{Li}_2(\text{H}_2\text{O})_4(\text{B}_{12}\text{F}_{12})$ and $\text{K}_2(\text{H}_2\text{O})_2(\text{B}_{12}\text{F}_{12})$. The samples were prepared by evaporating aqueous solutions (100% H_2O) on the ZnSe crystal. The Lorentzian fit peak positions are shown above the FWHM in parentheses (cm^{-1}). The ratio of integrated intensities of the 1656 and 1637 cm^{-1} bands in the spectrum on the left is 0.05. Underneath each spectrum is the structure of the $\text{Li}_2(\text{H}_2\text{O})_4^{4+}$ (ref 49) or $\text{K}_2(\text{H}_2\text{O})_2^{2+}$ (ref 50) cores in the crystal structures of these compounds (50% probability ellipsoids except for H atoms).

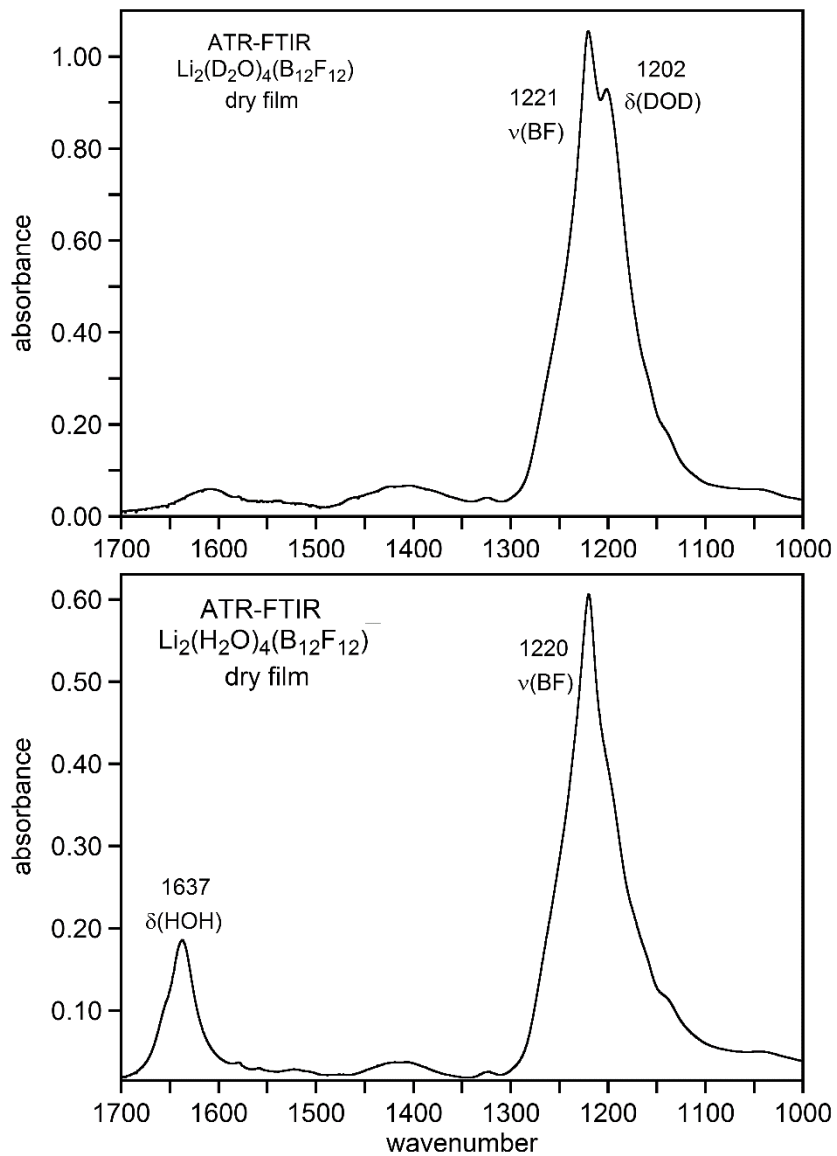


Figure 3.16. The $\delta(\text{HOH})/\nu(\text{BF})/\delta(\text{DOD})$ region of FTIR spectra of $\text{Li}_2(\text{D}_2\text{O})_4(\text{B}_{12}\text{F}_{12})$ (top) and $\text{Li}_2(\text{H}_2\text{O})_4(\text{B}_{12}\text{F}_{12})$ (bottom).

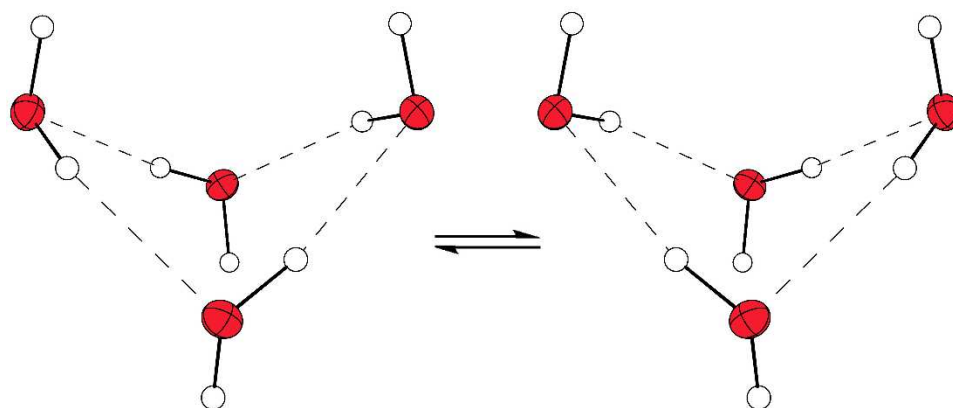


Figure 3.17. The proposed interconversion of disordered hydrogen-bonded H atoms in the X-ray crystal structure of $\text{Li}_2(\text{H}_2\text{O})_4(\text{B}_{12}\text{F}_{12})$ (ref 49).

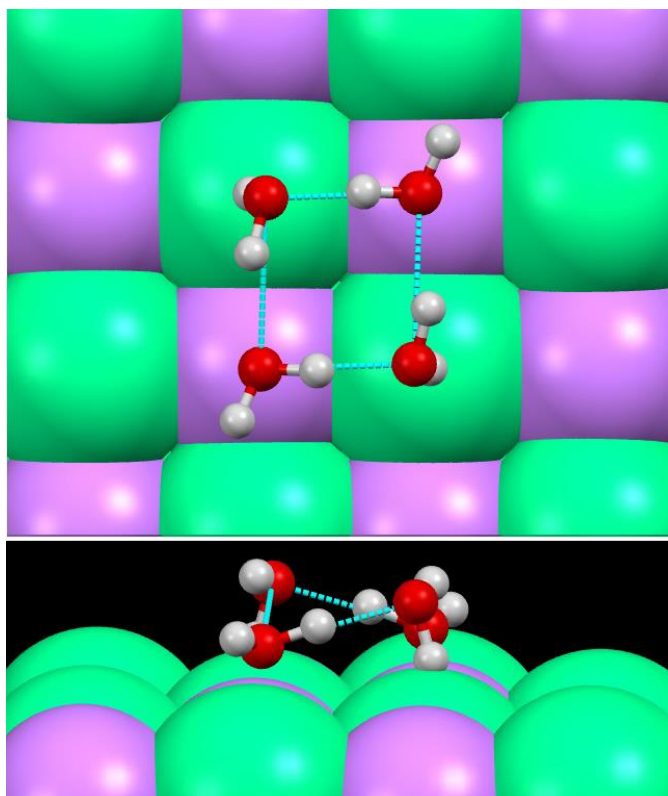


Figure 3.18. The predicted $C_2(H_2O)_4$ cluster adsorbed to the NaCl(001) surface (ref 60). This figure was modified from Figure 6 in ref 60. The author thanks Prof. Yong Yang for a high-resolution image of that figure from which this modified figure was prepared.

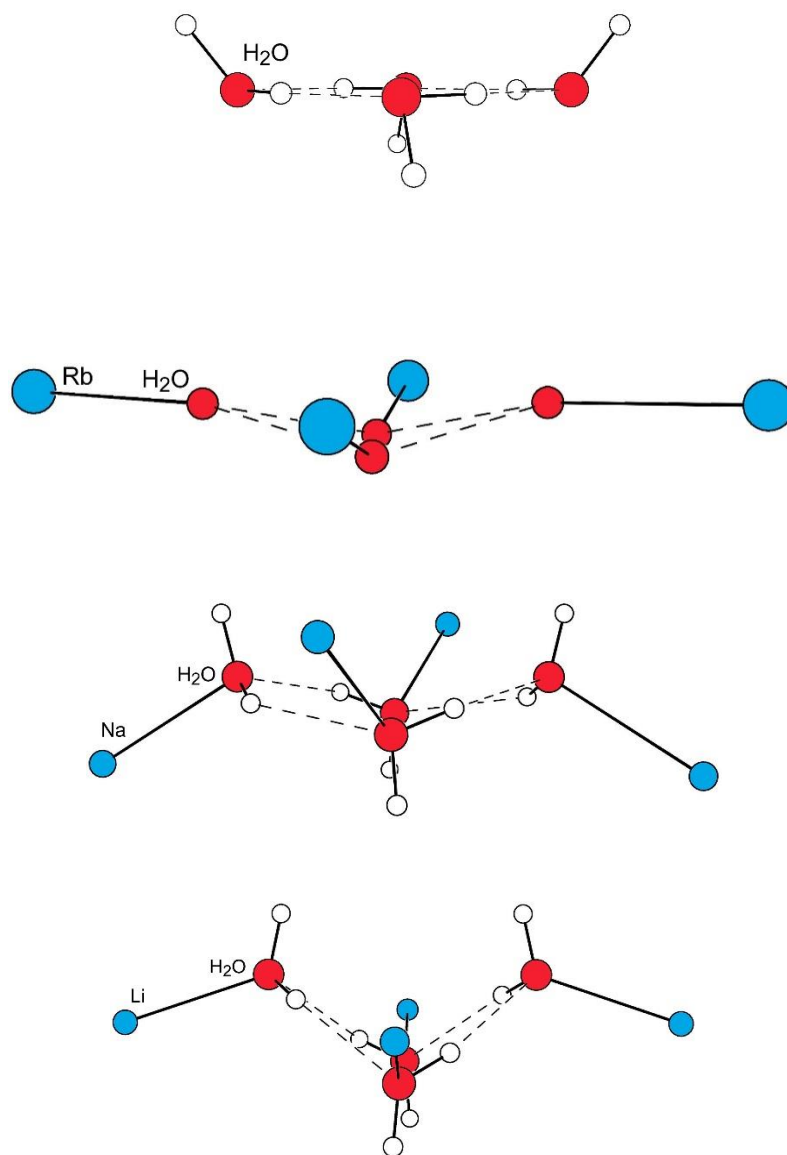


Figure 3.19. Calculated and experimental $(\text{H}_2\text{O})_4$ clusters. Top-to-bottom: CCSD(T)/aVQZ (ref 25, S_4 symmetry), $\text{Rb}_2[\text{Pt}_2(\text{pop})_4\text{I}]\cdot 4\text{H}_2\text{O}$ (ref 48, C_2 symmetry, $\text{pop}^{2-} = \text{HOOPOPOOH}^{2-}$; the H atoms on the H_2O molecules were not located in this structure), $\text{Na}_4[\text{Mo}_{12}\text{O}_{46}(\text{AsC}_6\text{H}_4\text{-4-OH-3-NO}_2)_4]\cdot 8\text{H}_2\text{O}$ (ref 47, S_4 symmetry), and $\text{Li}_2(\text{H}_2\text{O})_4(\text{B}_{12}\text{F}_{12})$ (ref 49, effective S_4 symmetry (crystallographic D_2 symmetry)).

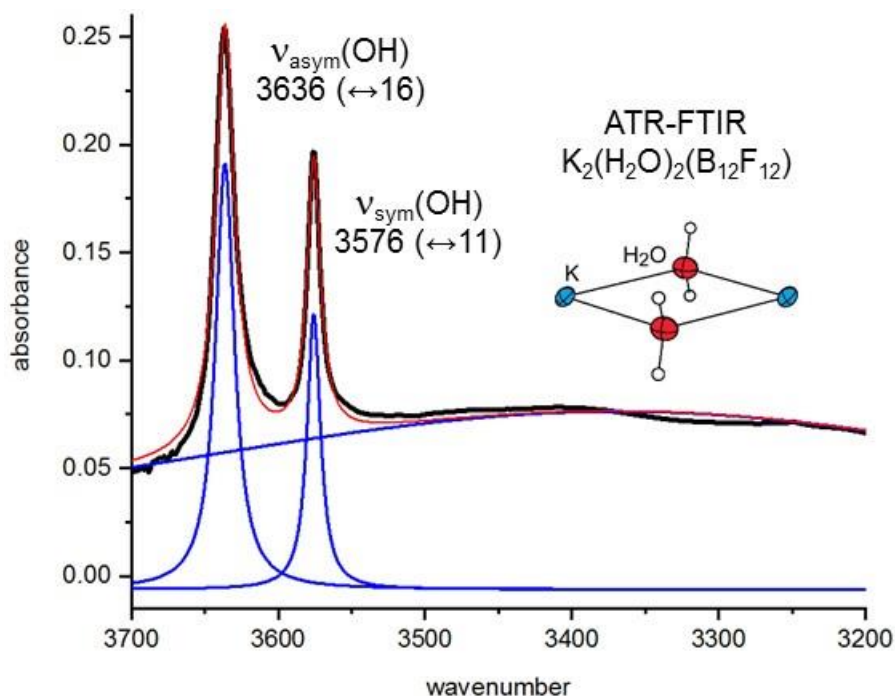


Figure 3.20. The ATR-FTIR spectrum of an evaporated microcrystalline film of $\text{K}_2(\text{H}_2\text{O})_2(\text{B}_{12}\text{F}_{12})$. A version of this spectrum was first published in ref 38, and was discussed at length in Chapter 2. The $\text{K}_2(\text{H}_2\text{O})_2^{2+}$ core of the structure is shown as an inset (the crystal structure was published in ref 49). The O–H bonds only interact with F atoms of the anions, with O–H \cdots F distances of 2.972(1) and 2.978(1) Å. The broad $\nu(\text{OH})$ band at ca. 3400 cm^{-1} is due to non-crystalline H_2O on the surface of the particles of $\text{K}_2(\text{H}_2\text{O})_2(\text{B}_{12}\text{F}_{12})$ (the sample had to be recorded under a partial pressure of $\text{H}_2\text{O}(\text{g})$ to avoid the rapid dehydration of the sample in a dry atmosphere (see ref 49)).

Mass-selective depletion spectra
Schwan, Havenith et al. *PCCP* 2016

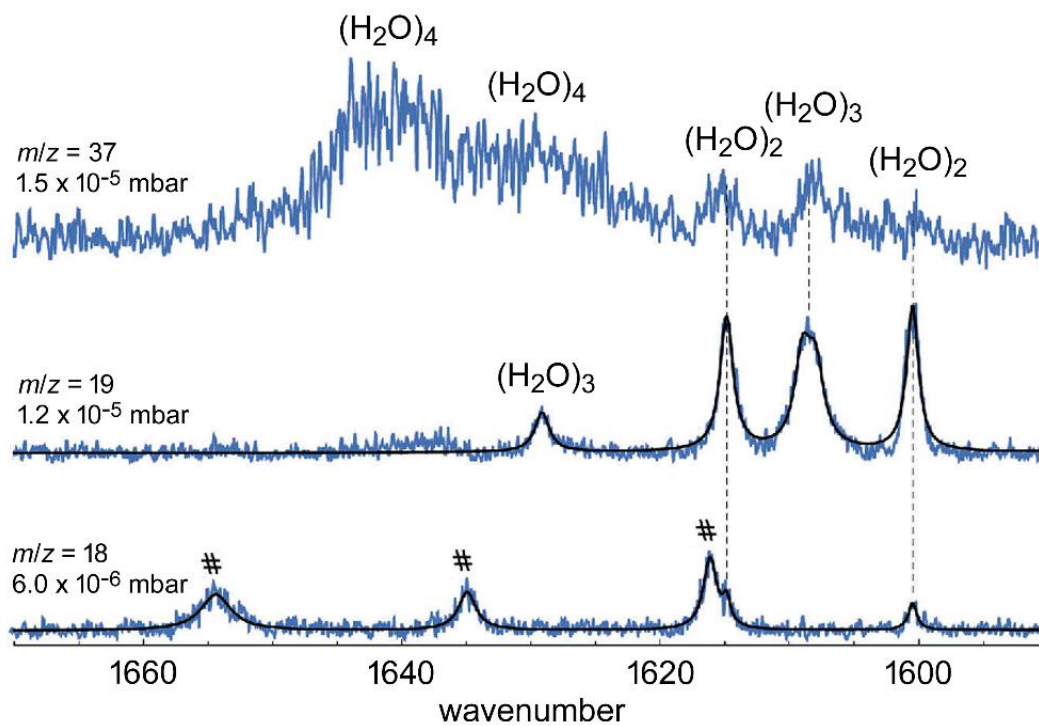


Figure 3.21. Mass-selective depletion IR spectra for $(\text{H}_2\text{O})_n$ clusters in liquid He droplets. This figure was modified for this work from Figure 1 in ref 52. The peaks marked with # were assigned to the H_2O monomer.

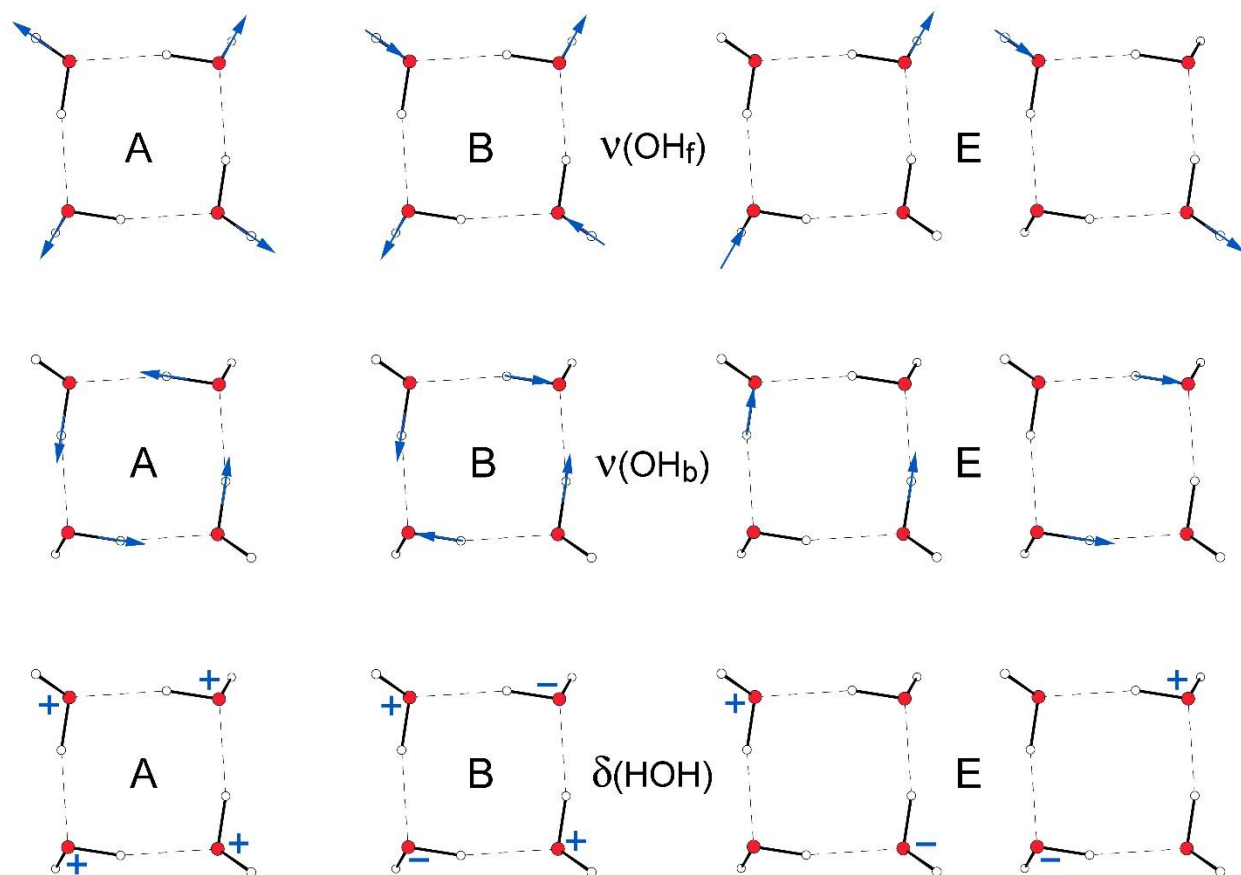


Figure 3.22. Simplified representations of the A, B, and E O–H stretching and H–O–H bending vibrations of a cyclic $(\text{H}_2\text{O})_4$ cluster with S_4 symmetry. The $\nu(\text{OH}_f)$ normal modes are for the four O–H bonds that do not form the four O–H \cdots O hydrogen bonds. The $\nu(\text{OH}_b)$ normal modes are for the four O–H bonds that do form the four O–H \cdots O hydrogen bonds. For the $\delta(\text{HOH})$ normal modes, the + and – signs designate an increase and decrease, respectively, in the H–O–H angle. This figure was adapted from a similar figure in ref 57.

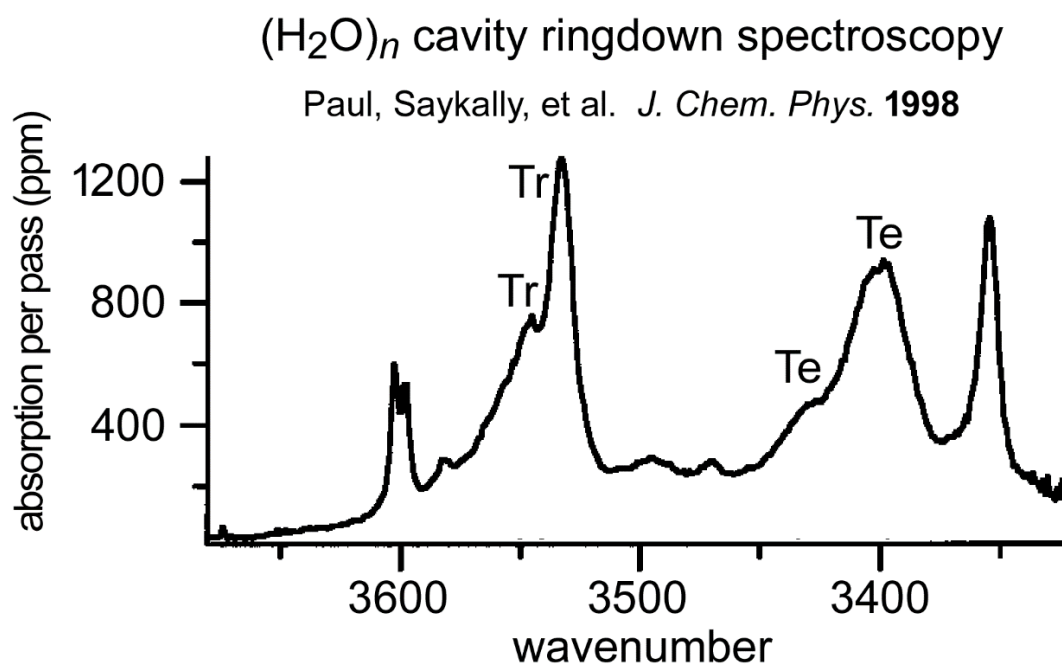


Figure 3.23. IR-CRLAS spectrum of $(\text{H}_2\text{O})_n$ clusters. This figure was modified from Figure 4 in ref 43. The peaks marked Tr were assigned to the cyclic $(\text{H}_2\text{O})_3$ trimer and the bands marked Te were assigned to the cyclic $(\text{H}_2\text{O})_4$ tetramer.

Table 3.1. Structural parameters for calculated and experimental cyclic (H₂O)₄ clusters^a

cluster compound or method of calculation	O(H)···O, Å	O–H···O, deg	O oop, Å	O···O···O, deg	O–H _b	O–H _f
S ₄ (H ₂ O) ₄ CCSD(T)/aVQZ ^b	2.746	167.3	0	90	0.977	0.958
S ₄ (H ₂ O) ₄ (Doroshenko) DFT ^c	2.727	168.5	0	90	0.985	0.961
C ₂ (H ₂ O) ₄ on NaCl(001) DFT ^d	2.683, 2.955	137.4, 172.1	±0.374	82.6, 89.3	0.891, 1.004	0.988, 0.973
S ₄ Li ₄ (H ₂ O) ₄ Li ₂ (H ₂ O) ₄ (B ₁₂ F ₁₂) ^e	2.778(2), 2.785(2)	152.6, 169.1	±0.633	78.1	0.90(2), 0.85(2)	0.81(2)
S ₄ Na ₄ (H ₂ O) ₄ Na ₄ [POM]·8H ₂ O ^f	2.935(9)	142	±0.299	88	0.85 ^g	0.85 ^f
C ₂ Rb ₄ (H ₂ O) ₄ Rb ₂ [Pt ₂ (pop) ₄ I]·4H ₂ O ^g	2.803(3), 3.000(3)	—	±0.265	99.4(2), 76.7(2)	— ^g	— ^g
S ₄ (H ₂ O) ₄ (NMe ₄)MnCo(CN) ₆ ·8H ₂ O ^h	2.809(3)	156	±0.160 ^w	89.3(3)	0.901)	0.90(1)
C _i (H ₂ O) ₄ Zn[(bdc)(bim)]·2H ₂ O ⁱ	2.733(4), 2.972(6)	160(6), 164(5)	0	100(1), 80(1)	0.85(2), 0.86(2)	0.85(2), 0.85(2)
C _i (H ₂ O) ₄ Cu(3-amp)(C ₂ O ₄)·3H ₂ O ^j	2.739(4), 2.946(4)	167, 173	0	88.8(3), 91.2(3)	0.79, 0.81	0.79, 0.80
C _i (H ₂ O) ₄ Cu ₂ (pydc) ₂ (1,2-Me ₂ Im) ₄ ·6H ₂ O ^k	2.791(5), 2.804(5)	159(5), 157(5)	0	85.6, 94.4	0.83(3), 0.82(2)	0.83(3), 0.82(3)

^a The abbreviation "oop O" refers to the perpendicular displacement of the O atoms from the mean plane of the four O atoms. O–H_b = the O–H bonds involved in the O–H···O hydrogen bonds that form the cluster. O–H_f = the O–H bonds that are not involved in the O–H···O hydrogen bonds that form the cluster. The O–H_f bonds do form hydrogen bonds to O, N, or F atoms in the various structures. ^b Ref 25. ^c Ref 32. ^d Ref 60. ^e This work; Li–O = 1.995(1) Å. ^f Ref 47; POM = Mo₁₂O₄₆(AsC₆H₄-4-OH-3-NO₂)₄; Na–O = 2.386(7) Å; OH distances were fixed at 0.85 Å. ^g Ref 48; H atoms on H₂O molecules were not included in the structure; Rb–O = 2.927(2), 3.149(1) Å; pop²⁻ = HOPOPOOH²⁻. ^h Ref 61; four H atoms are ±0.03 Å from the O₄ mean plane, and the other four H atoms are ±1.00 Å from that plane. ⁱ Ref 62; H₂bdc = 5-hydroxyisophthalic acid, bim = bis(*N*-imidazolyl)methane. ^j Ref 15; 3-amp = 3-aminomethylpyridine. ^k Ref 21; pydc²⁻ = pyridine-2,3-dicarboxylate(2-).

Table 3.2. Infrared $\nu(\text{OH})$ stretching frequencies for $(\text{H}_2\text{O})_4$, $(\text{D}_2\text{O})_4$, $[\text{HOD}(\text{D}_2\text{O})_3]$, and $[\text{HOD}(\text{H}_2\text{O})_3]$ clusters^a

sample	$(\text{H}_2\text{O})_4$		$(\text{D}_2\text{O})_4$		$[\text{HOD}(\text{D}_2\text{O})_3]$		$[\text{HOD}(\text{H}_2\text{O})_3]$		ref
	$\nu(\text{OH}_b)$	$\nu(\text{OH}_f)$	$\nu(\text{OD}_b)$	$\nu(\text{OD}_f)$	$\nu(\text{OH}_b)$	$\nu(\text{OH}_f)$	$\nu(\text{OD}_b)$	$\nu(\text{OD}_f)$	
$\text{Li}_2(\text{water})_4(\text{Z})^b$	3401 [67], 3441 [44]	3583 [26], ^c 3596 [7] ^c	2513 [33] 2538 [13]	2651 [25] ^c	3411 [59]	3587 [10] ^c	2518 [29]	2642 [6] ^c	TW
$(\text{H}_2\text{O})_n/\text{liquid He}$	3394								9
$(\text{water})_n/\text{Ne, 9K}$	3383	3719	2489, 2492, 2494	2745	3374				14
$(\text{water})_n/\text{Ar, 30 K}$	3372	3695	2487, 2488	2733					14
$(\text{H}_2\text{O})_n$ (gas)	3416 [58]	3714 [< 20]							41
$(\text{H}_2\text{O})_n$ (gas)	ca. 3400, ca. 3425 ^d								43
$(\text{D}_2\text{O})_n$ (gas)			2501, 2505(sh)						43
$(\text{D}_2\text{O})_n/\text{Ne, 7 K}$			2492 ^e						31
$(\text{H}_2\text{O})_n/\text{Ar, 29 K}$	3327, 3371								32
$(\text{H}_2\text{O})_n/\text{Ar, 25 K}$	3373								11
$(\text{H}_2\text{O})_n/\text{Kr, 25 K}$	3370								11

^a All values in cm^{-1} , including FWHM values in square brackets. Abbreviations: $\text{Z}^{2-} = \text{B}_{12}\text{F}_{12}^{2-}$; TW = this work. ^b For $\text{Li}_2(\text{H}_2\text{O})_4(\text{Z})$, $\delta(\text{HOH}) = 1637 \text{ cm}^{-1}$ (FWHM = 30 cm^{-1}) and 1656 cm^{-1} (FWHM = 11 cm^{-1}). For $\text{Li}_2(\text{D}_2\text{O})_4(\text{Z})$, $\delta(\text{DOD}) = \text{ca. } 1202 \text{ cm}^{-1}$ (the overlap with the strong $\nu(\text{BF})$ band prevents a more precise value for $\delta(\text{DOD})$). ^c These are not "free" O–H or O–D bonds; they form weak O–H \cdots F or O–D \cdots F hydrogen bonds (see text and ref 49). ^d These values are approximate because the authors of ref 43 did not list the band positions; they stated "our observed splitting is $\sim 26 \text{ cm}^{-1}$ "; see Figure 3.23). ^e This is the value listed in Table 3 of ref 31, but the published spectrum shows that the band maximum was closer to 2488 cm^{-1} with a shoulder at 2492 cm^{-1} (see Figure 3.3).

Table 3.3. Experimental and calculated $\delta(\text{HOH})$ or $\delta(\text{DOD})$ values for $(\text{H}_2\text{O})_4$ or $(\text{D}_2\text{O})_4$ clusters^a

cluster compound or method of calculation	$\delta(\text{HOH})$	$\delta(\text{DOD})$	ref
$\text{Li}_2(\text{H}_2\text{O})_4(\text{B}_{12}\text{F}_{12})$ (solid)	1637, 1656		this work
$\text{Li}_2(\text{D}_2\text{O})_4(\text{B}_{12}\text{F}_{12})$ (solid)		ca. 1202	this work
$S_4 (\text{H}_2\text{O})_4/\text{Ar}$, 19 K	1637, 1660		28
$S_4 (\text{H}_2\text{O})_4/\text{Ar}$, 15 K	1608, 1624		32
$S_4 (\text{H}_2\text{O})_4/\text{liquid He}$	1629, 1641		52
$S_4 (\text{H}_2\text{O})_4/\text{gas phase}$ ⁷¹	1629		71
$S_4 (\text{H}_2\text{O})_4/\text{CCSD(T)}/\text{aug-cc-pVDZ}$	1612, 1632 \times 2, 1671		19
$S_4 (\text{H}_2\text{O})_4/\text{CCSD(T)}/\text{haTZ}$	1666, 1678 \times 2, 1703 ^b		24
$S_4 (\text{H}_2\text{O})_4/\text{LCCSD(T)}/\text{aVDZ}$ ⁷²	1676, 1688 \times 2,		72
$S_4 (\text{H}_2\text{O})_4/\text{CCSD(T)}/\text{SCF 6-31G}^*$	1651 \times 3, 1666		2
$S_4 (\text{H}_2\text{O})_4/\text{CCSD(T)}/\text{VSCF}/\text{VCI}^c$	1629, 1634 \times 2, 1654		27
$S_4 (\text{H}_2\text{O})_4/\text{B3LYP}/6-311++\text{G}(3\text{df},3\text{pd})$	1643, 1656 \times 2, 1684		14
$S_4 (\text{H}_2\text{O})_4/\text{B3LYP}/\text{cc-pVTZ}^d$	1614, 1623 \times 2, 1649		32
$S_4 (\text{H}_2\text{O})_4/\text{B3LYP}/\text{cc-pVTZ}^e$	1612, 1621 \times 2, 1645		32

^a All values in cm^{-1} . Calculated anharmonic frequencies unless otherwise indicated. ^b Harmonic frequencies. ^c Anharmonic coupled-mode calculations. ^d Vacuum. ^e In argon.

CHAPTER 4 WEAK O–H···F HYDROGEN BONDING IN $M(\text{H}_2\text{O})_n(\text{B}_{12}\text{F}_{12})$ SALT
HYDRATES (M = Mg, Ca, Sr, Ba, Co, Ni, Zn)

4.1 Introduction and Relevant Literature

The second chapter of this dissertation is focused on the alkali metal salt hydrates of WCAs. In the section discussing future work (section 2.4.2), studying the FTIR spectra of salt hydrates with M^{2+} ions was proposed. One reason that the charge/oxidation state of the cation is relevant relates to the strength of the $\text{H}_2\text{O}-M^{m+}$ bond. It is known that the acidity of a cation increases with oxidation number,¹ and the more acidic a cation is, the stronger the cation–water coordination bond. A stronger (and shorter) M–O bond will result in a lengthening and weakening of the O–H bond. By weakening the O–H bond the H atom becomes more Brønsted acidic, and that increased acidity translates into forming stronger hydrogen bonds.¹ As a result, it is unlikely that the hydrogen bonds in metal salt hydrates composed of divalent metal cations and WCAs will rival the salt hydrates discussed in Chapter 2 in terms of weakness. What can be learned from the relatively stronger hydrogen bonds formed in divalent metal salt hydrates of WCAs is the effect of cation acidity on hydrogen bond strength.

In this chapter the structures and FTIR spectra of four divalent metal salt hydrates of the WCA $\text{B}_{12}\text{F}_{12}^{2-}$ (M = Mg, Co, Ni, Zn) are discussed. In the FTIR spectra of these four salts, two pairs of relatively narrow $\nu_{\text{asym}}(\text{OH})$ and $\nu_{\text{sym}}(\text{OH})$ bands were observed, for a total of four bands in the $\nu(\text{OH})$ region. These two sets of bands result from two different sets of three symmetry related H_2O ligands in the $M(\text{H}_2\text{O})_6^{2+}$ cation complex. Use of isotopically dilute solutions containing a small percentage of the $M(\text{HOD})(\text{H}_2\text{O})_5^{2+}$ cation complex will be used to show that these two unique H_2O positions cause the multiplicity of the $\nu(\text{OH})$ bands observed in the FTIR spectrum, and not intermolecular coupling of the O–H oscillators in the octahedrally coordinated $M(\text{H}_2\text{O})_6^{2+}$ cation complex (factor group splitting).² Comparison of the $\Delta\nu(\text{OH})$ of the $\nu_{\text{asym1}}(\text{OH})$, $\nu_{\text{asym2}}(\text{OH})$, $\nu_{\text{sym1}}(\text{OH})$, and $\nu_{\text{sym2}}(\text{OH})$ bands for the four $M(\text{H}_2\text{O})_6(\text{B}_{12}\text{F}_{12})$ salts (M = Mg, Co, Ni, Zn) salts will show the effect of cation pKa on the strength of the hydrogen bond formed between

the water ligands and the $B_{12}F_{12}^{2-}$ anions. As expected the most acidic cation (Zn^{2+}) possessed the largest red-shift from the idealized band positions for an isolated, uncoupled, H_2O molecule (3756 and 3657 cm^{-1} ; ref. 3), as seen in Figure 4.1.

The FTIR spectra of the salt hydrates $Ca(H_2O)_n(B_{12}F_{12})$, $Sr(H_2O)_n(B_{12}F_{12})$, and $Ba(H_2O)_n(B_{12}F_{12})$ are presented and discussed in this chapter as well. The values of n for the samples in some of these spectra are not explicitly known. Where available, the spectra are compared to data from TGA experiments to hypothesize the value of n . In most cases, the stable hydration states observed in the TGA and FTIR experiments differ from the known SC-XRD structures for these compounds. As a result, comparison of the $\nu(OD)$ stretching frequency as a function of $O(D)\cdots F$ bond length cannot be made for these compounds. What these spectra do show is that the salt hydrates formed with divalent cations generally have a greater red-shift than the salt hydrates with monovalent cations. This observation shows that, as expected, the more acidic divalent cations induce stronger water–anion hydrogen bonds, but those hydrogen bonds are still relatively weak to the point where the $\nu(OH)$ bands can be individually resolved at room temperature.

All of the work presented in this chapter was published in two papers in *Inorganic Chemistry*.^{4,5} The first publication was titled *Manifestations of Weak O–H \cdots F Hydrogen Bonding in $M(H_2O)_n(B_{12}F_{12})$ Salt Hydrates: Unusually Sharp Fourier Transform Infrared $\nu(OH)$ Bands and Latent Porosity ($M = Mg\text{--}Ba, Co, Ni, Zn$)*. The author of this dissertation is the first author. All the FTIR work presented in this chapter, and in the publication, was performed by the author of this dissertation. The second publication is *Hydrated Metal Ion Salts of the Weakly Coordinating Fluoroanions PF_6^- , TiF_6^{2-} , $B_{12}F_{12}^{2-}$, $Ga(C_2F_5)_4^-$, $B(3,5\text{-}C_6H_3(CF_3)_2)_4^-$, and $Al(OC(CF_3)_3)_4^-$. In Search of the Weakest HOH \cdots F Hydrogen Bonds*. The author of this dissertation was the first author, and the only graduate student or postdoc author. The structures presented in this chapter were collected and determined by previous Strauss group members.

4.2 Experimental

4.2.1 Reagents and Solvents

Solid $K_2(B_{12}H_{12})$ (Air Products) was dissolved in dd- H_2O and brought to dryness with a rotary evaporator a minimum of three times before being dried under dynamic vacuum overnight to remove any residual methanol contained within the solid. The following reagents and solvents were obtained from the indicated supplier: deuterium oxide (D_2O , Cambridge Isotopes 99.9% D); Acetonitrile (CH_3CN), $MgCl_2 \cdot 6H_2O$, $CaCO_3$, $SrCO_3$, $BaCO_3$, $CoCl_2 \cdot 6H_2O$, $NiCl_2 \cdot 6H_2O$, $ZnCl_2 \cdot 6H_2O$ (Sigma-Aldrich); $CoCO_3$, thionyl chloride ($SOCl_2$, Fisher Scientific); $NiCO_3$ (Baker and Adamson); $ZnCO_3$ (Alfa Aesar 99.5%). The mixed N_2/F_2 gas (Matheson, 80:20 $N_2:F_2$) was used as received.

4.2.2 General Procedures

Anhydrous compounds were prepared using standard airless-ware glassware and a Schlenk-style vacuum line and were stored in a dinitrogen filled glovebox. Preparation of anhydrous MCl_2 ($M = Co, Ni, Zn$) was performed by stirring the appropriate $MCl_2 \cdot 6H_2O$ with a large excess of $SOCl_2$ and heated until reflux for several hours. Filtration followed by vacuum drying afforded anhydrous $CoCl_2$, $NiCl_2$, and $ZnCl_2$. Distilled water was deionized with a Barnstead Nanopure system. The deionized distilled water (dd- H_2O) had a resistivity greater than 18 $M\Omega$ (all samples of H_2O used in this work correspond to dd- H_2O prepared in this way).

4.2.3 Synthesis of $M(H_2O)_6(B_{12}F_{12})$ ($M = Mg, Co, Ni, Zn$)

Equivalent amounts of $Ag_2(CH_3CH)_4(B_{12}F_{12})$ dissolved in CH_3CN and anhydrous MCl_2 ($M = Co, Ni, Zn$), or $MgCl_2 \cdot 6H_2O$, dissolved H_2O were quickly mixed and allowed to stir vigorously for 10 minutes. The solutions were filtered to remove $AgCl$. Slow evaporation of the filtrate resulted in colorless crystals of $Mg(H_2O)_6(B_{12}F_{12})$ (85% yield), pink crystals of $Co(H_2O)_6(B_{12}F_{12})$ (70% yield), pale green crystals of $Ni(H_2O)_6(B_{12}F_{12})$ (60% yield), or colorless crystals of $Zn(H_2O)_6(B_{12}F_{12})$ (50% yield) all of which were suitable for SC-XRD. Photographs of crystals of $Co(H_2O)_6(B_{12}F_{12})$ and $Ni(H_2O)_6(B_{12}F_{12})$ are shown in Figure 4.2.

In alternate syntheses, equivalent amounts of $(H_3O)_2(H_2O)_6(B_{12}F_{12})$ and the corresponding anhydrous MCO_3 salt were mixed in H_2O . The solution was stirred vigorously and boiled for 10 minutes before the

solution was cooled to room temperature. Slow evaporation yielded crystals of $M(\text{H}_2\text{O})_6(\text{B}_{12}\text{F}_{12})$. Optimization of crystalline $M(\text{H}_2\text{O})_6(\text{B}_{12}\text{F}_{12})$ isolation was not attempted for this procedure, and therefore yields were not determined.

4.2.4 Synthesis of $\text{Ca}(\text{H}_2\text{O})_7(\text{B}_{12}\text{F}_{12})$, $\text{Sr}(\text{H}_2\text{O})_7(\text{B}_{12}\text{F}_{12})$, $\text{Ba}(\text{H}_2\text{O})_5(\text{B}_{12}\text{F}_{12})$

Equivalent amounts of $(\text{H}_3\text{O})_2(\text{H}_2\text{O})_6(\text{B}_{12}\text{F}_{12})$ and the corresponding anhydrous MCO_3 salt were mixed in H_2O . The solution was stirred vigorously and boiled for 10 minutes before the solution was cooled to room temperature. Slow evaporation of the filtrate yielded colorless crystals of $\text{Ca}(\text{H}_2\text{O})_7(\text{B}_{12}\text{F}_{12})$, $\text{Sr}(\text{H}_2\text{O})_7(\text{B}_{12}\text{F}_{12})$, and $\text{Ba}(\text{H}_2\text{O})_5(\text{B}_{12}\text{F}_{12})$ suitable for diffraction (these were kept in the mother liquor: for this reason a meaningful yield was not recorded).

4.2.5 FTIR Spectroscopy

Variable-humidity ATR-FTIR spectra were recorded with a Nicolet 6700 FTIR spectrometer equipped with a stainless-steel Harrick Horizon™ ATR variable-temperature/variable-humidity flow reactor described in detail in previous publications⁶⁻⁸ (and discussed in section 2.2.10 of Chapter 2) or a Nicolet IS-50 FTIR spectrometer. Aliquots of dilute solutions of the compounds in H_2O , D_2O , 90:10 (v:v) $\text{H}_2\text{O}:\text{D}_2\text{O}$, or a 90:10 (v:v) $\text{D}_2\text{O}:\text{H}_2\text{O}$ mixture were allowed to evaporate to insipient dryness on a 5 cm × 1 cm × 0.2 cm ZnSe ATR crystal (New Era Enterprise) after it was placed in the flow reactor of the Nicolet 6700 instrument. No attempt was made to control the size or distribution of the microcrystalline particles that formed. The IR beam was directed into the ATR crystal at an incident angle of 45° by mirrors after leaving the interferometer, and the reflected light was returned to a liquid N_2 cooled MCT detector. The vapor pressure of the H_2O over the sample was controlled in real time as spectra were recorded with a purge of dry N_2 gas, or N_2 passed through either a V-Gen M1-120 dew point generator, or a bubbler containing a saturated aqueous salt solution. The rate of gas flow through the 5 cm³ stainless steel reactor was controlled using an Alicat Scientific flowmeter. The flow rate was 1 L min⁻¹ for dry N_2 passed through the dew point generator, and 0.060 L min⁻¹ for dry N_2 passed through the solutions in the bubblers. Spectra were recorded at specific intervals of time depending on the experiment (typically 128 scans at 1 cm⁻¹ resolution, unless otherwise indicated).

Samples of $M(\text{HOD})_n(\text{H}_2\text{O})_{n-1}(\text{B}_{12}\text{F}_{12})$ and $M(\text{HOD})_n(\text{D}_2\text{O})_{n-1}(\text{B}_{12}\text{F}_{12})$ ($M = \text{Mg}^{2+}$, Co^{2+}) were prepared by dissolving the appropriate salt in either a 90:10 (v:v) mixture of $\text{H}_2\text{O}:\text{D}_2\text{O}$ or a 90:10 (v:v) mixture

of D₂O:H₂O. Aliquots of the solution were allowed to dry on the ZnSe ATR crystal until incipient dryness under a purge of N₂.

4.2.6 Thermogravimetric Analysis

Samples for TGA (Pt sample pans; 4–15 mg of finely ground microcrystalline powders) were analyzed using TA Instruments series 2950 or TGA Q500 instrumentation. The temperatures for isothermal TGA experiments, which ranged from 18–100 °C, were held to within 0.01 °C for several minutes before a change in the carrier gas was made. Dry He, dry N₂ or either bubbled through H₂O, D₂O, or a saturated salt solution (Table 4.1), the vapor pressure of H₂O, or D₂O, in the sample chamber was 18(1) torr of H₂O (g), 16(1) torr of D₂O (g), or between 6 and 15.0 torr of H₂O (g), respectively. Whenever the carrier gas was switched (e.g., from dry gas to a gas containing H₂O (g) or from a gas containing H₂O (g) to a gas containing D₂O (g) or vice versa), ca. 0.5 minutes elapsed before the composition of the carrier gas in the sample chamber became constant, as monitored in several control experiments by recording the mass spectrum of the carrier gas exiting the sample chamber (see Figure 4.3, which was reproduced from ref. 9). The carrier gas flow rate was 60 mL min⁻¹.

4.3 Results and Discussion

4.3.1 Isomorphous M(H₂O)₆(B₁₂F₁₂) (M = Mg, Co, Ni, Zn)

The four isomorphous SC-XRD structures of the salts of M(H₂O)₆(B₁₂F₁₂) (M = Mg, Co, Ni, Zn) were originally published in 2018.⁴ All four salts crystallize in the $R\bar{3}$ space group (Table 4.2). There are six H₂O ligands octahedrally coordinated around the metal cation. Of the six H₂O ligands, only two are crystallographically unique resulting in two sets of *fac*-(H₂O)₃ ligands per cation. Each M(H₂O)₆²⁺ complex is surrounded by eight B₁₂F₁₂²⁻ anions at the corners of a [(B₁₂F₁₂)²⁻]₈ pseudo-cubic array. Each set of *fac*-(H₂O)₃ ligands has different M–O bond distances. For each unique H₂O molecule there are two different O(H)···F bond distances. The set of *fac*-(H₂O)₃ ligands with the shorter M–O distance also have shorter O(H)···F bond distances. For Mg(H₂O)₆(B₁₂F₁₂) (Figure 4.4) the two M–O bond distances are 2.0390(11) and 2.0659(11) Å (Table 4.3). The two O(H)···F bond distances for the H₂O with the 2.0390(11) Å M–O bond distance are 2.723(3) and 2.749(2) Å. The two O(H)···F bond distances for the H₂O with the 2.0659(11) Å M–O bond distance are 2.904(2) and 2.914(2) Å. For Co(H₂O)₆(B₁₂F₁₂) the two M–O bond distances are

2.0663(4) and 2.0907(4) Å (Table 4.4). The two O(H)⋯F bond distances for the H₂O with the 2.0663(4) Å M–O bond distance are 2.734(1) and 2.739(1) Å. The two O(H)⋯F bond distances for the H₂O with the 2.0907(4) Å M–O bond distance are 2.886(1) and 2.919(1) Å. For Ni(H₂O)₆(B₁₂F₁₂) (Figure 4.5) the two M–O bond distances are 2.0290(7) and 2.0515(7) Å (Table 4.5). The two O(H)⋯F bond distances for the H₂O with the 2.0290(7) Å M–O bond distance are 2.732(1) and 2.735(1) Å. The two O(H)⋯F bond distances for the H₂O with the 2.0515(7) Å M–O bond distance are 2.859(1) and 2.919(1) Å. For Zn(H₂O)₆(B₁₂F₁₂) (Figure 4.6) the two M–O bond distances are 2.0611(4) and 2.0926(4) Å (Table 4.6). The two O(H)⋯F bond distances for the H₂O with the 2.0611(4) Å M–O bond distance are 2.733(1) and 2.734(1) Å. The two O(H)⋯F bond distances for the H₂O with the 2.0926(4) Å M–O bond distance are 2.869(1) and 2.894(1) Å. All of these distances are summarized in Table 4.7.

The $\nu(\text{OH})$ region for all four M(H₂O)₆(B₁₂F₁₂) salts are shown in Figure 4.7. In each spectrum there are four $\nu(\text{OH})$ bands. For Mg(H₂O)₆(B₁₂F₁₂) these four bands appear at 3628, 3596, 3561, and 3544 cm⁻¹. For Co(H₂O)₆(B₁₂F₁₂) these four bands appear at 3617, 3581, 3544, and 3524 cm⁻¹. For Ni(H₂O)₆(B₁₂F₁₂) these four bands appear at 3615, 3579, 3540, and 3523 cm⁻¹. For Zn(H₂O)₆(B₁₂F₁₂) these four bands appear at 3613, 3573, 3541, and 3518 cm⁻¹. These values are summarized in Table 4.8.

In many of the spectra discussed in Chapters 2 and 3 of this dissertation only two $\nu(\text{OH})$ bands are observed in the $\nu(\text{OH})$ region of the spectra. In these spectra there was an increase in the number of peaks observed when an H₂O molecule was substituted by an HOD molecule where the D (or H) atom can exist in one of two orientations, and the O(H/D)⋯F distances are significantly different from each other. The two different positions thus resulted in additional $\nu(\text{OD})$ bands being observed. Thus, for these four $\nu(\text{OH})$ bands it was hypothesized that they may actually be two sets of $\nu_{\text{asym}}(\text{OH})$ and $\nu_{\text{sym}}(\text{OH})$ bands, one set of bands for each of the unique set of *fac*-(H₂O)₃ ligands. This is not the only potential hypothesis for the observed multiplicity; the other is splitting of the $\nu_{\text{asym}}(\text{OH})$ and $\nu_{\text{sym}}(\text{OH})$ bands due to intermolecular coupling of adjacent O–H oscillators in a process known as factor group splitting.² Due to the close proximity of O–H oscillators around the M²⁺ cation it is possible that their vibrations can couple in the solid state. Thus the $\nu(\text{OH})$ band splits into $\nu_{\text{asym}}(\text{OH})$ and $\nu_{\text{sym}}(\text{OH})$ bands due to intramolecular coupling of the O–H oscillators on the same H₂O molecule, and these bands each split again due to intermolecular coupling between two adjacent

H₂O molecules resulting in four bands. To determine which of these hypotheses is the most likely correct cause of the multiplicity, removal of both the inter- and intramolecular coupling by substituting one H₂O ligand in the M(H₂O)₆²⁺ complex with a single HOD molecule is all that is required. If the cause of the multiplicity is due to two sets of unique H₂O positions each giving rise to a set of $\nu_{\text{asym}}(\text{OH})$ and $\nu_{\text{sym}}(\text{OH})$ bands, then the $\nu(\text{OD})$ region of the spectrum of M(HOD)(H₂O)₅(B₁₂F₁₂) will have two bands; one for each different HOD position. If intermolecular coupling is what is splitting the two $\nu_{\text{asym}}(\text{OH})$ and $\nu_{\text{sym}}(\text{OH})$ bands into four bands, the $\nu(\text{OD})$ region of the spectrum for M(HOD)(H₂O)₅(B₁₂F₁₂) will only have one band since the O–D oscillator cannot couple intra- or intermolecularly to any of the O–H oscillators, as the difference in energy is too great.

Figure 4.8 shows the $\nu(\text{OD})$ region of the FTIR spectrum for Mg(HOD)(H₂O)₅(B₁₂F₁₂) and Co(HOD)(H₂O)₅(B₁₂F₁₂). In both spectra a total of 6 bands are observed. The four smaller bands correspond to $\nu(\text{OD})$ vibrations for the trace amount of M(D₂O)(H₂O)₅(B₁₂F₁₂) present (M = Mg, Co). The remaining two bands are assigned to the $\nu(\text{OD})$ vibrations of HOD in M(HOD)(H₂O)₅(B₁₂F₁₂). The presence of two HOD bands supports the first hypothesis, that the four $\nu(\text{OH})$ bands are in fact two sets of $\nu_{\text{asym}}(\text{OH})$ and $\nu_{\text{sym}}(\text{OH})$ bands, being the causes of the observed multiplicity. Assignment of FTIR bands to the different H₂O positions was based on two criteria, the relative intensity of each band, as well as the band-to-band separation. First it is required to assign temporary labels to the four bands in the spectrum. By labeling the bands from left to right $\nu(\text{OH})_{\text{A}}$, $\nu(\text{OH})_{\text{B}}$, $\nu(\text{OH})_{\text{C}}$, $\nu(\text{OH})_{\text{D}}$ (see Figure 4.9) two pairing schemes are possible. In the first scheme, bands $\nu(\text{OH})_{\text{A}}$ and $\nu(\text{OH})_{\text{B}}$ are grouped as one possible set of $\nu_{\text{asym}}(\text{OH})$ and $\nu_{\text{sym}}(\text{OH})$ bands due being the two highest energy bands, and bands $\nu(\text{OH})_{\text{C}}$ and $\nu(\text{OH})_{\text{D}}$ are grouped as the other possible set of $\nu_{\text{asym}}(\text{OH})$ and $\nu_{\text{sym}}(\text{OH})$ bands due being the two lowest energy bands. The second pairing scheme groups $\nu(\text{OH})_{\text{A}}$ and $\nu(\text{OH})_{\text{C}}$ together due to their similar band intensities, and the bands $\nu(\text{OH})_{\text{B}}$ and $\nu(\text{OH})_{\text{D}}$ are grouped together due to their similar peak intensities. Additionally, it should be noted that the bands $\nu(\text{OH})_{\text{B}}$ and $\nu(\text{OH})_{\text{D}}$ are significantly more intense than the bands $\nu(\text{OH})_{\text{A}}$ and $\nu(\text{OH})_{\text{C}}$.

In the spectra presented in Chapter 2 the $\nu_{\text{asym}}(\text{OH})$ band appears at higher wavenumbers than the $\nu_{\text{sym}}(\text{OH})$ band. The $\nu_{\text{asym}}(\text{OH})$ band is also generally more intense than the $\nu_{\text{sym}}(\text{OH})$ band. This general trend would indicate that the pairing of $\nu(\text{OH})_{\text{A}}$ with $\nu(\text{OH})_{\text{B}}$ as $\nu_{\text{asym}}(\text{OH})$ and $\nu_{\text{sym}}(\text{OH})$, respectively, is not

correct due to $\nu(\text{OH})_{\text{B}}$ being centered at lower wavenumbers and more intense than $\nu(\text{OH})_{\text{A}}$. Alternatively, the pairing of $\nu(\text{OH})_{\text{A}}$ with $\nu(\text{OH})_{\text{C}}$ as $\nu_{\text{asym1}}(\text{OH})$ and $\nu_{\text{sym1}}(\text{OH})$, respectively, does follow this trend with $\nu(\text{OH})_{\text{A}}$ being both more intense, and at higher wavenumbers than $\nu(\text{OH})_{\text{C}}$. In addition to this, comparing the peak-to-peak distances between bands further supports the second pairing. The difference in band positions for the $\nu_{\text{asym}}(\text{OH})$ and $\nu_{\text{sym}}(\text{OH})$ bands in Chapter 2 range from 53–95 cm^{-1} (ave. 70 cm^{-1}). The difference in band position for the $\nu(\text{OH})_{\text{A}}$ and $\nu(\text{OH})_{\text{B}}$ bands in the four compounds range from 32–41 cm^{-1} with an average of 37 cm^{-1} . The difference in band position for the $\nu(\text{OH})_{\text{C}}$ and $\nu(\text{OH})_{\text{D}}$ bands in the four compounds range from 17–23 cm^{-1} with an average of 19 cm^{-1} . These differences are half, or even a third, of the differences seen in Chapter 2, which would mean that the asymmetric and symmetric coupled vibrations are much closer in energy in this subset of hydrates, than for all of the other hydrates studied. Instead, in the second pairing schemes the difference in band position for the $\nu(\text{OH})_{\text{A}}$ and $\nu(\text{OH})_{\text{C}}$ bands in the four compounds range from 67–75 cm^{-1} with an average of 72 cm^{-1} , the difference in band position for the $\nu(\text{OH})_{\text{B}}$ and $\nu(\text{OH})_{\text{D}}$ bands in the four compounds range from 52–57 cm^{-1} with an average of 55 cm^{-1} . These values are much closer to the values for the compounds in Chapter 2, and when coupled with the relative intensity argument, indicate that the $\nu(\text{OH})_{\text{A}}$ and $\nu(\text{OH})_{\text{C}}$ bands correspond to $\nu_{\text{asym1}}(\text{OH})$ and $\nu_{\text{sym1}}(\text{OH})$, respectively, for the H_2O molecule with longer $\text{O}(\text{H})\cdots\text{F}$ distances and $\nu(\text{OH})_{\text{B}}$ and $\nu(\text{OH})_{\text{D}}$ bands correspond to $\nu_{\text{asym2}}(\text{OH})$ and $\nu_{\text{sym2}}(\text{OH})$, respectively, for the H_2O molecule with shorter $\text{O}(\text{H})\cdots\text{F}$ distances. The assignment of $\nu_{\text{asym1}}(\text{OH})$ and $\nu_{\text{sym1}}(\text{OH})$ to the H_2O position with the longer $\text{O}(\text{H})\cdots\text{F}$ distances is consistent with all other assignments in this dissertation because the $\nu_{\text{asym2}}(\text{OH})$ and $\nu_{\text{sym2}}(\text{OH})$ bands are more red shifted than the $\nu_{\text{asym1}}(\text{OH})$ and $\nu_{\text{sym1}}(\text{OH})$ bands.

For the FTIR spectra of the $\nu(\text{OD})$ region of $\text{M}(\text{HOD})(\text{H}_2\text{O})_5(\text{B}_{12}\text{F}_{12})$ salts ($\text{M} = \text{Mg}, \text{Co}$) the $\nu(\text{OD})$ band at 2645 cm^{-1} is assigned to the HOD molecule in $\text{Mg}(\text{HOD})(\text{H}_2\text{O})_5(\text{B}_{12}\text{F}_{12})$ occupying the H_2O position with a 2.0659(11) Å $\text{M}-\text{O}$ bond distance, and the $\nu(\text{OD})$ band at 2633 cm^{-1} representing the HOD molecule in the H_2O position with the 2.0390(11) Å $\text{M}-\text{O}$ bond distance. For $\text{Co}(\text{HOD})(\text{H}_2\text{O})_5(\text{B}_{12}\text{F}_{12})$ the $\nu(\text{OD})$ band at 2635 cm^{-1} representing the HOD molecule in the H_2O position with the 2.0907(4) Å $\text{M}-\text{O}$ bond distance and the $\nu(\text{OD})$ band at 2618 cm^{-1} representing the HOD molecule in the H_2O position with the 2.0663(4) Å $\text{M}-\text{O}$ bond distance. A Four peak Lorentzian least squares fits of the $\nu(\text{OH})$ and $\nu(\text{OD})$ regions of the FTIR

spectrum of $\text{Mg}(\text{H}_2\text{O})_6(\text{B}_{12}\text{F}_{12})$ and $\text{Mg}(\text{D}_2\text{O})_6(\text{B}_{12}\text{F}_{12})$, respectively, are shown in Figure 4.9. A Four peak Lorentzian least squares fit of the $\nu(\text{OH})$ region of the FTIR spectrum of $\text{Co}(\text{H}_2\text{O})_6(\text{B}_{12}\text{F}_{12})$ is shown in Figure 4.10. For these two compounds different orientations of the HOD molecule, in a single H_2O site, could not be resolved. The difference in $\text{O}(\text{H})\cdots\text{F}$ distances are very small (0.026(4) and 0.010(4) Å for $\text{Mg}(\text{HOD})(\text{H}_2\text{O})_5(\text{B}_{12}\text{F}_{12})$; and 0.033(2) Å for $\text{Co}(\text{HOD})(\text{H}_2\text{O})_5(\text{B}_{12}\text{F}_{12})$) or virtually identical (0.005(2) for $\text{Co}(\text{HOD})(\text{H}_2\text{O})_5(\text{B}_{12}\text{F}_{12})$). Of these four different HOD positions, only the H_2O position in $\text{Co}(\text{HOD})(\text{H}_2\text{O})_5(\text{B}_{12}\text{F}_{12})$ with a $\text{M}-\text{O}$ bond distance of 2.0907(4) Å and $\text{O}(\text{H})\cdots\text{F}$ distances of 2.886(1) and 2.919(1) Å is close to having separate resolvable bands for the different $\text{O}(\text{H})\cdots\text{F}$ distances as evidenced by the plateauing of the 2635 cm^{-1} band in Figure 4.8. The difference of 0.033(2) Å in the $\text{O}(\text{H})\cdots\text{F}$ distances is still not sufficient to resolve, or model, the two different bands, but it is close and informs on the potential lower limit of resolvable difference in $\text{O}(\text{H})\cdots\text{F}$ distances by FTIR spectroscopy.

4.3.2 Direct Spectroscopic Observation of the Effect of Cation Acidity on Water–Anion Hydrogen Bond Strength

There is a small, but unambiguous and therefore meaningful, progression of $\nu(\text{OH})$ values from higher to lower wavenumbers in the $\text{M}(\text{H}_2\text{O})_6(\text{B}_{12}\text{F}_{12})$ spectra in the order $\text{Mg} > \text{Co} > \text{Ni} > \text{Zn}$, as shown in Figure 4.1. This is essentially the same order as the pK_a values for aqueous Mg^{2+} (11.3(1)), Co^{2+} (9.7), Ni^{2+} (9.86), and Zn^{2+} (9.0),¹⁰⁻¹¹ which is a sensible result because the more acidic $\text{M}(\text{H}_2\text{O})_6^{2+}$ ions should form stronger hydrogen bonds to a common anion, resulting a greater $\nu(\text{OH})$ red-shift. This observation, which was also unprecedented when first published,⁴ was only possible because of the $\nu(\text{OH})$ bands were sufficiently narrow to allow such small differences to be unambiguously determined.

Returning to Figure 2.43 (reproduced as Figure 4.11 in this chapter for convenience), the $\nu(\text{OD})$ band positions for an HOD molecule in both $\text{Mg}(\text{HOD})(\text{H}_2\text{O})_5(\text{B}_{12}\text{F}_{12})$ and $\text{Co}(\text{HOD})(\text{H}_2\text{O})_5(\text{B}_{12}\text{F}_{12})$ are plotted along with many of the other salt hydrates discussed in Chapter 2. Except for $\text{Li}(\text{HOD})(\text{H}_2\text{O})_3(\text{B}_{12}\text{F}_{12})$, all of the alkali metal salt hydrates of the $\text{B}_{12}\text{F}_{12}^{2-}$ anion are less red shifted than the divalent salt hydrates of the $\text{B}_{12}\text{F}_{12}^{2-}$ anion. It is likely that the reason that the $\nu(\text{OD})$ band for $\text{Li}(\text{HOD})(\text{H}_2\text{O})_3(\text{B}_{12}\text{F}_{12})$ is more red shifted than

Mg(HOD)(H₂O)₅(B₁₂F₁₂) (but not Co(HOD)(H₂O)₅(B₁₂F₁₂)) is a result of the O–H···O hydrogen bond having some intramolecular effect on the O–H···F hydrogen bond. The salt hydrates with alkali metal cations that are more red shifted than Co(HOD)(H₂O)₅(B₁₂F₁₂) all have anions with stronger coordination strengths (more basic) than B₁₂F₁₂²⁻, reinforcing the idea that the coordination strength (basicity) of the anion is more important to the relative strength of the water–anion hydrogen bond than the oxidation state (acidity) of the cation, but that the acidity of the cation can still have an observable effect on the strength of the relative hydrogen bonds strength. Though to date, the later has only been observed when comparing isomorphous M(H₂O)₆(B₁₂F₁₂) salts with cations of similar size and identical oxidation state.

The fact that coordination strength of the anion has a greater effect on the hydrogen bond strength is also seen by comparing Co(HOD)(H₂O)₅(B₁₂F₁₂) and Co(HOD)(H₂O)₅(SnF₆) in Figure 4.12 both compounds, Co is octahedrally coordinated by six H₂O ligands, and centered in a CsCl-like lattice with the anions at the corners of the pseudo-cubic array. Their O(D)··F hydrogen bond distances differ by < 0.1 Å, but the difference in $\nu(\text{OD})$ band position is between 80–100 cm⁻¹. This highlights the significance that anion coordination strength, the only significantly different component between the two, has on the relative hydrogen bond strength. A similar comparison can be made between Mg(HOD)(H₂O)₅(B₁₂F₁₂) and Mg(HOD)(H₂O)₅(SiF₆) which have at least one virtually identical O(D)··F hydrogen bond distance, but a 50 cm⁻¹ difference in $\nu(\text{OD})$ band position. By comparison, a difference in pK_a of 2.3(1) for isomorphous Mg(H₂O)₆(B₁₂F₁₂) and Zn(H₂O)₆(B₁₂F₁₂) only results in a red shift of ca. 15–26 cm⁻¹ (Figure 4.1).

4.3.3 SC-XRD Structures and TGA of M(H₂O)_n(B₁₂F₁₂) salts (M = Ca²⁺, Sr²⁺, Ba²⁺; n = 1, 4, 5, 7)

The Ca²⁺ and Sr²⁺ salts of the B₁₂F₁₂²⁻ anion crystallize from aqueous solutions as heptahydrates. Drawings of the structures of Sr(H₂O)₇(B₁₂F₁₂) and Ca(H₂O)₇(B₁₂F₁₂) are shown in Figure 4.13 and 4.14, respectively. Both structures contain one unique M(H₂O)₇²⁺ cation and one unique B₁₂F₁₂²⁻ anion that forms a distorted CsCl-like packing arrangement. Tables 4.9 and 4.10 list the individual M–O bond distances and band valences for these two structures. Drawings of the SrO₇F₂ and CaO₇ coordination spheres are shown in

Figures 4.13 and 4.14, respectively. The O–H···F hydrogen bonding in $\text{Ca}(\text{H}_2\text{O})_7(\text{B}_{12}\text{F}_{12})$ is shown in Figure 4.13. Unlike the $\text{Sr}(\text{H}_2\text{O})_7(\text{B}_{12}\text{F}_{12})$ structure, which has two Sr–F bonds, there are no Ca–F distances shorter than 3.97 Å. This corresponds to a Ca–F bond valence of 0.004.

The structures of $\text{Ba}(\text{H}_2\text{O})_5(\text{B}_{12}\text{F}_{12})$ and $\text{Ba}(\text{H}_2\text{O})_4(\text{B}_{12}\text{F}_{12})$ were originally published in 2018⁴ and are shown in Figure 4.15 and 4.16, respectively. The structure of $\text{Ba}(\text{H}_2\text{O})_5(\text{B}_{12}\text{F}_{12})$ consists of a unique $\text{Ba}(\text{H}_2\text{O})_5^{2+}$ cation and a unique $\text{B}_{12}\text{F}_{12}^{2-}$ anion, forming a CsCl-like lattice with $\odot\cdots\odot$ distances of 6.943, 7.530, and 7.720 Å and $90^\circ \odot\cdots\odot\cdots\odot$ angles, but with the $\text{Ba}(\text{H}_2\text{O})_5^{2+}$ cation (i.e., the Ba atom) displaced 2.077 Å from the center of the parallelepiped formed by the eight $\text{B}_{12}\text{F}_{12}^{2-}$ anions. Drawings of the BaO_5F_6 coordination sphere in $\text{Ba}(\text{H}_2\text{O})_5(\text{B}_{12}\text{F}_{12})$ and the BaO_4F_5 coordination sphere in $\text{Ba}(\text{H}_2\text{O})_4(\text{B}_{12}\text{F}_{12})$ are shown in Figure 4.15 and 4.16, respectively. Table 4.11 and 4.12 list individual M–O bond distances and bond valences for these two structures. The Ba atoms in both structures are on the general positions. In spite of the difference in the number of H_2O molecules per Ba atom, the difference in the formula unit volume (FUVs) for $\text{Ba}(\text{H}_2\text{O})_5(\text{B}_{12}\text{F}_{12})$ (403.6 Å³) and $\text{Ba}(\text{H}_2\text{O})_4(\text{B}_{12}\text{F}_{12})$ (399.7 Å³) is less than 4 Å³. Interestingly, this is comparable to the DFT predicted 5 Å³ differences in FUVs for $\text{Cs}_2(\text{H}_2\text{O})(\text{B}_{12}\text{F}_{12})$ and anhydrous $\text{Cs}_2(\text{B}_{12}\text{F}_{12})$.^x The Structure of $\text{Ba}(\text{H}_2\text{O})_5(\text{B}_{12}\text{F}_{12})$ is one of only four $\text{B}_{12}\text{F}_{12}^{2-}$ salt hydrates in which coordinated H_2O molecules are hydrogen bonded to other coordinated H_2O molecules in neighboring $\text{M}(\text{H}_2\text{O})_n^{m+}$ cations ($m = 1, 2$; the other examples are $\text{K}_2(\text{H}_2\text{O})_4(\text{B}_{12}\text{F}_{12})$,¹² $\text{Li}_2(\text{H}_2\text{O})_4(\text{B}_{12}\text{F}_{12})$,¹³ and $\text{Sr}_2(\text{H}_2\text{O})_7(\text{B}_{12}\text{F}_{12})$ ⁴).

The assignments of the hydration states for all of the FTIR spectra in this, and previous, chapters have been confirmed by TGA. Until this point, the crystal structures and stable hydrations states observed in TGA experiments have agreed with each other, hence the lack of discussion of the thermograms. Assignment of the hydration state from the crystal structure alone has been sufficient. Agreement between the two allows for correlations between $\nu(\text{OH/D})$ band position and $\text{O}(\text{H/D})\cdots\text{F}$ bond distances. Unfortunately, this agreement between TGA data and SC-XRD structures does not exist for the $\text{B}_{12}\text{F}_{12}^{2-}$ salt hydrates of the Ca^{2+} , Sr^{2+} , and Ba^{2+} cations. The thermogram in Figure 4.17 shows the rapid complete hydration of $\text{Ca}(\text{H}_2\text{O})_4(\text{B}_{12}\text{F}_{12}) \rightarrow \text{Ca}(\text{H}_2\text{O})_6(\text{B}_{12}\text{F}_{12})$ under an atmosphere with $P_{\text{water}} = 18$ torr followed by the rapid isothermal dehydration $\text{Ca}(\text{H}_2\text{O})_6(\text{B}_{12}\text{F}_{12}) \rightarrow \text{Ca}(\text{H}_2\text{O})_4(\text{B}_{12}\text{F}_{12})$ at 50 °C under a dry atmosphere. This figure, and the assignments of the phases of the end members of the transitions, as first published in 2018.⁴ This is at odds with the known

structure of $\text{Ca}(\text{H}_2\text{O})_7(\text{B}_{12}\text{F}_{12})$. To reconcile this discrepancy the crystal structure needs to be set aside, and the hydration state observed in the FTIR spectra for $\text{Ca}(\text{H}_2\text{O})_n(\text{B}_{12}\text{F}_{12})$ need to be assigned based on the TGA. Dehydrating a sample of $\text{Ca}(\text{H}_2\text{O})_n(\text{B}_{12}\text{F}_{12})$ to $\text{Ca}(\text{H}_2\text{O})_4(\text{B}_{12}\text{F}_{12})$ under a dry atmosphere (where $6 > n > 4$) in the TGA is similar enough to the drying of an aqueous solution of $\text{Ca}(\text{B}_{12}\text{F}_{12})$ to a polycrystalline solid on the ATR crystal. Since the $\text{Ca}(\text{H}_2\text{O})_4(\text{B}_{12}\text{F}_{12})$ species is the stable species under the dry atmosphere in the TGA, that would imply the solid on the ATR crystal is most likely $\text{Ca}(\text{H}_2\text{O})_4(\text{B}_{12}\text{F}_{12})$. Similarly, hydrating a sample of $\text{Ca}(\text{H}_2\text{O})_4(\text{B}_{12}\text{F}_{12})$ on the ATR crystal under an atmosphere with $P_{\text{water}} = 18$ torr should result in the conversion $\text{Ca}(\text{H}_2\text{O})_4(\text{B}_{12}\text{F}_{12}) \rightarrow \text{Ca}(\text{H}_2\text{O})_6(\text{B}_{12}\text{F}_{12})$ as is observed in the TGA. To bridge the gap between the room temperature ATR-FTIR spectra and the 50 °C TGA data an additional series of spectra collected at 50 °C is required. If the room temperature and 50 °C spectra are identical, then the TGA assignments can be assigned to the room temperature spectra.

The top thermogram in Figure 4.18 shows a series of rapid hydration–dehydration cycles for the reaction $\text{Ba}(\text{H}_2\text{O})_5(\text{B}_{12}\text{F}_{12}) \leftrightarrow \text{Ba}(\text{H}_2\text{O})_8(\text{B}_{12}\text{F}_{12})$ at 25 °C. The lower thermogram in Figure 4.18 shows that $\text{Ba}(\text{H}_2\text{O})_5(\text{B}_{12}\text{F}_{12})$ appears to be metastable. Holding the sample under a dry atmosphere at 25 °C causes a slow loss of mass over time. A SC-XRD structure of both $\text{Ba}(\text{H}_2\text{O})_4(\text{B}_{12}\text{F}_{12})$ and $\text{Ba}(\text{H}_2\text{O})_8(\text{B}_{12}\text{F}_{12})$ are known, and it is not unreasonable to assume with sufficient time that the dehydration reaction $\text{Ba}(\text{H}_2\text{O})_5(\text{B}_{12}\text{F}_{12}) \rightarrow \text{Ba}(\text{H}_2\text{O})_4(\text{B}_{12}\text{F}_{12})$ would occur at 25 °C based on the trend in Figure 4.18. Unfortunately, the member of the group who performed the TGA experiment in 2010 originally did not allow for this to transformation to complete before increasing the temperature to observe the dehydration $\text{Ba}(\text{H}_2\text{O})_n(\text{B}_{12}\text{F}_{12})$ ($5 > n > 4$) $\rightarrow \text{Ba}(\text{H}_2\text{O})(\text{B}_{12}\text{F}_{12})$. Due to the ambiguity of the hydration state that is stable under a dry atmosphere at room temperature the assignment of the FTIR spectra under these conditions is not possible, though as discussed below, a hypothesis is proposed. Holding the polycrystalline sample on the ATR crystal under a humid atmosphere at room temperature, or a dry atmosphere at 80 °C should yield spectra assigned to $\text{Ba}(\text{H}_2\text{O})_8(\text{B}_{12}\text{F}_{12})$ and $\text{Ba}(\text{H}_2\text{O})(\text{B}_{12}\text{F}_{12})$, respectively.

Finally, at the time the $\text{Ba}(\text{H}_2\text{O})_n(\text{B}_{12}\text{F}_{12})$ and $\text{Ca}(\text{H}_2\text{O})_n(\text{B}_{12}\text{F}_{12})$ were collected, the TGA of $\text{Sr}(\text{H}_2\text{O})_n(\text{B}_{12}\text{F}_{12})$ was not. The TGA has become inaccessible making the assignment of the solid $\text{Sr}(\text{H}_2\text{O})_n(\text{B}_{12}\text{F}_{12})$ species on an ATR crystal not possible at this time. In lieu of making definitive correlations

between H₂O environments, O(H)···F bond lengths, and $\nu(\text{OH})$ band multiplicity and positions, hypothesis to the change in symmetry, potential assignments, and general position of $\nu(\text{OH})$ bands will be made for these three materials.

4.3.4 FTIR Spectra of $\text{M}(\text{H}_2\text{O})_n(\text{B}_{12}\text{F}_{12})$ salts ($\text{M} = \text{Ca}^{2+}, \text{Sr}^{2+}, \text{Ba}^{2+}; n = 1, 4, 5, 7$)

The FTIR spectrum of $\text{Ca}(\text{H}_2\text{O})_4(\text{B}_{12}\text{F}_{12})$ is shown in Figure 4.19. There are four distinct bands observed in the $\nu(\text{OH})$ region of this spectrum. These bands are centered at 3664, 3641, 3595, and 3582 cm^{-1} . While $\text{Ca}(\text{H}_2\text{O})_4(\text{B}_{12}\text{F}_{12})$ has four $\nu(\text{OH})$ bands, like the $\text{M}(\text{H}_2\text{O})_6(\text{B}_{12}\text{F}_{12})$ discussed earlier in the chapter, they differ greatly in terms of integrated intensity, with only the two bands at 3595 and 3582 cm^{-1} being similar in terms of the integrated intensity. Thus, the spectrum does not have the same obvious relationship between $\nu(\text{OH})$ bands that the $\text{M}(\text{H}_2\text{O})_6(\text{B}_{12}\text{F}_{12})$ salts did. This likely indicates a $\text{Ca}(\text{H}_2\text{O})_4^{2+}$ complex with a lower symmetry than in the $\text{M}(\text{H}_2\text{O})_6^{2+}$ complex. If the solid sample on the ATR crystal is then exposed to a wet atmosphere with a $P_{\text{water}} = 6$ torr at 22 °C, or 17 torr at 50°C, the sample will rapidly convert to the hexahydrate salt $\text{Ca}(\text{H}_2\text{O})_6(\text{B}_{12}\text{F}_{12})$. The spectrum of $\text{Ca}(\text{H}_2\text{O})_6(\text{B}_{12}\text{F}_{12})$ is shown in Figure 4.19. Spectra showing the reaction $\text{Ca}(\text{H}_2\text{O})_4(\text{B}_{12}\text{F}_{12}) \leftrightarrow \text{Ca}(\text{H}_2\text{O})_6(\text{B}_{12}\text{F}_{12})$ is also shown in Figure 4.19. The spectrum in Figure 4.19 only contains two $\nu(\text{OH})$ bands centered at 3627 and 3586 cm^{-1} . The band at 3627 cm^{-1} is broader than the other bands in the $\text{Ca}(\text{H}_2\text{O})_4(\text{B}_{12}\text{F}_{12})$ spectrum. This band is also the only one which is asymmetrical, indicating a shoulder on the higher energy side of the band. The band at 3586 cm^{-1} also possesses a shoulder on the higher energy side of the band, though this shoulder is much sharper and indicates that a second band is sitting very close to the 3586 cm^{-1} band. The shoulder on the 3627 cm^{-1} band is thus also likely due to a second band laying under the 3627 cm^{-1} band. Based on the number of bands, during the conversion of the tetrahydrate into the hexahydrate there appears to be an increase in the symmetry of the $\text{M}(\text{H}_2\text{O})_n^{2+}$ complex. This may not be entirely true since, as mentioned, there appears to be additionally bands hiding under the two prominent bands in the spectrum of the hexahydrate. Without SC-XRD structure of either the tetrahydrate or the hexahydrate it is difficult to probe this, or the O–H···F bonding environments further.

The FTIR analysis of the Sr salt hydrates of the $\text{B}_{12}\text{F}_{12}^{2-}$ is limited similarly to the Ca salts discussed above, in that only the $\text{Sr}(\text{H}_2\text{O})_7(\text{B}_{12}\text{F}_{12})$ structure is known. What further complicates the analysis of this salt hydrate is that TGA of the $\text{Sr}(\text{H}_2\text{O})_n(\text{B}_{12}\text{F}_{12})$ was not previously collected, and the instrument has since

become indefinitely inaccessible, so determining the hydration states of the species observed by FTIR is not currently possible. Two different hydration states were explored for the Sr^{2+} salt hydrate, $\text{Sr}(\text{H}_2\text{O})_n(\text{B}_{12}\text{F}_{12})$ and $\text{Sr}(\text{H}_2\text{O})_m(\text{B}_{12}\text{F}_{12})$, where $n < m$. For the n-hydrate there appears to be as many as five $\nu(\text{OH})$ bands at 3651, 3625, 3587, 3572, and 3562 cm^{-1} (Figure 4.20). The m-hydrate only has two sharp, symmetrical, bands at 3648 and 3587 cm^{-1} (Figure 4.20). As with the Ca^{2+} salt hydrate FTIR spectra, the n-hydrate is converted to the m-hydrate by exposing the solid sample on the ATR crystal to a humid environment. The m-hydrate, like the $\text{Ca}(\text{H}_2\text{O})_6(\text{B}_{12}\text{F}_{12})$ species, remains stable indefinitely under this humid atmosphere. Unlike the $\text{Ca}(\text{H}_2\text{O})_6(\text{B}_{12}\text{F}_{12})$ spectra the two bands in the m-hydrate do not appear to be hiding any additional bands, so conversion to a higher symmetry $\text{Sr}(\text{H}_2\text{O})_m^{2+}$ appears to be much more likely for this salt species. Due to the number of unique H_2O environments in the SC-XRD structure of $\text{Sr}(\text{H}_2\text{O})_7(\text{B}_{12}\text{F}_{12})$ it is unlikely that $m = 7$. The possibility exists that $n = 7$, but this will need to be confirmed with TGA before more can be said about the relationship between $\text{Sr}(\text{H}_2\text{O})_n(\text{B}_{12}\text{F}_{12})$ and $\text{Sr}(\text{H}_2\text{O})_7(\text{B}_{12}\text{F}_{12})$.

The first spectrum in Figure 4.21 is assigned to $\text{Ba}(\text{H}_2\text{O})_8(\text{B}_{12}\text{F}_{12})$, and contains four $\nu(\text{OH})$ bands at 3626, 3590, 3570, and 3553 cm^{-1} . The second two spectra in Figure 4.21 show the dehydration of $\text{Ba}(\text{H}_2\text{O})_8(\text{B}_{12}\text{F}_{12}) \rightarrow \text{Ba}(\text{H}_2\text{O})_n(\text{B}_{12}\text{F}_{12})$ after 10 and 25 minutes under a dry atmosphere. Importantly, the $\nu(\text{OH})$ bands appear to change between the two spectra. The hypothesis is that this change represents conversion of one intermediate hydration state to another; quite possible the conversion $\text{Ba}(\text{H}_2\text{O})_5(\text{B}_{12}\text{F}_{12}) \rightarrow \text{Ba}(\text{H}_2\text{O})_4(\text{B}_{12}\text{F}_{12})$ that is hinted at in the TGA and SC-XRD results. The final spectrum in Figure 4.21 is the complete dehydration of $\text{Ba}(\text{H}_2\text{O})_n(\text{B}_{12}\text{F}_{12})$ to $\text{Ba}(\text{H}_2\text{O})(\text{B}_{12}\text{F}_{12})$ at 80 °C. The spectrum for the $\text{Ba}(\text{H}_2\text{O})(\text{B}_{12}\text{F}_{12})$ species contains only two bands at 3651 and 3557 cm^{-1} , as expected for a structure with a single crystallographically unique H_2O molecule. Originally it was believed that the mass after 60 minutes in Figure 4.18 corresponded to $\text{Ba}(\text{B}_{12}\text{F}_{12})$, not $\text{Ba}(\text{H}_2\text{O})(\text{B}_{12}\text{F}_{12})$. The presence of stable $\nu(\text{OH})$ bands at 80 °C after a significant length of time lead to reevaluation of the original TGA experimental results. This was further confirmed by comparing the ratio of the molar mass for the two possible dehydration pathways ($\text{Ba}(\text{H}_2\text{O})_8(\text{B}_{12}\text{F}_{12}) \rightarrow \text{Ba}(\text{H}_2\text{O})(\text{B}_{12}\text{F}_{12})$ vs $\text{Ba}(\text{H}_2\text{O})_7(\text{B}_{12}\text{F}_{12}) \rightarrow \text{Ba}(\text{B}_{12}\text{F}_{12})$) to the ratio of the molar masses from the TGA experiment (Table 4.13).

4.4 Conclusions and Future Work

4.4.1 Conclusions

The FTIR spectra of the $\nu(\text{OH})$ region for the four isomorphous $\text{M}(\text{H}_2\text{O})_6(\text{B}_{12}\text{F}_{12})$ salt hydrates ($\text{M} = \text{Mg}, \text{Co}, \text{Ni}, \text{Zn}$) has four $\nu(\text{OH})$ bands. These bands have been shown to be two sets of $\nu_{\text{asym}}(\text{OH})$ and $\nu_{\text{sym}}(\text{OH})$ bands, one for each of the two unique *fac*- $(\text{H}_2\text{O})_3$ sets of ligands in the $\text{M}(\text{H}_2\text{O})_6^{2+}$ complexes. Comparison of the band positions for all four of the different cations revealed that the degree of red shifting is consistent with the pK_a of the cations, with Mg^{2+} being the most basic cation (least red shifted) and Zn^{2+} being the most acidic (most red shifted). This is direct spectroscopic evidence of the effect of cation acidity on ligand water–anion hydrogen bond strength, when all other environmental and structural considerations are taken equal. Additionally, reevaluation of the correlation curves from Chapter 2, through the lens of cation oxidation number, shows that within a family of salts, with the same anion, the acidity of the cation has an observable effect on the $\text{O}-\text{D}\cdots\text{F}$ hydrogen bond strength with larger oxidation numbers resulting in stronger hydrogen bonds, and thus, a larger red shift. When salt hydrates of different anions are compared in this manner, the anion coordination strength appears to have a stronger influence on the relative strength of the hydrogen bonds than the cation acidity. Finally, further evidence that using only the $\text{O}(\text{D})\cdots\text{F}$ bond distance as a measure of hydrogen bond strength is fundamentally flawed when $\text{M}(\text{H}_2\text{O})_6(\text{X})$ salts ($\text{M} = \text{Mg}, \text{Co}$; $\text{X} = \text{SiF}_6, \text{SnF}_6$) with nearly identical $\text{O}(\text{D})\cdots\text{F}$ bond distances and pseudo-cubic CsCl-like crystallographic environments, have $\nu(\text{OD})$ values differing by 50–100 cm^{-1} . This further reinforces that the anion coordination strength heavily influences the strength of the hydrogen bond (magnitude of the red-shift) even in cases where differences in $\text{O}(\text{D})\cdots\text{F}$ bond distances are virtually indistinguishable.

The metal salt hydrates formed using the anions Ca^{2+} , Sr^{2+} , Ba^{2+} with the $\text{B}_{12}\text{F}_{12}^{2-}$ have some of the most complex $\nu(\text{OH})$ regions of all the salt hydrates explored in this dissertation. Discrepancies between TGA and known SC-XRD structures make only general evaluations possible at this time. From these general evaluations the three material are consistent with the

observations made for the $M(H_2O)_6(B_{12}F_{12})$ salts in terms of the effects of cation acidity on the degree of red-shift, and thus hydrogen bond strength.

4.4.2 Future Work

The future work driven by the results presented in this chapter are similar to the ones present in section 2.4.2 of Chapter 2 of this dissertation. Determination of more precise H atom positions for the studied divalent salt hydrates is as critical to improving the correlation curves discussed in chapter 2 as it is to the monovalent salts that are the focus of that chapter. Synthesis, and experimental evaluation, of new divalent salt hydrates will increase the number of data points on the correlation curves, further improving the modeled fit of the data. Attempting to reconcile the discrepancy between TGA and SC-XRD data for the Ca^{2+} , Sr^{2+} , and Ba^{2+} salts will be extremely important for being able to fit them into the larger picture of the work discussed in this dissertation. Finally, trivalent (or higher oxidation state) cations represent an untapped class of metal salt hydrates that have yet to be explored in great depth, compared to the monovalent and divalent cations discussed in Chapters 2 and 4.

References

1. Hawkes, S. J. All Positive Ions Give Acid Solutions in Water. *J. Chem. Educ.* **1996**, *73*, 516.
2. Cotton, F. A. *Chemical Applications of Group Theory*; Wiley 1963.
3. Fraley, P. E.; Rao, K. N. High Resolution Infrared Spectra of Water Vapor ν_1 and ν_3 Bands of H_2^{16}O . *J. Mol. Spectrosc.* **1969**, *29*, 348–364.
4. Lacroix, M. R.; Bukovsky, E. V.; Lozinsek, M.; Folsom, T. C.; Newell, B. S.; Liu, Y.; Peryshkov, D. V.; Strauss, S. H. Manifestations of Weak O–H \cdots F Hydrogen Bonding in $\text{M}(\text{H}_2\text{O})_n(\text{B}_{12}\text{F}_{12})$ Salt Hydrates: Unusually Sharp Fourier Transform Infrared $\nu(\text{OH})$ Bands and Latent Porosity (M = Mg–Ba, Co, Ni, Zn). *Inorg. Chem.* **2018**, *57*, 14983–15000.
5. Lacroix, M. R.; Liu, Y.; Strauss, S. H. Hydrated Metal Ion Salts of the Weakly Coordinating Fluoroanions PF_6^- , TiF_6^{2-} , $\text{B}_{12}\text{F}_{12}^{2-}$, $\text{Ga}(\text{C}_2\text{F}_5)_4^-$, $\text{B}(3,5\text{-C}_6\text{H}_3(\text{CF}_3)_2)_4^-$, and $\text{Al}(\text{OC}(\text{CF}_3)_3)_4^-$. In Search of the Weakest HOH \cdots F Hydrogen Bonds. *Inorg. Chem.* **2019**, *58*, 14900–14911.
6. Zeng, G.; Holladay, S.; Langlois, D.; Zhang, Y.; Liu, Y. Kinetics of Heterogeneous Reaction of Ozone with Linoleic Acid and its Dependence on Temperature, Physical State, RH, and Ozone Concentration. *J. Phys. Chem. A* **2013**, *117*, 1963–1974.
7. Leng, C.; Hiltner, J.; Pham, H.; Kelley, J.; Mach, M.; Zhang, Y.; Liu, Y. Kinetics Study of Heterogeneous Reactions of Ozone with Erucic Acid Using an ATR-IR Flow Reactor. *Phys. Chem. Chem. Phys.* **2014**, *16*, 4350–4360.
8. Gao, X.; Zhang, Y.; Liu, Y. A Kinetics Study of the Heterogeneous Reaction of *n*-Butylamine with Succinic Acid Using an ATR-FTIR Flow Reactor. *Phys. Chem. Chem. Phys.* **2018**, *20*, 15464–15472.
9. Peryshkov, D. V.; Popov, A. A.; Strauss, S. H. Latent Porosity in Potassium Dodecafluorocloso-dodecaborate(2-). Structures and Rapid Room Temperature Interconversions of Crystalline $\text{K}_2\text{B}_{12}\text{F}_{12}$, $\text{K}_2(\text{H}_2\text{O})_2\text{B}_{12}\text{F}_{12}$, and $\text{K}_2(\text{H}_2\text{O})_4\text{B}_{12}\text{F}_{12}$ in the Presence of Water Vapor. *J. Am. Chem. Soc.* **2010**, *132*, 13902.
10. Martell, A. E.; Smith, R. M. *Critical Stability Constants*; 1974. 1–6,
11. Baes, C. F.; Mesmer, R. E. *Hydrolysis of Cations*; 1976.
12. Peryshkov, D. V.; Popov, A. A.; Strauss, S. H. Latent porosity in potassium dodecafluorocloso-dodecaborate(2-). Structures and rapid room temperature interconversions of crystalline

$\text{K}_2\text{B}_{12}\text{F}_{12}$, $\text{K}_2(\text{H}_2\text{O})_2\text{B}_{12}\text{F}_{12}$, and $\text{K}_2(\text{H}_2\text{O})_4\text{B}_{12}\text{F}_{12}$ in the presence of water vapor. *J. Am. Chem. Soc.* **2010**, *132*, 13902–13913.

13. Peryshkov, D. V.; Bukovsky, E. V.; Lacroix, M. R.; Wu, H.; Zhou, W.; Jones, W. M.; Lozinsek, M.; Folsom, T. C.; Heyliger, D. L.; Udovic, T. J.; Strauss, S. H. Latent Porosity in Alkali-Metal $\text{M}_2\text{B}_{12}\text{F}_{12}$ Salts: Structures and Rapid Room-Temperature Hydration/Dehydration Cycles. *Inorg. Chem.* **2017**, *56*, 12023–12041.

14. Cherkasova, T. G.; Tatarinova, E. S.; Cherkasova, E. V. Crystal Structure of Hexaaquamagnesium Hexafluorosilicate. *Russ. J. Inorg. Chem.* **2004**, *49*, 1064–1067.

15. Halasyamani, P.; Willis, M. J.; Stern, C. L.; Poepelmeier, K. R. Crystal growth in aqueous hydrofluoric acid and $(\text{HF})_x \cdot \text{pyridine}$ solutions: syntheses and crystal structures of $[\text{Ni}(\text{H}_2\text{O})_6]^{2+}[\text{MF}_6]^{2-}$ ($\text{M} = \text{Ti}, \text{Zr}, \text{Hf}$) and $\text{Ni}_3(\text{py})_{12}\text{F}_6 \cdot 7\text{H}_2\text{O}$. *Inorg. Chim. Acta* **1995**, *240*, 109–115.

16. Voit, E.; Didenko, N.; Gayvoronskaya, K.; Slobodyuk, A.; Gerasimenko, A. Synthesis and Complex Study of the Crystal Hydrate $\text{Zn}_2\text{ZrF}_8 \cdot 12\text{H}_2\text{O}$. *Z. Anorg. Allg. Chem.* **2016**, *642*, 643–651.

17. Cappa, C. D.; Smith, J. D.; Drisdell, W. S.; Saykally, R. J.; Cohen, R. C. Interpreting the H/D Isotope Fractionation of Liquid Water during Evaporation without Condensation. *J. Phys. Chem. C* **2007**, *111*, 7011–7020, and references therein

18. Liu, J.; Andino, R. S.; Miller, C. M.; X., C. W., D. M.

Ceriotti, M.; Manopoulos, D. E. A Surface-Specific Isotope Effect in Mixtures of Light and Heavy Water. *J. Phys. Chem. C* **2013**, *117*, 2944–2951, and references therein.

19. Barker, E. F.; Sleator, W. W. The Infrared Spectrum of Heavy Water. *J. Chem. Phys.* **1935**, *3*, 660–663.

20. Benedict, W. W.; Gailar, N.; Plyler, E. K. Rotation-Vibration Spectra of Deuterated Water Vapor. *J. Chem. Phys.* **1956**, *24*, 1139–1165.

21. Rank, D. H.; Larsen, K. D.; Bordner, E. B. The Raman Spectrum of Heavy Water Vapor. *J. Chem. Phys.* **1934**, *2*, 464–467.

22. Ayers, G. P.; Pullin, A. D. E. The I.R. Spectra of Matrix Isolated Water Species – I. Assignment of Bands to $(\text{H}_2\text{O})_2$, $(\text{D}_2\text{O})_2$, and HDO Dimer Species in Argon Matrices. *Spectrochim. Acta, Part A* **1976**, *32A*, 1629–1639.

23. Engdahl, A.; Nelander, B. Water in Krypton Matrices. *J. Mol. Struct.* **1989**, *193*, 101–109.

24. Mikenda, W.; Steinböck, S. Stretching frequency versus bond distance correlation of O–D(H)···F hydrogen bonds in solid hydrates *J. Mol. Struct.* **1994**, *326*, 123–130.
25. Wexler, A. Constant humidity solutions. *Handbook of chemistry and physics* **1995**, *73*, 15-20.
26. Mikenda, W.; Pertlik, F.; Steinböck, S. Crystal Structures and Vibrational Spectra of $M\text{SnF}_6 \cdot 6\text{H}_2\text{O}$ ($M = \text{Fe}, \text{Co}, \text{Ni}$). *Monatsh. Chem.* **1995**, *126*, 61–66.
27. Guillermet, J.; Novak, A.; Foglizzo, E. Étude par spectroscopie infrarouge de la structure du cation $\text{Mg}(\text{H}_2\text{O})_6^{2+}$ dans quelques sels de magnésium hydratés. *J. Mol. Struct.* **1973**, *17*, 91–104.
28. ben Hassan, D.; Rekik, W.; Naïhi, H.; Mhiri, T. A new organically templated magnesium sulfate: structure, spectroscopic analysis, and thermal behaviour. *Chem. Pap.* **2014**, *68*, 210–216.
29. Mikuli, E.; Hetmanczyk, J.; Grad, B.; Kozak, A.; Wasicki, J. W.; Bilski, P.; Holderna-Natkaniec, K.; Medycki, W. The relationship between reorientational molecular motions and phase transitions in $[\text{Mg}(\text{H}_2\text{O})_6](\text{BF}_4)_2$, studied with the use of ^1H and ^{19}F NMR and FT-MIR. *J. Chem. Phys.* **2015**, *142*, 069507.
30. Serezhkin, V. N.; Grigoriev, M. S.; Abdulmyanov, A. R.; Fedoseev, A. M.; Savchenkov, A. V.; Serezhkina, L. B. Synthesis and X-ray Crystallography of $[\text{Mg}(\text{H}_2\text{O})_6][\text{AnO}_2(\text{C}_2\text{H}_5\text{COO})_3]_2$ ($\text{An} = \text{U}, \text{Np}, \text{or Pu}$). *Inorg. Chem.* **2016**, *55*, 7688–7693.
31. Nitschke, C.; Köckerling, M.; Bernhardt, E.; Küppers, T.; Willner, H. Structural diversity and spectral and thermal properties of the first alkaline earth metal tetracyanidoborates: $[\text{Mg}(\text{H}_2\text{O})_6][\text{B}(\text{CN})_4]_2$, $[\text{Mg}(\text{H}_2\text{O})_2][\text{B}(\text{CN})_4]_2$, $[\text{Mg}(\text{DMF})_6][\text{B}(\text{CN})_4]_2$, $[\text{Ca}(\text{H}_2\text{O})_3][\text{B}(\text{CN})_4]_2$, and $[\text{Ca}(\text{H}_2\text{O})_2(\text{CH}_3\text{CN})][\text{B}(\text{CN})_4]_2$. *Dalton Trans.* **2014**, *43*, 7128–7138.
32. Chen, X.; Liu, Y. H.; Alexander, A. M.; Gallucci, J. C.; Hwang, S. J.; Lingam, H. K.; Huang, Z.; Wang, C.; Li, H.; Zhao, Q.; Ozkan, U. S.; Shore, S. G.; Zhao, J. C. Desolvation and dehydrogenation of solvated magnesium salts of dodecahydrododecaborate: relationship between structure and thermal decomposition. *Chemistry* **2014**, *20*, 7325–7333.
33. Tai, X. S.; Jie, Y. Synthesis, Crystal Structure and Antibacterial Activity of Mg(II) Complex $[\text{Mg}(\text{H}_2\text{O})_6] \cdot (4\text{-amino-3-methylbenzenesulfonate})_2$. *Crystals* **2015**, *5*, 294–301.
34. Kammoun, O.; Loulou, N.; Rekik, W.; Naïli, H.; Mhiri, T.; Bataille, T. Synthesis, Crystal Structure and Characterization of a New Dabcodiium Hexaaquacobalt(II) Bis(Selenate), $(\text{C}_6\text{H}_{14}\text{N}_2)[\text{Co}(\text{H}_2\text{O})_6](\text{SeO}_4)_2$. *J. Chem. Crystallogr.* **2012**, *42*, 103–110.
35. Hoshino, R.; Nakamura, T.; Adachi, S. Structural change induced by thermal annealing of red-light-emitting $\text{ZnSnF}_6 \cdot 6\text{H}_2\text{O} : \text{Mn}^{4+}$ hexahydrate phosphor. *Jap. J. Appl. Phys.* **2016**, *55*, article 052601.

36. Donakowski, M. D.; Gautier, R.; Yeon, J.; Moore, D. T.; Nino, J. C.; Halasyamani, P.; Poeppelmeier, K. R. The Role of Polar, Lambda (Λ)-Shaped Building Units in Noncentrosymmetric Inorganic Structures. *J. Am. Chem. Soc.* **2012**, *134*, 7679–7689.
37. Voit, E. I.; Didenko, N. A.; Gayvoronskaya, K. A.; Gerasimenko, A. V. Structure of $\text{ZnZrF}_6 \cdot n\text{H}_2\text{O}$ ($n = 6-2$) and ZnZrF_6 Crystallohydrates According to Vibrational Spectroscopy Data. *Opt. Spectrosc.* **2016**, *121*, 229–240.
38. Karadjova, V.; Kovacheva, D.; Stoilova, D. Study on the cesium Tutton compounds, $\text{Cs}_2\text{M}(\text{XO}_4)_2 \cdot 6\text{H}_2\text{O}$ ($\text{M} = \text{Mg}, \text{Co}, \text{Zn}$; $\text{X} = \text{S}, \text{Se}$): Preparation, X-ray powder diffraction and infrared spectra. *Vib. Spectrosc.* **2014**, *75*, 51–58.

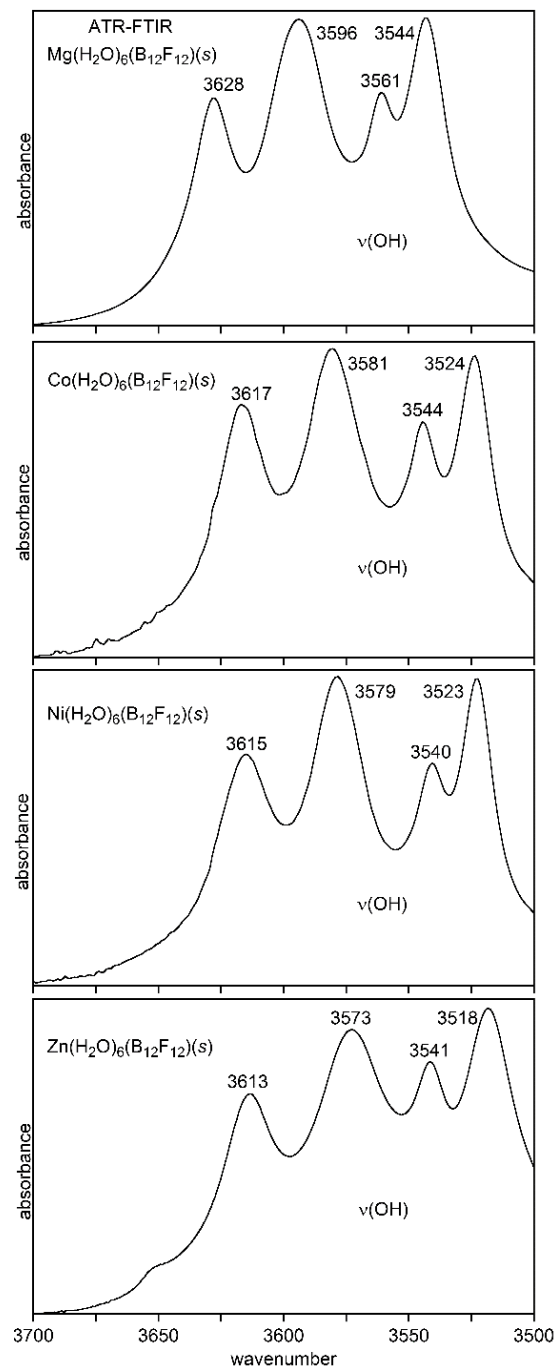


Figure 4.1. Expansions of the $\nu(\text{OH})$ regions of ATR-FTIR spectra of $\text{M}(\text{H}_2\text{O})_6(\text{Z})$ ($\text{M} = \text{Mg}, \text{Co}, \text{Ni}, \text{Zn}$). The samples were evaporated on the ZnSe ATR crystal from aqueous solutions.

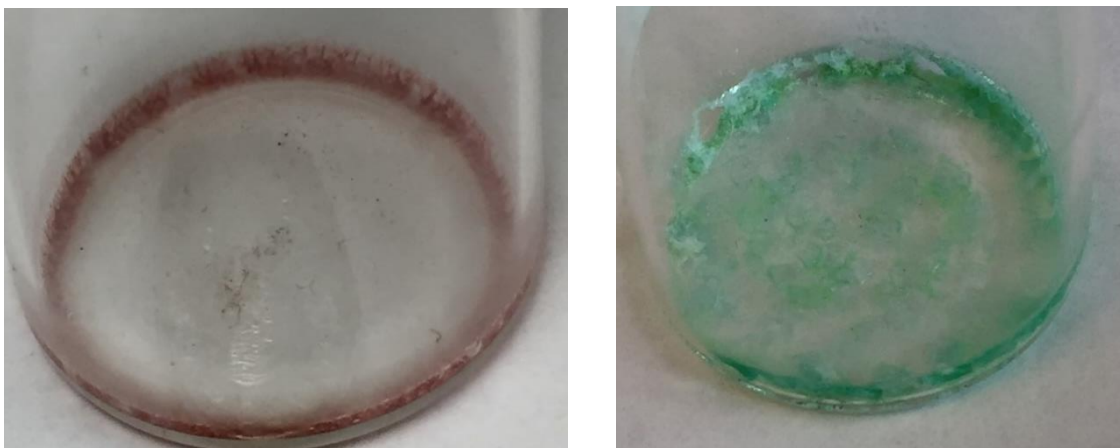


Figure 4.2. Photographs of crystals of $\text{Co}(\text{H}_2\text{O})_6(\text{B}_{12}\text{F}_{12})$ (left) and $\text{Ni}(\text{H}_2\text{O})_6(\text{B}_{12}\text{F}_{12})$ (right).

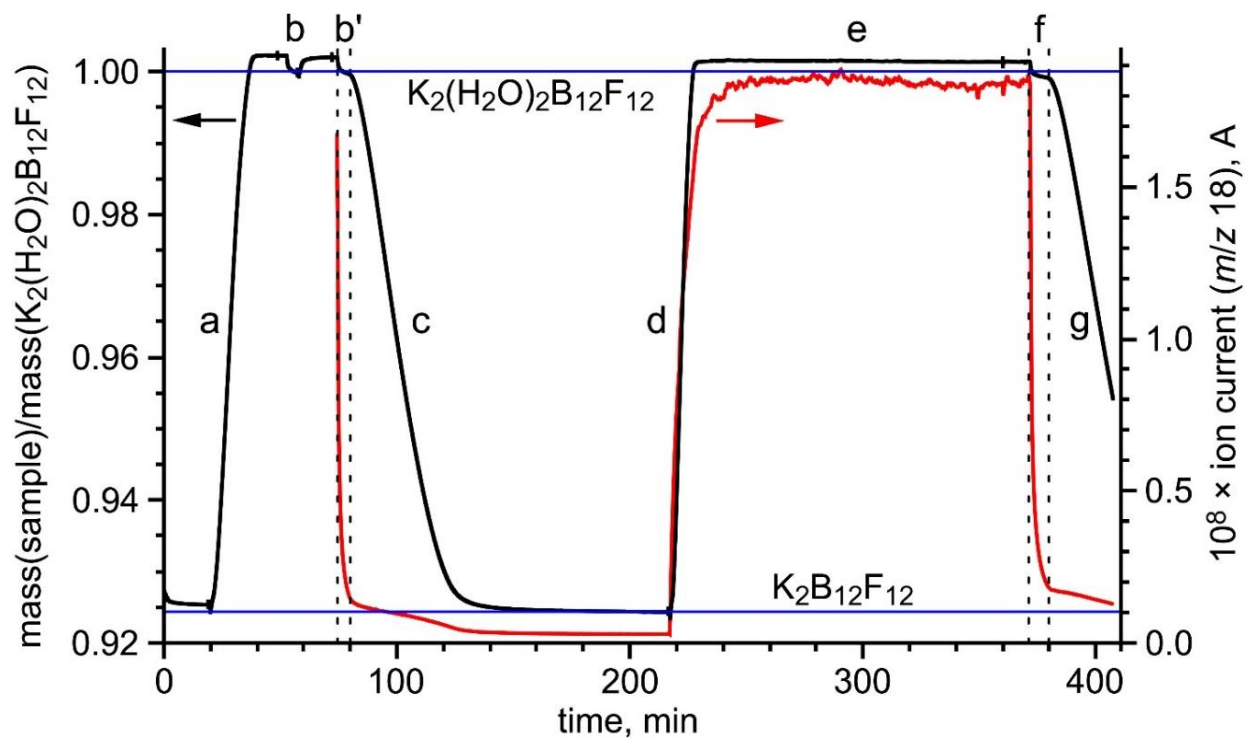


Figure 4.3. TGA-MS plot for two cycles of hydration/dehydration of $K_2(B_{12}F_{12})$ at 25 °C. The black plot shows the relative mass of the sample; the red plot shows the mass-spectrometer response to $H_2O(g)$. The carrier gas was dry He during dehydration and He containing 21(1) torr $H_2O(g)$ during hydration, both at 60 mL min^{-1} . The horizontal blue lines represent the relative molar masses of $K_2(H_2O)_2(B_{12}F_{12})$ ($1.000 \equiv 471.940 \text{ g mol}^{-1}$) and $K_2(B_{12}F_{12})$ ($0.9237 \equiv 435.909 \text{ g mol}^{-1}$). Reproduced with permission from Ref. 9.

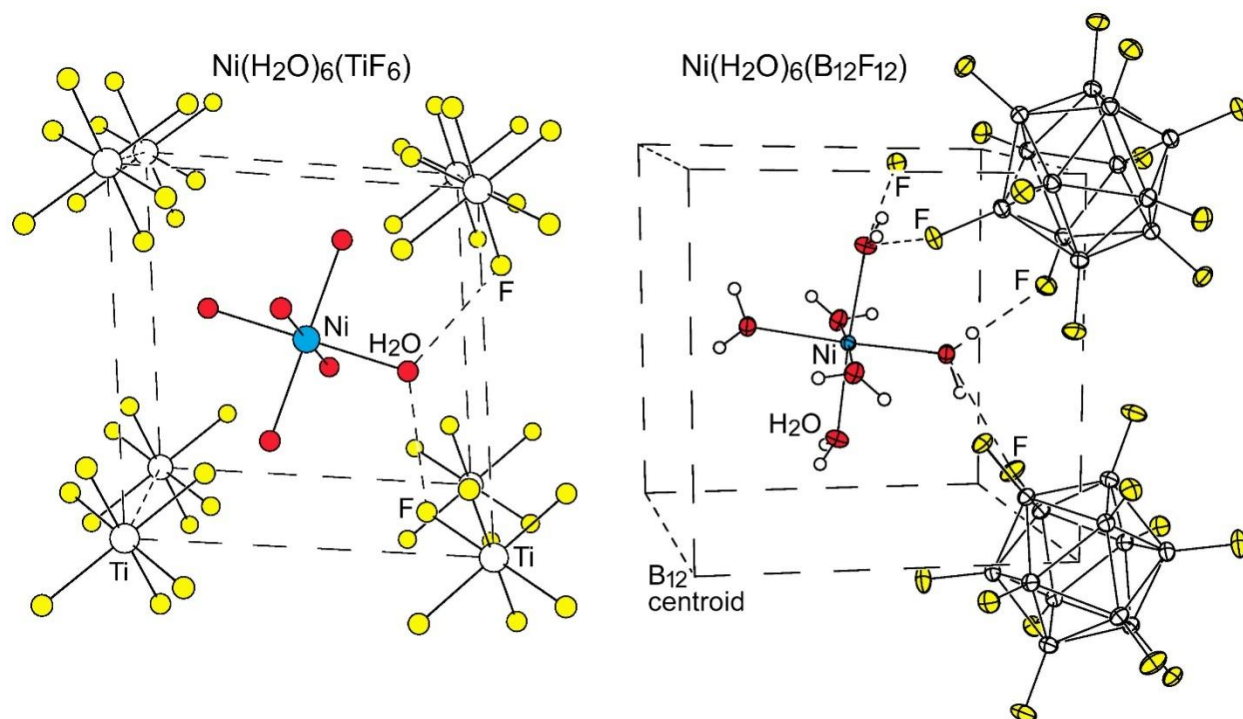


Figure 4.5. The structure of $\text{Ni}(\text{H}_2\text{O})_6(\text{TiF}_6)$ (left; the H atoms were not located; ref. 15). This is an example of the $\text{Co}(\text{H}_2\text{O})_6(\text{SiF}_6)$ structure type (space group $R\bar{3}$). The unique Ni–O and Ti–F distances are 2.044(5) and 1.791(5) Å, respectively. The unique Ti···Ti distance is 6.372 Å and the unique acute Ti···Ti···Ti angle is 83.8°. The two O(H)···F hydrogen bond distances for each of the six coordinated H_2O molecules are 2.709(7) and 2.760(7) Å, and the F···O···F angle is 115.0°. For comparison, in $\text{Ni}(\text{H}_2\text{O})_6(\text{B}_{12}\text{F}_{12})$ (right) the Ni–O distances are 2.0290(7) and 2.0515(7) Å and the O(H)···F hydrogen bond distances are 2.732(1), 2.735(1), 2.859(1), and 2.910(1) Å.

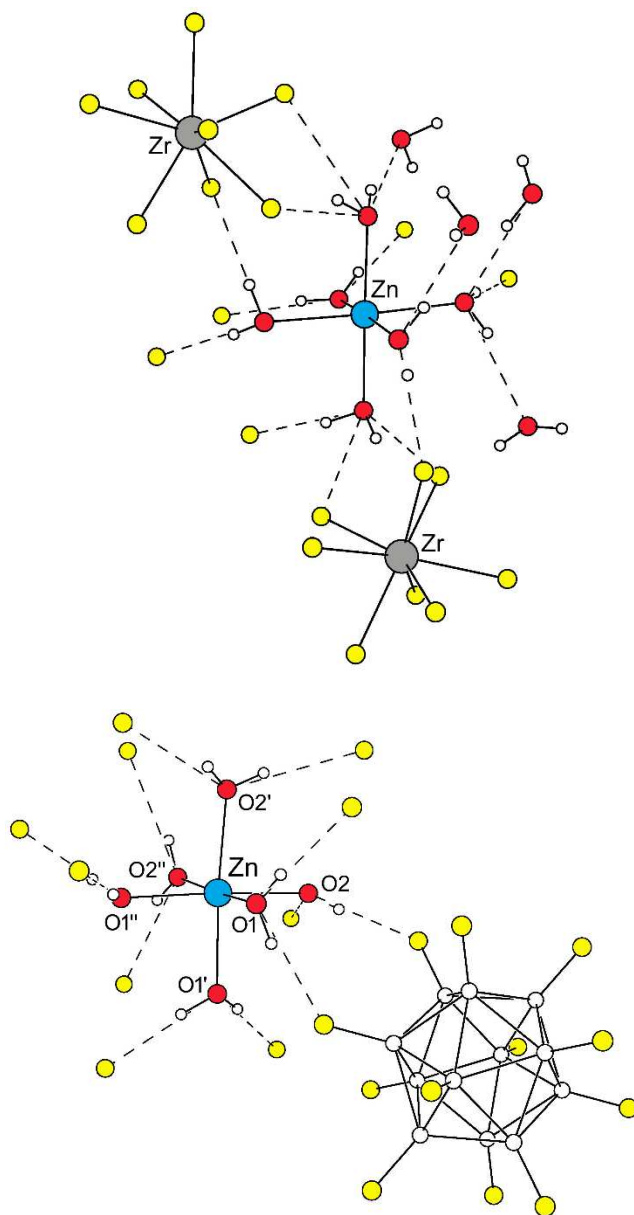


Figure 4.6. Part of the structures of $(\text{Zn}(\text{H}_2\text{O})_6)_2(\text{ZrF}_8)$, showing the network of $\text{O}-\text{H}\cdots\text{F}$ and $\text{O}-\text{H}\cdots\text{O}$ hydrogen bonds (top: ref. 16) and $\text{Zn}(\text{H}_2\text{O})_6(\text{B}_{12}\text{F}_{12})$ (bottom; ref. 4). The $\text{Zn}-\text{O}$ distances in $(\text{Zn}(\text{H}_2\text{O})_6)_2(\text{ZrF}_8)$ range from 2.0367(6) to 2.1638(6) Å (cf. $\text{Zn}(\text{H}_2\text{O})_6(\text{B}_{12}\text{F}_{12})$, 2.0611(4) and 2.0926(4) Å). Some of the $\text{O}(\text{H})\cdots\text{F}$ hydrogen bond distances in $(\text{Zn}(\text{H}_2\text{O})_6)_2(\text{ZrF}_8)$, which range from 2.580(1) to 2.973(1) Å, are bifurcated (cf. $\text{Zn}(\text{H}_2\text{O})_6(\text{B}_{12}\text{F}_{12})$, 2.733(1)–2.894(1) Å, none of which are bifurcated). The $\text{O}(\text{H})\cdots\text{O}$ distances in $(\text{Zn}(\text{H}_2\text{O})_6)_2(\text{ZrF}_8)$ range from 2.852(1) to 2.889(1) Å. There are no $\text{O}-\text{H}\cdots\text{O}$ hydrogen bonds in $\text{Zn}(\text{H}_2\text{O})_6(\text{B}_{12}\text{F}_{12})$.

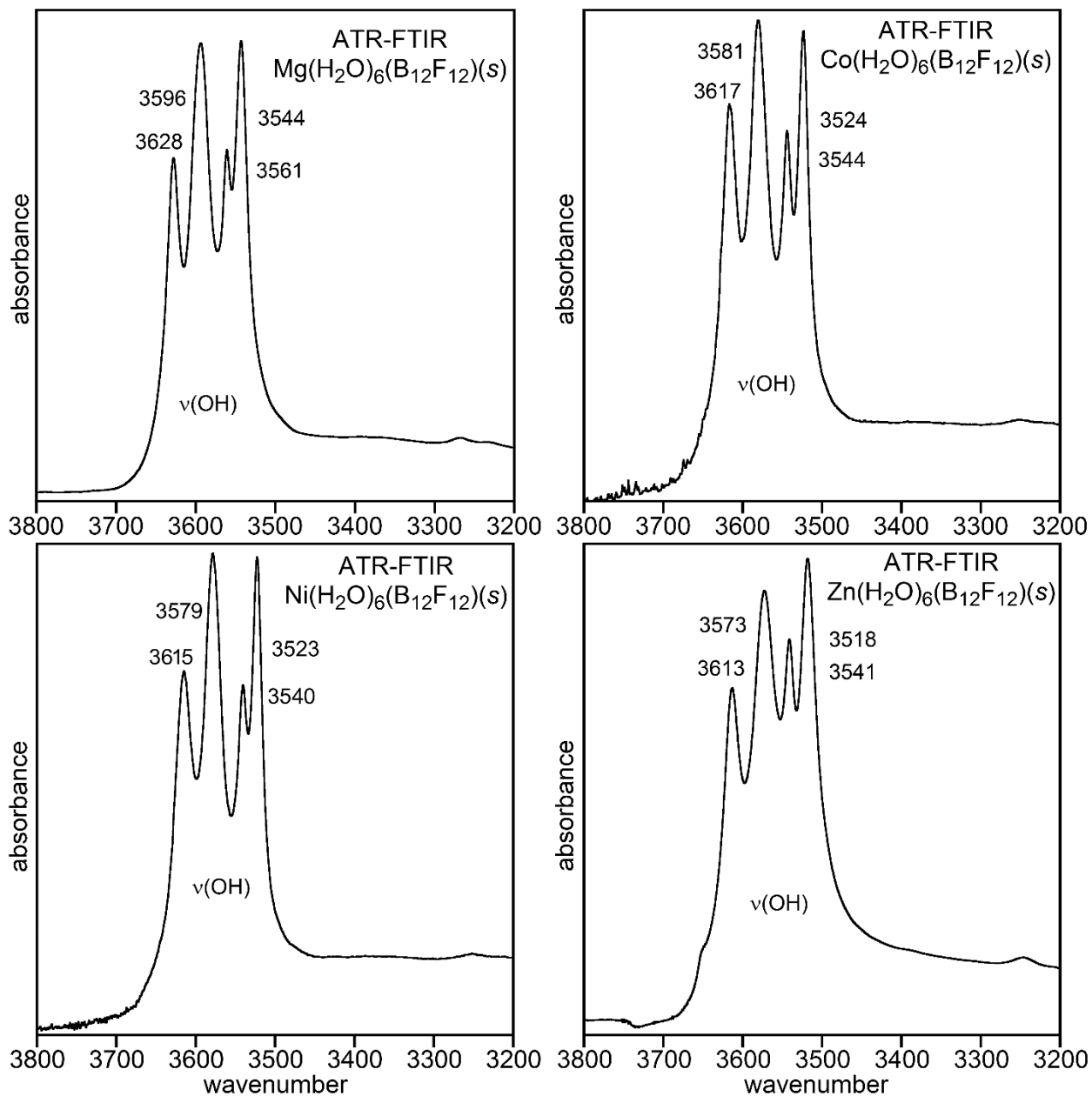


Figure 4.7. The $\nu(\text{OH})$ regions of ATR-FTIR spectra of microcrystalline $\text{M}(\text{H}_2\text{O})_6(\text{B}_{12}\text{F}_{12})$ ($\text{M} = \text{Mg}, \text{Co}, \text{Ni}, \text{Zn}$). The samples were evaporated from aqueous solutions on the ZnSe ATR crystal. The small peaks at ca. 3250 cm^{-1} are assigned to $2\delta(\text{HOH})$.

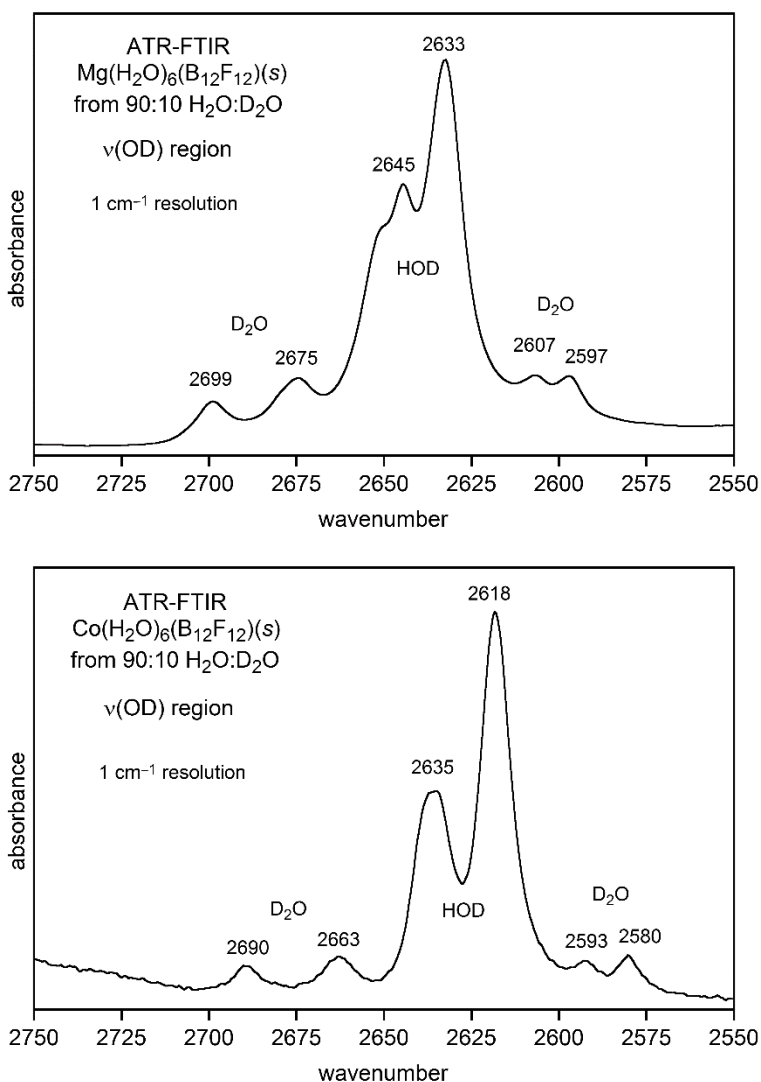


Figure 4.8. The $\nu(\text{OD})$ regions of ATR-FTIR spectra of $\text{Mg}(\text{HOD})(\text{H}_2\text{O})_5(\text{B}_{12}\text{F}_{12})$ (top) and $\text{Co}(\text{HOD})(\text{H}_2\text{O})_5(\text{B}_{12}\text{F}_{12})$ (bottom). Both samples were prepared by evaporation to dryness of 90:10 (v:v) $\text{H}_2\text{O}:\text{D}_2\text{O}$ solutions on the ZnSe ATR crystal. On average, ca. 15% of all of the hexaaqua 2+ complex cations will have one HOD ligand and five H_2O ligands, ca. 2% will have two HOD ligands and four H_2O ligands, and ca. 1% will have one D_2O ligand and five H_2O ligands. A negligible percentage will have more than two HOD ligands, an HOD and a D_2O ligand simultaneously, or more than one D_2O ligand. However, since H_2O evaporates faster than D_2O ,¹⁷⁻¹⁸ the actual percentages in the dried samples may be higher than the above-mentioned values.

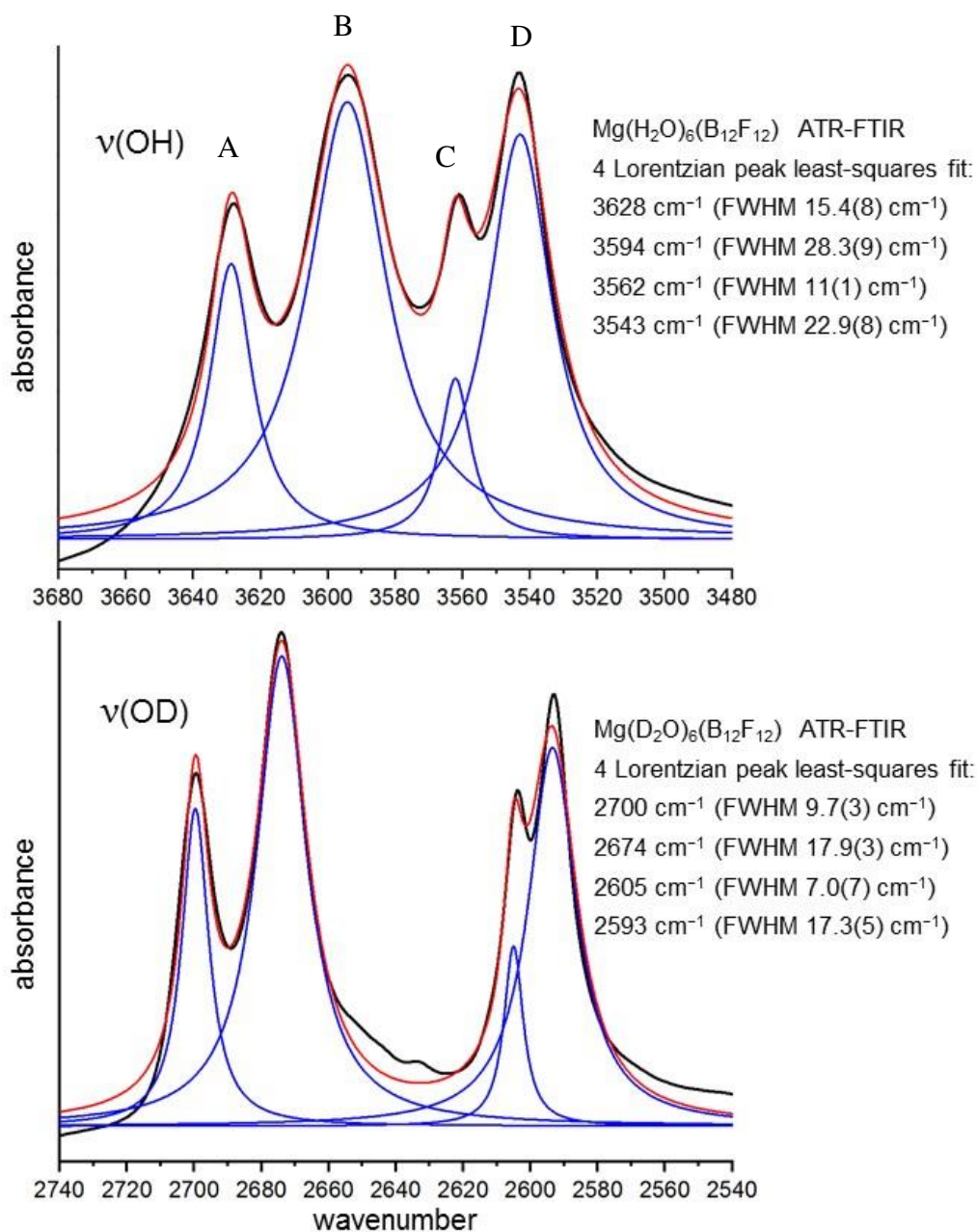


Figure 4.9. Experimental ATR-FTIR spectra (black traces) of $\text{Mg}(\text{H}_2\text{O})_6(\text{B}_{12}\text{F}_{12})$ (top) and $\text{Mg}(\text{D}_2\text{O})_6(\text{B}_{12}\text{F}_{12})$ (bottom) and their deconvolution into four Lorentzian peaks (blue). The fitted peak positions and full-widths at half-max are shown. The resultants of the four fitted peaks are the red traces. Note that the wavenumber axes both span 200 cm^{-1} . Both samples were evaporated on the ZnSe ATR crystal from H_2O or D_2O solutions.

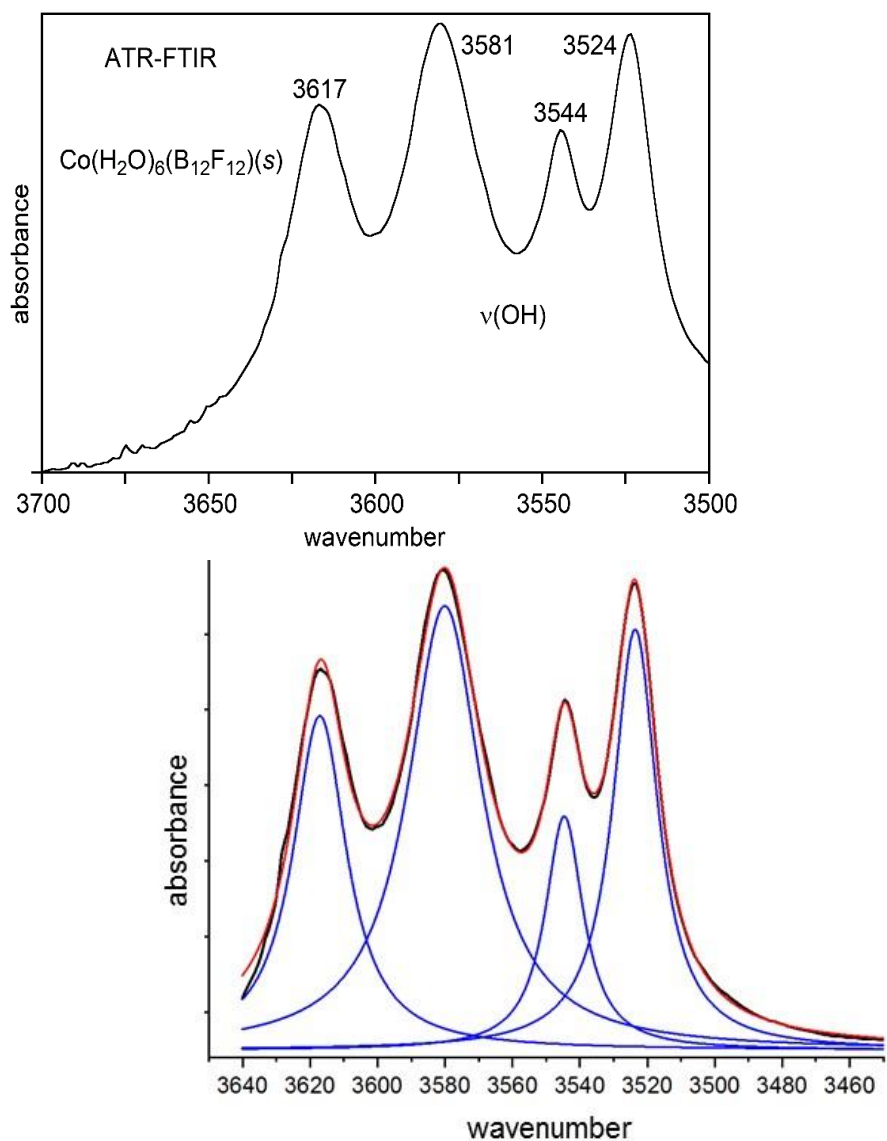


Figure 4.10. Top: Experimental ATR-FTIR spectrum of $\text{Co}(\text{H}_2\text{O})_6(\text{B}_{12}\text{F}_{12})$ (sample evaporated on the ZnSe ATR crystal from aqueous solution). Bottom: Deconvolution of a portion of the experimental spectrum (black trace) into four Lorentzian peaks. The positions of the four blue fitted peaks are (left to right) 3617, 3580, 3546, and 3524 cm^{-1} . The full-widths at half-max (FWHM) are (left to right) 19.4(2), 26.6(2), 13.8(3), and 16.0(2) cm^{-1} . The relative areas are (left to right) 2.0, 3.7, 1.0, 2.1. The resultant of the four fitted peaks is the red trace. Note that the wavenumber axes are scaled equally and are aligned.

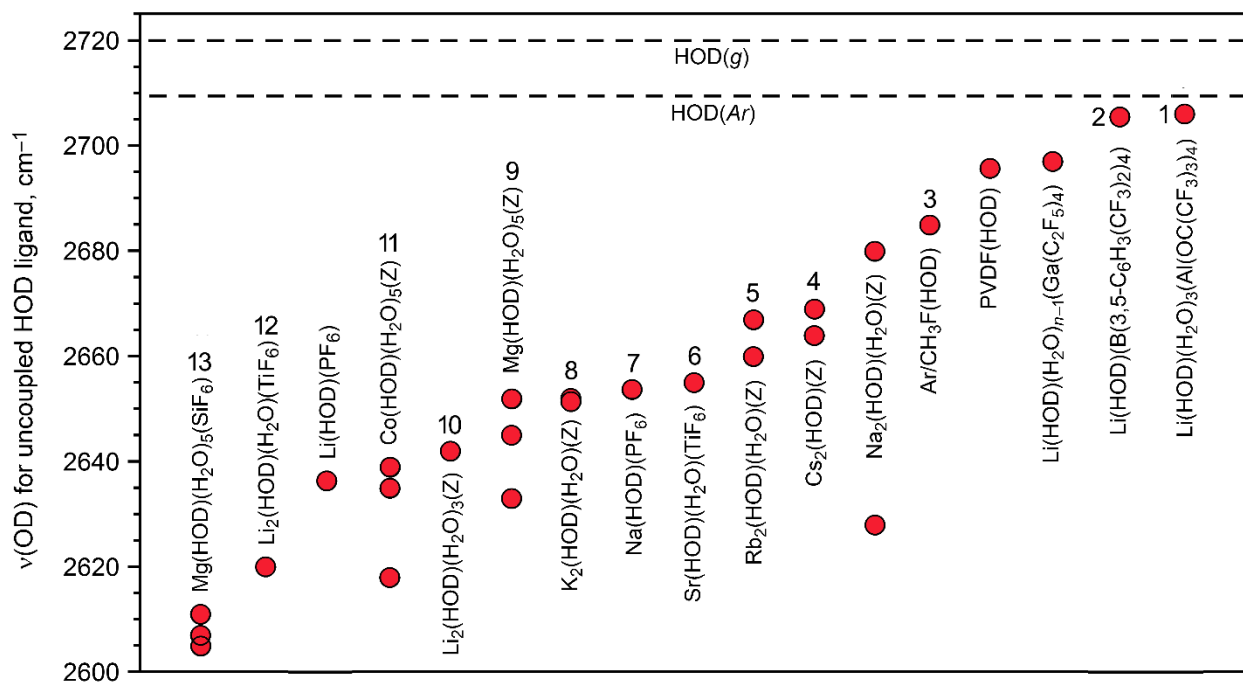


Figure 4.11. Plot of $\nu(\text{OD})$ values in ascending order from left to right for compounds with one HOD molecule per formula unit and $\nu(\text{OD}) > 2600 \text{ cm}^{-1}$ ($Z^{2-} = \text{B}_{12}\text{F}_{12}^{2-}$). The dashed lines are $\nu(\text{OD})$ values for HOD(*g*) (2720 cm^{-1} , refs. ¹⁹⁻²¹) and for HOD in an Ar matrix at 17 K (2709 cm^{-1} , refs. ²² and ²³). See Table 2.1 for references. The numbers 1–13 refer to the 25 numbered red data points in the $\nu(\text{OD})$ vs. O(D)···F correlation in Figure 2.52, only two of which (for Mg(HOD)(H₂O)₅(SiF₆)) are $< 2600 \text{ cm}^{-1}$.

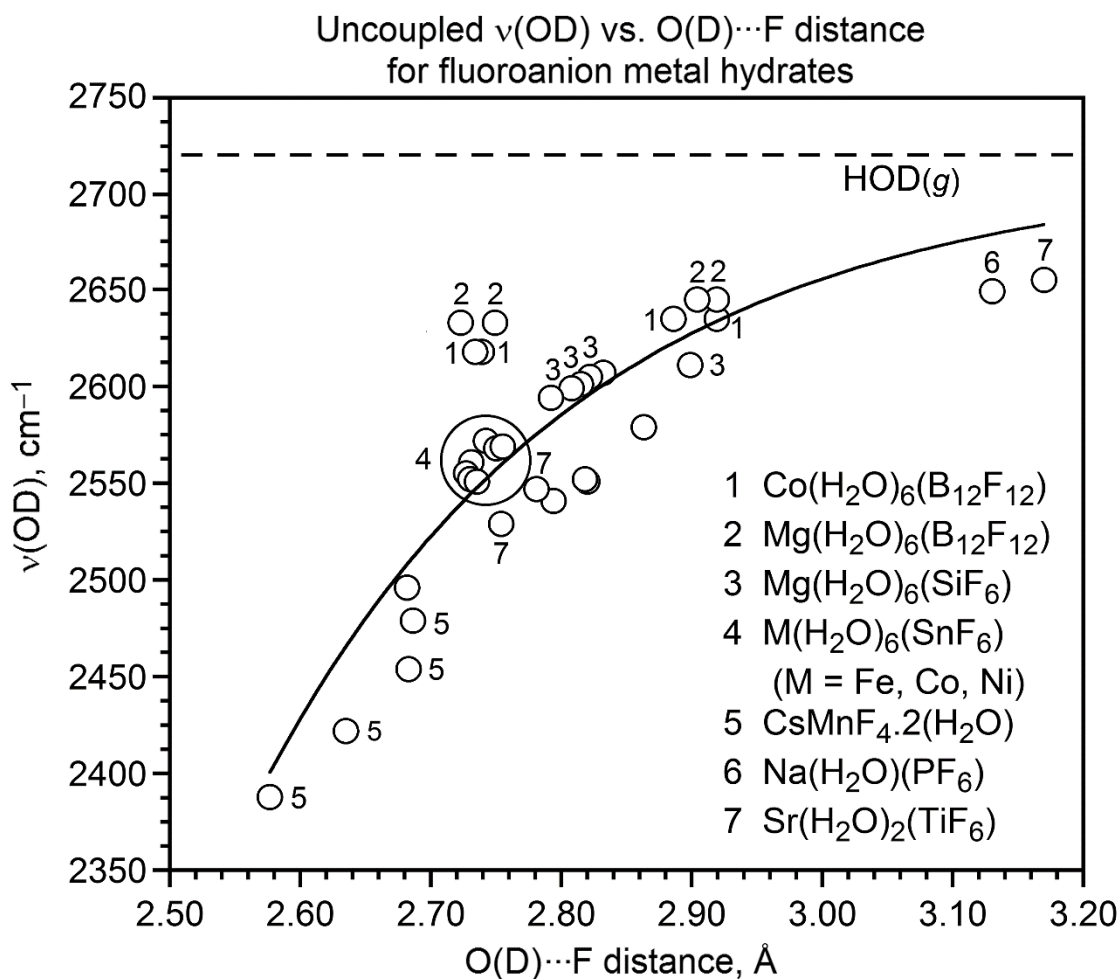


Figure 4.12. Plot of $\nu(\text{OD})$ vs. $\text{O}(\text{D})\cdots\text{F}$ distance for metal salt hydrates containing one, and only one, HOD molecule (for brevity, the formulas for the compounds do not show this). Except for the points numbered 1, 2, and 3, for $\text{Co}(\text{HOD})(\text{H}_2\text{O})_5(\text{B}_{12}\text{F}_{12})$, $\text{Mg}(\text{HOD})(\text{H}_2\text{O})_5(\text{B}_{12}\text{F}_{12})$ (ref. 4), and $\text{Mg}(\text{HOD})(\text{H}_2\text{O})_5(\text{SiF}_6)$ (refs. ¹⁴ and ²⁴), the data for this plot were taken from ref. 24. The points that are not numbered are for the following compounds (all with one HOD molecule): $\text{KMnF}_4 \cdot 2\text{H}_2\text{O}$, $\text{K}_2\text{MnF}_5 \cdot \text{H}_2\text{O}$, $\text{SrMnF}_5 \cdot \text{H}_2\text{O}$, and $\text{MnFeF}_5 \cdot 2\text{H}_2\text{O}$. The dashed line shows the 2719 cm^{-1} value for HOD(g). The curved line is an exponential fit to the data and is included only as a visual aid.

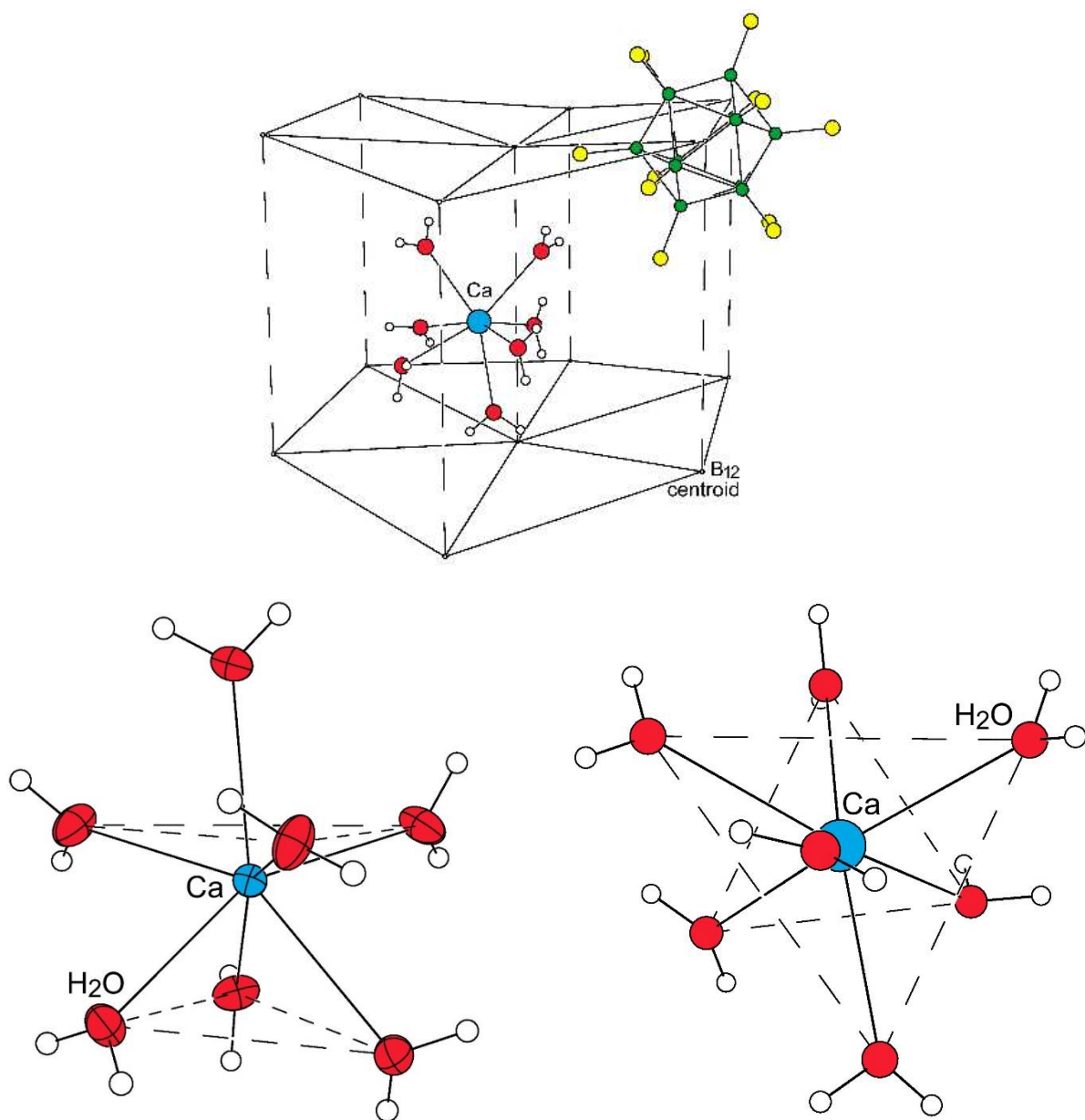


Figure 4.13. (Top) The offset stacks of corrugated pseudo-close-packed layers of Z^{2-} anion centroids in the structure of $\text{Ca}(\text{H}_2\text{O})_7(\text{B}_{12}\text{F}_{12})$. (Bottom) Two perpendicular views of the monocapped triangular antiprism (monocapped octahedral) CaO_7 coordination sphere in $\text{Ca}(\text{H}_2\text{O})_7(\text{B}_{12}\text{F}_{12})$ (50% probability ellipsoids except for H atoms in the drawing on the left). The $\text{Ca}-\text{OH}_2$ distances are listed in Table 4.9.

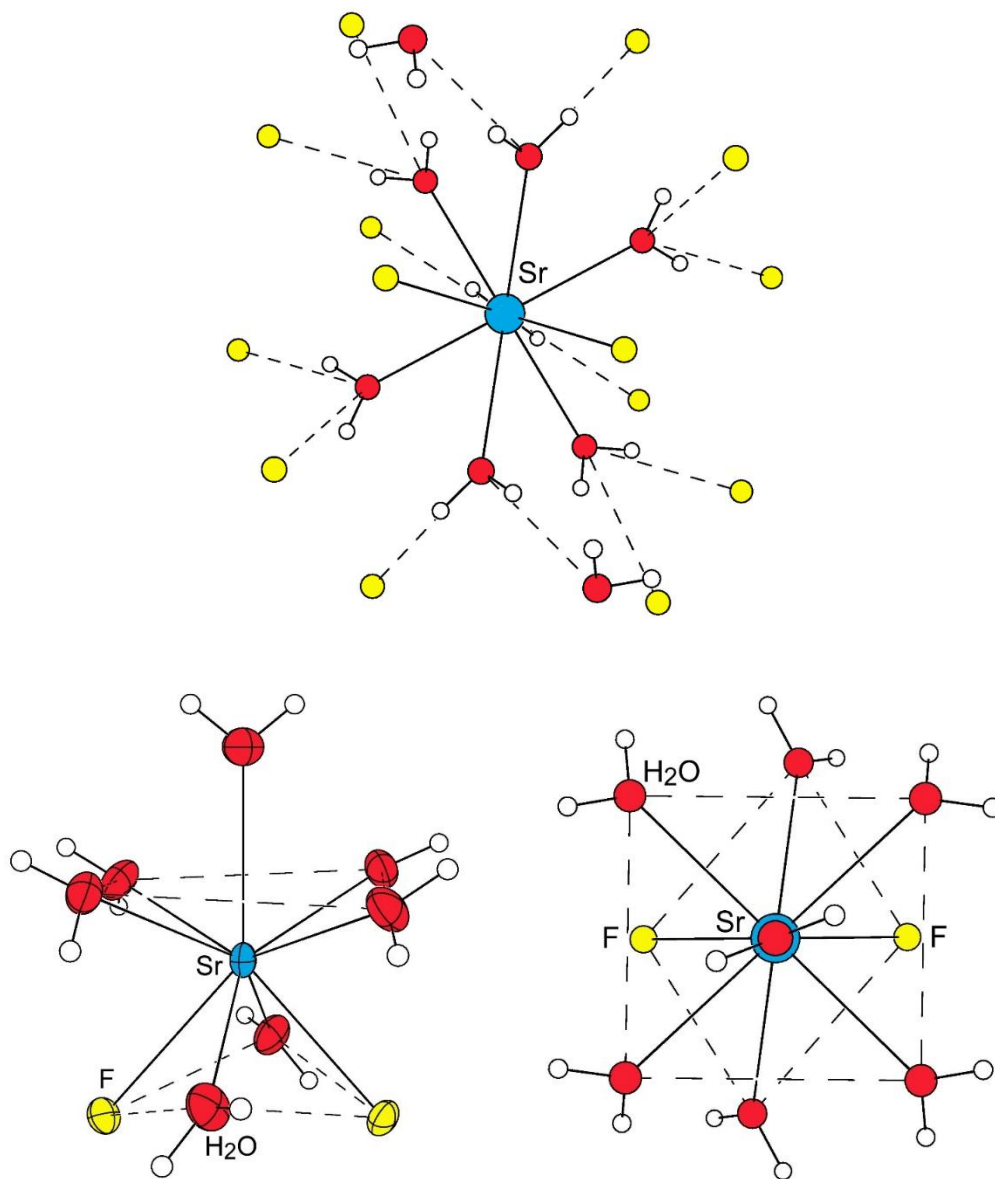


Figure 4.14. (Top) The O(H)⋯F (2.880(6)–2.902(6) Å) and O(H)⋯O (3.016(6) Å) hydrogen bonding distances in the structure of Sr(H₂O)₇(B₁₂F₁₂). Note that one of the H₂O molecules is hidden from view behind the Sr atom. (Bottom) Two perpendicular views of the distorted monocapped square antiprism SrO₇F₂ coordination sphere in Sr(H₂O)₇(B₁₂F₁₂) (50% probability ellipsoids except for H atoms in the drawing on the left). The orientation of the drawing on the right is looking down the [010] direction (the crystallographic C₂ axis). The Sr–OH₂ and Sr–F distances are listed in Table 4.10.

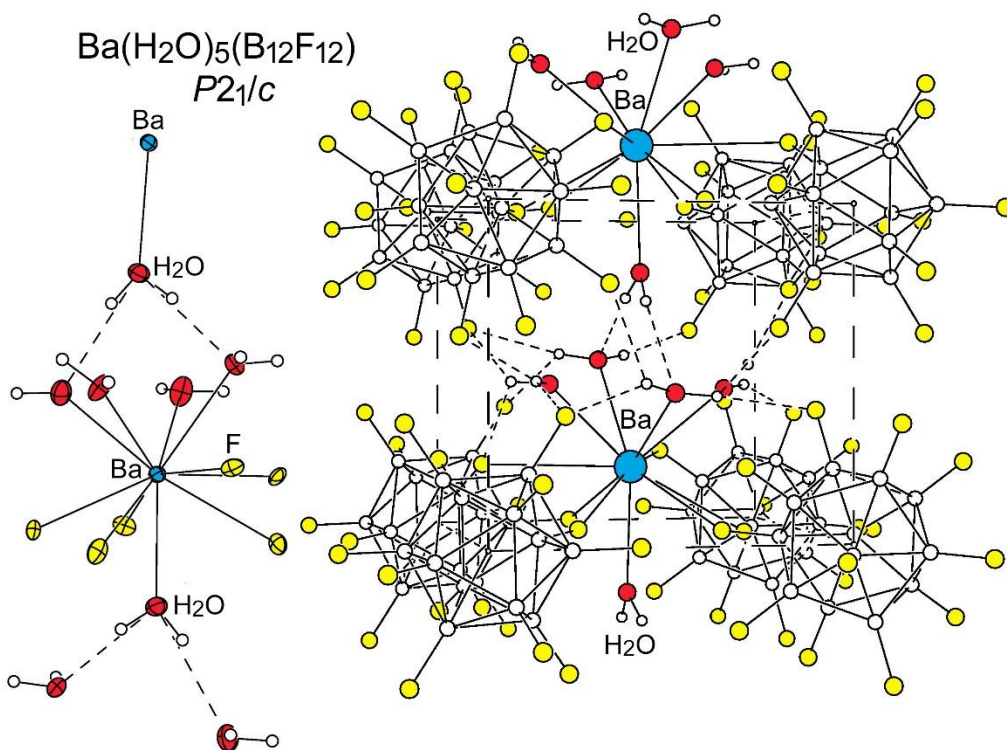


Figure 4.15. The structure of Ba(H₂O)₅(Z). The drawing on the left includes 50% probability ellipsoids except for H atoms and includes the two weak O–H···O hydrogen bonds, with O(H)···O distances of 2.940(3) and 3.072(3) Å. The drawing on the right shows the CsCl-like anion-cation packing of one Ba(H₂O)₅²⁺ contained in a cube-like array of Z²⁻ anions, with ⊙···⊙ distances of 6.94, 7.53, and 7.72 Å and ⊙···⊙···⊙ angles of 90° (⊙ = B₁₂ centroid). Some of the weak O–H···F hydrogen bonds are shown.

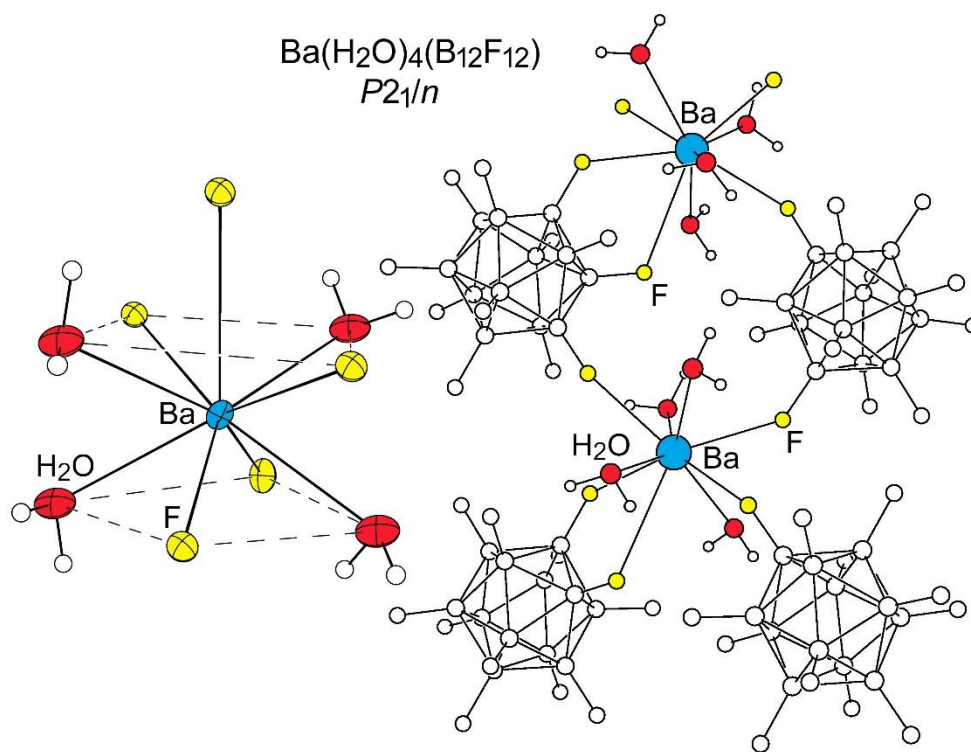


Figure 4.16. The structure of Ba(H₂O)₄(Z). The drawing on the left includes 50% probability ellipsoids except for H atoms and highlights one of the monocapped square antiprism BaO₄F₅ coordination spheres.

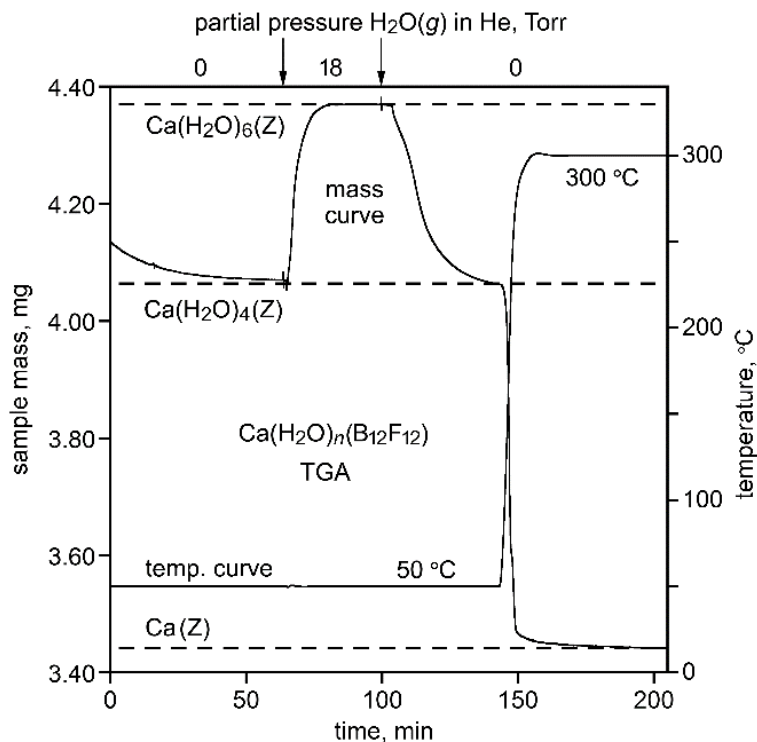


Figure 4.17. Top: Thermogravimetric behavior of $\text{Ca}(\text{H}_2\text{O})_n(\text{Z})(s)$ under 0 or 18 torr $\text{H}_2\text{O}(g)$ in He at 50 °C (0–145 min) and under 0 torr $\text{H}_2\text{O}(g)$ in He (dry He) as the temperature increased from 50 to 300 °C (145–207 min; $\text{Z}^{2-} = \text{B}_{12}\text{F}_{12}^{2-}$). At 50 °C, the dehydration $\text{Ca}(\text{H}_2\text{O})_6(\text{Z})(s) \rightarrow \text{Ca}(\text{H}_2\text{O})_4(\text{Z})(s) + 2\text{H}_2\text{O}(g)$ was 90% complete in ca. 25 min (99% complete in ca. 35 min) and the rehydration $\text{Ca}(\text{H}_2\text{O})_4(\text{Z})(s) + 2\text{H}_2\text{O}(g) \rightarrow \text{Ca}(\text{H}_2\text{O})_6(\text{Z})(s)$ was >90% complete in 10 min (99% complete in ca. 15 min). Dehydration of $\text{Ca}(\text{H}_2\text{O})_4(\text{Z})(s)$ to anhydrous $\text{Ca}(\text{Z})(s)$ in dry He was ca. 90% complete at ca. 250 °C and 99+% complete after 1 h at 300 °C. Bottom: Constant-temperature (50 °C) gravimetric behavior of $\text{Ca}(\text{H}_2\text{O})_6(\text{Z})(s)$ under 16 torr $\text{D}_2\text{O}(g)$ in He (0–58 min) and under 18 torr $\text{H}_2\text{O}(g)$ in He (58–105 min). The $\text{H}_2\text{O}/\text{D}_2\text{O}$ exchange was complete in ca. 1 h.

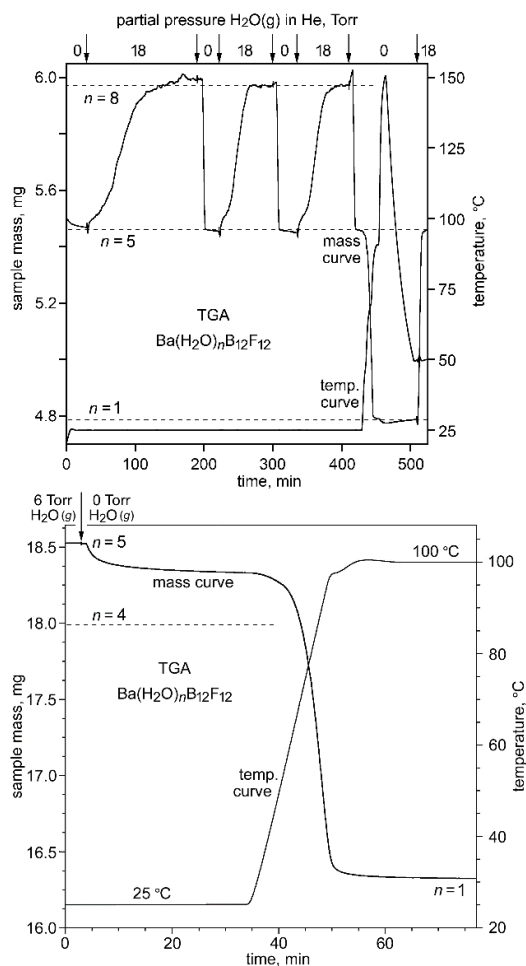


Figure 4.18. Top: Thermogravimetric behavior of $\text{Ba}(\text{H}_2\text{O})_n(\text{Z})(\text{s})$ under 0 or 18 torr $\text{H}_2\text{O}(\text{g})$ in He at 25 °C (0–425 min), under 0 torr $\text{H}_2\text{O}(\text{g})$ in He (dry He) as the temperature was increased from 25 to 150 °C and decreased from 150 to 50 °C (425–510 min), and under 18 torr $\text{H}_2\text{O}(\text{g})$ in He as the temperature was held constant at 50 °C (510–525 min); $\text{Z}^{2-} = \text{B}_{12}\text{F}_{12}^{2-}$. At 25 °C, each repeatable dehydration $\text{Ba}(\text{H}_2\text{O})_8(\text{Z})(\text{s}) \rightarrow \text{Ba}(\text{H}_2\text{O})_5(\text{Z})(\text{s}) + 3\text{H}_2\text{O}(\text{g})$ was 99% complete in 5 min and each repeatable rehydration $\text{Ba}(\text{H}_2\text{O})_5(\text{Z})(\text{s}) + 3\text{H}_2\text{O}(\text{g}) \rightarrow \text{Ba}(\text{H}_2\text{O})_8(\text{Z})(\text{s})$ was >90% complete in ca. 40 min. Dehydration of $\text{Ba}(\text{H}_2\text{O})_5(\text{Z})(\text{s})$ in dry He occurred slowly at 25 °C but was 99% complete to $\text{Ba}(\text{H}_2\text{O})(\text{Z})$ in 22 min as the temperature was raised from 25 to 90 °C at the rate of 3 °C min^{-1} . Further heating to 150 °C did not result in the dehydration of the monohydrate. Finally, when $\text{Ba}(\text{H}_2\text{O})(\text{Z})$ was cooled to 50 °C, it was quickly (15 min) rehydrated to $\text{Ba}(\text{H}_2\text{O})_5(\text{Z})$ under 18 torr $\text{H}_2\text{O}(\text{g})$ in He. Bottom: Thermogravimetric behavior of $\text{Ba}(\text{H}_2\text{O})_5(\text{Z})(\text{s})$ under 6 torr $\text{H}_2\text{O}(\text{g})$ in He at 25 °C (0–3 min) and under dry He at 25 °C (3–35 min) and as the temperature was increased from 25 to 100 °C at the rate of 3 °C min^{-1} . The dehydration of $\text{Ba}(\text{H}_2\text{O})_5(\text{Z})(\text{s})$ to the monohydrate $\text{Ba}(\text{H}_2\text{O})(\text{Z})(\text{s})$ became rapid when the temperature reached ca. 60 °C.

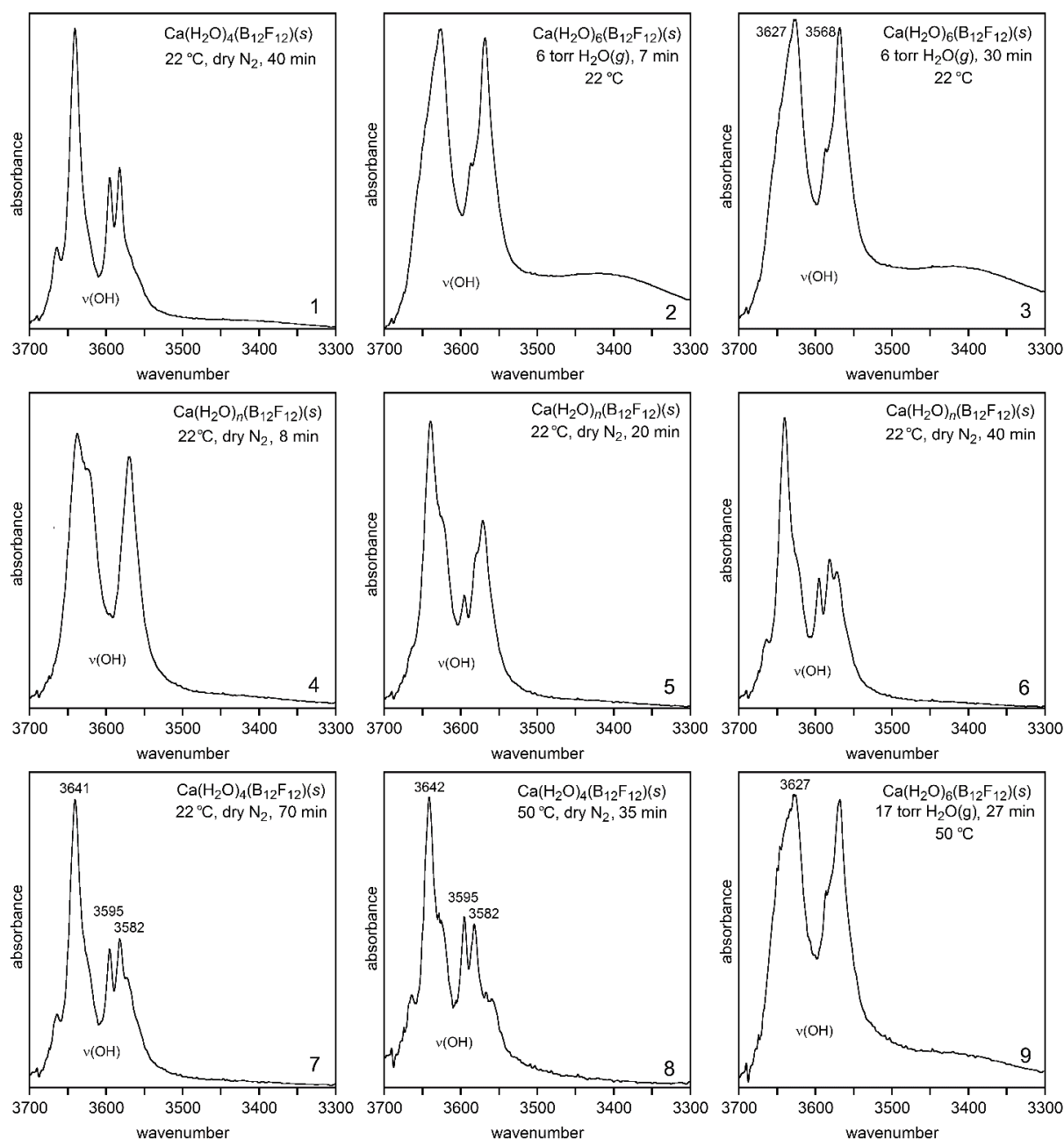


Figure 4.19. ATR-FTIR spectra of a microcrystalline $\text{Ca}(\text{H}_2\text{O})_n(\text{B}_{12}\text{F}_{12})$ dried from aqueous solution on the ATR crystal under various conditions of temperature and humidity. The compositions indicated for the sample in spectrum 8 ($\text{Ca}(\text{H}_2\text{O})_4(\text{B}_{12}\text{F}_{12})$) and in spectrum 9 ($\text{Ca}(\text{H}_2\text{O})_6(\text{B}_{12}\text{F}_{12})$) are commensurate with the 50 °C gravimetric experiment shown in Figure 4.17. The compositions indicated for the samples in spectra 1, 2, 3, and 7 are based on the similarity of those spectra with either spectrum 8 or 9. These spectra show that $\text{Ca}(\text{H}_2\text{O})_4(\text{B}_{12}\text{F}_{12})$ is hydrated to $\text{Ca}(\text{H}_2\text{O})_6(\text{B}_{12}\text{F}_{12})$ at 22 °C under 6 torr $\text{H}_2\text{O}(\text{g})$ in only 7 min, and is dehydrated back to $\text{Ca}(\text{H}_2\text{O})_4(\text{B}_{12}\text{F}_{12})$ at 22 °C under dry N_2 in about 1 h.

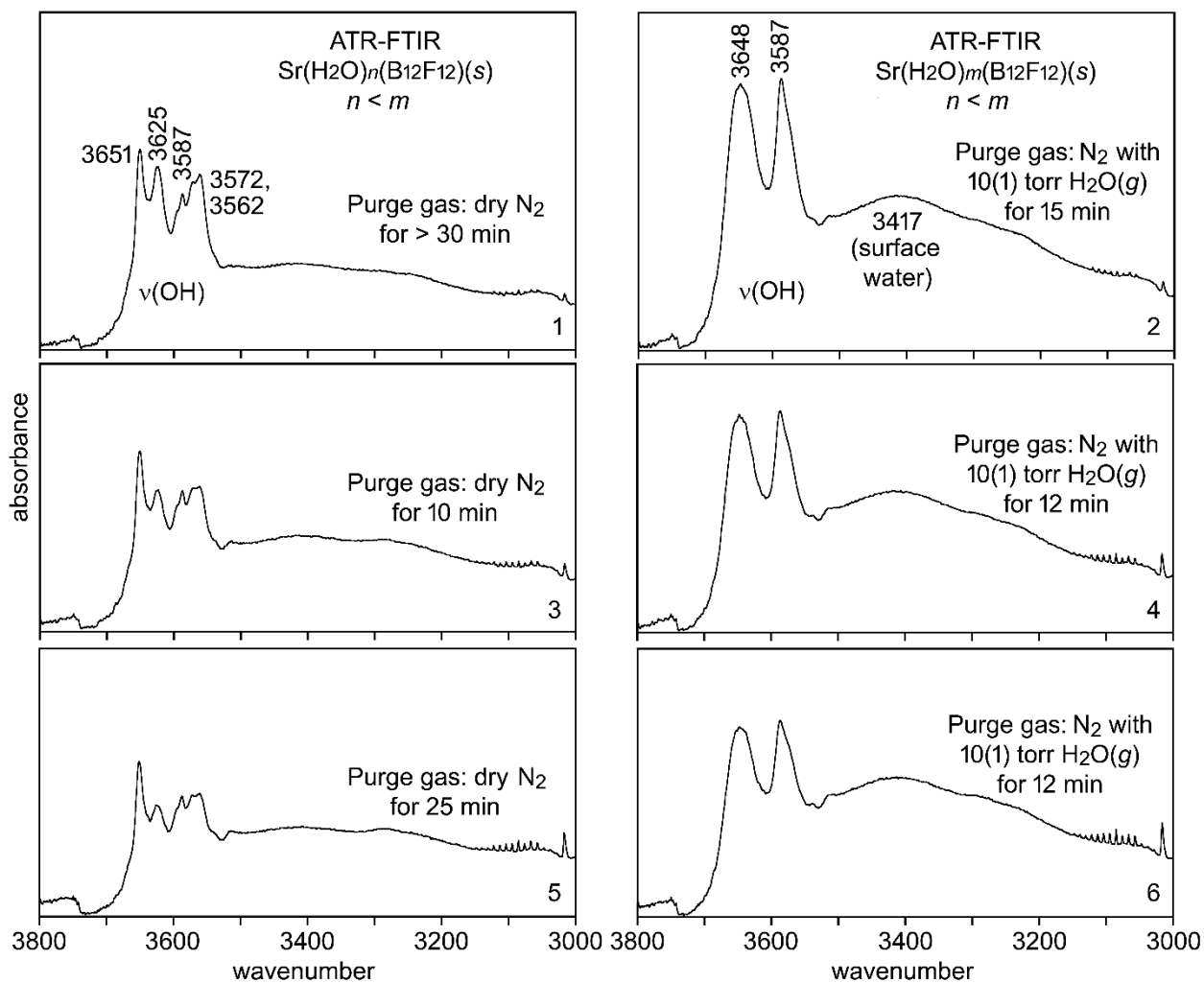


Figure 4.20. Room-temperature ATR-FTIR spectra showing the reaction $\text{Sr}(\text{H}_2\text{O})_n(\text{B}_{12}\text{F}_{12}) \leftrightarrow \text{Sr}(\text{H}_2\text{O})_m(\text{B}_{12}\text{F}_{12})$. Spectrum 2 did not change at longer times under $\text{N}_2/10(1)$ torr $\text{H}_2\text{O}(\text{g})$. The values of n and m for the two sets of hydration-state spectra (dry N_2 purge vs. $\text{N}_2/10(1)$ torr $\text{H}_2\text{O}(\text{g})$ purge) are not known, nor is it known if the samples for the two sets of spectra contain a mixture of compounds with more than one value of n and/or m .

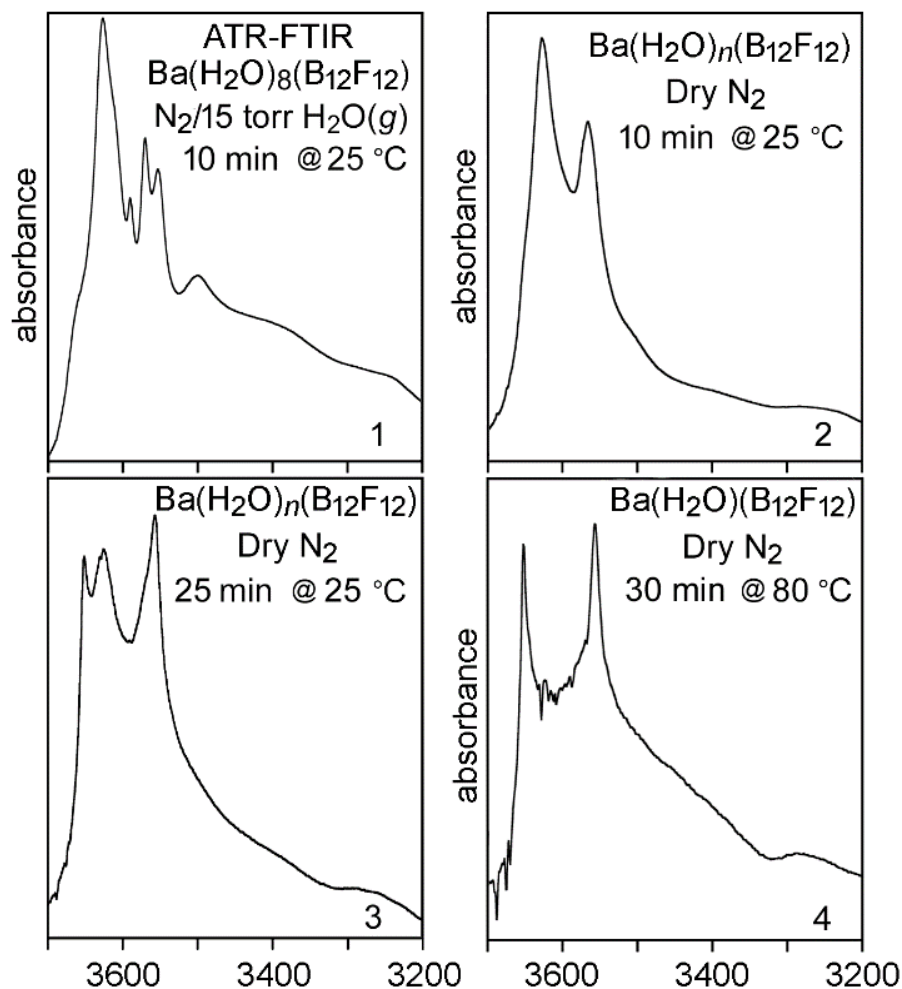


Figure 4.21. Comparison of the FTIR spectra of microcrystalline $\text{Ba}(\text{H}_2\text{O})_8(\text{B}_{12}\text{F}_{12})$ at $25\text{ }^\circ\text{C}$ in $\text{N}_2/15(1)\text{ torr H}_2\text{O}(g)$ (top; spectrum 1), $\text{Ba}(\text{H}_2\text{O})_n(\text{B}_{12}\text{F}_{12})$ at $25\text{ }^\circ\text{C}$ in dry N_2 (top right and middle left; spectra 2 and 3; $n = 4\text{--}5$), and $\text{Ba}(\text{H}_2\text{O})(\text{B}_{12}\text{F}_{12})$ at $80\text{ }^\circ\text{C}$ in dry N_2 (middle right; spectrum 4). The composition $\text{Ba}(\text{H}_2\text{O})_8(\text{B}_{12}\text{F}_{12})$ in spectrum 1 is based on the $25\text{ }^\circ\text{C}$ gravimetric experiment shown in Figure 4.18. The four relatively sharp peaks in spectrum 1 are at (left to right) 3626 , 3590 , 3570 , and 3553 cm^{-1} .

Table 4.1 Calculated vapor pressure above saturated salt solutions^a

Saturated Salt	A	B	Temp	Temp	RH ^b	H2O Pressure at Temp Cc
			C	K	%	Torr
MgCl ₂	29.26	34	20	293.15	32.86	5.73
NaBr	20.49	308	20	293.15	58.59	10.22
KCl	49.38	159	20	293.15	84.94	14.81

^aRef. 25. ^b $RH = A * \exp(B/T)$.

Table 4.2 Crystal Data and Final Refinement Parameters for the X-ray Diffraction Structures^a

compound	Mg(H ₂ O) ₆ (Z)	Ca(H ₂ O) ₇ (Z)	Sr(H ₂ O) ₇ (Z)	Ba(H ₂ O) ₅ (Z)	Ba(H ₂ O) ₄ (Z)	Co(H ₂ O) ₆ (Z)	Ni(H ₂ O) ₆ (Z)	Zn(H ₂ O) ₆ (Z)
formula	B ₁₂ F ₁₂ H ₁₂ MgO ₆	B ₁₂ CaF ₁₂ H ₁₄ O ₇	B ₁₂ F ₁₂ H ₁₄ O ₇ Sr	B ₁₂ BaF ₁₂ H ₁₀ O ₅	B ₁₂ BaF ₁₂ H ₈ O ₄	B ₁₂ F ₁₂ H ₁₂ CoO ₆	B ₁₂ F ₁₂ H ₁₂ NiO ₆	B ₁₂ F ₁₂ H ₁₂ ZnO ₆
formula wt., g mol ⁻¹	490.13	523.91	571.45	585.14	567.12	527.75	524.53	531.19
crystal system	trigonal	monoclinic	orthorhombic	monoclinic	monoclinic	trigonal	trigonal	trigonal
space group, Z	$\bar{R}3, 6$	$P2_1/c, 4$	$Pbcn, 4$	$P2_1/c, 4$	$P2_1/n, 8$	$\bar{R}3, 6$	$\bar{R}3, 6$	$\bar{R}3, 6$
<i>a</i> , Å	10.4993(6)	8.3922(11)	11.5062(9)	7.7197(2)	13.8368(10)	10.4562(3)	10.4289(4)	10.4575(9)
<i>b</i> , Å	10.4993(6)	11.2270(13)	8.9992(7)	13.8865(4)	11.0796(7)	10.4562(3)	10.4289(4)	10.4575(9)
<i>c</i> , Å	26.8485(17)	19.812(3)	17.6796(13)	15.0598(5)	20.8572(14)	27.0213(15)	26.930(2)	27.040(2)
α , deg	90	90	90	90	90	90	90	90
β , deg	90	90.101(4)	90	90 (twinned)	90.049(3)	90	90	90
γ , deg	120	90	90	90	90	120	120	120
<i>V</i> , Å ³	2563.1(3)	1866.6(4)	1830.7(2)	1614.40(8)	3197.5(4)	2558.5(2)	2536.6(3)	2560.9(5)
ρ_{calc} g cm ⁻³	1.905	1.864	2.073	2.407	2.356	2.043	2.060	2.067
<i>T</i> , K	100(2)	120(2)	100(2)	100(2)	100(2)	120(2)	80(2)	100(2)
<i>R</i> (<i>F</i>) (<i>I</i> > 2 σ (<i>I</i>)) ^b	0.0316	0.0283	0.0380	0.0185	0.0693	0.0186	0.0197	0.0141
<i>wR</i> (<i>F</i> ²) [all data] ^b	0.0837	0.0772	0.1027	0.0376	0.1314	0.0521	0.0539	0.0398
GOF	1.068	1.050	1.036	0.982	1.067	1.056	1.190	1.135

^a $Z^{2-} = B_{12}F_{12}^{2-}$. ^b $R(F) = \Sigma||F_o| - |F_c|| / \Sigma|F_o|$; $wR(F^2) = (\Sigma[w(F_o^2 - F_c^2)^2] / \Sigma[w(F_o^2)^2])^{1/2}$.

Table 4.3. Bond distances and bond valences for the SC-XRD structure of Mg(H₂O)₆(B₁₂F₁₂)

Mg(H ₂ O) ₆ (B ₁₂ F ₁₂)	bond	distance, Å	<i>bv</i> param.	<i>bv</i>
This work	Mg-O	2.0390	1.693	0.393
	Mg-O	2.0390	1.693	0.393
	Mg-O	2.0390	1.693	0.393
	Mg-O	2.0659	1.693	0.365
	Mg-O	2.0659	1.693	0.365
	Mg-O	2.0659	1.693	0.365
		Σ (Mg-O(<i>bv</i>)) =		2.273
	ave. Mg-O =	2.052		

Table 4.4. Bond distances and bond valences for the SC-XRD structure of Co(H₂O)₆(B₁₂F₁₂)

Co(H ₂ O) ₆ (B ₁₂ F ₁₂)	bond	distance, Å	<i>bv</i> param.	<i>bv</i>		bond	distance, Å	<i>bv</i> param.	<i>bv</i>	
This work	Co-O	2.0663	1.692	0.364		Co-O	2.0663	1.661	0.334	
	Co-O	2.0663	1.692	0.364		Co-O	2.0663	1.661	0.334	
	Co-O	2.0663	1.692	0.364		Co-O	2.0663	1.661	0.334	
	Co-O	2.0907	1.692	0.340		Co-O	2.0907	1.661	0.313	
	Co-O	2.0907	1.692	0.340		Co-O	2.0907	1.661	0.313	
	Co-O	2.0907	1.692	0.340		Co-O	2.0907	1.661	0.313	
		Σ (Co-O(<i>bv</i>)) =			2.112		Σ (Co-O(<i>bv</i>)) =			1.942
	ave. Co-O =	2.079								

Table 4.5. Bond distances and bond valences for the SC-XRD structure of Ni(H₂O)₆(B₁₂F₁₂)

Ni(H ₂ O) ₆ (B ₁₂ F ₁₂)	bond	distance, Å	<i>bv</i> param.	<i>bv</i>
This work	Ni-O	2.0290	1.654	0.363
	Ni-O	2.0290	1.654	0.363
	Ni-O	2.0290	1.654	0.363
	Ni-O	2.0515	1.654	0.342
	Ni-O	2.0515	1.654	0.342
	Ni-O	2.0515	1.654	0.342
		Σ (Ni-O(<i>bv</i>)) =		2.113
	ave. Ni-O =	2.040		

Table 4.6. Bond distances and bond valences for the SC-XRD structure of Zn(H₂O)₆(B₁₂F₁₂)

Zn(H ₂ O) ₆ (B ₁₂ F ₁₂)	bond	distance, Å	<i>bv</i> param.	<i>bv</i>
This work	Zn-O	2.0611	1.704	0.381
	Zn-O	2.0611	1.704	0.381
	Zn-O	2.0611	1.704	0.381
	Zn-O	2.0926	1.704	0.350
	Zn-O	2.0926	1.704	0.350
	Zn-O	2.0926	1.704	0.350
		Σ (Zn-O(<i>bv</i>)) =		2.192
	ave. Zn-O =	2.077		

Table 4.7. Comparisons of M–O and O(H)⋯X distances in some metal salt hexahydrates^a

compound	M–O, Å	O(H)⋯X, Å	reference
Mg(H ₂ O) ₆ (B ₁₂ F ₁₂) ^b	2.0390(11) × 3, 2.0659(11) × 3; ave. 2.053	2.723(2), 2.749(2), 2.904(2), 2.914(2) ^c	this work
Mg(H ₂ O) ₆ (SiF ₆) ^b	2.0480(8), 2.0550(7), 2.0571(8); ave. 2.053	2.792(1)–2.899(1) ^c	14
Co(H ₂ O) ₆ (B ₁₂ F ₁₂) ^b	2.0663(4) × 3, 2.0907(4) × 3; ave. 2.079	2.734(1), 2.739(1), 2.886(1), 2.919(1) ^c	this work
Co(H ₂ O) ₆ (SnF ₆) ^b	2.077(5) × 6	2.727(5), 2.755(4) ^c	26
Ni(H ₂ O) ₆ (B ₁₂ F ₁₂) ^b	2.0290(7) × 3, 2.0515(7) × 3; ave. 2.040	2.732(1), 2.735(1), 2.859(1), 2.919(1) ^c	this work
Ni(H ₂ O) ₆ (SnF ₆) ^b	2.045(3) × 6	2.730(3), 2.750(3) ^c	26
Ni(H ₂ O) ₆ (TiF ₆) ^b	2.044(5) × 6	2.709(7), 2.760(7) ^c	15
Zn(H ₂ O) ₆ (B ₁₂ F ₁₂) ^b	2.0611(4) × 3, 2.0926(4) × 3; ave. 2.077	2.733(1), 2.734(1), 2.869(1), 2.894(1) ^c	this work
(Zn(H ₂ O) ₆) ₂ (ZrF ₈) ^b	2.0367(6)–2.1638(6); ave. 2.093	2.580(1)–2.973(1); ^c 2.852(1)–2.889(1) ^d	16

Table 4.7. (continued) Comparisons of M–O and O(H)···X distances in some metal salt hexahydrates

^a All structures at low temperature (≤ 150 K) unless otherwise indicated. ^b Single-crystal X-ray diffraction ^c X = F. ^d X = O.

Table 4.8. FTIR Stretching and Bending Vibration Frequencies for $M(\text{H}_2\text{O})_6^{2+}$ Salt Hydrates^a

compound	$\nu_{\text{asym}}(\text{OH})$	$\nu_{\text{sym}}(\text{OH})$	$\delta(\text{HOH})$
$\text{Mg}(\text{H}_2\text{O})_6(\text{B}_{12}\text{F}_{12})$	3628, 3596	3561, 3544	1640, 1624
$\text{Mg}(\text{D}_2\text{O})_6(\text{B}_{12}\text{F}_{12})$	2699, 2674 ^b	2604, 2593 ^b	1206, 1196 ^b
$\text{Mg}(\text{HOD})(\text{H}_2\text{O})_5(\text{B}_{12}\text{F}_{12})$	2645, 2633 ^{b,c}		— ^c
$\text{Mg}(\text{H}_2\text{O})_6(\text{SiF}_6)^{\text{d}}$	3569, 3551, 3536	3513, 3503, 3493 ^d	nr/no
$\text{Mg}(\text{D}_2\text{O})_6(\text{SiF}_6)^{\text{d}}$	2640, 2633, 2625 ^b	2566, 2560 ^b	nr/no
$\text{Mg}(\text{HOD})(\text{H}_2\text{O})_5(\text{SiF}_6)^{\text{d}}$	2611, 2607, 2605, 2601, 2599, 2594 ^b		—
$\text{Mg}(\text{H}_2\text{O})_6(\text{SO}_4)_2 \cdot \text{C}_5\text{H}_{14}\text{N}_2^{\text{e}}$	ca. 3242 (very broad)		1628
$\text{Mg}(\text{H}_2\text{O})_6(\text{BF}_4)_2$ ($T = 295 \text{ K}$) ^f	3500 (sh, vb)	3406 (vb)	1630, 1606 ^g
$\text{Mg}(\text{H}_2\text{O})_6(\text{BF}_4)_2$ ($T = 8.5 \text{ K}$) ^f	3498, 3475	3435, 3405	1630, 1602, 1595 ^g
$\text{Mg}(\text{H}_2\text{O})_6(\text{UO}_2(\text{EtCO}_2)_3)_2^{\text{h}}$	3395 (bd)	ca. 3300 (sh)	nr/no
$\text{Mg}(\text{H}_2\text{O})_6(\text{B}(\text{CN})_4)_2^{\text{i}}$	3529, 3450 (sh), 3387	3370 (sh), 3248	nr/no
$\text{Mg}(\text{H}_2\text{O})_6(\text{B}_{12}\text{H}_{12})^{\text{j}}$	ca. 3550 (vb)		ca. 1610
$\text{Mg}(\text{H}_2\text{O})_6(\text{ArSO}_3)_2^{\text{k}}$	ca. 3280 (vb)		nr/no
$\text{Co}(\text{H}_2\text{O})_6(\text{B}_{12}\text{F}_{12})$	3617, 3581	3544, 3524	1635, 1617
$\text{Co}(\text{D}_2\text{O})_6(\text{B}_{12}\text{F}_{12})$	2690, 2663 ^b	2593, 2580 ^b	— ^c
$\text{Co}(\text{HOD})(\text{H}_2\text{O})_5(\text{B}_{12}\text{F}_{12})$	2635, 2618 ^{b,c}		— ^c
$\text{Co}(\text{HOD})(\text{H}_2\text{O})_5(\text{SnF}_6)^{\text{l}}$	2569, 2555 ^b		1456 ^b
$\text{Co}(\text{H}_2\text{O})_6(\text{SeO}_4)_2 \cdot (\text{C}_6\text{H}_{14}\text{N}_2)^{\text{m}}$	ca. 3200 (vb)		1674 ^m
$\text{Ni}(\text{H}_2\text{O})_6(\text{B}_{12}\text{F}_{12})$	3615, 3579	3540, 3523	1637, 1616
$\text{Ni}(\text{H}_2\text{O})_6(\text{B}_{12}\text{H}_{12})^{\text{n}}$	3520 (bd)	3461 (bd)	1606
$\text{Ni}(\text{H}_2\text{O})_6(\text{TiF}_6)^{\text{o}}$	3408 (vb)	ca. 3350 (vb sh)	nr/no
$\text{Ni}(\text{H}_2\text{O})_6(\text{VOF}_4(\text{H}_2\text{O}))^{\text{p}}$	3345 (vb)		1634
$\text{Zn}(\text{H}_2\text{O})_6(\text{B}_{12}\text{F}_{12})$	3613, 3573	3541, 3518	1631, 1613
$\text{Zn}(\text{H}_2\text{O})_6(\text{SnF}_6)^{\text{q}}$	3477 (bd)	3431 (bd)	1647
$\text{Cs}_2\text{Zn}(\text{H}_2\text{O})_6(\text{SeO}_4)_2^{\text{r}}$	3202 (vb)		1634

Table 4.8. (continued) FTIR Stretching and Bending Vibration Frequencies for $M(H_2O)_6^{2+}$ Salt Hydrates^a

^a Microcrystalline samples at room temperature unless otherwise indicated. All data from this work unless otherwise indicated. Abbreviations: *T* = temperature; sh = shoulder; bd = broad; vb = very broad; nr/no = not reported or not observed. ^b $\nu(OD)$ and $\delta(DOD)$ values. ^c These $\nu(OD)$ values are for the two types of HOD ligands in the $M(HOD)(H_2O)_5^{2+}$ cation. The $\delta(HOD)$ band(s) is(are) masked by other bands. ^d ref. 27; spectra recorded at 77 K. ^e ref. 28; KBr pellet; $C_5H_{14}N_2^{2+}$ = 2-methyl-piperazinium(2+). ^f ref. 29. ^g Bands at 3236 cm^{-1} in the 295 K spectrum and at 3238 cm^{-1} in the 8.5 K spectrum were assigned to $2\delta(HOH)$. ^h ref. 30. ⁱ Spectrum provided by E. Bernhardt (personal communication). The compound was originally reported in ref. 31 but the FTIR spectrum was not. ^j ref. 32. ^k Ref. 33; KBr pellet; $ArSO_3^-$ = 4-amino-3-methylbenzenesulfonate(1-). ^l refs. 24 and 26. ^m ref. 34; $C_6H_{14}N_2^{2+}$ = 1,4-H₂(1,4-diaza-bicyclo-[2.2.2]octane)²⁺; the band at 1674 cm^{-1} may be due to another vibration and may be masking the true $\delta(HOH)$ band, which is probably at ca. 1600 cm^{-1} . ⁿ ref. 35; from Raman spectrum. ^o This work; sample provided by L. Liu and Prof. P. S. Halasyamani. ^p ref. 36. ^q ref. 37. ^r ref. 38; KBr disc.

Table 4.9. Bond distances and bond valences for the SC-XRD structure of $\text{Ca}(\text{H}_2\text{O})_7(\text{B}_{12}\text{F}_{12})$

$\text{Ca}(\text{H}_2\text{O})_7(\text{B}_{12}\text{F}_{12})$	bond	distance, Å	<i>bv</i> param.	<i>bv</i>
This work	Ca-O	2.347	1.967	0.358
	Ca-O	2.360	1.967	0.346
	Ca-O	2.367	1.967	0.339
	Ca-O	2.389	1.967	0.319
	Ca-O	2.394	1.967	0.315
	Ca-O	2.403	1.967	0.308
	Ca-O	2.489	1.967	0.244
			$\Sigma (\text{Ca-O}(bv) =$	2.230
	ave. Ca-O =	2.393		

Table 4.10. Bond distances and bond valences for the SC-XRD structure of $\text{Sr}(\text{H}_2\text{O})_7(\text{B}_{12}\text{F}_{12})$

$\text{Sr}(\text{H}_2\text{O})_7(\text{B}_{12}\text{F}_{12})$	bond	distance, Å	<i>bv</i> param.	<i>bv</i>
This work	Sr-O	2.560	2.118	0.303
	Sr-O	2.650	2.118	0.237
	Sr-O	2.617	2.118	0.260
	Sr-O	2.674	2.118	0.223
	Sr-O	2.560	2.118	0.303
	Sr-O	2.617	2.118	0.260
	Sr-O	2.674	2.118	0.223
	Sr-F	2.665	2.019	0.174
	Sr-F	2.665	2.019	0.174
			$\Sigma(bv) =$	2.156
			$\Sigma(\text{Sr-O } bv) =$	1.807
				83.8%

Table 4.11. Bond distances and bond valences for the SC-XRD structure of Ba(H₂O)₄(B₁₂F₁₂)

Ba(H ₂ O) ₄ (B ₁₂ F ₁₂)	bond	distance, Å	<i>bv</i> param.	<i>bv</i>		bond	distance, Å	<i>bv</i> param.	<i>bv</i>
This work	Ba1-O	2.698	2.29	0.332		Ba2-O	2.685	2.29	0.344
	Ba1-O	2.783	2.29	0.264		Ba2-O	2.703	2.29	0.328
	Ba1-O	2.785	2.29	0.262		Ba2-O	2.750	2.29	0.288
	Ba1-O	2.786	2.29	0.262		Ba2-O	2.851	2.29	0.220
	Ba1-F	2.652	2.19	0.287		Ba2-F	2.741	2.19	0.226
	Ba1-F	2.657	2.19	0.283		Ba2-F	2.743	2.19	0.224
	Ba1-F	2.754	2.19	0.218		Ba2-F	2.757	2.19	0.216
	Ba1-F	2.767	2.19	0.210		Ba2-F	2.778	2.19	0.204
	Ba1-F	3.243	2.19	0.058		Ba2-F	3.116	2.19	0.082
			$\Sigma(bv) =$	2.176				$\Sigma(bv) =$	2.131
			$\Sigma(\text{Ba-O } bv) =$	1.120				$\Sigma(\text{Ba-O } bv) =$	1.179
				51.5%					55.3%

Table 4.12. Bond distances and bond valences for the SC-XRD structure of Ba(H₂O)₅(B₁₂F₁₂)

Ba(H ₂ O) ₅ (B ₁₂ F ₁₂)	bond	distance, Å	<i>bv</i> param.	<i>bv</i>
This work	Ba-O	2.7440	2.29	0.293
	Ba-O	2.7158	2.29	0.316
	Ba-O	2.8202	2.29	0.239
	Ba-O	2.8232	2.29	0.237
	Ba-O	2.8702	2.29	0.208
	Ba-F	2.7927	2.19	0.196
	Ba-F	3.2670	2.19	0.054
	Ba-F	2.9305	2.19	0.135
	Ba-F	3.0620	2.19	0.095
	Ba-F	3.1934	2.19	0.066
	Ba-F	2.8220	2.19	0.181
			$\Sigma(bv) =$	2.021
			$\Sigma(\text{Ba-O } bv) =$	1.293
				51.5%

LIST OF ABBREVIATIONS

\odot	Centroid of a B12 cage
$\angle(\text{OHX})$	O–H···X bond angle
$\nu(\text{OH})$	O–H stretching vibration
$\nu(\text{BF})$	B–F stretching vibration
$\nu_{\text{asym}}(\text{OH})$	Asymmetric O–H stretching vibration of an H ₂ O molecule
$\nu_{\text{sym}}(\text{OH})$	Symmetric O–H stretching vibration of an H ₂ O molecule
$\Delta\nu(\text{OH})$	Difference in band position of a O–H stretching vibration band compared to a reference
$\delta(\text{HOH})$	H–O–H bending vibration
$^{11}\text{B}\{^{19}\text{F}\}$	^{11}B NMR with ^{19}F decoupling
$^{19}\text{F}\{^{11}\text{B}\}$	^{19}F NMR with ^{11}B decoupling
ATR	Attenuated Total Reflectance
ATR-FTIR	Attenuated Total Reflectance Fourier Transform Infrared Spectroscopy
BVS	Bond Valence Sums
bv	Bond Valence
dd-H ₂ O	Distilled Deionized Water
DFT	Density Functional Theory
FTIR	Fourier Transform Infrared Spectroscopy
FWHM	Full Width at Half Max
H/D	Hydrogen or Deuterium
IR	Infrared
NEt ₄	Tetraethyl ammonium
NI-ESI-MS	Negative Ion Electrospray Mass Spectrometry
NMR	Nuclear Magnetic Resonance
P-XRD	Powder X-ray Diffraction
PTFB	Perfluoro-tert-butyl
PVDF	Polyvinylidene fluoride

R(O···X)	O···X distance along the O···X vector
R(O(H)···O)	O···O distance along the O–H···O vector
RH	Relative Humidity
RT	Room Temperature
SC-XRD	Single Crystal X-ray Diffraction
TGA	Thermogravimetric Analysis
v:v	Volume to Volume
WCA	Weakly-Coordinating Anion
wt%	Weight percent
Z ²⁻	B ₁₂ F ₁₂ ²⁻